PFC/RR-86-22 DOE/ET-51013-197

Extraordinary Mode Absorption at the Electron Cyclotron Harmonic Frequencies as a Tokamak Plasma Diagnostic

Arnold Pachtman

Plasma Fusion Center
Massachusetts Institute of Technology
Cambridge, MA 02139

September 1986

This work was supported by the U.S. Department of Energy Contract No. DE-AC02-78ET51013. Reproduction, translation, publication, use and disposal, in whole or in part by or for the United States government is permitted.

EXTRAORDINARY MODE ABSORPTION AT THE ELECTRON CYCLOTRON HARMONIC FREQUENCIES AS A TOKAMAK PLASMA DIAGNOSTIC

by

ARNOLD PACHTMAN

B.S., Polytechnic Institute of New York, 1978
M.S., Polytechnic Institute of New York, 1978

Submitted to the
Department of Nuclear Engineering
in Partial Fulfillment of the Requirements
for the Degree of

DOCTOR OF PHILOSOPHY

at the

MASSACHUSETTS INSTITUTE OF TECHNOLOGY

September, 1986

Signature of Author _____
Department of Nuclear Engineering, September, 1986

Certified by _____
Dr. Stephen M. Wolfe, Thesis Supervisor

Certified by _____
Professor Ian H. Hutchinson, Thesis Reader

Accepted by _____
Professor Allan F. Henry, Chairman
Departmental Graduate Committee

EXTRAORDINARY MODE ABSORPTION AT THE ELECTRON CYCLOTRON HARMONIC FREQUENCIES AS A TOKAMAK PLASMA DIAGNOSTIC

by

ARNOLD PACHTMAN

Submitted to the Department of Nuclear Engineering
in August, 1986 in Partial Fulfillment of the Requirements
for the Degree of Doctor of Philosophy

ABSTRACT

Measurements of Extraordinary mode absorption at the electron cyclotron harmonic frequencies are of unique value in high temperature, high density Tokamak plasma diagnostic applications. An experimental study of Extraordinary mode absorption at the semi-opaque second and third harmonics has been performed on the ALCATOR C Tokamak. A narrow beam of submillimeter laser radiation was used to illuminate the plasma in a horizontal plane, providing a continuous measurement of the one-pass, quasi-perpendicular transmission.

Experimental electron cyclotron absorption (ECA) data has been found to agree with lowest significant order finite density and finite Larmor radius theoretical results, and to follow $n_e T_e^2/B_t'$ scaling from 1 to 12×10^{21} [$\mathrm{cm^{-3}\ eV^2/(Tesla/cm)}$] at the third harmonic. ECA data has been used along with Tokamak electron density and magnetic field data to determine local electron temperatures in the range $75 \leq T_e(\mathrm{eV}) \leq 3300$. Plasmas with line averaged electron densities $.3 \leq n_e(10^{14}\mathrm{cm^{-3}}) \leq 3.3$, plasma currents $I_p \leq 500$ kA, and magnetic fields $7.5 \leq B_t(\mathrm{Tesla}) \leq 10.5$ have been studied. ECA measurements produce CW temperature data with a large T_e dynamic range and a spatial resolution ≤ 1 cm. Conditions studied include Ohmic and Lower Hybrid frequency RF (LHRF) Heating and Current Drive, with powers $P_{RF} \leq 1$ MW. Transmission during LHRF injection remains unaffected by suprathermal electrons due to their low density and the relativistic downshift of the absorption line. This allowed the ECA technique to be used to measure the bulk plasma temperature during LHRF Heating.

Sawtooth and m= 1 MHD activity were observed on the raw ECA signal. These behaved in the expected manner, and were well correlated with other diagnostics of MHD activity. A density dependent non-resonant attenuation (NRA) was observed which, when present, was taken into account in the data analysis. The NRA is thought to possibly originate in scattering of the submillimeter wave radiation by turbulence in the plasma edge region.

Thesis Supervisor: Dr. Stephen M. Wolfe
Title: Research Staff, MIT Plasma Fusion Center

Thesis Reader: Professor Ian H. Hutchinson
Titles: Associate Professor of Nuclear Engineering
Research Staff, MIT Plasma Fusion Center

ACKNOWLEDGEMENTS

The investigations comprising this work were conducted under the auspices of the ALCATOR group at the MIT Plasma Fusion Center, in the period beginning January 1979 through August 1986. As part of a collaborative effort, I have become indebted, in ways both large and small, to the scientists, engineers, technicians and administrative personnel who are ALCATOR.

I would like to begin by thanking Professor Ronald R. Parker, Director of the ALCATOR project, and my research advisor, Dr. Stephen M. Wolfe, for sponsoring and supporting my scholastic endeavors over a period of some seven and one half years. I also thank Professor Ian H. Hutchinson, who served as as my thesis reader, and advisor as well. I have always reserved my toughest and most perplexing problems for Professor Hutchinson, and he has never failed to astound me with the alacrity, accuracy, and elegance of his solutions. My thanks also go to Professor Lawrence M. Lidsky, for his years of guidance and friendship.

I would like to thank Mr. Frank Tambini, and Mr. Bob Childs, who have generously shared their time and technical expertise, as well as personal friendship. Mr. Frank Silva, Mr. Charlie Park, Mr. Ed Thibeault, Mr. Joe Daigle, Mr. Norton Pierce, Mr. George Chihoski, and their talented crews, have all contributed immeasurably to the experiment and its success. I thank Mr. Francis Woody Woodworth, head of the Nuclear Reactor Machine Shop at the time the experiment was constructed, and his expert staff of artisans, who crafted the experiment hardware with rare precision. My thanks go to Mr. Don Nelson, Computer Systems Manager, and his able associates. I would like to thank Mr. Anatole Chernomordik, the consummate artist *cum* engineer, for beautifying this work with figures 3.1, 3.2 and 3.5, and for bringing a splash of color to a sometimes drab and calculating business. I am grateful to Dr. Paul Woskoboinikow, and Mr. William Mulligan, who have time after time come through generously with key materials and astute advice in times of need. Thanks are due Mr. Kosuke Kato, my colleague of many years, who began by assisting me as a UROP student, and is currently finishing his Ph.D. along with me. I thank Mr. Frank Camacho, a fellow graduate student, for allowing me to use his clever TEX macros in typesetting this thesis. I also thank Mr. Tue Nguyen and Mr. David Hoenig, who assisted in the project as UROP students.

Finally, and perhaps most of all, I would like to thank my instructors at Harvard University, Teacher Shou-Ying L. Lin, Teacher Ai-ling Chen, Teacher Cindy Hu, and Teacher Yi-Hua Wang, for their genuine personal interest in my development and success, and for helping to ensure that my life will continue to unfold as in my wildest dreams.

TABLE OF CONTENTS

LIST OF FIGURES

LIST OF TABLES

Chapter 1

INTRODUCTION

The practical importance of radiation phenomena in the electron cyclotron resonance (ECR) range of frequencies was recognized early on in controlled thermonuclear fusion research and throughout its development. Topics which have been considered theoretically or investigated experimentally include the role of cyclotron emission in fusion reactor power balance,[1,2] the diagnostic potential of emission at ω_c and its harmonics, [3,4,5] and plasma heating at or near the electron cyclotron frequency ω_c.[6]

In this work, the unique plasma diagnostic capabilities offered by electron cyclotron harmonic absorption in a Tokamak plasma are suggested and demonstrated experimentally. A narrow beam of laser radiation was used to illuminate the plasma and provide a continuous measurement of the plasma transmission. The measured transmission is shown to be directly related to the plasma conditions at the resonance, and such information is used to fulfill a variety of plasma diagnostic applications.

1.1 Motivation For and Goals Of the Experiment

The physical attributes of electron cyclotron harmonic absorption processes render ECR based schemes superlative in plasma operation and control applications, as well as in plasma diagnostic applications. However, due to the difficulty in obtaining high power submillimeter wave sources, experimental studies of ECRH and cyclotron absorption have generally been limited to conditions of low field and frequency, in bands covered by extant klystron technology. With the advent of Free Electron Laser[7] (FEL) and Gyrotron[8] technologies, powerful CW sources in the .1 to 1 THz range are becoming available which are well suited for plasma diagnostic experiments at the cyclotron harmonics $n \geq 2$, and hold promise in practical applications such as Tokamak plasma startup, RF Heating, profile control, and CW Current Drive. For both plasma operation and diagnostic schemes we desire

- Reliable CW technologies available in the frequency range of interest;
- Good accessibility and coupling to the absorption region;
- Spatially localized energy deposition for optimum resolution;
- Selective energy deposition in either the thermal electron bulk (RF Heating or thermal diagnostic scheme) or a suprathermal component (Current Drive or suprathermal diagnostic scheme);
- Description within a tractable theoretical framework.

For schemes in which a change in the bulk plasma is intended, we must also require

- Reliable, efficient, high power technologies available in the frequency range of interest;
- Benevolent scaling of absorption with n_e, T_e in the range of application;
- Efficient, linear absorption mechanism which does not degrade confinement.

While the physics requirements are benignly satisfied for ECR frequencies, more progress is needed in areas relating to technological resource issues. With continued advances in Gyrotron performance and Free Electron Laser development, these final obstacles may soon be overcome in the electron cyclotron harmonic range of frequencies for contemporary and next generation high field devices.

Due to the general unavailability of reliable submillimeter sources, and to the widespread success achieved in related diagnostic applications involving $n\omega_c$ emission, relatively little has been done to exploit the rich diagnostic potential of cyclotron absorption. In this work, the unique diagnostic capabilities offered by cyclotron harmonic absorption are demonstrated in an experimental study of Extraordinary mode transmission at $\omega = 2, 3\,\omega_c$. The ranges of density, temperature, and frequency studied approach those expected for future high field ignition devices, under a variety of reactor relevant conditions such as RF Heating and Current Drive.

The specific goals targeted and realized in the course of this endeavor are highlighted as follows:

- To investigate ECR harmonic absorption at high frequencies under thermonuclear- relevant conditions of high density and temperature, and to evaluate the accuracy of theoretical descriptions in an extended parameter range;
- To study ECR harmonic absorption during Lower Hybrid Heating (LHH) and Current Drive (LHCD), and to experimentally verify theoretical predictions regarding absorption by suprathermal electrons under these conditions;
- To provide a powerful diagnostic of bulk plasma electron temperature which is valid during Ohmic and LHRF Heating and Current Drive operation;
- To document other effects which are relevant to the propagation of high frequency radiation in the high density, high temperature Tokamak plasma regime.

1.2 Descriptions of Prior and The Current Work

Experimental studies of ECR harmonic absorption were reported as early as 1967 on the Model C Stellarator,[9] in which 75 GHz radiation was used to study Extraordinary mode absorption at $2\omega_c$ in a plasma with $T_e = 35$ eV, $n_e = 10^{12}$ cm^{-3}. Investigations of cyclotron absorption in Tokamaks began with the ECRH work of Alikaev, et al on TM−3 in 1975.[6] In the ensuing years, ECRH investigations have met with considerable success in practically every major and minor magnetic confinement configuration, with experiments on the ISX-B and T−10 Tokamaks, EBT and NBT Bumpy Tori, and the TMX Tandem Mirror of particular note.

In contrast to the ECRH related work, there have been relatively few studies of expressly plasma diagnostic intent, and these have been quite limited in depth and scope. These efforts are summarized in table 1.1, along with the present work.

Table 1.1

Major Electron Cyclotron Absorption Diagnostic Experiments To Date

Group	Machine	ω/ω_c; Mode	B_{t0}(Tesla)	$\bar{n}_e(10^{13}\text{cm}^{-3})$	T_e(eV)
Arunasalam, et al,[9] 1968	Model C Stellarator	2; X	1.3	.1	< 35
Efthimion, et al,[10] 1979	PLT	1; O	2.5	2.7	< 900
McDermott,[11] 1984	ISX-B	2; X	1.3	2.	800
Mazzucato, et al,[12] 1985	PLT	$.7 - .9$; O	3.2	< 1	Supra-Thermal
This Work: Pachtman, et al,[13] $1983 - 1985$	ALCATOR C	2,3; X	$7.5 - 10.5$	$3. - 33.$	$75 - 3300$

In all except the current work, the transmission measurements were conducted as in 1968, with a 4 mm Klystron and microwave detection apparatus. The present work is seen to represent a multifold advance in the magnetic field, electron density, and electron temperature regimes studied, and for the first time, absorption measurements at $3\omega_c$ have been made. As the 700 GHz frequencies used are well beyond the range of conventional microwave technologies, an optically pumped far infra-red waveguide laser source was constructed. The laser radiation was transported in free space as a Gaussian beam, or quasi-optically in overmoded circular metallic waveguide.

In the experiment operation, a narrow beam of laser radiation at the second or third cyclotron harmonic frequency illuminated the plasma in a perpendicular

plane. The radiation was focused onto the aperture of a waveguide located at the back wall of the Tokamak, protected from the discharge by full poloidal limiters. The transmitted radiation was transported via waveguide to the detector, which provided a continuous measurement of the one pass perpendicular plasma transmission. With laser power data which was recorded simultaneously, the plasma absorption at the laser frequency was obtained, and was related to the plasma parameters at the location where the cyclotron resonance occurs. This information was used to fulfill a variety of diagnostic functions, providing an independent plasma measurement, or an evaluation of a theoretical prediction.

1.3 The ALCATOR C Tokamak

The ALCATOR program is dedicated to the investigation of magnetic confinement physics and the development of ancillary fusion research methods and plasma technologies. The ALCATOR confinement approach is based on a high field, compact Tokamak design which has proven itself repeatedly with record breaking plasma performance. The program began in 1974 with the operation of ALCATOR A, which had a major radius $R = 54$ cm, and a minor radius $a = 9$ cm. This device held a record in both plasma density and Lawson product until its decommission in 1980. A second, larger device, ALCATOR C, with $R = 64$ cm, and $a = 16.5$ cm, began operation in 1978, and is still active. In 1983, ALCATOR C achieved the Lawson product $n\tau_e = 8 \times 10^{13}$ sec cm^{-3}, a figure which stands to date as a world record, and exceeds the theoretical minimum thermalized breakeven value at a 30 KeV ion temperature. A succeeding device, ALCATOR C-MOD, is the heir apparent to the ALCATOR concept, and is in the final stages of planning.

The key to the success of the ALCATOR approach is the Bitter plate toroidal magnet construction,[14] in which the Copper magnet turns are interlocked with stress bearing Nitronic 40 Steel plates in a monolithic design. This allows operation at extremely high toroidal fields, in a nearly force free, free standing configuration. Nearly 30,000 pounds of Copper comprise the toroidal field coil, with the remaining

ohmic and equilibrium field coils constituting an additional 10,000 pounds. Cryogenic operation of the magnets at liquid Nitrogen temperature (77° K) diminishes the overall power consumption by a factor of 8. Power is supplied to the Tokamak by a 225 MW alternator which was donated by Con Edison in 1979. An artist's rendering of ALCATOR C is shown in figure 1.1, and a summary of the parameters describing its operation is presented in table 1.2.

Table 1.2

ALCATOR C Parameters

Parameter	Standard Value (Maximum Value)
Major Radius	$R = 64$ cm
Minor Radius	$a = 16.5$ cm
Aspect Ratio	$\epsilon = 3.9$
Toroidal Magnetic Field	$B_t = 8$ Tesla (12 T)
Plasma Current	$I_p = 500$ kA (700 kA)
Safety Factor	$q_{\text{limiter}} = 3.4$
Central Electron Density	$n_{e0} = 2.2 \times 10^{14}$ cm^{-3} (2×10^{15} cm^{-3})
Central Electron Temperature	$T_{e0} = 2$ keV (3.5 keV)
Central Ion Temperature	$T_{i0} = 1.5$ keV (2 keV)
Energy Confinement Time	$\tau_e = 25$ msec (50 msec)
Lawson Number	$n_e\tau_e = 6 \times 10^{12}$ sec/cm^{-3} (8×10^{13} sec/cm^{-3})

In addition to the extraordinary ohmic performance achieved on ALCATOR, much attention has been devoted to the study of auxiliary RF Heating and Current Drive, and to solid pellet fueling. Up to 4 MW of 4.6 GHz radiation is available

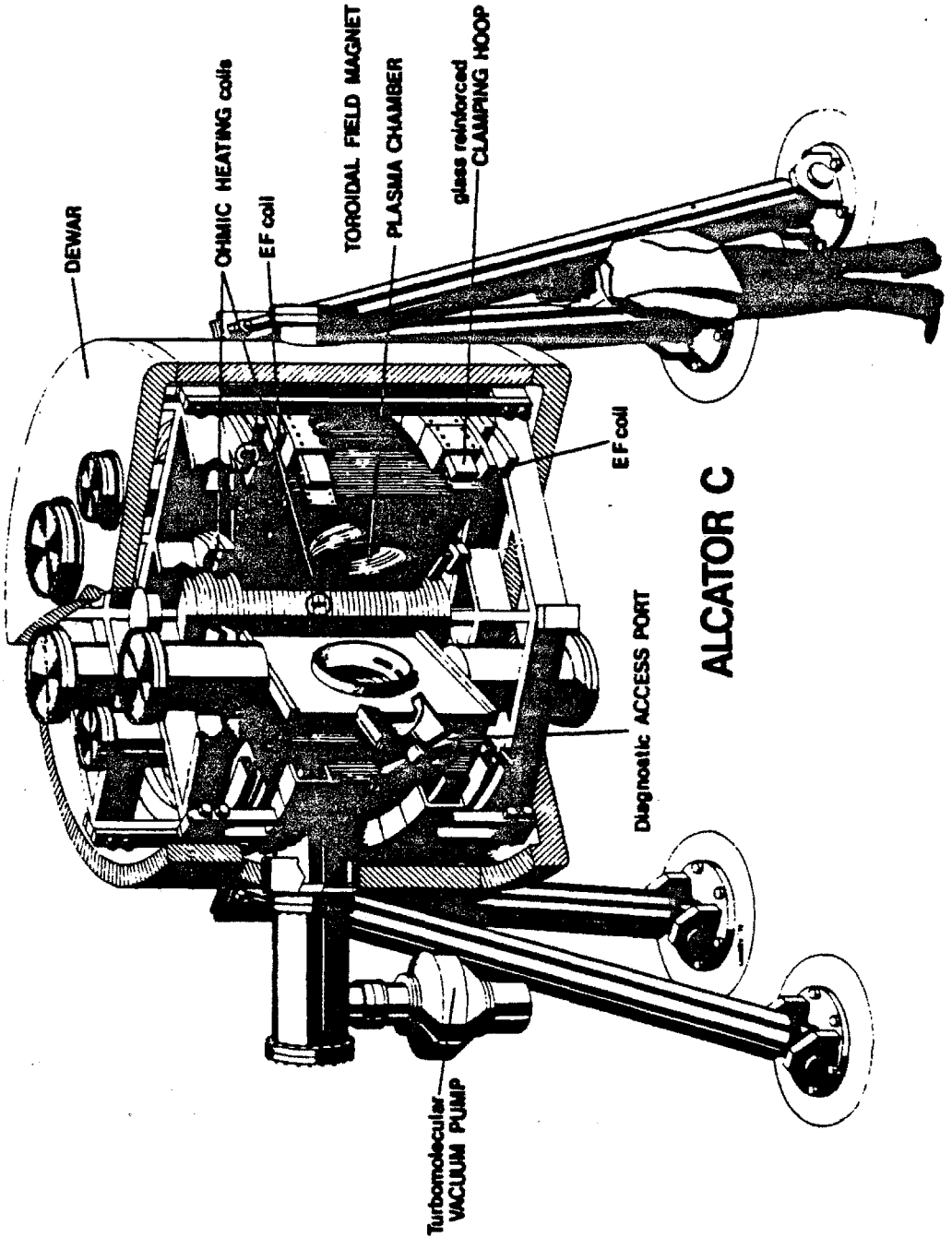

Figure 1.1 — The ALCATOR C Tokamak. Vertical diagnotic slots are visible at the bottom of the access port flange (foreground).

for Lower Hybrid Heating and Current Drive studies, and impressive performance at high densities has been achieved in these areas. In addition, 6 MW of 180 MHz radiation are available for Ion Cyclotron Heating experiments. Experiments have been performed in which solid pellets of frozen Hydrogen are injected across the magnetic field at speeds approaching 800 m/sec, ablating in and rapidly fueling the hot discharge. These pellet fueling experiments have provided important insights into mechanisms of energy confinement in Tokamaks, a physics issue of paramount importance to the realization of plasma ignition and controlled energy production in future plasma devices.

1.4 Organization of This Work

In this work, the plasma diagnostic applications of Extraordinary mode electron cyclotron harmonic absorption in a hot, dense Tokamak plasma are suggested, developed and demonstrated for the second and third harmonic frequencies. The experiment was introduced from the historical perspective of studies of electron cyclotron resonance phenomena. Specific goals were set forth, and it was seen that the present work represents a multifold advance in the regimes of several key parameters. This renders the current experiment and its results relevant to present day as well as next generation plasma confinement devices.

In chapter 2, we begin with an exposition of numerous theoretical issues which are requisite to developing an appreciation of the subject of cyclotron harmonic absorption, and of the present work. Topics are introduced and developed on physical grounds, with emphasis placed on motivating a sound physical understanding. Analytical procedures are reviewed in conjunction with important results, but the bulk of computational detail is relegated to the now venerable corpus of literature.

We proceed to a description of the physical implementation of the experiment in chapter 3. The general layout of the apparatus is discussed, and important considerations relating to experiment geometry are detailed. The various subsystems for producing, transporting, processing, and detecting the $3\omega_c$ probe radiation

are considered individually, and the performance characteristics and peculiarities of each component are documented.

Chapter 4 describes the analytical tools developed to proceed from raw data to final result. Numerous computer codes which process, reduce and analyze the transmission and reference data produced by the experiment are discussed, and the generation and propagation of errors are examined in detail.

In chapter 5 we present the key diagnostic results of this work. Experimental data is shown which verifies the theoretical framework formulated in Chapter 2, and demonstrates the temperature diagnostic function of the experiment in a wide variety of applications and an extended temperature range.

Chapter 6 delves into the nature and origins of a non-resonant effect which was discovered in the course of this work. Various mechanisms are modeled and their effects assessed, and the full complexity of the issues at hand is made evident in a series of speculative discussions.

The work concludes in chapter 7 with a summary of the thesis' salient results. Based on these, conclusions are drawn, and recommendations are made which may be of relevance to future undertakings in this area.

Chapter 2

THEORETICAL ASPECTS OF THE EXPERIMENT

In this chapter, the theoretical aspects of the experiment are presented. The discussions open with a brief outline of the basic features and results of linear plasma wave dynamics and cold plasma dispersion. Attributes and quantities which divide the general problem of ECR absorption and emission along physical lines are examined, and a general formalism is introduced to describe the propagation of radiation in a plasma medium. These principles are applied to the specific case of the thermal plasma bulk in ALCATOR, and optical depths appropriate to the experiment conditions are presented and discussed. Numerical values are calculated which fully characterize the experiment and quantify key parameters for future reference. The discussions conclude with a consideration of absorption by suprathermal electrons, in which theoretical treatments are reviewed and numerical results of relevance to the experiment are presented.

2.1 Plasma Wave Processes

2.1.1 Linear Plasma Wave Dynamics

A description of plasma wave phenomena begins with Maxwell's equations, which determine the electromagnetic properties of the plasma via the source terms for current density and charge density[15,16]

$$\mathbf{J} = -e \int \mathbf{p} f(\mathbf{p})\, d\mathbf{p}$$

$$\rho = -e \int f(\mathbf{p})\, d\mathbf{p}$$

where $f = f(\mathbf{r},\mathbf{p},t)$ is the electron distribution function, and $\mathbf{p} = m_0 \gamma \mathbf{v}$ is the electron momentum. $\mathbf{J}$ and ρ are in turn related by a continuity equation. The distribution function evolves under the influence of the electromagnetic fields in a self-consistent manner according to the Vlasov equation,

$$\frac{\partial f}{\partial t} + \mathbf{v} \cdot \frac{\partial f}{\partial \mathbf{r}} - e\left[\mathbf{E} + \frac{\mathbf{v} \times \mathbf{B}}{c}\right] \cdot \frac{\partial f}{\partial \mathbf{p}} = 0\,,$$

which may be thought of as an equation of motion in phase space for each charge species. This system of equations can be Fourier-Laplace transformed, linearized to first order in the perturbed quantities, and solved for the linear current density and the dielectric coefficient,

$$\mathbf{J} = -\boldsymbol{\sigma} \cdot \boldsymbol{E}$$

$$\boldsymbol{\epsilon} = \boldsymbol{\epsilon}_h + \boldsymbol{\epsilon}_{a-h} \equiv \mathbf{I} - \frac{4\pi i}{\omega}\boldsymbol{\sigma}$$

where the conductivity tensor $\boldsymbol{\sigma}$ is itself a function of the distribution function. From Maxwell's equations a wave-type equation also results,

$$\mathbf{k} \times (\mathbf{k} \times \mathbf{E}) + \left(\frac{\omega}{c}\right)^2 \boldsymbol{\epsilon} \cdot \mathbf{E} \equiv \mathbf{K} \cdot \mathbf{E} = 0$$

which describes the wave propagation characteristics of the plasma medium. The dielectric coefficient $\boldsymbol{\epsilon}$, or conductivity tensor $\boldsymbol{\sigma}$, via their Hermitian and anti-Hermitian parts, are the starting point for obtaining a description of both the wave propagation and damping. Due to the asymmetry incurred by the external magnetic field $\mathbf{B} = B_z\mathbf{z}$, $\boldsymbol{\epsilon}$ and $\boldsymbol{\sigma}$ are in general 3×3 tensors whose components retain the Onsager symmetry

$$[\ ]_{xy} = -[\ ]_{yx}\ ,\ [\ ]_{yz} = -[\ ]_{zy}\ ,\ [\ ]_{zx} = -[\ ]_{xz}\ .$$

The vector wave equation for $\mathbf{E}$ has non-trivial solutions only when the determinant of coefficients of the components of $\mathbf{E}$ vanishes. This yields the so called dispersion relation,

$$det\,\mathbf{K} = 0\,,\ \text{or just}\ \mathbf{K}(\omega, \mathbf{k}, \mathbf{r}) = 0$$

the eigenvalues of which specify the normal modes of the plasma.

2.1.2 Cold Magnetized Plasma Electromagnetic Wave Dispersion

When particles are assumed to have no initial velocities, and to act only under the influence of the externally applied and oscillating wave fields, the dielectric response is independent of $\mathbf{k}$, and the dispersion relation, in the form $\mathbf{K}[\boldsymbol{\epsilon}(\omega)] = 0$, describes so called cold, uniform plasma dispersion. This less than realistic limit

of zero plasma temperature nevertheless constitutes a fundamental view of plasma behavior, the influence of which is seen throughout all plasma regimes. Of particular importance are the basic cutoff and resonance frequencies and the fundamental modes which result in this formalism.

In the electron cyclotron range of frequencies $\omega \geq \omega_c$, the cold plasma description reveals two fundamental modes. As a consequence of finite density, these modes generally possess an electrostatic component, and are thus elliptically polarized in the plane of propagation. For an angle $\theta \approx 90°$ between the wave vector $\mathbf{k}$ and the external magnetic field $\mathbf{B_0}$, these correspond to the Extraordinary ("X") mode, with $\mathbf{E} \perp \mathbf{B_0}$, and the Ordinary ("O") mode, with $\mathbf{E} \parallel \mathbf{B_0}$. The X mode retains its elliptical character in this limit, while the O mode becomes completely transverse and linearly polarized.

In the cold plasma limit, wave dispersion for the X mode propagating perpendicular to $\mathbf{B_0}$ is described by the Appleton-Hartree relation,[16]

$$Re(N_\perp^2) = 1 - \left(\frac{\omega_p^2}{\omega^2}\right)\left(\frac{\omega^2 - \omega_p^2}{\omega^2 - \omega_c^2 - \omega_p^2}\right) ,$$

where ω_c is the single particle electron gyrofrequency, ω_p is the electron plasma frequency, and $N_\perp$ is the index of refraction. In order for the X mode to propagate, with $Re(N_\perp^2) > 0$, we must have either $\omega > \omega_r$ or $\omega_l < \omega < \omega_{uh}$. Here ω_r and ω_l are the Right and Left cutoffs, respectively, at which the index of refraction tends to zero, and ω_{uh} is the Upper Hybrid resonance, at which the index of refraction tends to infinity.

The O mode is found to have the simpler dispersion relation

$$Re(N_\perp^2) = 1 - \left(\frac{\omega_p^2}{\omega^2}\right) ,$$

with propagation for $\omega > \omega_p$, and no resonances.

Expressions for these important frequencies, and their approximate ranges in Alcator C, are given below.

Table 2.1

Important Frequencies in ALCATOR C

$\omega_r = \frac{\omega_c}{2}\left[\sqrt{1+(2\omega_p/\omega_c)^2}+1\right]$	$1.2 < \frac{\omega_r}{\omega_c} < 1.6$
$\omega_l = \frac{\omega_c}{2}\left[\sqrt{1+(2\omega_p/\omega_c)^2}-1\right]$	$.2 < \frac{\omega_l}{\omega_c} < .6$
$\omega_{uh} = \sqrt{\omega_p^2+\omega_c^2}$	$1.1 < \frac{\omega_{uh}}{\omega_c} < 1.4$
$\omega_p = \sqrt{\frac{4\pi n_e^2}{m_e}}$	$.5 < \frac{\omega_p}{\omega_c} < 1.0$
$\omega_c = \frac{eB_0}{m_e c}$	$200 < \omega_c(\text{Ghz}) < 300$

It is seen that the cold plasma cutoff and resonance frequencies are not generally encountered in ALCATOR C for measurements at the cyclotron harmonics n= 2 , 3.

As θ approaches zero, the X and O mode branches, in a broad sense, map into the Right (R) and Left (L) circularly polarized modes travelling along $\mathbf{B_0}$, which are purely transverse. The R mode resonates with the electron gyromotion, exhibiting a resonance at $\omega = \omega_c$, while the L mode posesses a similar resonance at the Ion Cyclotron frequency, which is smaller than ω_c by the electron/ion mass ratio and thus well out of the band of interest. These modes each have one cutoff, at ω_r for the R mode, and at ω_l for the L mode. Thus, propagation along $\mathbf{B_0}$ occurs when $\omega > \omega_l$ for the L mode, and when either $0 < \omega < \omega_c$ or $\omega > \omega_r$ for the R mode. The R mode propagation band below ω_c is the "Whistler" branch associated with atmospheric radiofrequency activity.

It is important to observe that no resonant behavior occurs at the cyclotron harmonics in a cold plasma; harmonic absorption is solely a consequence of finite plasma temperature. Another important consequence of finite temperature is the appearance of an entire class of electrostatic waves, the so called Bernstein modes, which can couple strongly to the X mode branches around ω_c and ω_{uh}, and can dramatically alter wave dispersion and propagation in this range. However, even with the inclusion of thermal effects, the cold plasma dispersion equations given

above remain valid for the X mode at harmonics n$\geq$ 3, excluding the vicinity of the Upper Hybrid resonance, and for the O mode at harmonics n$\geq$ 2.

2.2 Cyclotron Absorption and Emission Processes

The general problem of magnetized plasma absorption and emission processes in the electron cyclotron range of frequencies $\omega = n\omega_c$ can be quite complex. Theoretical treatments for high temperature plasmas include B.A. Trubnikov's landmark thesis in 1958,[1] and at present comprise a corpus of over 300 works. Fortunately, the problem does lend itself to division along certain physical lines, and numerous specialized solutions, each appropriate to a particular region of parameter space, may be sought.

2.2.1 The Role of Electron Temperature

The parameter v_e/c, where v_e is a characteristic electron velocity such as the thermal velocity, at once identifies several regimes:

1) "Strongly Relativistic" Regime ($v_e/c \approx 1$):

   In this regime one usually speaks of Synchrotron radiation, in which most of the emission resides in a continuum which extends to very high harmonics. This regime applies to a rather restricted domain within Magnetic Fusion plasma research.

2) "Weakly Relativistic" Regime ($v_e/c \ll 1$):

   Here one finds the discrete harmonic absorption/emission structure usually associated with the term Cyclotron radiation. This structure may consist of narrow lines near the frequencies $\omega = n\omega_c$, or may show considerable overlap of the harmonic contributions with increasing v_e/c. In this regime one finds most of the problems relevant to Magnetic Fusion.

3) "Cold Plasma" Regime ($v_e = 0$):

   In this regime one finds the classical magnetic bremsstrahlung problem, in which single particle radiation processes only occur at $\omega = \omega_c$. Wave propagation in a cold plasma, presented in the preceding section, is simple, yet

revealing, and provides a firm basis from which to pursue more realistic formulations.

Within the weakly relativistic regime, the parameter v_e/c determines the size of the electron gyroradius, $\rho_l = v_\perp/\omega_c$, and the important "small" parameter

$$x \equiv (k_\perp \rho_l)^2 = \left(\frac{\omega}{\omega_c}\frac{v_\perp}{c} N \sin\theta\right)^2 ,$$

which describes the so called "Finite Larmor Radius (FLR) Effects". FLR effects are indeed responsible for the appearance of absorption and emission at the cyclotron harmonics. The FLR effects vary in importance not always commensurate to the absolute size of x, and can in certain cases completely determine the characteristics of the absorption.

Another area in which relativistic effects are essential pertains to the frequency linewidth of emission and absorption around each harmonic. For trajectories which are rather oblique with respect to the external magnetic field ("Oblique Propagation"),the linewidth is primarily determined by parallel Doppler broadening due to the electron velocity component along the magnetic field. For angles near 90°, ("Perpendicular" or "Quasiperpendicular Propagation") the broadening is primarily due to the dependence of the cyclotron frequency on electron velocity via the relativistic electron mass variation, an effect known as transverse Doppler broadening. Emission at angles near perpendicular is of particular importance, so that a fully relativistic description is generally warranted.

Within the weakly relativistic regime one can effect a further subdivision based on the actual size of the parameters v_e/c and x:

1) "Low Temperature" Regime ($T_e < 10$ keV):

   In this regime, interactions are significant for low harmonics $n < 5$, and a description by discrete harmonic contributions is most appropriate. In the event that we have $x = (k_\perp \rho_l)^2 \ll 1$ as well, we may calculate quantities to "lowest significant FLR order" in the small quantity x, i.e. to the lowest order for which one finds a qualitative effect on the results. This constitutes a vast

simplification, and such a description is best for temperatures $T_e < 5$ keV or harmonics $n \leq 3$, and angles near $\pi/2$, with a few special exceptions.

2) "High Temperature" Regime ($T_e > 20$ kev):
For this case the strongest interaction resides in the high harmonics $n > 5$, the spectrum tends to become continuous, and an integral formulation is therefore most convenient.

3) "Intermediate Temperature" Regime:
Lying between the above two regimes, this regime has features of both continuum and harmonic emission. Here one finds the greatest complexity, and descriptions entail a sum over harmonic contributions, each containing integrals which must be done numerically.

Of these three, descriptions in the Low temperature regime are the most tractable, albeit with an abundance of fine detail. Fortunately, this regime encompasses many problems of relevance to present day and next generation plasma devices, in applications such as plasma diagnostics, pre-ignition DT plasma heating, and plasma temperature and current profile control.

Another consideration of some import in the selection of an appropriate description of cyclotron radiation processes is the nature of the electron distribution function, $f(p_\parallel, p_\perp)$. Considerable simplifications obtain for isotropic distributions, $f = f(p)$. Of particular importance is the case of thermal equilibrium, where electrons are characterized by a Maxwellian, in either relativistic or non-relativistic form. Nature is tenacious in seeking to restore a semblance of thermal equilibrium to a perturbed system via collisions, and consequently, treatments for the relativistic Maxwellian have received the most attention, and have yielded the most useful results. These include decidedly non-equilibrium states, such as those consisting of superimposed streaming Maxwellian components, and bi-Maxwellians.

2.2.2 The Role of Electron Density

The first descriptions of cyclotron radiation processes assumed that the electron density is low enough to treat cyclotron radiation as magnetic bremsstrahlung

from an ensemble of individual electrons. In this "Tenuous Plasma" limit the resulting formulation is quite simple. Plasma dispersion and electron correlation effects are negligible, polarization and mode coupling effects are weak, the flow of power through the plasma is non-kinetic in character and is adequately represented by the Poynting flux, and plasma effects tend to be proportional to density.

The criterion which sufficiently identifies the tenuous plasma limit is that all elements of the susceptibility tensor

$$\chi_{ij} \equiv (\epsilon - 1)_{ij} = -\frac{4\pi i}{\omega}\sigma_{ij}$$

are small compared to unity. Finite density effects enter the dielectric tensor via powers of the parameter $(\omega_p/\omega)^2$, where $\omega = n\omega_c$. Thus, when the frequency under consideration is large compared to the plasma frequency, we may in many cases use results of lowest significant order in $(\omega_p/\omega)^2$, with confidence.

However, as the frequency under consideration approaches ω_p, the Hermitian part of the susceptibility tensor approaches unity, and dispersion and polarization effects enter strongly, causing a nonlinear or even inverse dependence on the density. In this "Finite Density" limit, the complexity of the problem grows rapidly, with a detailed dependence on temperature, propagation angle, polarization, and harmonic, which may vary considerably from one set of circumstances to the next. This complexity is partly due to the appearance of "cross effects" such as the finite density-FLR effects $\mathcal{O}[(\omega_p/\omega)^{2j}, (k_\perp \rho_l)^{2k}]$ found for the X mode at $n = 1$, or the finite density-finite temperature effects $\mathcal{O}[(\omega_p/\omega)^{2j}, (v_e/c)^{2k}]$ found for the X and O modes at $n = 2$.

2.2.3 The Geometrical Optics Radiative Transfer Formulation

When plasma variations occur on a scale which is large compared to a wavelength, and a time which is long compared to a wave period, one may employ a powerful simplification in which the wave propagation and damping is described via a statement of local energy conservation along the ray path. This situation is generally appropriate for conditions of "Weak Absorption", which is sufficiently

specified for a wave vector $\mathbf{k} = \mathbf{k}' + i\mathbf{k}''$ by the condition $\mathbf{k}'' \ll \mathbf{k}'$. This WKB-type formulation not only requires that global plasma variations are weak, but also rules out circumstances where mode conversion is important or near a resonance where $\epsilon_{anti-hermitian} \approx \epsilon_{hermitian}$.

When "Strong Absorption" prevails, absorption takes place over one wavelength or less, and one can no longer speak of wave propagation, per se. Damping must then be described by an explicit calculation of the imaginary part of the index of refraction, $N_\perp''$, in which finite Larmor radius and/or finite temperature corrections are essential. This situation may be encountered for the O mode at $n = 1$, and for the X mode, at $n = 2$ or when coupling to electrostatic Bernstein-like modes is strong.

However, when $\epsilon_{a-h} \ll \epsilon_h$ or $\mathbf{k}'' \ll \mathbf{k}'$ applies and the plasma equilibrium is quasi-stationary, the radiation transfer problem is described in a Geometrical Optics formulation by the "Equation of Transfer":[15]

$$N_r^2 \frac{\partial}{\partial s}\left(\frac{I_\omega}{N_r^2}\right) = j_\omega - \alpha_\omega I_\omega \qquad [2.1]$$

where we define

Spectral Intensity	I_ω [Power/Area $\cdot\, \omega \cdot \Omega$]
Emission coefficient	j_ω [Power/Volume $\cdot\, \omega \cdot \Omega$]
Absorption coefficient	α_ω [1/Length]
Ray Refractive Index	N_r

The Ray Refractive index is a measure of the anisotropy of the medium, and is equal to a constant for homogeneous plasmas. N_r approaches N' when the angle between k' and the Group Velocity

$$\mathbf{v}_{gr} \equiv \frac{\partial \omega}{\partial \mathbf{k}'}$$

tends to 0, in which case the power flows in the direction of k'. We also introduce the useful quantities[15]

Optical Depth	$\tau = -\int_{\text{entry}}^{\text{exit}} \alpha_\omega(\mathbf{s}) ds$
Source Function	$S_\omega \equiv \frac{1}{N_r^2}\frac{j_\omega}{\alpha_\omega}$[Power/Area $\cdot\,\omega\cdot\,\Omega$]
	$S_\omega \Rightarrow \frac{\omega^2}{8\pi^3 c^2} kT_r$
Radiation Temperature	T_r [keV] ,

with T_r defined by the preceding two relations. The Optical Depth is a measure of the opacity of an entire region to the radiation under consideration. The Source function describes the emission characteristics of the medium, and the Radiation temperature, as defined above, is seen to reflect the degree of departure from thermal equilibrium. These expressions, relating S_ω or T_r, j_ω, and α_ω, can be taken as a general statement of Kirchoff's Law, valid in thermal equilibrium or otherwise. When thermal equilibrium does prevail, the Radiation temperature is equal to the Maxwellian temperature, and the Source function is seen to become the Blackbody function in the Rayleigh–Jeans limit, $h\nu/kT \ll 1$. For isotropic distribution functions $f = f(p)$, the absorption and emission coefficients and the Radiation temperature can be directly related to the microscopic spontaneous emission coefficient $\eta_\omega(\mathbf{p})$ [Power/Volume $\cdot\,\omega\cdot\,\Omega$] and $f(p)$ via

$$j_\omega = \int \eta_\omega(\mathbf{p}) f(p)\, d\mathbf{p}$$

$$\alpha_\omega = -\frac{8\pi^3 c^2}{N_r^2 \omega^2} \int \eta_\omega(\mathbf{p}) \frac{\partial f}{\partial E}\, d\mathbf{p} \qquad [2.2]$$

$$kT_r \Rightarrow -\frac{\int \eta_\omega(\mathbf{p}) f(p)\, d\mathbf{p}}{\int \eta_\omega(\mathbf{p}) \frac{\partial f(p)}{\partial E}\, d\mathbf{p}}$$

where E is the particle energy $p^2/2m$. For an isotropic Maxwellian distribution in the classical limit,

$$f(p) \propto e^{-\frac{p^2/2m}{kT_e}} \quad , \quad \frac{\partial f(p)}{\partial E} = -\frac{1}{kT_e} f(p)$$

so that in thermal equilibrium $kT_r = kT_e$. Away from thermal equilibrium, the difference seen in the structure of j_ω and α_ω has a profound impact on the behavior

of absorption and emission at the cyclotron harmonics for suprathermal electron distributions. This point will be elaborated on in section 2.4 .

Equation 2.1 can be reformulated in terms of the above quantities, and with the further assumption that the Source function is constant along the portion of the ray path where absorption occurs, a particularly useful expression is obtained for I_ω:

$$I_\omega = I_{\omega 0} e^{-\tau_0} + S_\omega (1 - e^{-\tau_0}) \qquad [2.3]$$

$$\mathbf{T} \equiv e^{-\tau_0}.$$

Here we have introduced the Transmission **T**, the principle measured quantity of this work. The limiting behavior of this solution specifies three conditions:

1) $\tau_0 \ll 1$ "Optically Thin" : $I_\omega = I_{\omega 0} + \tau_0 S_\omega$, $\mathbf{T} \approx 1 - \tau_0$

   Here the transmission is close to unity, and radiation emitted anywhere along the ray path is received at the exit point. This regime finds application in the study of non-thermal electron distribution functions, such as those found during Lower Hybrid Current Drive.

2) $\tau_0 \gg 1$ "Optically Thick" : $I_\omega = S_\omega$, $\mathbf{T} \approx 0$

   In this limit, the medium becomes opaque to the external radiation, and only emitted radiation which originates near an optical depth of unity from the exterior can be received at the exit point. As the emission in this case is a direct measure of the Source function, this limit finds considerable use in plasma diagnostic applications. For thermal plasmas, S_ω becomes the Blackbody function, so that emission in a "black" harmonic provides a direct measure of the the electron temperature. Second harmonic X mode emission is widely used in this application.

3) $\tau_0 \approx 1$ "Semi-opaque" :

   This situation requires I_ω as written above. While being the most complex, this regime also has the greatest diagnostic potential, providing information about τ_0 as well as S_ω. This is the domain of transmission experiments, which have transmissions of $10 - 90\%$. In this work, second and third harmonic X

mode transmissions are used to diagnose the electron temperature at various positions in the plasma.

Thus, a theoretical description of the plasma transmission entails a calculation of the absorption coefficient and the optical depth at the working frequency.

As discussed in the beginning of this section, there are several methods which can be used to calculate the wave damping. A method of general validity entails a calculation of the index of refraction $N = N' + iN''$, from which α_ω is derived as

$$\alpha_\omega \equiv 2\mathbf{k}'' \cdot \frac{\mathbf{v}_{gr}}{v_{gr}}, \text{ with}$$

$$\mathbf{k}'' \equiv \frac{\omega}{c} N'',$$

Under the WKB assumptions discussed above, we can also represent α_ω as

$$\alpha_\omega = \frac{\langle P_{abs} \rangle}{S}$$

$\langle P_{abs} \rangle \equiv$ Power Absorbed, per unit frequency, volume in $\mathbf{k}'$ space

$S \equiv$ Power Flux Density per unit frequency, volume in $\mathbf{k}'$ space

$\langle \ \ \rangle =$ Time Average ,

a formulation which brings considerable savings in computational effort and detail. S includes the electromagnetic (Poynting) flux, as well as the kinetic (reactive or "sloshing") flux associated with the particles, for finite temperature plasmas.

Using the relations between the linear current density, dielectric coefficient, and conductivity tensor presented in section 2.1.1, the absorbed power can be expressed as

$$\langle P_{abs} \rangle = \langle \mathbf{J} \cdot \mathbf{E} \rangle$$

$$= \frac{\omega}{4\pi} \mathbf{E}^* \cdot \epsilon_{a-h} \cdot \mathbf{E}$$

$$= \mathbf{E}^* \cdot \sigma_h \cdot \mathbf{E} \ .$$

The power flux density vector has two components,

$$\mathbf{S} = \frac{c}{4\pi}\, Re\,(\mathbf{E} \times \mathbf{B}^*) - \frac{\omega}{8\pi}\, \mathbf{E}^* \cdot \frac{\partial \epsilon_h}{\partial \mathbf{k}'} \cdot \mathbf{E}$$

the first term corresponding to the Poynting flux, and the second to the coherent particle energy flux.

Thus, if one obtains an expression for the dielectric tensor which is valid in a region of the physical parameter space outlined in the preceding sections, one can easily obtain the damping under those conditions, to lowest WKB order.

2.3 Thermal Plasma Transmission in the Weakly Relativistic Regime

2.3.1 General Physical Considerations

Plasmas with bulk electron temperatures in the tens of keV range and below are well modeled in the weakly Relativistic limit. In this regime, which encompasses most of the problems relevant to Magnetic Fusion research, much of the fundamental physics governing the absorption process is forthcoming in a direct manner.

By the integration of the linearized Vlasov equation over the appropriate orbits $\mathbf{p}'(\mathbf{p}, t', t)$, $\mathbf{r}'(\mathbf{r}, t', t)$ and the use of Maxwell's equations, one can obtain a formal integral prescription for the dielectric tensor ϵ. The integrand may be expanded in a Bessel function series, and recast in the general form[15]

$$\epsilon = \mathbf{1} + \frac{\omega_p^2}{\omega^2} \int \sum_{n=-\infty}^{\infty} \frac{\mathbf{S}(x, \mathbf{p}, \mathbf{k}, \omega)}{\gamma(\omega - k_\parallel v_\parallel - n\omega_c/\gamma)}\, d\mathbf{p}\,, \qquad [2.4]$$

$$\gamma \equiv \sqrt{1 - \frac{v^2}{c^2}}\,.$$

The function $\mathbf{S}$ is a 3×3 Hermitian tensor, whose components are explicit functions of the FLR parameter $x \equiv \frac{k_\perp v_\perp}{\omega_c/\gamma}$, Bessel terms $J_n(x)$ and $J_n'(x)$, and assorted derivatives of $f(p_\parallel, p_\perp)$ with respect to $p_\parallel$ and $p_\perp$.

This form of ϵ, which is fully relativistic and valid for arbitrary $f(\mathbf{p})$, contains several interesting features. First, $1/x$ is a key quantity in the components the tensor $\mathbf{S}$ and the dielectric function. This dependence underlies the central role

which the FLR parameter played in the physical discussions of section 2.2. Second, although the summation is over all n, in certain cases only the terms near $n = \omega/\omega_c$ contribute appreciably; this introduces some latitude in selecting a strategy for calculating the dielectric response and damping. For cases in which many orders contribute, such as in the High temperature regime, more specialized and compact formulations may sometimes be desirable.

Resonant contributions for each harmonic occur when the denominator of the integrand tends to zero. In the weakly relativistic limit, we may expand γ in the small parameter $\mu \equiv (v_e/c)^2$ and rewrite the denominator in a form which directly displays the lineshape dynamics,

$$\omega - k_\parallel v_\parallel - \frac{n\omega_c}{\gamma} = 0$$

$$\omega - n\omega_c = n\omega_c \frac{v_e}{c} N' \cos\theta - \frac{1}{2} n\omega_c \left(\frac{v_e}{c}\right)^2 , \qquad [2.5]$$

where we have used

$$\frac{1}{\gamma} \approx 1 - \frac{1}{2}\left(\frac{v_e}{c}\right)^2$$

$$\omega \approx n\omega_c$$

$$k_\parallel \approx \frac{\omega}{c} N' \cos\theta$$

$$v_\parallel \approx v_e$$

and the WKB assumption of weak damping. With the exception of numerical coefficients to be given later, the first term in equation 2.5 is the the parallel Doppler shift, $\Delta\omega_{Dop}$, while the second is the relativistic transverse Doppler shift, $\Delta\omega_{rel}$. Thus, the conditions

$$|\Delta\omega_{Dop}| \ll |\Delta\omega_{rel}| , \text{ or } N' \cos\theta \ll \frac{v_e}{c} ,$$

define Quasi-perpendicular propagation, in which relativistic broadening dominates, while in the opposite limit,

$$|\Delta\omega_{Dop}| \gg |\Delta\omega_{rel}| , \text{ or } N' \cos\theta \gg \frac{v_e}{c} ,$$

Oblique propagation occurs, in which parallel Doppler broadening dominates. For N' of of order unity, the size of $\cos\theta$ relative to v_e/c thus determines which angular regime is appropriate.

The relativistic effect is seen to consist of a downshift of the absorption line to $\omega < \omega_c$, which in Tokamak geometry, occurs inside of the toroidal axis $r < 0$ when $\omega \approx n\omega_c(0)$. This feature persists in more rigorous treatments, and is responsible for the transparency of a high energy tail to cyclotron harmonic radiation, for which much of the absorption line is relativistically shifted out of the plasma. It should also be noted that in circumstances where absorption far from line center is important, relativistic effects can dominate even for angles far from perpendicular. Resonance in this case is primarily with high energy electrons.

2.3.2 Thermal Plasma Transmission Coefficients

As long as collective (particle correlation) effects are unimportant, we may consider the plasma to be a superposition of electron components of various temperatures, densities, and distributions, and calculate the transmission of each component seperately. As will be shown in section 2.3.3, for the conditions studied in this work, calculations to lowest order in the finite temperature, finite density, WKB and FLR parameters suffice to describe the absorption of the bulk plasma. We proceed by calculating the physical properties of the main plasma for the conditions appropriate to the experiment, which may be summarized as

- Lowest WKB Order: Quasi-homogeneous and stationary, Weakly Absorbing
- Isotropic Maxwellian electron distribution
- Weakly Relativistic: $.04 < \frac{v_e}{c} < .08$; $\mu < .01$
- Quasi-perpendicular propagation: $\cos\theta \ll .02$; $N'\cos\theta \ll \frac{v_e}{c}$
- Quasi-tenuous: $n = 2, 3$; $\left(\frac{\omega_p}{\omega}\right)^2 < .1$
- Lowest Finite-Temperature/FLR Order: $n = 2, 3$; $x \approx n^2\left(\frac{v_e}{c}\right)^2 < .06$.

We begin with the general integral prescription for ϵ obtained by integration of the Vlasov equation over particle orbits (section 2.3.1), which is valid to lowest WKB

and Linearized Vlasov order. For the instance of an isotropic plasma, Trubnikov has cast this prescription for ϵ into several useful forms,[17] in one of which a formal integration over solid angle ω in momentum space is explicitly performed for an isotropic, relativistic Maxwellian. The functional constituents of this form of ϵ can be written in the weakly relativistic limit to second order in μ (x itself is $\mathcal{O}(\mu)$), and after expansion in the FLR parameter x, to first order in x. This result, which is due to Shkarovsky,[18] constitutes the most tractable description of ϵ, expressed in terms of the Cyclotron Resonance Function $\mathcal{F}_q$. This treatment is specifically not valid for τ_1^X where the lowest significant FLR order is 2, or outside of the limits set forth above. An important feature of this result is that well within the quasi-perpendicular regime, there is little actual dependence on θ, all the way through to $\theta = \pi/2$. Also, one finds that $\epsilon_{a-h} \approx \epsilon_h \approx \mathcal{O}(1)$ when $\omega_p = \omega_c$ for $n = 2$, and when $\omega_p = n\omega_c$ for $n \geq 3$, delineating the finite density regime, with the tenuous plasma limit applicable at lower densities.

With an explicit form of the plasma dielectric coefficient in hand, we may substitute the elements ϵ_{ij} into the linear plasma wave local dispersion relation and solve for the plasma modes, as described in section 2.1.1, in the weakly relativistic limit. As one might expect, the fundamental wave dispersion which results resembles cold plasma dispersion. Specifically, except for the X mode at $n = 1$ or near ω_{uh}, or in the finite density limit $(\omega_p/\omega_c)^2 \approx 1$ for the X mode at $n = 2$ and the O mode at $n = 1$, thermal corrections to the real part of the index $N'_{X,O}$ are small, and the Appleton-Hartree cold Plasma dispersion of section 2.1.2 obtains.

Proceeding as outlined in section 2.2.3, we use ϵ_{a-h} and $\mathbf{E}$ to calculate the absorbed power density, the power flux, and thus α_ω. We find that for the X mode, dispersion, polarization, and kinetic power flux related effects each add a correction factor to the tenuous plasma expression for α_ω which diminishes as $(\omega_p/\omega_c)^2$ or faster. These factors tend to become unimportant for $(\omega_p/\omega_c)^2 \ll 1$, or for $n \geq 3$, the less stringent condition $(\omega_p/n\omega_c)^2 \ll 1$. For the O mode, the kinetic flux contribution can be important at $n = 1$, but is negligible at the harmonics, or for $(\omega_p/\omega_c)^2 \ll 1$. These results, taken to lowest order in density and temperature,

are specifically not valid when damping is strong or near the cold plasma cutoffs or resonance, but describe the regime of the present experiment very well.

We calculate τ_0 by the integration of α along the ray path through the plasma. Since, as will be shown in section 2.3.3, for quasi-perpendicular propagation in a Tokamak the absorption is spatially well localized, we may go to a frequency integral with the linewidth replaced by $\delta(\omega - n\omega_c(r_n))$, where $\omega_{\text{laser}} = n\omega_c(r_n)$, as has been done by Engelmann and Curatolo [4] and others. The result is

$$\tau_0 = \frac{\alpha(s)}{\left|\frac{\partial n\omega_c(s)}{\partial s}\right|_{s=r_n}}.$$

For the case of semi-opaque, localized absorption at the cyclotron harmonics $n \geq 2$ for quasi-perpendicular propagation, the X mode optical depth is thus[16]

$$\tau_n^X = \frac{\pi^2 n^{2(n-1)}}{2^{n-1}(n-1)!}\left(\frac{\omega_p}{\omega_c}\right)^2\left(\frac{v_e}{c}\right)^{2(n-1)}\frac{\omega_c}{2\pi c}\frac{B_0}{\left|\frac{\partial B_0}{\partial s}\right|_{s=r_n}}\mathcal{A}_n \equiv \tau_n^{X,EC}\mathcal{A}_n \propto \frac{nT_e^{n-1}}{\left|\frac{\partial B_0}{\partial s}\right|}$$

The factor $\mathcal{A}_n$ contains the density related dynamics discussed above. For $n \geq 3$, and not necessarily tenuous plasma,

$$\mathcal{A}_n = N_\perp'^{2(n-3/2)}\left[1 + \frac{(\omega_p/\omega_c)^2}{n\left(n^2 - 1 - (\omega_p/\omega_c)^2\right)}\right]^2 \mathcal{B}_n$$

$$N_\perp'^{\,2} = 1 - \left(\frac{\omega_p}{\omega}\right)^2 \frac{\omega^2 - \omega_p^2}{\omega^2 - \omega_c^2 - \omega_p^2}$$

$N_\perp'^{\,2}$ represents the effect of plasma dispersion, and is given by the Appleton-Hartree expression. The factor in brackets, representing polarization effects, is just $1 + i\frac{E_s}{E_y}$, and shows how the electrostatic field component scales with finite plasma density. $\mathcal{B}_n$ represents the kinetic contribution to the power flow and is unity in this range. Excluding the finite density factor $.9 < \mathcal{A}_n < 1.0$, τ_n^X as written is equivalent to the result of Engelmann and Curatolo.

For $n = 2$ in the finite density regime, significant deviations from Appleton-Hartree dispersion occur before the entire WKB formalism breaks down, and $\mathcal{A}_n$ is

given by a complicated integral over a heirarchy of functions which must be done numerically, even in this simplest of finite temperature regimes. However, for the $n = 2$ cases studied in this work, $(\omega_p/\omega_c)^2 \leq .02$, and $\mathcal{A}_n$ is unity.

Thus, since for the conditions of this work $\mathcal{A}_n > .9$, the effect of finite density on the transmission is a few percent or less, and the Engelmann and Curatolo expression may be expected to provide a description which is well within the accuracy of the data.

For the Ordinary mode,

$$\tau_n^O = \tau_n^{X,EC}\left[1 - \left(\frac{\omega_p}{n\omega_c}\right)^2\right]^{n-\frac{1}{2}}\left(\frac{v_e}{c}\right)^2 \propto \frac{nT_e^n}{\left|\frac{\partial B_0}{\partial s}\right|}$$

The O mode absorption is seen to be weaker than the X mode by a factor of .01 or less, and may be considered negligible for the conditions studied in this work.

For the relative magnitude of the optical depths, we typically find that τ_1^X is slightly larger than $\tau_3^X \approx \tau_2^O$, comprising the semi-opaque harmonics, that $\tau_1^O \approx \tau_2^X$ are the black harmonics which usually feature strong absorption, and that $\tau_{n\geq 4}^X$ and $\tau_{n\geq 3}^O$ are transparent. Outside of the conditions described above these relations can change substantially. For example, when $\omega_p = \omega_c$, mode conversion from the X mode to electrostatic modes which are strongly damped near the cyclotron harmonics has the effect of increasing absorption at the fundamental and the already black second harmonic.

2.3.3 Physical Conditions Describing This Work

The analytical description of absorption at the cyclotron harmonics presented in the last section was purportedly obtained for the physical and geometrical conditions of the experiment. We must now quantify and examine the practical origins of these conditions, and address a number of other practical issues which bear on the interpretation of the transmission data and the validity of the results.

Angular Range and Absorption Linewidths:

Due to the restricted access in Alcator C, the injected radiation is geometrically constrained to nearly perpendicular propagation. Also, because the points studied in the plasma lie within one half Rayleigh range of the Gaussian beam waist, we may state that the deviation from perpendicular incidence is much less than the far field free space Gaussian divergence half angle. Thus, for the laser mode,

Field e^{-1} radius at beam waist: $S_0 = .57$ cm, located at $r = -14.2$ cm

Rayleigh range: $R(S_0) = \dfrac{\pi S_0^2 N'}{\lambda} = 23.3$ cm

Gaussian far field divergence half angle: $\theta_{\text{Gaussian}} = \dfrac{\lambda}{\pi S_0 N'} \approx 1.4^\circ$

from which we obtain

$$\frac{\pi}{2} - \theta \ll 1.4^\circ, \quad \cos\theta \ll .024 \, .$$

On the other hand, in Alcator C we find that for the bulk (thermal) plasma

$$1 < T_e(\text{keV}) < 3.5, \quad .04 < v_e/c < .08 \Rightarrow \cos\theta \ll v_e/c$$

so that in the plasma interior we may indeed classify the propagation as Quasi-perpendicular. Note that in the outside few centimeters where this condition becomes marginally satisfied, the absorption is negligible for the cases under consideration. Also note that in this range of v_e/c we find the plasma well into the weakly relativistic regime. The relativistic linewidths appropriate to this case are given by[16]

$$\text{X mode}: \Delta\omega_{rel,n} = \sqrt{\frac{\pi}{2}} \left(\frac{e}{2n+1}\right)^{n+\frac{1}{2}} (2n+1)!!\, n\omega_c \left(\frac{v_e}{c}\right)^2$$

$$\text{O mode}: \Delta\omega_{rel,n} = \sqrt{\frac{\pi}{2}} \left(\frac{e}{2n+3}\right)^{n+\frac{3}{2}} (2n+3)!!\, n\omega_c \left(\frac{v_e}{c}\right)^2$$

where[19] $(2n+1)!! \equiv (2n+1)(2n-1)(2n-3)\cdot\cdot\cdot 1$. For the $n = 3$ X mode we obtain $.03 < \Delta\omega^X_{rel,3}/\omega_C < .1$.

FLR and Finite Density Effects:

In the aforementioned temperature range, the FLR parameter is found to be

$$x \leq n^2\left(\frac{v_e}{c}\right)^2 \leq .06 \ll 1$$

which implies that lowest FLR order results should be quite adequate in the regime of this work.

For the finite density parameter, in the range of densities found at the plasma center, we obtain

$$\frac{1}{4n^2} \leq (\frac{\omega_p}{n\omega_c})^2 \leq \frac{1}{n^2}.$$

For $n = 3$, even for $\omega_p = \omega_c$, this gives $(\omega_p/n\omega_c)^2 \leq .11$. For measurements away from the plasma center this parameter is even smaller ($\leq .02$) due to the lower densities. Since the dynamics of the semi-opaque X mode harmonic absorption considered in this work are devoid of any sensitive interplay between small parameters, we may expect calculations to lowest order in the density parameter to provide an adequate description of the interaction.

Spatial Resolution:

The spatial variation of the toroidal magnetic field in a Tokamak is given by $B_t(r) = B_{t0}\frac{R}{R+r}$. In ALCATOR C, the toroidal field variation for the Tokamak parameters of table 1.2 is given by

$$\text{Variation of } B_t \text{ for } -a < r < a : \quad \frac{\Delta_x B_t}{B_{t0}} = \left|\frac{2\epsilon}{1-\epsilon^2}\right| = .55$$

$$\text{Variation of harmonic } n \text{ for } -a < r < a : \quad \frac{\Delta_x(n\omega_c)}{\omega_c} = .55n$$

For $n = 3$, the relativistic linewidth $\Delta\omega_{rel,n}$ is less than $.1\omega_c$, while the variation due the magnetic field inhomogeneity $\Delta_x n\omega_c$ is $1.65\,\omega_c$. The condition $\Delta\omega_{rel,n} \ll \Delta_x n\omega_c$ implies that away from the position where exact resonance is struck the cyclotron frequency changes rapidly, and resonance is lost. The spatial resolution inferred by this variation of B_t is thus

$$\frac{\partial B_t(r)}{\partial r} = -\frac{B_t}{R+r}\,, \quad \frac{\partial n\omega_c(r)}{\partial r} = -\frac{n\omega_c}{R+r}$$

$$\Delta X_n = \frac{\Delta\omega_{rel,n}}{\left|\frac{\partial n\omega_c}{\partial r}\right|}\ , \quad .01(R+r) < \frac{\Delta\omega_{rel,n}}{n\omega_c} < .03(R+r)$$

For absorption in the plasma center, we obtain .5 cm $< \Delta X_n <$ 2 cm. For propagation along the major radius, the vertical extent of the absorption region is less than the Gaussian beam width, which is $\leq$ 1.3 cm. Thus, in a typical case the absorption can be considered to occur primarily in a 1 to 2 cm^3 volume adjoining the resonance point. Since the plasma temperature profile is Gaussian with a width of 7 to 10 cm, the effect of averaging the temperature over this volume is generally small. Near $T_e(0) = 3$ keV, the effect of finite resonance width adds approximately 100 eV to a point estimate of the plasma central temperature, constituting a 3% temperature effect. Below this temperature, the effect quickly passes below the inherent uncertainty of the measurements and is not specifically corrected for in the analysis. For $n = 2$ measurements near the plasma edge, the lower temperatures result in essentially plane absorption.

Thus, the relativistic absorption linewidth associated with perpendicular propagation and the significant variation of B_t across the resonance combine to yield absorption only in the vicinity of the vertical plane(s) where the resonance condition $\omega_{laser} = n\omega_c(r_n)$ is met. Other line broadening effects exist, which may include radiation, collisional, and quantum effects, but in the domain of this work these are miniscule compared to the above linewidths.

Uniqueness of the Absorption Measurement:

The large variation of the cyclotron frequency along the horizontal ray path can introduce an additional complication in a cyclotron harmonic absorption diagnostic scheme. If the harmonic variation across the plasma is greater than ω_c, two adjacent harmonics can occur in the plasma simultaneously, at two different locations. However, the above circumstance is easily avoided in the cases considered in the present work. The harmonics of concern are $n = 2, 3$, and 4. At $n = 4$, the plasma is transparent due to the additional factor of $(v_e/c)^2 < .01$ multiplying the already

semi-transparent $n = 3$ optical depth. The remaining harmonic, $n = 2$, occurs inside of $n = 3$ (toward the inner plasma edge) and is separated enough from $n = 3$ to be out of the plasma for central third harmonic transmission measurements, when $\omega_{laser} = 3\omega_c(r = 0)$. For fixed ω_{laser}, as one increases B_t, the $n = 2$ resonance moves into the plasma from the inboard side, while the $n = 3$ resonance moves outward, away from the plasma center. Thus, the rising $n = 2$ absorption quickly dominates over the waning $n = 3$ effect. The result is that dual contributions are comparable only in the region $r_{n=2} < -15$cm, with a negligible $n = 3$ contribution elsewhere.

The dynamics relating to the toroidal field and resonance position are illustrated below, for a typical case in which $\lambda_{laser} = 432.5\ \mu$, $\bar{n}_{14}(0) = 1.7$, and $T_e(0) = 2$ keV. Shown is the toroidal field on axis, the radial positions of adjacent resonances, the optical depth due to each resonance, and the expected overall transmission through the plasma, obtained using the results of section 2.3.2.

Table 2.2

Cyclotron Harmonic Resonance Transmissions

B_{t0}(T)	n	r_n(cm)	τ_n	$T_{overall}$	Configuration
6.2	4	0.0	.01	.99	centered $n = 4$
	3	−16.	.00		transparent
8.3	3	0.0	.25	.78	centered $n = 3$
	2	−21.3	.00		$T_e(0)$ diagnostic
9.2	3	+7.3	.07	.86	$n = 2$ and $n = 3$
	2	−16.5	.08		in the plasma
9.5	3	+10.0	.01	.77	outer $n = 2$
	2	−14.7	.25		$T_e(r)$ diagnostic

Another factor which has the potential to corrupt the unique spatial point-single harmonic correspondence in the Tokamak geometry is that of harmonic overlap, in which more than one harmonic contributes at a single frequency. As one

might expect, this becomes a problem at higher temperatures, where the widths of each harmonic approach ω_c. To avoid this, we must have

$$\Delta\omega_{rel,n} < \omega_c, \text{ or } n\left(\frac{v_e}{c}\right)^2 < 1$$

which is extremely well satisfied for the cases of interest here.

Thus, in the domain of this work, the features associated with near perpendicular propagation and relatively low electron temperature and density (in the context of the preceding discussions) imply not only nearly optimum diagnostic capabilities but theoretical simplicity as well.

Plasma Anisotropy:

The angle which the Tokamak magnetic field makes with the toroidal axis is a function of radius, $\Phi(r)$, and arises due to the variation of the internal poloidal field produced by the plasma current. This angle can be represented as

$$\text{Tan}\,\Phi(r) = \frac{B_p(r)}{B_t(r)} \equiv \frac{1}{q(r)}\frac{r}{R},$$

where B_p and B_t are the toroidal and poloidal magnetic field components, R and r are the major and minor radii, and $q(r)$ is related to the local magnetic shear.

As a consequence of propagation in the sheared Tokamak magnetic geometry, radiation which enters the plasma with a polarization which is Extraordinary relative to the toroidal axis may arrive at the plasma center with its polarization rotated, so that it has a small Ordinary component. This magneto-optic effect occurs in plasmas for which the X and O modes propagate independently, so that the wave E field follows the apparent local magnetic field in angle. In the strongly anisotropic regime, the angle between the wave and external fields is fixed throughout the propagation. This condition occurs when[20]

$$A \equiv 2(N_X - N_O)\frac{a}{\lambda} \gg 1$$

where N_X, N_O are the indices of refraction for the X and O modes, a is the plasma minor radius, and λ is the free space wavelength. In the opposite limit, weakly

anisotropic propagation occurs, and the wave propagates with its external orientation unperturbed. The above criterion becomes more difficult to satisfy with increasing frequency, when N_X, N_O approach unity. For the extreme case of $(\omega_p/\omega_c)^2 = 1$ and $\omega = 3\omega_c(0)$, we find that $N_X - N_X = .01$, and $A = 8$, which places the propagation in the strongly anisotropic regime. For a more typical case with a toroidal field of 8 Tesla and a peak density of 2.2×10^{14} cm^{-3}, we find $(\omega_p/\omega_c)^2 = .35$, $N_X - N_X = .003$, and $A = 1.5$. Thus, for frequencies near $n = 3$, plasma conditions may be expected to vary in the degree of anisotropy, becoming strongly anisotropic in portions of the plasma at very high densities.

The Ordinary component which develops as a result of the rotation is $E_O = E\sin\Phi$. The $3\omega_c$ transmission of this component is unity, and the effect which this has on the overall external X mode energy transmission measurement is, for small angles Φ,

$$T_{X\ \mathrm{mode}} = T_{\mathrm{measured}} - \Phi^2.$$

For the typical value $q(a) = 4$, we obtain

$$\Phi^2 \approx \left[\frac{1}{q(a)}\frac{a}{R}\right]^2 = .004,$$

so that the amplitude correction is typically less than 1% even for the strongly anisotropic case.

2.4 Suprathermal Electron Component Transmission

In addition to the low temperature plasma bulk considered in the preceding section one or more energetic electron components may exist. These may consist of a group of electrons which run away in the DC Ohmic heating toroidal electric field, or an extended electron tail which results from acceleration in a large plasma wave field, such as during Lower Hybrid RF Current Drive or Heating. The components are rather tenuous, constituting a fraction of 10^{-3} or less of the bulk plasma density, but can contain electrons of up to MeV energies, and can carry most or all of the plasma current.

For electron components in the High temperature regime for harmonics $n \leq 3$, in the Intermediate temperature regime, in the Low temperature regime for $n \geq (c/v_e)$, or for some non-Maxwellian electron distributions, one must resort to numerical techniques in the evaluation of ϵ and calculation of optical properties of the distribution.

The work of Tamor[21-24] in these areas is of great relevance to understanding the absorption characteristics of Maxwellian-class suprathermal distributions. The suprathermal features most likely to have been present in this work can be represented as superpositions of these distributions, and it is these specific applications that we will consider.

The starting point is again the general integral prescription for ϵ. For isotropic distributions, the Bessel series formulation of section 2.3.1 simplifies considerably. For the case of weak damping and $\epsilon_{a-h} \ll \epsilon_h$, thermal corrections to N' are small, and are only important in the calculation of ϵ_{a-h}, which is responsible for the damping. One can then directly solve the dispersion relation for $\mathbf{k}'' \parallel \mathbf{v}_{gr}$ to first order in ϵ_{a-h}, with $\mathbf{k}''$ furnishing the more general definition of α_ω given in section 2.2.3. For an isotropic, relativistic Maxwellian, the resulting expression for ϵ_{a-h} involves a single complicated integral over γ. The Bessel functions are expanded in a power series, and the integrals are calculated term by term via a recursion relation.

This treatment is implemented for tenuous Maxwellian components by Tamor's OPAKE2 code,[21] a state of the art version of his earlier, well known OPAKE code,[22] which computes the harmonic contributions to ϵ_{a-h} at a given frequency until convergence occurs at arbitrarily high harmonic. The code is run on the Cray, and generates a tabulation of normalized opacity $\frac{\alpha_\omega}{(\omega_p^2/c\omega_c)}$, versus frequency $\frac{\omega}{\omega_c}$, reported to be valid to at least 500 keV for frequencies near $\omega = 3\omega_c$.

Properties of streaming Maxwellian components are calculated with the same code using a clever scheme.[23] Calculations of ϵ are performed by the code in a co-moving frame in which the distribution is isotropic. The resulting components of ϵ are referred back to the rest frame by an appropriate Lorentz transformation

and a rotation, as is the Doppler shifted frequency. The final tabulation of the opacity is with all quantities in the rest frame.

Tenuous, weakly damping, anisotropic distributions are handled by Tamor's ECSORB code,[21,24] which is also run on the Cray. In this code, the dispersion properties are assumed to be controlled by a cool background thermal plasma which determines ϵ_h, the wave propagation $\mathbf{k}'$ and normal modes $\mathbf{E}$, while the tenuous suprathermal component determines ϵ_{a-h} and the damping, which is calculated via the power balance formalism of section 2.2.3. Again a Bessel expansion in the general representation of ϵ is effected, with the resulting integrals and ϵ_{a-h} computed numerically, including thermal effects. This program is applied to distribution functions which can be represented as a sum of two temperature Maxwellians $f = f(p_\parallel, p_\perp, T_\parallel, T_\perp)$, and loss cone distributions $f = f(p^{2i}, \sin^{2j}\theta)$, where θ is the angle in phase space between $\mathbf{p}$ and $\mathbf{B}_{t0}$. Results again appear as a tabulation of normalized opacity versus frequency.

The above harmonic summation methods, while appearing rather straightforward, turn out to be suprisingly efficient compared to other integral formulations for calculating ϵ, within the framework described. In this manner, the transmission characteristics of high temperature, streaming, two temperature, loss-cone and anti-loss-cone weighted Maxwellian electron components were studied. These encompass the types of suprathermal attributes most likely to exist in ALCATOR C.

Results obtained using these codes are shown in figures 2.1 to 2.3. In these figures, the density required to produce a 10% absorption of X mode radiation at $3\omega_c$ is plotted versus temperature for the suprathermal distributions described above. The component is assumed to be uniformly distributed in the plasma, and absorption is assumed to occur over the entire ray path. The laser frequency is chosen so that the thermal $2\omega_c$ resonance is just out of the plasma at $r < -a$, allowing a maximum path length for absorption of the downshifted $3\omega_c$ resonance inside the plasma. The results thus constitute a measure of the strength of the entire resonance in the vicinity of $n = 3$. In actuality, the spatial distribution of suprathermal electrons is localized near the plasma center, and the thermal $3\omega_c$

resonance is typically located at $r = 0$, so that the expected absorption is a fraction of that shown in the figures.

Figure 2.1 shows the 10% absorption density required for streaming Maxwellians, for various values of γ of the frame in which the distribution is isotropic and at rest. It is seen that a minimum density is required near 100 keV, and that streaming, with $\gamma > 1.0$, decreases the absorption. A similar trend is observed for the O mode, which is also shown.

The role of $T_{\|}$ and $T_{\perp}$ is examined in figure 2.2, for bi-Maxwellian distributions. With $T_{\|}$ fixed, a minimum is observed in the $T_{\perp}$ scaling at $T_{\perp} = 150$ keV, as with the isotropic distribution. For $T_{\perp}$ fixed at this minimum value, increasing $T_{\|}$ monotonically decreases the absorption, indicating that enhancements of $T_{\|}$ alone tend to reduce the absorption, due to an increasing relativistic shift which scales with $T_{\|}$.

In figure 2.3, the loss-cone weighting is seen to enhance the absorption over the isotropic case, while the anti-loss-cone weighting tends to decrease the absorption. As in figure 2.1, all three curves exhibit a minimum near 100 keV.

The temperature and phase space anisotropies described above constitute a schematic representation of the distribution function produced during Lower Hybrid RF injection, when the action of strong wave fields can create a temperature anisotropy with an enhanced $T_{\|}$. A portion of the electron population can be pulled out of the bulk distribution, forming a high temperature tail with a possibly large velocity drift, or an extended plateau. At high parallel energy, the electrons may undergo pitch angle scattering by fast velocity space instabilities, which can spread the electrons out in phase space in an anti-loss-cone configuration.

Whereas at bulk plasma densities of several 10^{14}cm^{-3} the requirements for appreciable absorption are easily met, even at low temperatures, the 10% absorption density is in all cases at least a factor of 5 to 10 greater than that of probable LHRF produced components, which are typically a fraction of 10^{-3} of the bulk density at the center. This places the expected absorption effect at the 1% level, and with the inclusion of the energy dependence and spatial profile factors, the effect

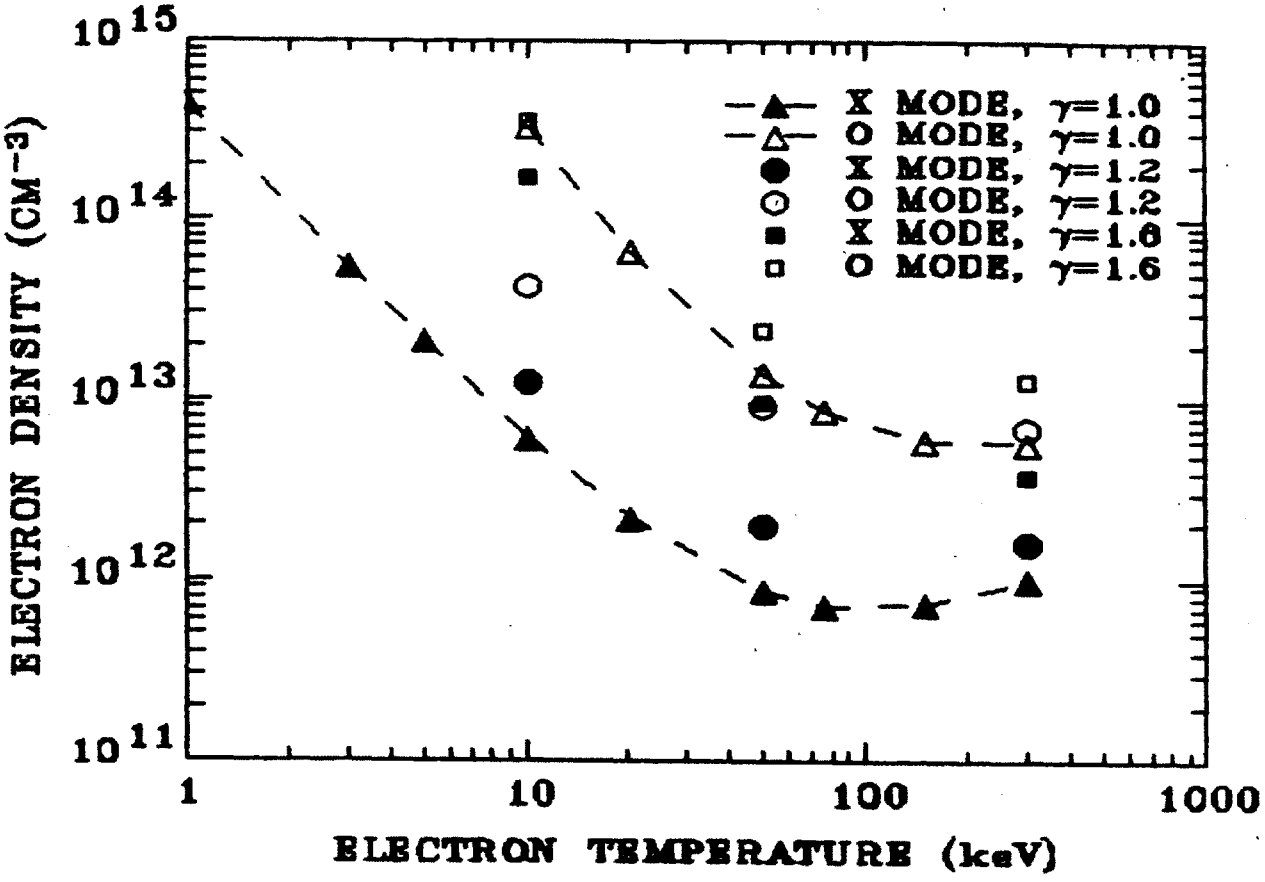

Figure 2.1 — Density Required for 10% Absorption Vs. Temperature for Streaming Maxwellian Distributions. Homogeneous plasma model, $B_t = 9$ T, $\omega_{laser} > 2\omega_c(-a)$, with the second harmonic just beyond the limiter radius.

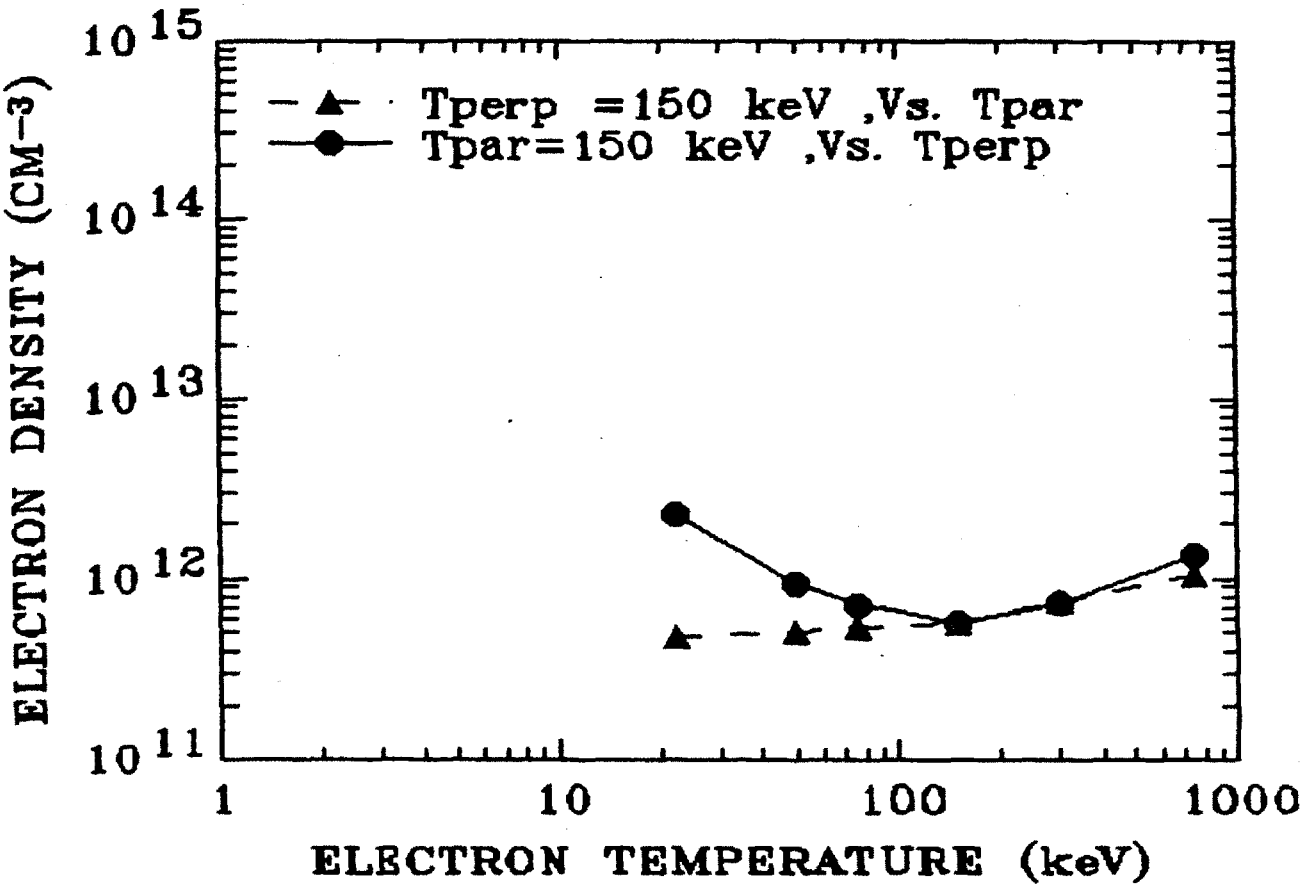

Figure 2.2 — Density Required for 10% Absorption Vs. Temperature for Bi-Maxwellian (Two temperature) Distributions. Homogeneous plasma model, $B_t = 9$ T, $\omega_{laser} > 2\omega_c(-a)$, with the second harmonic just beyond the limiter radius.

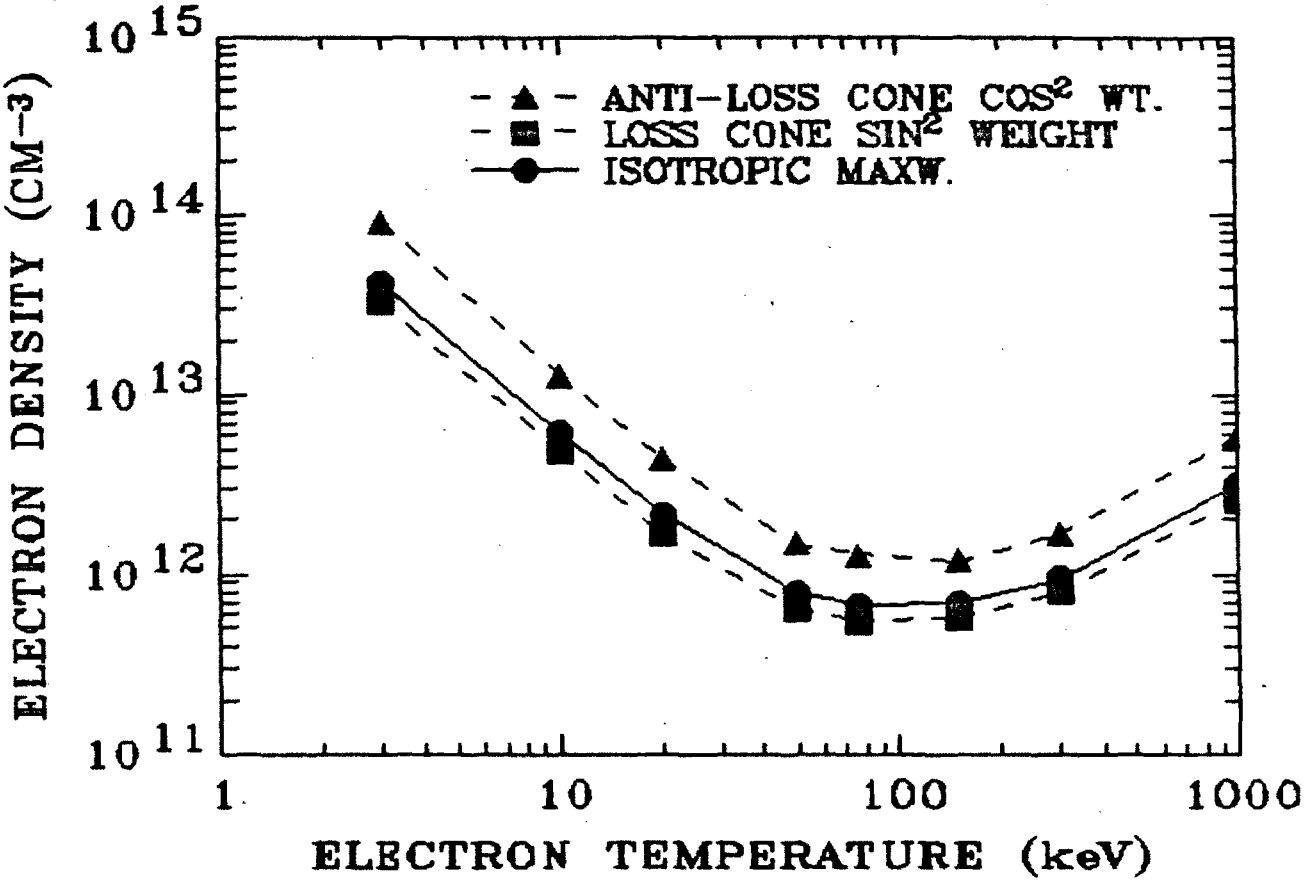

Figure 2.3 — Density Required for 10% Absorption Vs. Temperature for θ Weighted Maxwellian Distributions. Homogeneous plasma model, $B_t = 9$ T, $\omega_{\text{laser}} > 2\omega_c(-a)$, with the second harmonic just beyond the limiter radius.

must all but vanish. These considerations precludes the existence of significant absorption by tenuous Maxwellian class suprathermal distribution functions with $n_e < 10^{-3} n_{e,\text{bulk}}$.

The above observations answer a fundamental, and long open, question. Given that during Lower Hybrid RF injection prodigious plasma emission occurs at the cyclotron harmonics due to the formation of a high energy electron tail, is cyclotron harmonic absorption necessarily enhanced as well by these electrons? The answer we have found is, apparently not. The fundamental difference between the absorption and emission processes is rooted in the expressions for α_ω and j_ω of equations 2.2 of section 2.2.3. Absorption is seen to depend on the shape of $f(\mathbf{p})$, via the derivative of f which multiplies the spontaneous emission coefficient η_ω in the integrand. Emission depends not on the shape of $f(\mathbf{p})$ but on number, via f. Since η_ω can be very large for high energy electrons, prodigious broadband emission can occur whenever electrons couple to a source of free energy. Absorption, however, is sensitive to the detailed structure of f, and since the LHRF suprathermal features appear to have a small negative, or zero, slope in the tail region, no additional absorption should occur.

The scaling of the absorption with temperature finds interpretation in the relativistic dynamics described in section 2.3.1. Increasing the electron energy shifts the relativistic resonance further down in frequency away from the point at which $\omega_{\text{laser}} = n\omega_c$. Since we have seen that in Tokamak geometry this amounts to a spatial shift of the resonance as well, we find that any enhancement which may accrue to increasing temperature is soon offset by an increasing relativistic shift of the resonance out of the plasma. In fact, the additional absorption which one would expect tends to accumulate at or below ω_c, where the tenuous components indeed absorb strongly. This has been observed experimentally by Mazzucato and Efthimion[12] in June, 1985 on the PLT Tokamak. In low density ("Slideaway") discharges with $.6 < \frac{\omega}{\omega_c} < .9$, an optical depth of 1.4 was measured.

The transparency of low density suprathermal components which develop during Lower Hybrid Heating and Current Drive is demonstrated experimentally in

Chapter 5. In all of the routine cases examined, the absorption due to non-thermal components was found to be negligible in the regimes studied, within the experimental accuracy. The transparency of the electron tail at $n = 3$ has allowed a determination of the bulk electron temperature during LHRF Heating experiments.

2.5 Chapter Summary

In this chapter, the physical principles describing absorption at the electron cyclotron harmonic frequencies were developed and applied to the experiment. The fundamental roles of frequency, angle, and polarization, were seen, as was the importance of finite temperature, finite density, and relativistic effects in determining the character of the absorption. The domain of the present work was found to be clearly determined by physical and geometrical considerations. In the regime of the experiment, the dielectric coefficient and absorption coefficient could be obtained, resulting in an explicit expression for the optical depth in terms of experimentally measurable quantities. Criteria for a viable plasma diagnostic scheme were evaluated and applied to the present experiment, which was found to be nearly ideal in many respects. Finally, it was shown that as a consequence of the physical principles developed in the chapter, the transmission was unaffected by the types of tenuous suprathermal components likely to exist in ALCATOR, enabling the transmission to be used as a bulk plasma diagnostic during RF injection.

Chapter 3

EXPERIMENT CONFIGURATION AND COMPONENTS

The diagnostic implementation of the transmission experiment involved a direct, continuous observation of the plasma transmission. This required a radiation source at the working frequency, a method of transporting and detecting the radiation, and facilities for the observation and storage of data produced by or relevant to the experiment. In this chapter, the general layout of the equipment is discussed, and important considerations are highlighted. The various subsystems for producing, transporting, processing, and detecting the $3\omega_c$ probe radiation are described in detail. Performance characteristics and peculiarities of each component are documented, and in instances where a novel application is developed, particular note is made.

3.1 Experiment Arrangement

The main experiment components are shown schematically in figure 3.1 . Radiation in the electron cyclotron harmonic frequency range was produced by an optically pumped waveguide laser system located in the Alcator C cell on an enclosed laser table, adjacent to the Tokamak. The submillimeter radiation was focused and guided from the laser window to an elevated optics platform, which selected the polarization and transported the radiation to the injection optics platform. Here the radiation was focused and aligned for injection into the Tokamak, along a trajectory which was perpendicular to the magnetic field and intersected the toroidal axis in a plane inclined by eight degrees to the torus equatorial plane. Upon exiting the plasma, the radiation entered the radiation collection system, which consisted of waveguide assemblies located both inside and outside the Tokamak vacuum. The internal waveguide assembly consisted of a 45° collection horn which coupled the laser mode into a curved segment of circular steel waveguide which made its way out of the plasma chamber, protected from the discharge on both sides by limiter rings. At a vacuum window on top of the Tokamak, the radiation was coupled into the

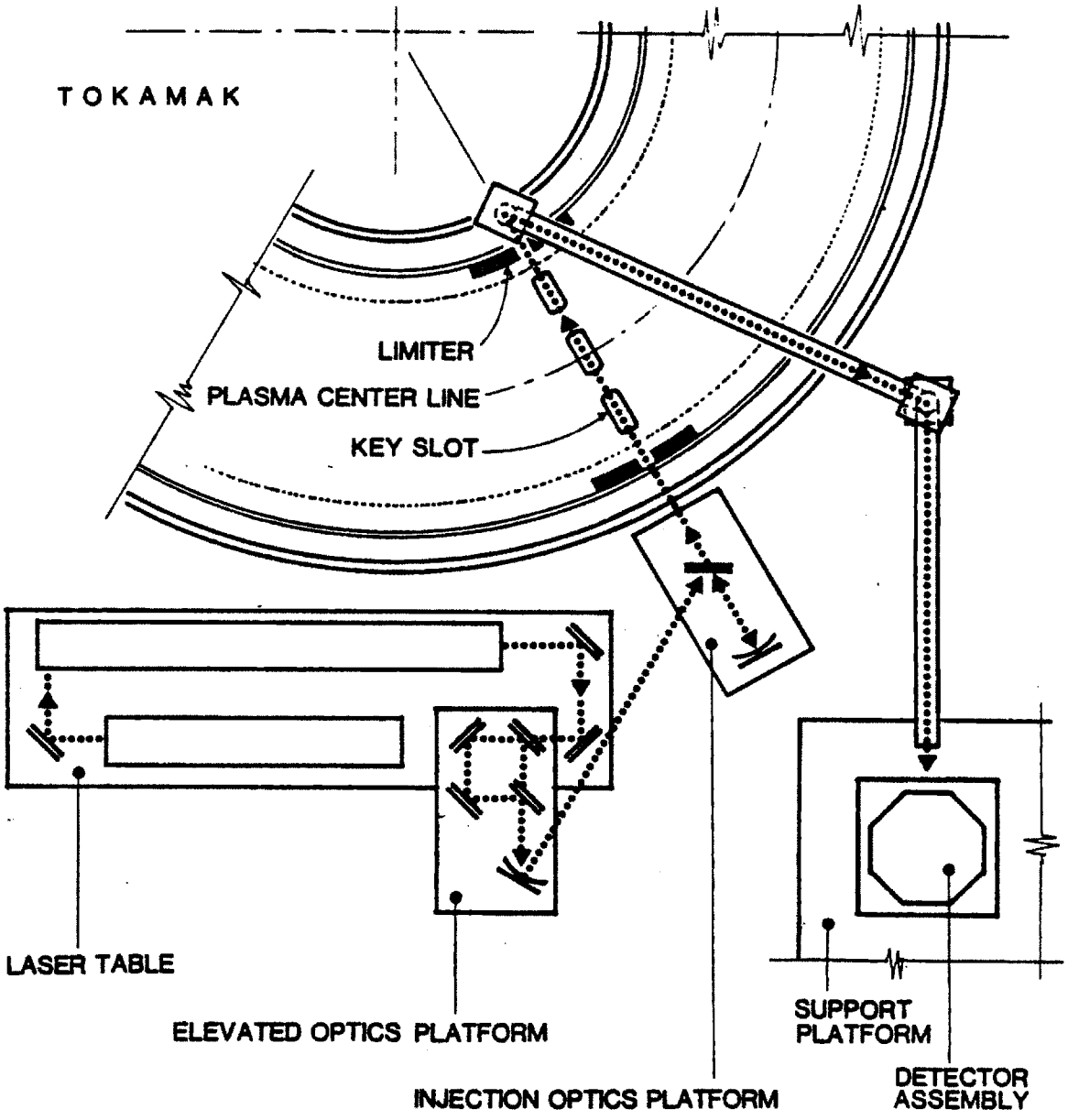

Figure 3.1 — Experiment Component Schematic Plan View. Shown are the relative locations of the laser table, Tokamak, and detector platform.

external waveguide assembly. This consisted of circular Copper waveguide which carried the radiation away from the Tokamak to the detector assembly platform, where it was processed and detected. The resulting raw signals were transferred upstairs to the control room (not shown) for digitization and storage.

3.2 Radiation Source

A CW Carbon Dioxide pump laser and a Far Infrared (FIR) waveguide laser submillimeter wave source were constructed, comprising the heart of the transmission experiment. A schematic view of the laser system is presented in figure 3.2 and the accompanying legend.

The CO_2 laser consisted of a 1.3 m long, .8 cm diameter spherical resonator. The flowing gas, water cooled 1.1 m discharge tube was fitted with ZnSe Brewster window flanges. The laser was tuned with a Gold coated Kanigen–Copper original grating with 100 grooves per mm, manufactured by PTR Optics. The ZnSe output coupler had a 70% reflecting, $R = 20$ m concave inner surface, and an anti-reflection coated, $R = 7.5$ m convex outer surface. Cavity adjustment was effected with a Burleigh Intruments PZ-80 piezoelectric translator (PZT), which translated the output coupler with a slew of 7 μm/1000 V. The CO_2 laser gas composition was typically 18% N_2, 7% CO_2, 75% He , and the operating pressure was the maximum allowed by the power supply, which was 25 Torr. The high voltage power supply was obtained from surplus, and was modified appropriate to its function in this application. Current regulation was accomplished with a feedback circuit based on a Motorola MC1436G op-amp, the output of which energized the control grid of an Eimac 4PR65 modulator tube. Typical discharge load values were $i = 17$ mA and $V = 4$kV. When feasible, stabilization was effected with a Lansing Research Model 80.215 Lock-in Stabilizer which drove the PZT while monitoring a sample of the FIR output. The power supply, gas flow regulation, and vacuum systems were all contained in a mobile control console. With new optics the laser produced 35 Watts on the 9R20 line, with good TEM_{00} mode quality, but both power and mode degraded substantially over the lifetime of the system, in part due to the effects of a harsh operating environment.

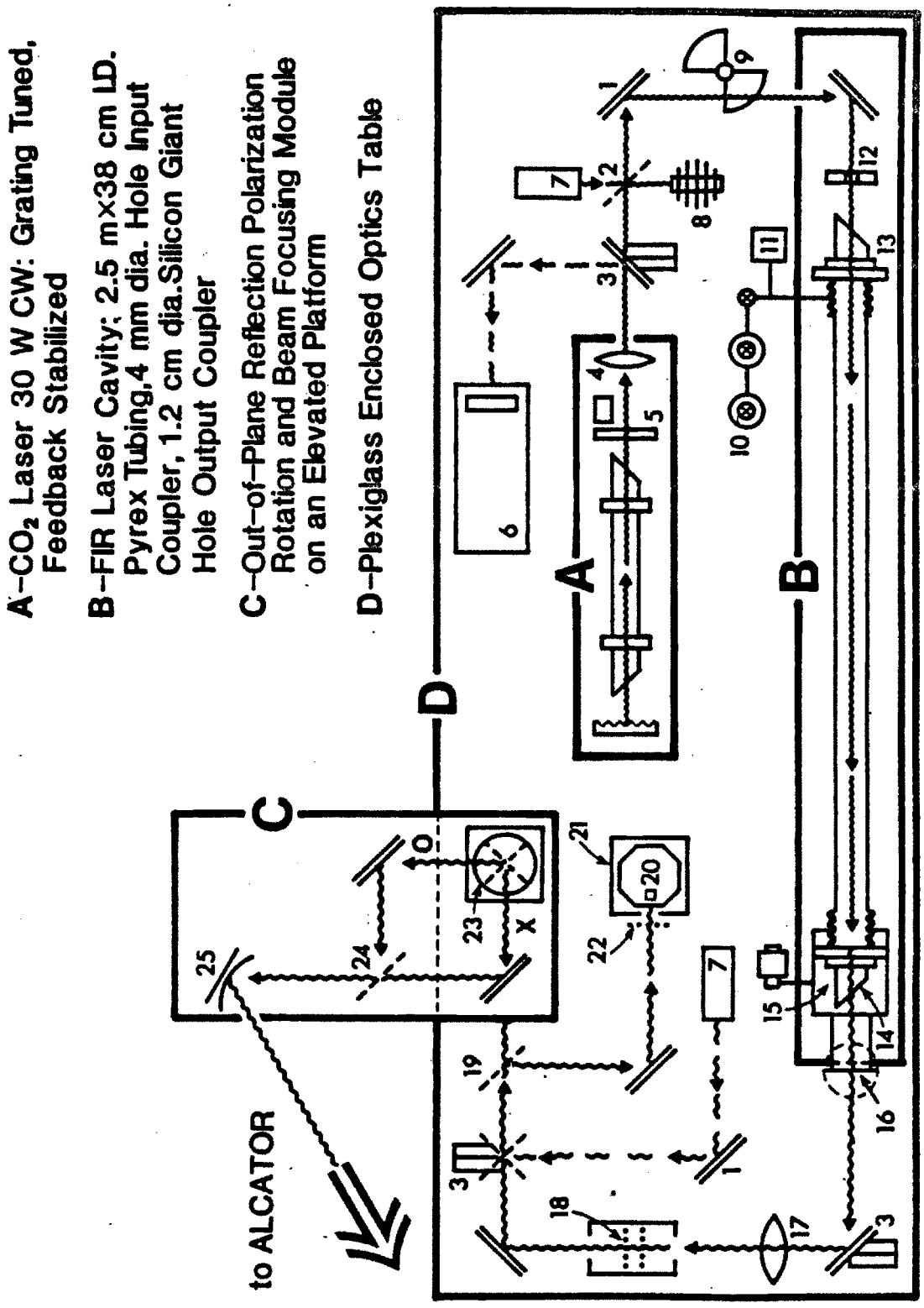

Figure 3.2 — Laser System Schematic Plan View. Show are the CO_2 laser, FIR laser, and polarization rotation module. Numbers refer to the legend.

1. FRONT SURFACE GOLD MIRROR
2. REMOVABLE ZnSe 7% BEAMSPLITTER
3. SLIDE MIRROR
4. ZnSe CO_2 FOCUSING LENS
5. ZnSe CO_2 LASER OUTPUT COUPLER IN A PZT TRANSLATOR
6. CO_2 SPECTRUM ANALYZER
7. HeNe ALIGNMENT LASER
8. CO_2 LASER CALORIMETER
9. 100 Hz MECHANICAL CHOPPER
10. FIR LASER GAS SOURCE
11. CAPACITANCE MANOMETER
12. CARBON APERTURE
13. ZnSe BREWSTER WINDOW
14. X-CUT QUARTZ BREWSTER WINDOW
15. MOTORIZED TRANSLATION STAGE
16. ATMOSPHERIC COUNTERWEIGHT ASSEMBLY
17. TPX FIR FOCUSING LENS, f = 55 cm
18. METAL MESH FABRY-PEROT INTERFEROMETER
19. 10% POLYETHYLENE BEAMSPLITTER
20. LIQUID HELIUM DEWAR AND INDIUM ANTIMONIDE PHOTOCONDUCTIVE DETECTOR; PROVIDES REFERENCE SIGNAL
21. VENTED ALUMINUM RF SHIELD ASSEMBLY
22. COPPER RF SCREEN AND ATTENUATORS
23. 90° ROTATABLE POLARIZATION SELECTION MIRROR
24. ORDINARY MODE MIRROR (REMOVABLE FOR X MODE PROPAGATION)
25. SPHERICAL FIRST SURFACE BEAM FOCUSING MIRROR, f = 1.52 M

Legend, Figure 3.2 — Laser System Components.

The FIR waveguide laser consisted of a 2.5 m long, 3.8 cm inner diameter Pyrex tube with plane end reflectors. The Pyrex waveguide tube was connected to the input and output coupler flanges via flexible bellows and compressed O-ring vacuum seals. CO_2 pump radiation was coupled into the laser through a 3 mm aperture in a polished OFHC Copper flat, preceded by a ZnSe Brewster vacuum window. Approximately 75% of the raw pump power was ultimately delivered to the FIR cavity. The beam was focused prior to injection so that it executed two passes in the FIR cavity before diverging to a spot size equal to the tube diameter. The resulting 5 M absorption length was necessary to insure good pump absorption in the tenuous FIR laser gas. Feedback between the CO_2 and FIR cavities was reduced by placing a Carbon collimator screen between the two cavities, adjusted to intercept any CO_2 pump radiation which may have been retro-reflected from the FIR cavity and its internal components. This seemingly trivial procedure is essential for the stable operation of lasers which are sensitive to cavity feedback, such as the HCOOH and DCOOD gases used in this work. The method worked satisfactorily, considering that alternative cavity isolation schemes require costly optical components and are wavelength specific,[25] but the more sensitive FIR lines still required continuous manual CO_2 adjustment, and could not be stabilized by the Lansing unit. The CO_2 beam was modulated at 100 Hz by a mechanical chopper, and combined with a collinear HeNe alignment beam prior to injection into the FIR cavity.

Submillimeter radiation was coupled out of the FIR cavity via a Silicon giant hole coupler,[26] which also served as a vacuum window. A 3 inch diameter, 2 mm thick polished Silicon flat optimized for transmission at 400 μm was masked with a 1.2 cm disk at its center, and a 3000 Å Aluminum thin film was vacuum deposited. The mask was removed, leaving a 1.2 cm aperture from which the FIR radiation emerged. The Fresnel reflectivity $R_f = .3$ of the bare Silicon provided sufficient optical feedback in the FIR for the cavity to operate routinely on the EH_{11} circular dielectric waveguide hybrid mode, while the large aperture size permitted a

low divergence FIR output. This linearly polarized fundamental mode has the lowest propagation loss for the circular dielectric waveguide, and couples strongly to the free space Gaussian mode, which it closely resembles. Satisfactory FIR performance was obtained without coating the Silicon substrate with an infrared reflection coating, although this may be expected to improve the laser performance by an additional 15 to 30%. The FIR radiation propagated away from the output coupling aperture of radius R_a as a free space Gaussian spherical mode with its beam waist at the aperture, for which the field and intensity profiles are given by

$$E(r) = E_0 e^{-(r/\omega)^2}, \quad I(r) = I_0 e^{-(r/\omega_I)^2}, \quad \omega_I = \omega/\sqrt{2}.$$

In standard operation, the half width of the waist from which the beam diverges was found to be $\omega_0 = R_a/\sqrt{2}$, or in terms of the intensity, $\omega_{0I} = R_a/2$. This also happens to be the maximum size Gaussian which may pass through the aperture with its field pattern nearly unperturbed by diffraction. The laser mode transverse profile is shown in figure 3.3, for $\lambda = 393.6$ μm and $R_a = .6$ cm, measured with a 1 mm pyroelectric detector located 67 cm from the output coupler. Figure 3.3a shows the freely propagated mode profile, while figure 3.3b shows the effect of placing a 45 cm focal length lens 44 cm from the output coupler. Also shown in these figures are the theoretical results of a Gaussian beam calculation which assumes the beam waist $\omega_0 = R_a/\sqrt{2} = .42$ cm is located at the laser. The theoretical profiles have been normalized to the peak laser power. For larger size apertures, narrower, more strongly divergent profiles have been found, possibly indicating that the laser was operating on a higher order transverse mode. The FIR power produced by the laser depends on the degree of output coupling, as illustrated below for the 393.6 μm HCOOH transition, where we have normalized the FIR powers to a raw 9R18 CO_2 pump power of 32 W.

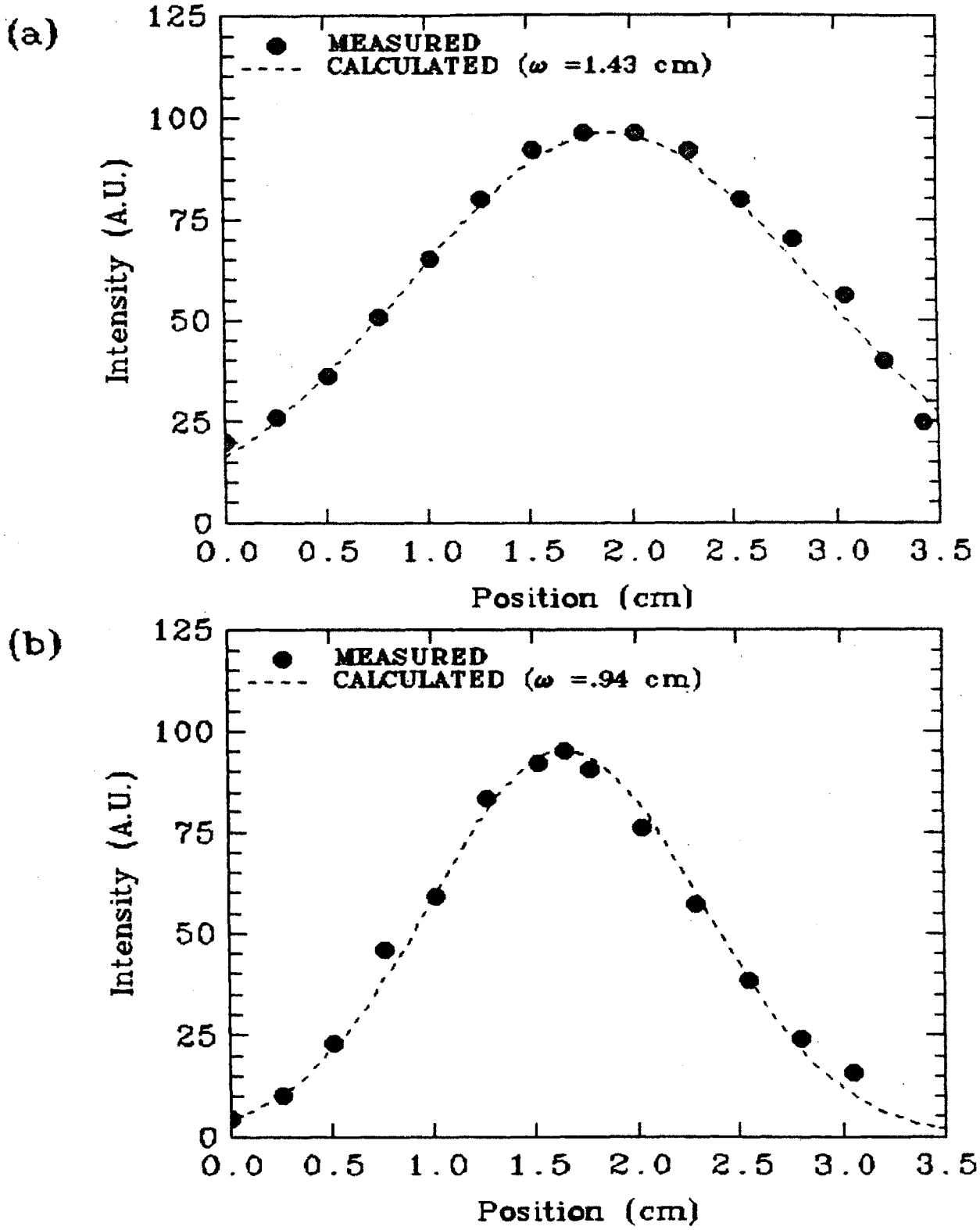

Figure 3.3 — $\lambda = 393.6\ \mu$m Laser Mode Transverse Profile. Taken 67 cm from the laser output coupler. (a) Freely propagated mode, no lens. (b) 23 cm from f=45 cm focal length lens.

Table 3.1

FIR Powers Produced With Various Output Couplers

$2R_a$ (cm)	P_{FIR} (mW)
1.48	23
1.20	29
0.85	24

The 29 mW figure represents 10% of the theoretical quantum efficiency for optical pumping,

$$\eta_q \equiv \frac{1}{2}\frac{f_{FIR}}{f_{pump}} ,$$

where f is the radiation frequency, and an overall conversion efficiency of 1.3 milliwatts of FIR per watt of pump radiation. It should be noted that due to the 50% duty cycle of the chopper, these figures should be multiplied by a factor two prior to comparison with laser performance data documented in the literature, and that the CW powers are twice the listed values. Weaker lines fared better with smaller aperture diameters, for which the stronger lines were undercoupled. The Silicon window was followed by a 1 mm thick Y-cut Quartz Brewster window, which served to filter any pump radiation from the FIR beam. Wavelength determination was accomplished with a metal mesh Fabry-Perot interferometer driven by a precision digital micrometer. By scanning several FPI orders, wavelengths were read directly off of the digital readout with an accuracy of approximately one micron.

The output coupler mount was located on a gearmotor driven translation stage, with which longitudinal mode FIR tuning was accomplished. Since the optimum FIR operating pressures were found to be less than .1 Torr, approximately 75 pounds of inward atmospheric force acted on the translation stage, which required balancing before tuning and fine optical adjustments could be accomplished. To balance this force, a novel counterweight design was implemented which functioned flawlessly in routine service. A summary of prior laser designs and their drawbacks is offered below.

Optically Pumped FIR Waveguide Laser Designs

1) Narrow Bore Tube – By using a narrow waveguide tube, the force is small enough for correction with light springs found in standard optical components. This cavity configuration does not optimize pump confinement and is suitable only for lines with very strong absorption.
2) End Boxes – The laser mounts are enclosed at the laser pressure, with mechanical adjustments made via vacuum feedthroughs. These lasers are bulky, expose the mechanical components to corrosive laser gases, and introduce outgasing and vacuum difficulties.
3) Spring Loading – Springs are used to provide the necessary force. The backlash of the stiff springs required interferes strongly with the optical adjustments, and the force applied is dependent on alignment and position.
4) Double Bellows – The output coupler mount is placed between two bellows at the laser pressure. These bellows are usually stiff and have limited travel, and to some extent posess the problems described above for springs. These designs are also particularly cumbersome and difficult to service.

In the Counterweight design, thin steel cables are run from the output coupler to the laser table underside, where a counterweight is suspended. This design is compact, simple, and independent of tube bore, allows for a single easily accessible output window, and provides a corrective force which is constant in direction and magnitude, free of backlash, and is completely decoupled from the fine cavity adjustments.

The molecular laser lines used in this work are the 393.6 μm and 432.6 μm rotational transitions in Formic acid, HCOOH,[27,28] and the 381 μm line in its deuterated analog, DCOOD.[28] The strong output of these lasers allowed satisfactory performance to be achieved with modest FIR cavity design and pump laser requirements. The frequencies of the 432.6 μm and 393.6 μm lines correspond to $3\omega_c$ at the plasma center for 8.25 and 9.07 Tesla, respectively. As these are approximately equal to the most common operating values of the toroidal field in

ALCATOR C, they are particularly convenient in this application. At 8 Tesla the resonances of the 381 μm line are located at $r(3\omega_c) = -9.2$ cm and $r(4\omega_c) = +9.1$ cm, with the X mode transmission expected to be unity. The 8 Tesla transmission of this line thus provides a direct measurement of any non-resonant attenuation of the beam due to effects other than cyclotron absorption. This has been used to study a non-resonant attenuation encountered in this work.

A summary of the experimental characteristics of the lasers used in this work is presented below. Shown are the laser gas, FIR wavelength and frequency, CO_2 pump transition, net pump power coupled into the FIR cavity, maximum FIR power obtained at the listed pump power, and the optimum FIR operating pressure.

Table 3.2

FIR Laser Characteristics

Gas	$\lambda(\mu m)$	f(GHz)	CO_2 line	P_{CO_2} (W)	P_{FIR} (mW)	p_{FIR} (mTorr)
HCOOH	432.6	693.5	9R20	22	29	45
HCOOH	393.6	762.2	9R18	22	29	65
DCOOD	381.0	787.4	10R12	20	11	95

The above data was taken with an output coupler aperture of 1.2 cm, which was found to be optimum for the HCOOH lines shown. The FIR lines were linearly polarized parallel to the pump, to the 1° accuracy of measurement. The above optimal HCOOH performance was obtained with new optics, but only about half of this power was available at the time of some of the experimental measurements due to degradation of the CO_2 mode quality over time. Pump mode quality has been found to be the most crucial factor in obtaining high power, stable FIR laser performance. Also, data for the two gases shown above were obtained at different times, so that a comparative evaluation of the above transitions is unjustified. The FIR output was observed to scale linearly with pump power, indicating that the pump absorption was unsaturated at the 20 W power level.

FIR powers were measured with a Scientech Model 36-0001 surface absorbing calorimeter. The convenience of this device, which requires only a DC voltmeter in its implementation, does not diminish the inherent difficulty of performing "accurate" absolute power level determinations in the submillimeter wavelength range. The importance of sensor transparency and diffraction in this range has been studied by Foote, et al, and others[29,30] and a sensor calibration factor of .5 was used in the present work. In addition, the coupling of radiation into the device was found to be an important complication, as was thermal hysteresis and drift of the zero, and background noise. The device was enclosed in thermal insulation, with an inserted Copper guide tube directly abutting the sensor element. An Eccosorb RF absorbing cap could be placed in the thermal insulation to seal the aperture. Zero, background, and power readings were made repeatedly and averaged to obtain absolute power figures.

The scaling of FIR power with laser pressure for the HCOOH lines is shown in figure 3.4. Absolute pressure determinations were made with an MKS Instruments capacitance manometer which was attached to the FIR laser tube vacuum seal flange. The pressures in figure 3.4 have not been adjusted for a drop from the sensor to the waveguide tube, but this is expected to be small due to the high conductance of the path joining them.

The FIR cavity was thermally loaded and insulated, and the entire assembly was placed on a wooden table surrounded by a Plexiglas enclosure. As a result, when CO_2 frequency stabilization was successful, the FIR output remained stable for 30 to 60 minutes before requiring a cavity adjustment. However, the free running stability of the the system with the CO_2 laser unstabilized was severely limited. As conceived, the system was designed using common structural materials, placing the burden of stability on the Lansing stabilizer unit and effective thermal isolation. Enclosure and thermal isolation of the laser system proved to be extremely valuable, and are highly recommended for any system destined to be operated in the harsh environment of an experiment cell. However, in many circumstances stabilization could not be effected, and laborious manual adjustment of the CO_2 laser was continually required. This

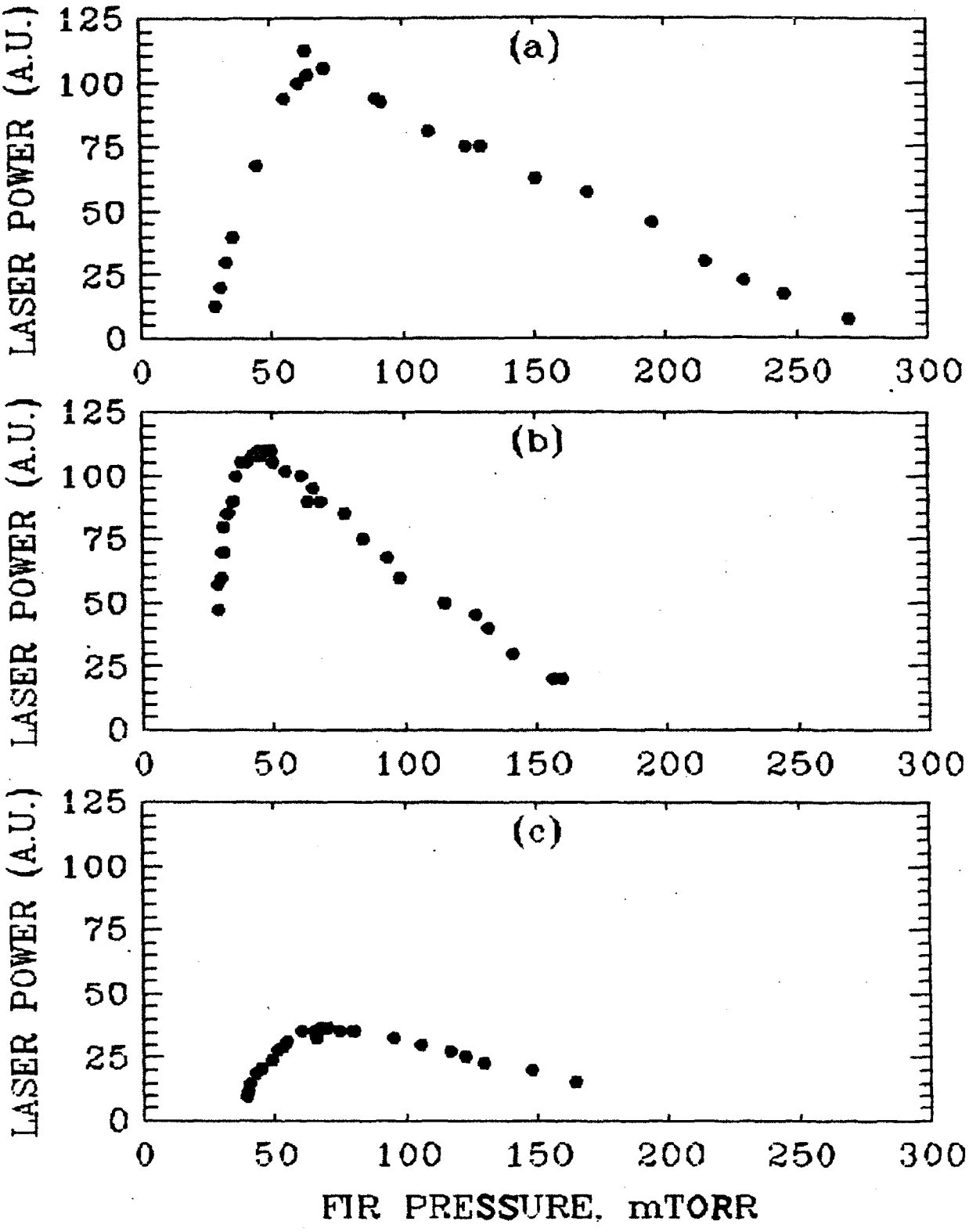

Figure 3.4 — Scaling of FIR Output Power with Laser Pressure for Strong Lines in HCOOH. (a) 9R18 pump, $\lambda_{FIR} = 393.6\ \mu m$. (b) 9R20 pump, $\lambda_{FIR} = 432.6\ \mu m$. (c) 9R22 pump, $\lambda_{FIR} = 418.6\ \mu m$.

situation occurred in the presence of strong cavity feedback, or when the CO_2 mode quality was poor. Unfortunately, these conditions prevailed often, and at times rendered a successful execution of the experimental program rather difficult.

An optimum configuration, based on experience with the above system, would feature Invar cage construction for both the CO_2 and FIR cavities, as well as isolation in a sealed enclosure. This is, of course, in addition to having a clean grating and good laser optics and a conservatively designed power supply, as well as pursuing further system optimization as outlined above.

3.3 Radiation Injection and Collection System

Following the laser output coupler, the FIR radiation was focused by a TPX plastic lens, and 10% of the radiation was diverted to the reference detector by a Polyethylene pellicle. The radiation was then reflected upward by 90° to an elevated polarization and focusing module. Here, an out-of-plane reflection was utilized to provide a 90° rotation of the beam polarization by selection of one of two orthogonal beam paths. In the Tokamak geometry, these correspond to X and O mode injection. Both paths converged on a Gold coated first surface spherical reflector, from which the radiation proceeded to the injection optics platform adjacent to the Tokamak.

At the injection optics platform, the beam arriving from the laser table was aligned in height and angle, and focused by an 8 inch diameter first surface parabolic reflector prior to injection into the Tokamak. The path of the radiation from the injection platform to the detector is shown schematically in figure 3.5, and the accompanying legend.

In order to arrive at the plasma, the probing radiation must make its way through the constricted diagnostic port structure of Alcator C. The beam must enter the 10 cm aperture vacuum window, traverse a 4.2 cm wide by 22 cm long slot in the port flange, then converge on the back wall of the plasma chamber, a distance of 1.2 m from the entry point. These narrow apertures serve to diffraction limit the minimum beam spot size, making a two pass excursion in and out of the device impossible without the use of a special flange design or a complex, vibration

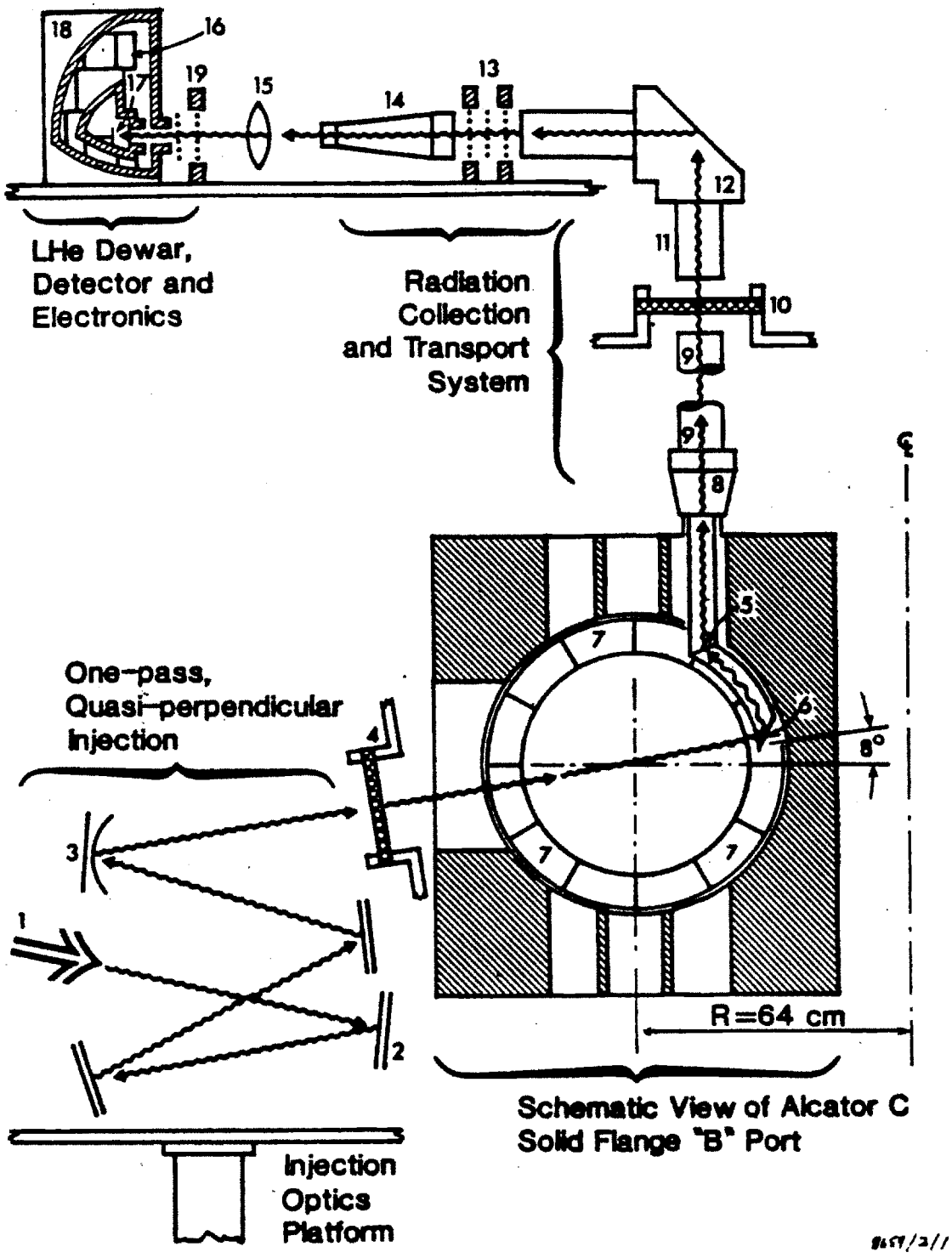

Figure 3.5 — Experiment Configuration and Geometry. Shown are the injection geometry, Tokamak cross section, internal and external Waveguide assemblies, and Detection assembly.

1. FIR GAUSSIAN BEAM INCIDENT FROM OPTICS PLATFORM
2. OUT-OF-PLANE REFLECTION MIRROR
3. SPHERICAL FIRST SURFACE FOCUSING MIRROR, f = 1.02 M
4. Z-CUT QUARTZ VACUUM WINDOW .5 cm x 4" APERTURE
5. INTERNAL WAVEGUIDE ASSEMBLY: 5/8 DIA. 304 S.S. TUBING WITH INTERIOR SILVER PLATE; 30" STRAIGHT SEGMENT MITERED TO A 40° ARC SEGMENT OF 7 1/2" RADIUS
6. 45° HORN MIRROR, POLISHED 304 S.S.; INTERNAL ASSEMBLY TRANSMISSION 80%
7. 360° DOUBLE RING LIMITER WHICH PROTECTS THE WAVEGUIDE
8. 5° EXPANSION CONE, 304 S.S. WITH INTERIOR SILVER PLATE
9. EXPANDED WAVEGUIDE SEGMENT, 304 S.S. 1" DIA. x 23", INTERIOR SILVER PLATE EXPANDED SEGMENT TRANSMISSION 95%
10. Z-CUT QUARTZ VACUUM WINDOW / DC BREAK 6 mm THICK
11. EXTERNAL WAVEGUIDE ASSEMBLY: 16 FT. OF 1 1/8" COPPER TUBING WITH (3) 90° BENDS; EXTERNAL WAVEGUIDE TRANSMISSION 75%
12. 90° MITER BEND ((3) TOTAL)
13. TRIPLE METAL MESH FABRY-PEROT FILTER
14. 3° COPPER CONDENSING CONE
15. POLYETHYLENE LENS
16. LIQUID HELIUM DEWAR WITH A 1/16" THICK Z-CUT QUARTZ WINDOW
17. INDIUM ANTIMONIDE PHOTOCONDUCTIVE DETECTOR; PROVIDES TRANSMITTED SIGNAL
18. VENTED ALUMINUM RF SHIELD ASSEMBLY
19. 880 GHZ LOW PASS FILTER, Cu RF SCREEN, ATTENUATORS

Legend, Figure 3.5 — Radiation Injection and Collection System Components.

sensitive, fundamental mode waveguide injection scheme. Alternatively, affixing a small retroreflecting mirror to the back wall would subject the exit beam to the erratic effects of machine motion during the plasma shot. This dilemma was solved by the use of a novel scheme which allowed all of the best features of free space Gaussian and metallic waveguide propagation to be implemented in the radiation transport. At the location where the injected Gaussian beam illuminates the plasma chamber back wall following its traversal of the discharge, a 45° collection horn coupled the radiation into a 5/8 inch diameter curved Silver plated circular steel waveguide. The waveguide proceeded along the back wall to a vertical slot, where it exited the plasma chamber. At a point in the machine where clearance allowed, the 5/8 inch diameter waveguide was expanded to a 1 inch diameter straight segment which continued on to the Z-cut Quartz exit vacuum window. Here the radiation was coupled across a 1 cm vacuum and DC break into the external waveguide assembly, which consisted of polished circular Copper waveguide of $1\frac{1}{8}$ inch diameter, and three 90° miter bends. The radiation was transported away from the device in the waveguide over a distance of 5 meters, to a platform where it was filtered, re-focused, and detected. The entire collection assembly was compatible with and utilized the existing limiter support structure internal to the device and the surrounding diagnostic support structure externally.

The use of waveguided radiation collection and transport allowed the optical design to be optimized for one pass propagation of the highly collimated Gaussian probe beam. This resulted in a narrow trajectory through the plasma, with optimum use of the source energy, and transport which was relatively insensitive to machine vibrations.

The probe beam focused to a 1.2 cm diameter spot on the waveguide aperture, where the diffraction limited spot size was 1.1 cm. This minimum size was dictated by the requirement that the laser mode traverse the outside slot edge, located some 62 cm away from the waveguide, as a Gaussian. The optical train was 9.76 m long from the laser window to the waveguide aperture, and used 8 flat mirrors, 2 focusing mirrors of commercially available curvature, and 1 TPX lens which was

fabricated in house, to implement the beam transport and focusing. Design of the optical train was accomplished with the use of a Gaussian beam propagation code, Program OPTICS, written for this purpose. With this code, the spot sizes at various points along the beam path were calculated, and the effects of changing the optical configuration were examined, leading to the final optimized configuration.

In order to verify that the final laser mode of the injected beam was indeed as expected, a transverse beam profile was taken prior to injection into the Tokamak, at a location 89 cm from the last mirror. A 1 mm pyroelectric element covered by an Eccosorb collimator was scanned across the beam, and the profile which resulted is shown in figure 3.6. Also shown is a Gaussian profile of a width calculated by the propagation code. The profile has been normalized to the peak power measured. Since agreement is good, we are justified in expecting the propagation in the Tokamak to proceed as designed.

The collected submillimeter radiation propagates as a highly overmoded spectrum in the 1.4 cm diameter waveguide. As only the radiation amplitude is required in the diagnostic determination, one has but to insure that the entire waveguide spectrum is detected. Because of the overmoding of the waveguide and mode conversion in the curved segment and subsequent miter bends, numerous modes carry the energy, and the waveguide spectra and polarization patterns measured were typically quite complex. However, we have found experimentally that although the detailed mode structure was very sensitive to alignment, the energy in the spectrum was conserved, and due to relatively low propagation losses in the Silver plated waveguide interior, the net amplitude transmission remained high. In the collection path, the use of guided propagation was a great asset, being compact and relatively insensitive to vibrations and alignment.

The internal waveguide segment consisted of a 33.9 cm long straight segment joined by a 45° miter bend to a 45° arc segment of 18.9 cm radius of curvature, for an overall length of 48.7 cm. A typical transverse mode profile for the waveguide segment is shown in figure 3.7 . 432.6 μm radiation was injected into the waveguide in P-polarization, with a beam waist equal to the 1.4 cm inner diameter, located

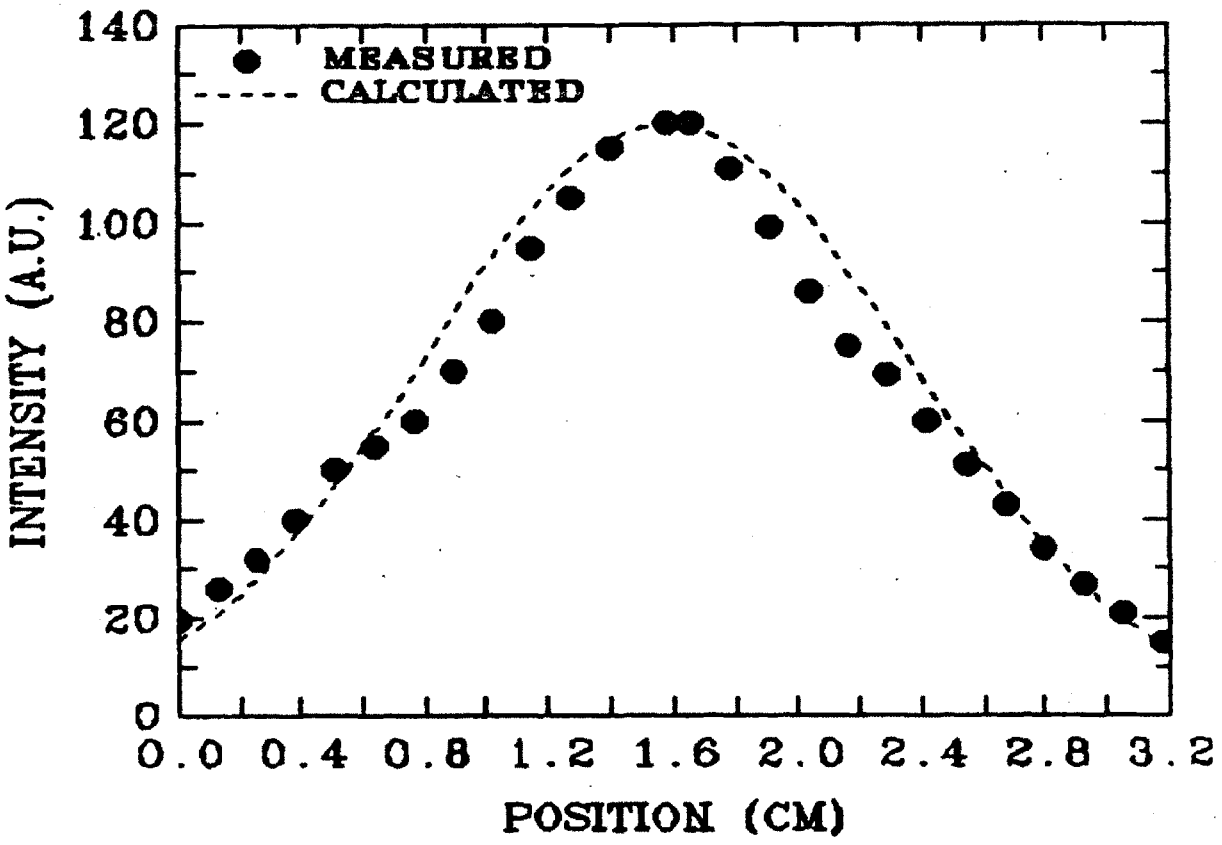

Figure 3.6 — Laser Mode Transverse Profile Taken 89 cm from the Last Injection Mirror, 8.9 m from the Laser Output Coupler. (Image lies 11 cm from the internal keyhole entrance slot.)

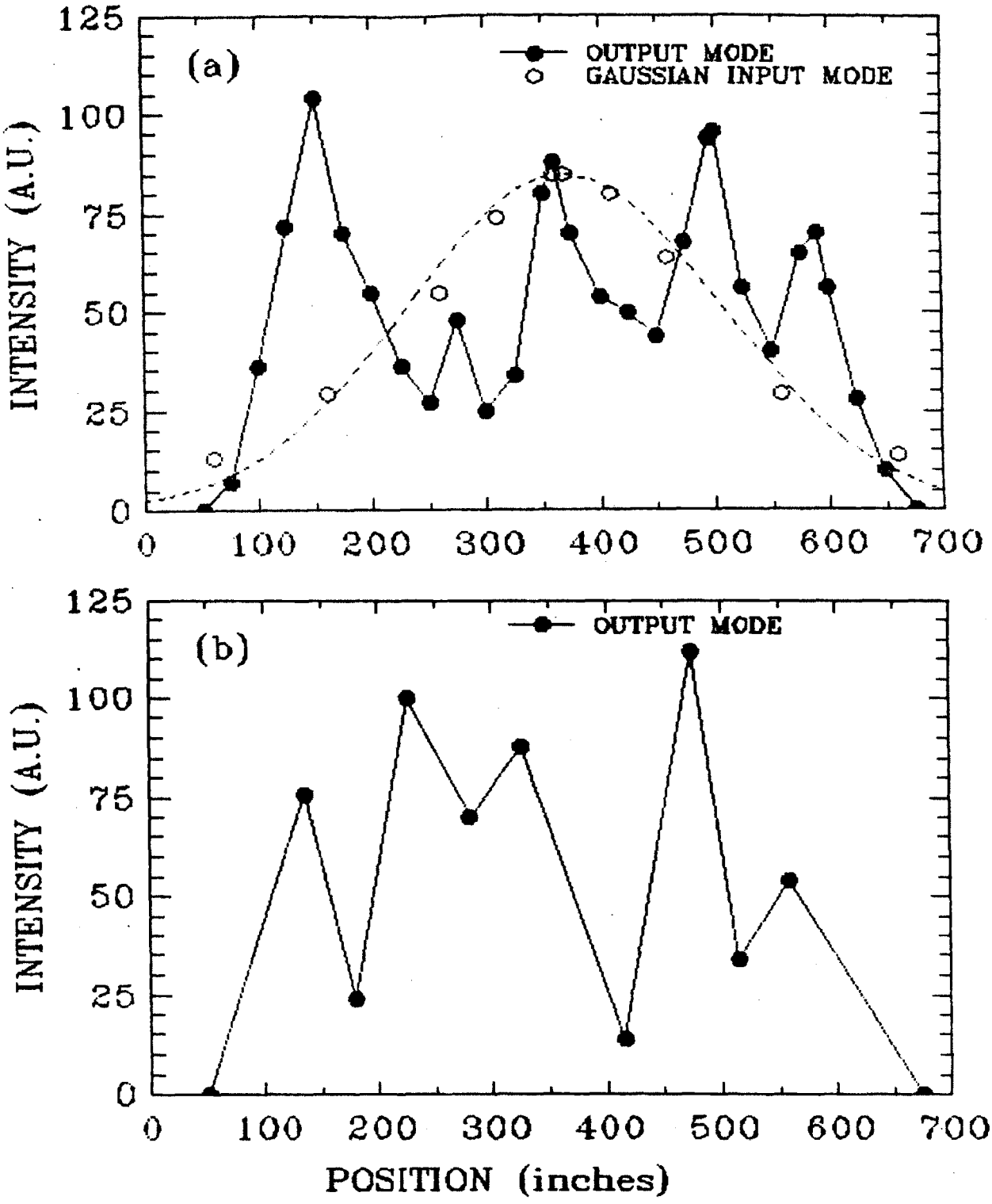

Figure 3.7 — Waveguide Output Mode Transverse Profile. Internal waveguide segment, λ = 432.6 μm, injected beam width = tube inner diameter = 1.4 cm, overall transmission = 79%. (a) Horizontal scan of output mode, and Gaussian input mode. (b) Vertical scan of same output mode.

at the waveguide aperture. Profiles were obtained by translating a 1 mm pyroelectric detector across the waveguide exit aperture, in both the horizontal (3.7a) and vertical (3.7b) directions. Also shown superimposed in figure 3.7a is the laser mode prior to injection into the waveguide. The transmission of the mode shown in the waveguide segment was 79%. The fraction of the Gaussian beam energy entering the waveguide is given by the aperture transmission ,

$$T_a \equiv 1 - e^{-2(a/\omega)^2},$$

where a is the aperture radius and ω is the beam half width. For $a = \omega$, $T_a = 86.5\%$, which gives an overall loss coefficient of approximately .8 dB/M.

The free space propagation and polarization characteristics of the waveguide generated mode are shown in figures 3.8 and 3.9. The profile at the waveguide exit aperture is shown in 3.8a, along with the laser Gaussian mode at the waveguide entrance. Figure 3.8b shows the profile 10 cm away from the waveguide exit aperture. The divergence half angle of radiation exiting the waveguide was found to be 1.5°. Polarization scans of the three peaks labeled (a) through (c) in figure 3.8b are shown in figure 3.9, taken 10 cm from the waveguide exit. Also shown, in 3.9d, is a scan of the linearly polarized input Gaussian mode prior to injection. Polarization scans were obtained by placing a 1000 line per inch Gold wire grid electroformed on a Mylar substrate between the waveguide exit and the pyroelectric detector element. For a 180° rotation of the grid, a linearly polarized component produces a sinusoid squared variation, and a randomly or circularly polarized component produces a constant level. As seen in the above figures, the waveguide generated free space mode may contain a linearly polarized component which is rotated by some arbitrary angle with respect to the injected Gaussian, or a small circularly polarized, or unpolarized, component. The total transmission of the mode shown was 83%, which corresponds to an overall loss coefficient of .4 dB/M.

The effect of waveguide injection at a 10° acute angle is shown in figure 3.10. Figure 3.10a shows the transverse profile at the waveguide exit, 3.10b shows the mode after propagating 10 cm in free space, and 3.10c shows the polarization of the

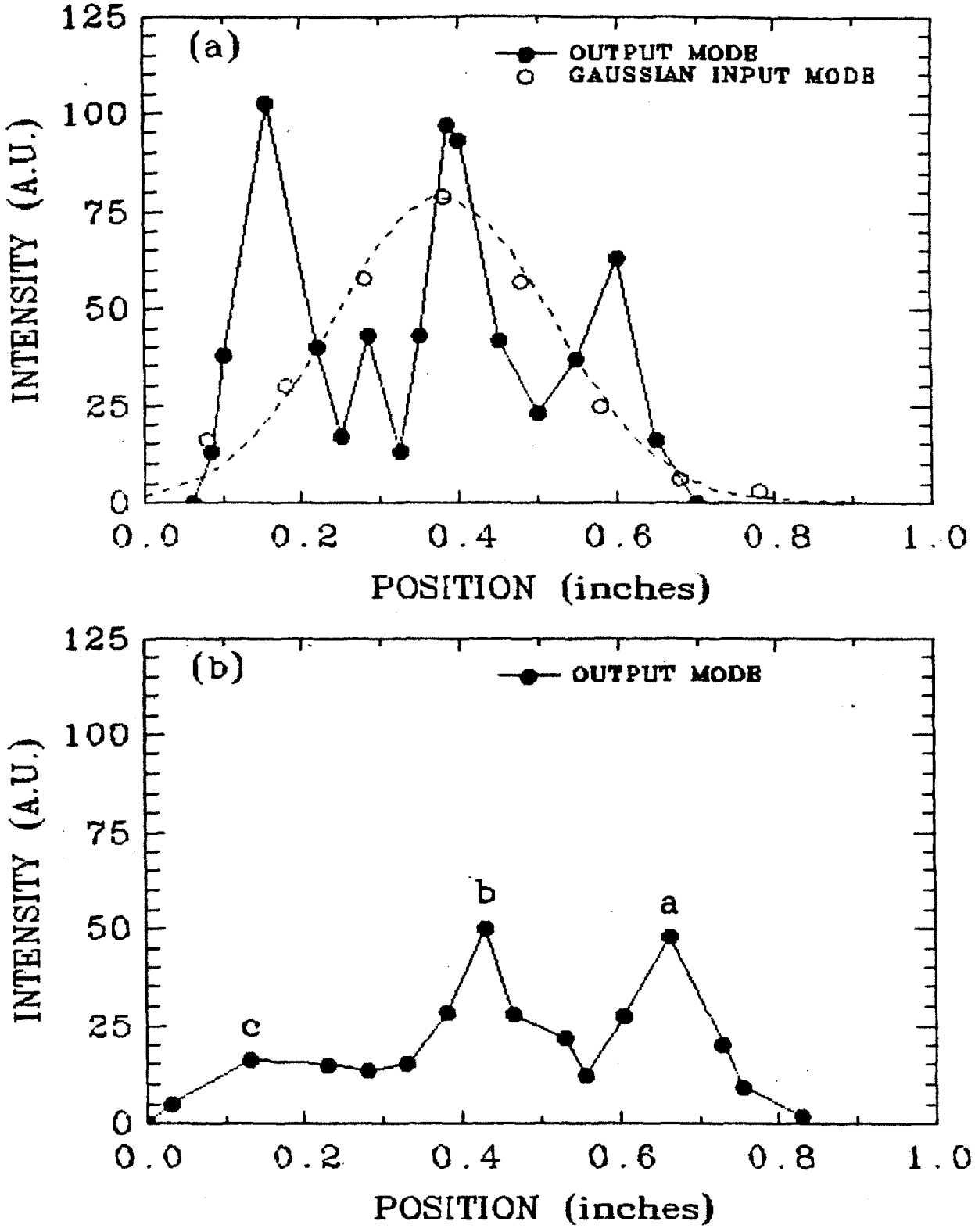

Figure 3.8 — Free Space Propagation of Waveguide Output Mode. Internal waveguide segment, $\lambda = 432.6\ \mu m$, injected beam width = tube inner diameter = 1.4 cm, overall transmission = 83%. (a) Transverse profile at the waveguide exit, and Gaussian input mode. (b) Transverse profile 10 cm from the waveguide exit.

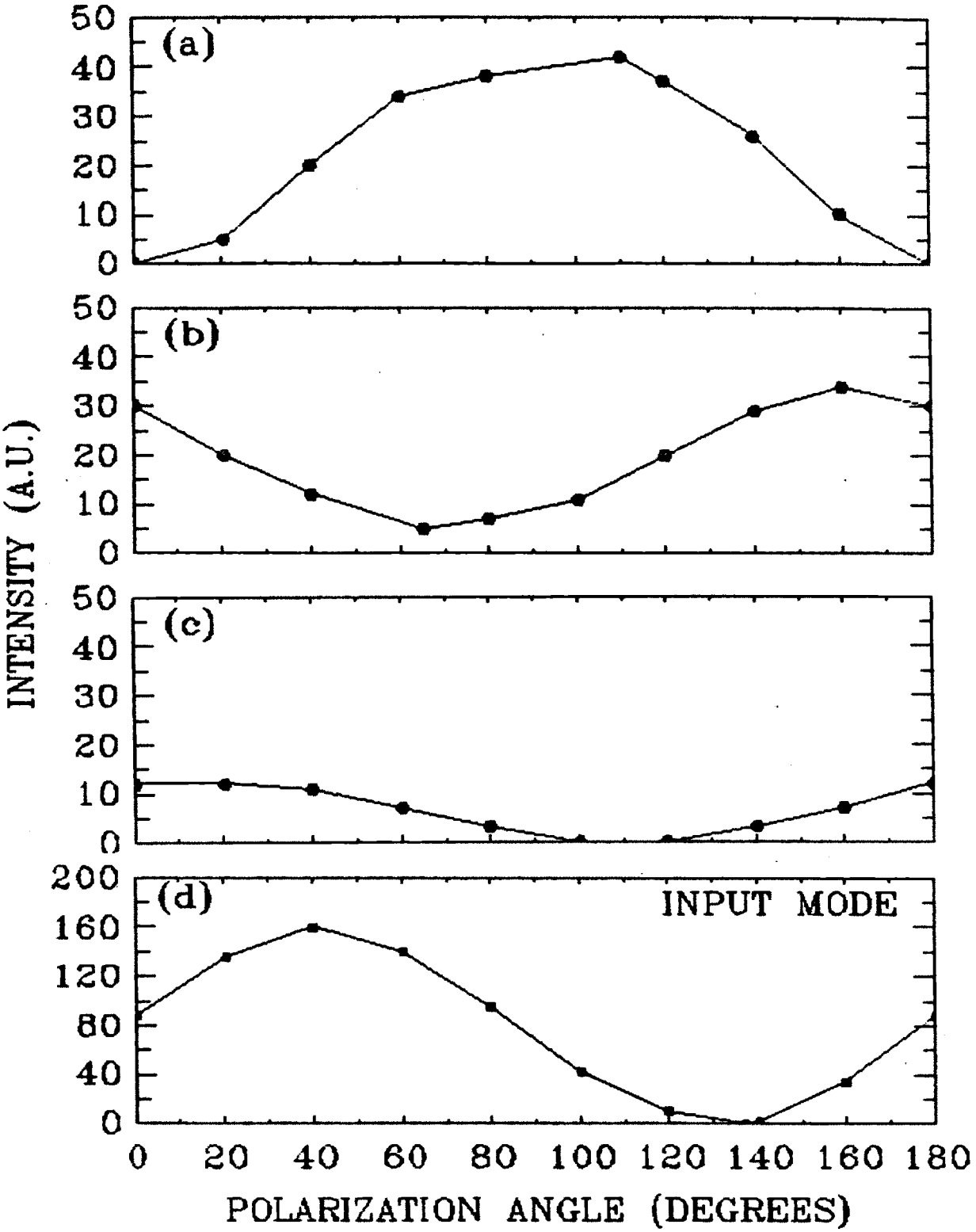

Figure 3.9 — Polarization of Waveguide Mode Shown in Figure 3.8(b). Plots refer to peaks labeled a,b,c in Figure 3.8. (a) Peak a. (b) Peak b. (c) Peak c. (d) Gaussian input mode.

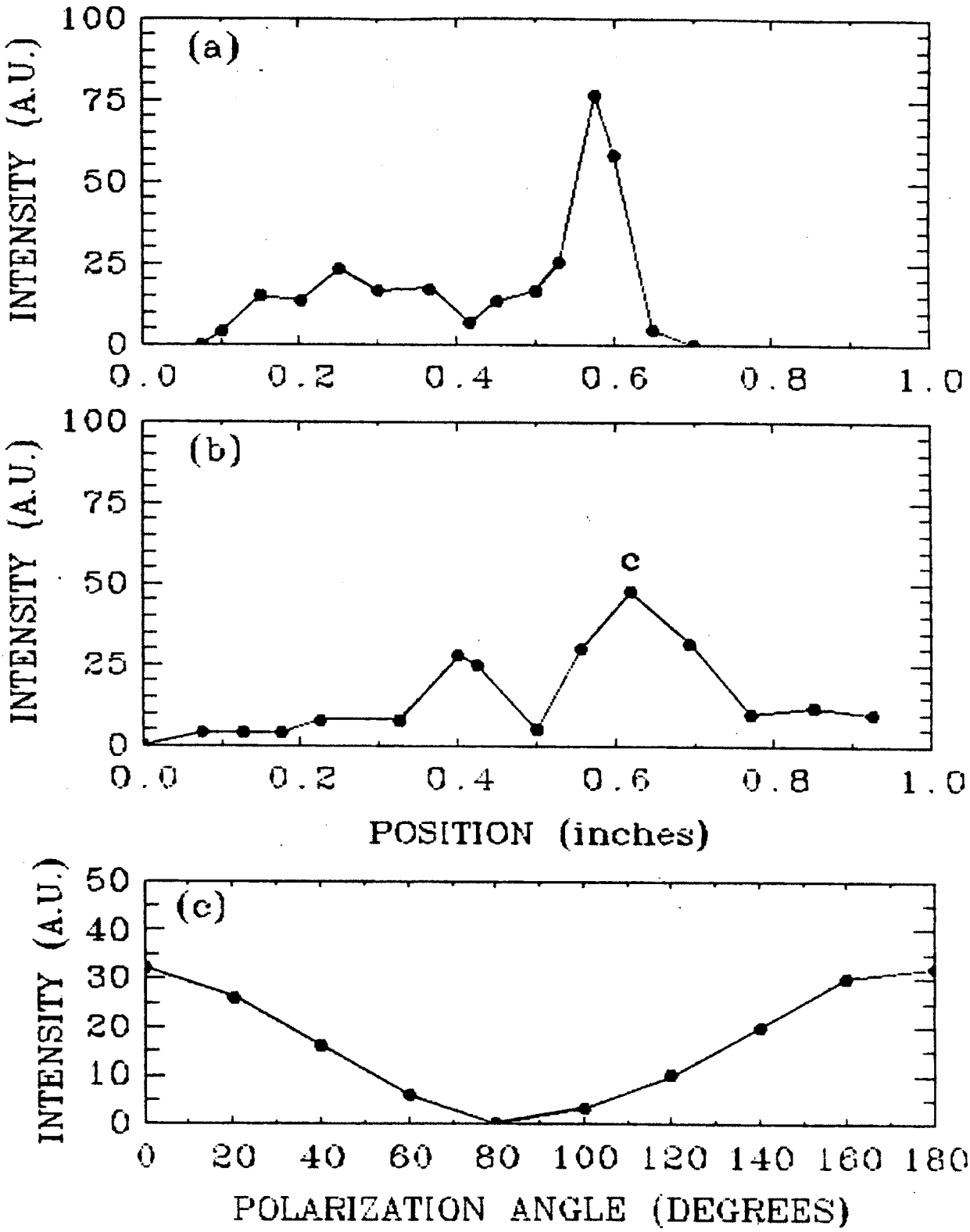

Figure 3.10 — Effect of 10° Acute Angle Waveguide Injection. Gaussian input mode as shown in figures 3.8(a) and 3.9(d). Overall transmission = 80%. (a) Mode at waveguide exit. (b) Mode at 10 cm from waveguide. (c) Polarization scan of peak c in (b).

largest peak at 10 cm from the exit aperture. The injection angle is seen to produce a marked asymmetry in the profile, but the overall transmission remains high, at 80%, which yields a loss coefficient of .6 dB/M. The divergence half angle was found to be 3.3°. The transmission decreased only slightly for acute injection angles of 10° or less, but declined rapidly above this. At 12° the transmission was found to decrease to 60%. The angle at which the decrease in the transmission occurs was found to increase with a/ω.

The effect of varying the location of the beam waist relative to the waveguide entrance is investigated in figure 3.11 . The radiation was focused to a waist $2\omega = .8$ cm and was injected into a 1.7 cm diameter unpolished Copper test assembly. This consisted of a 91 cm straight segment joined by a 45° miter bend to a 45° arc segment of 18.9 cm radius of curvature, with an overall length of 106 cm. The figure shows the measured transmission versus the distance s from the beam waist to the waveguide entrance. Also shown is the theoretical curve $\mathbf{T}_{th} = \mathbf{T}_0\,\mathbf{T}_a\left[\frac{a}{\omega(s)}\right]$, where $\mathbf{T}_0$ is the transmission when the waist is located at the waveguide entrance, and the second factor is the aperture transmission $\mathbf{T}_a$ for a beam half width $\omega(s)$. The theoretical curve obtains if all of the energy coupled into the waveguide is transmitted with the same transmission independent of the waist position. Agreement is seen to be good, indicating that although for selective coupling to the waveguide fundamental or other specific mode an optimum beam width may exist for a given waveguide diameter,[31,32] the overall amplitude transmission is apparently insensitive to the details of wave coupling. The transmission with the waist located at the waveguide aperture was 72%, which yields an overall loss coefficient of 1.3 dB/M. The slightly higher loss of the test assembly may be due to the use of unpolished Copper tubing, whereas the waveguide assembly used in figures 3.7 through 3.10 was newly electropolished and electroplated with Silver.[33] The spot size at the

waveguide when the waist was 50 cm away was 1.77 cm, for which 37% of the beam energy enters the waveguide aperture.

One may understand the overmoded transmission characteristics in terms of the properties of the modes of the circular metallic waveguide. A spatial plot of 30 of these modes has been performed by C.S. Lee, et al,[34] and these are reproduced here for reference, as figure 3.12. Modal cutoff frequencies and theoretical attenuation coefficients are tabulated below for the first ten modes of the circular metallic waveguide. These have been calculated using the convenient formulation of Crenn,[32] for a frequency $f = 750$ GHz and a resistivity $\rho_{Ag} = 1.5 \times 10^{-6}$ Ohm−cm. Entries have been normalized to the fundamental mode TE_{11} values, except for the last column which gives the attenuation coefficients in dB/M. The fundamental mode, TE_{11}, has a theoretical attenuation coefficient of .3 dB/M.

Table 3.3

Modal Cutoff Frequencies and Attenuations of the Circular Metallic Waveguide

Mode	$f/f(TE_{11})$	$\alpha/\alpha(TE_{11})$	α (dB/M)
TE_{11}	1.00	1.00	0.3
TM_{01}	1.31	2.41	0.72
TE_{21}	1.66	1.82	0.55
TM_{11}	2.08	2.41	0.72
TE_{01}	2.09	1×10^{-3}	3×10^{-4}
TE_{31}	2.29	2.51	0.75
TM_{21}	2.78	2.41	0.72
TE_{41}	2.88	3.13	0.94
TE_{12}	2.90	0.09	0.03
TM_{02}	3.00	2.41	0.72

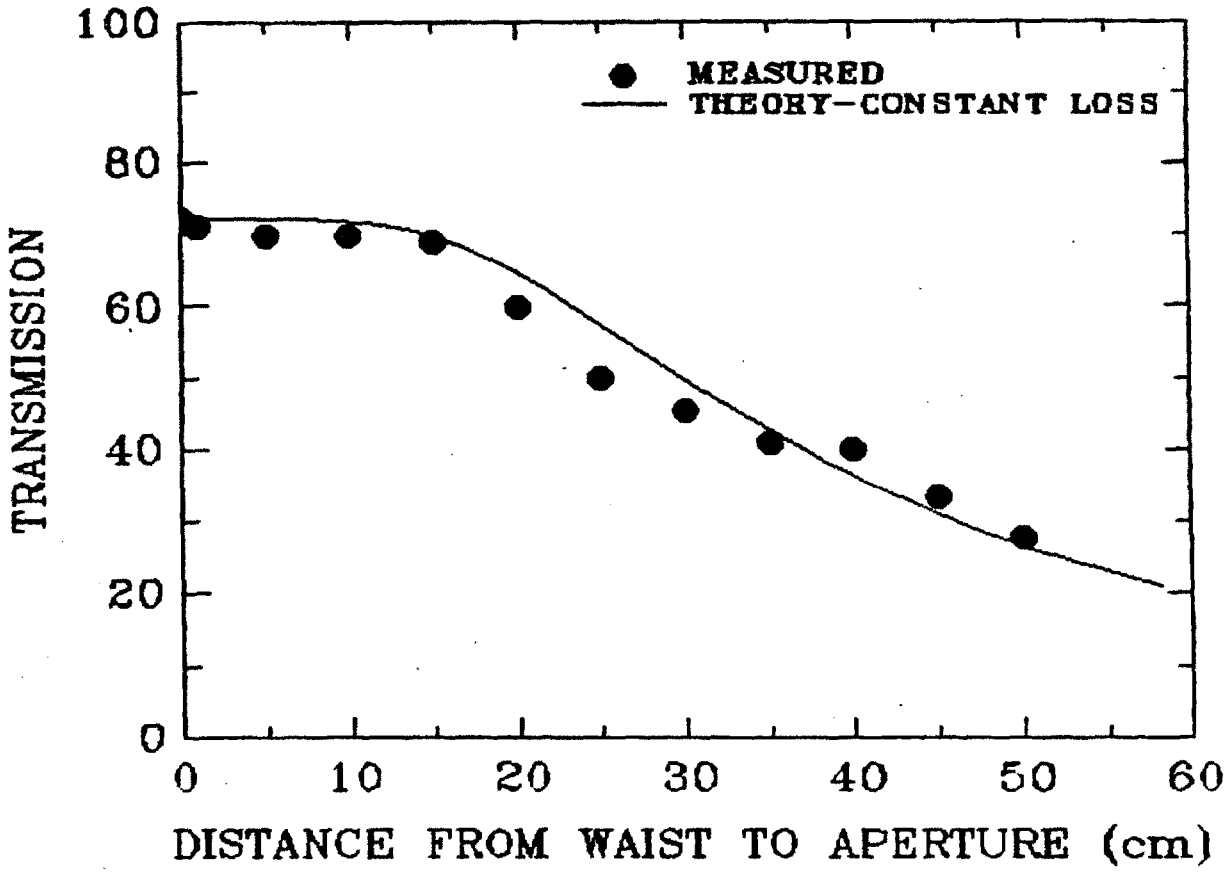

Figure 3.11 — Transmission of Waveguide Vs. Distance from Beam Waist to Waveguide Aperture. Cu test assembly, inner diameter = 1.7 cm, Gaussian width at beam waist 2ω = .8 cm.

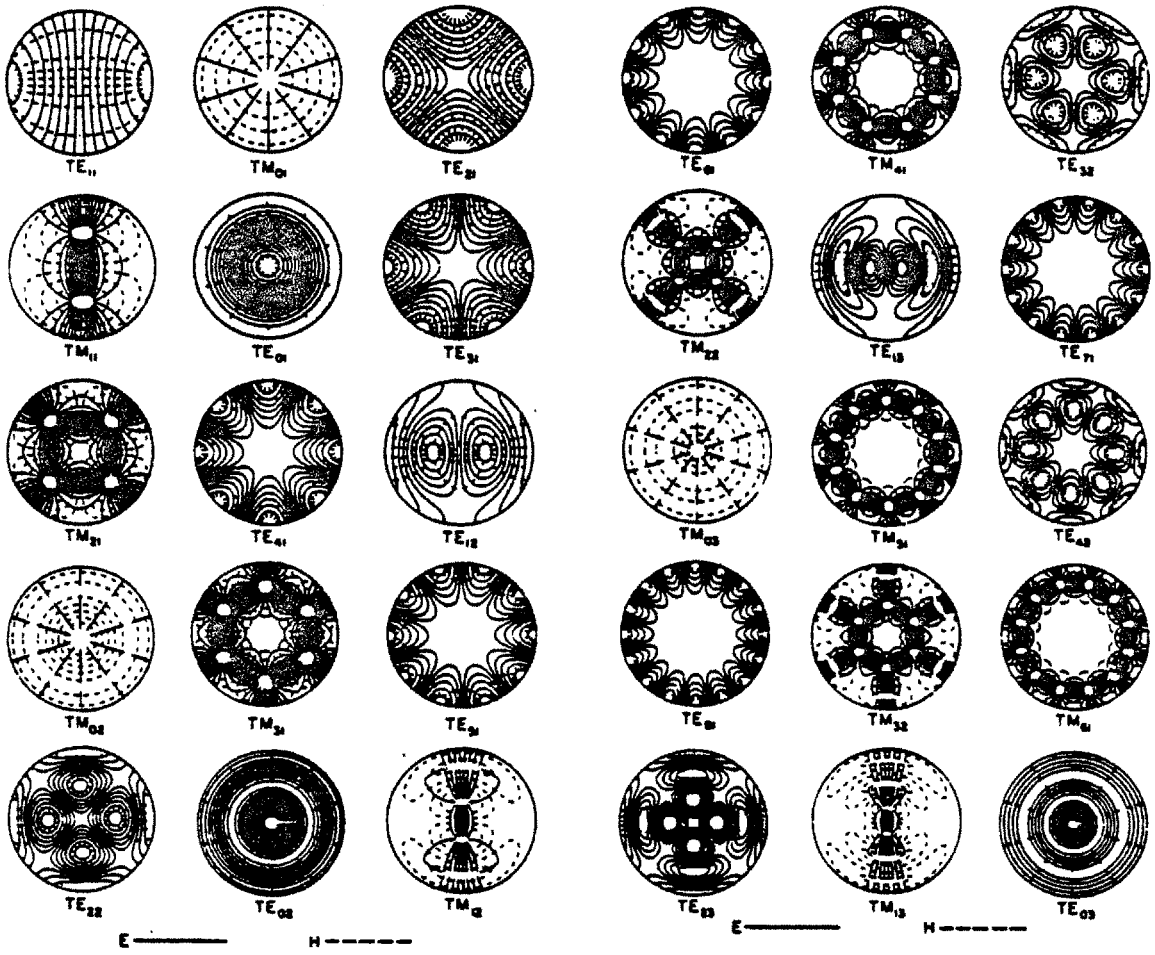

Figure 3.12 — Transverse Modal Field Distributions for the Circular Metallic Waveguide. The density of lines is approximately proportional to the field strength. (From reference 34.)

Unlike a dielectric or rectangular metallic waveguide, the lowest loss modes for the circular metallic case are not the lowest frequency modes but the TE_{0m} modes. These circularly polarized modes have an electric field null at the wall, and thus have losses orders of magnitude below the others. In the highly overmoded case of small $\lambda/2a$, these lowest loss modes propagate at frequencies many times the fundamental cutoff frequency. For the remainder of the modes listed, the attenuation coefficient is between .3 and .9 dB/M, in agreement with the experimental observations. The complicated transverse profiles seen in those figures result from the interference of modes with differing symmetries such as those listed above.[35] At the waveguide entrance, it is expected that the Gaussian mode should couple fairly well to the fundamental TE_{11}, which is the only linearly polarized mode. After mode conversion in the curved segment, however, the final spectrum may contain any or all of the above modes in varying proportions, and the measured overall loss is determined by the amount of radiation ultimately residing in each mode.

The transmission losses may be estimated for each component in the complete optical train based on experimental data and simple optical formulas. For the first surface mirrors, a 1% loss per mirror is expected, and for the TPX[36] lens, Polyethylene beamsplitter,[36,37] and Quartz[38] vacuum windows, abundant data on the optical properties of these materials found in the literature are used to calculate the absorption losses and Fresnel reflectivities. The waveguide transmissions are based on laboratory measurements in conjunction with theoretical predictions about the beam width at the waveguide aperture inside ALCATOR. The external waveguide transmission was measured *in situ*, at the time the experiment was initially installed. A summary of the transmissions of the various optical assemblies is shown below:

Injection Optics	.71
Quartz Vacuum Windows (2)	.41
Internal SS Waveguide Assembly	.85
External Cu Waveguide Assembly	.75
Net Transmission Expected	.19
Measured Transmission 4/18/83	.15

Water absorption can attenuate the detected signal from a few percent to as much as one half, depending on the line, atmospheric humidity, and effectiveness of the dry Nitrogen purge used in the laser enclosure and optical path. Thus, if 15 mW was available at the laser window, on the order 1 mW was available for detection. While this is, in itself, a large amount of radiation to detect, submillimeter background plasma emission signal can be orders of magnitude higher than the received laser signal. Emission from a thermal plasma in the first three cyclotron harmonics of both modes is typically in the 10 to 20 kW range. Of this, 1/3 to 2/3 Watt enters the collection system directly. In the presence of suprathermal electron components, this figure can increase by an order of magnitude.

A triple mesh Fabry-Perot filter was used to suppress the first and second harmonic emission while passing a band of about 50 GHz near the laser line. This provides a spatial resolution for emission in third harmonic equal to 5 cm about the center. Three 200 line per inch (LPI) Copper meshes were used in the device, each of which has a reflectivity of 65% at 700 GHz, rising linearly to 90% at 350 GHz, and then rolling over to unity. In the operation of the device, transmission orders of the two mesh pairs at the laser frequency were adjusted over successive shots to provide optimum rejection of the plasma emission. The transmission characteristics of this filter were found to be less sensitive to mechanical vibrations than those of a single high finesse mesh pair of comparable rejection.

Properties of the 200 LPI mesh were calculated using the equations of Baker and Walker[39] , along with an experimentally determined correction factor. The

theoretical mesh transmission was found to be low by a factor of 1.4 . A plot of the experimentally determined transmission spectrum is shown in figure 3.13, along with the corrected theoretical transmission and phase shift on reflection curves. Experimental spectra were taken with a rapid scanning Michelson interferometer.[40]

Triple mesh filter transmission spectra were calculated using the multicavity formalism of Hammer,[41] which was modified in a straightforward manner to include a metallic phase shift on reflection. The performance of the theoretical model is examined in figure 3.14, where an experimentally measured non-optimized transmission spectrum is shown along with the theoretical curve for a one pass attenuation factor of .12 and an experimental resolution of 16 GHz. Agreement is seen to be excellent. Theoretical transmission spectra for several plausible filter configurations are shown in figure 3.15, with the mesh pairs in various orders at the laser wavelength. Operation of the device is based on the coupling of the multiple cavities and the decrease in interferometeric Finesse for increasing frequency. At low frequencies, the reflectivity and Finesse are high, and it becomes difficult to satisfy pass conditions for all cavities simultaneously. At higher frequencies, the reflectivity and Finesse decrease, and the frequency width of each simple cavity passband increases considerably. Transmission through the stack occurs when the pass conditions of the multiple cavities are met at a single frequency.

Emission above the third harmonic was removed with a National Physical Laboratories 880 GHz low-pass filter, which has a transmission of .75 at 694 GHz (corresponding to 432.6 μm), .13 at 925 GHz ($4\omega_c$ for 432.6 μm in the center), and .02 for frequencies above 990 GHz.

The radiation was detected with a QMC Instruments, Ltd. Indium Antimonide submillimeter photoconductive detector mounted in a liquid Helium dewar. Bias currents of 50 and 140 μA were used for the transmission and reference detectors, respectively, and the radiation was attenuated to provide a 1 V level signal after a gain of 1000 amplifier. Due to strong pickup of Lower Hybrid frequency klystron radiation in the detection circuitry, the detectors and electronics were enclosed in sealed Aluminum RF cabinets. Radiation was admitted into each cabinet via a

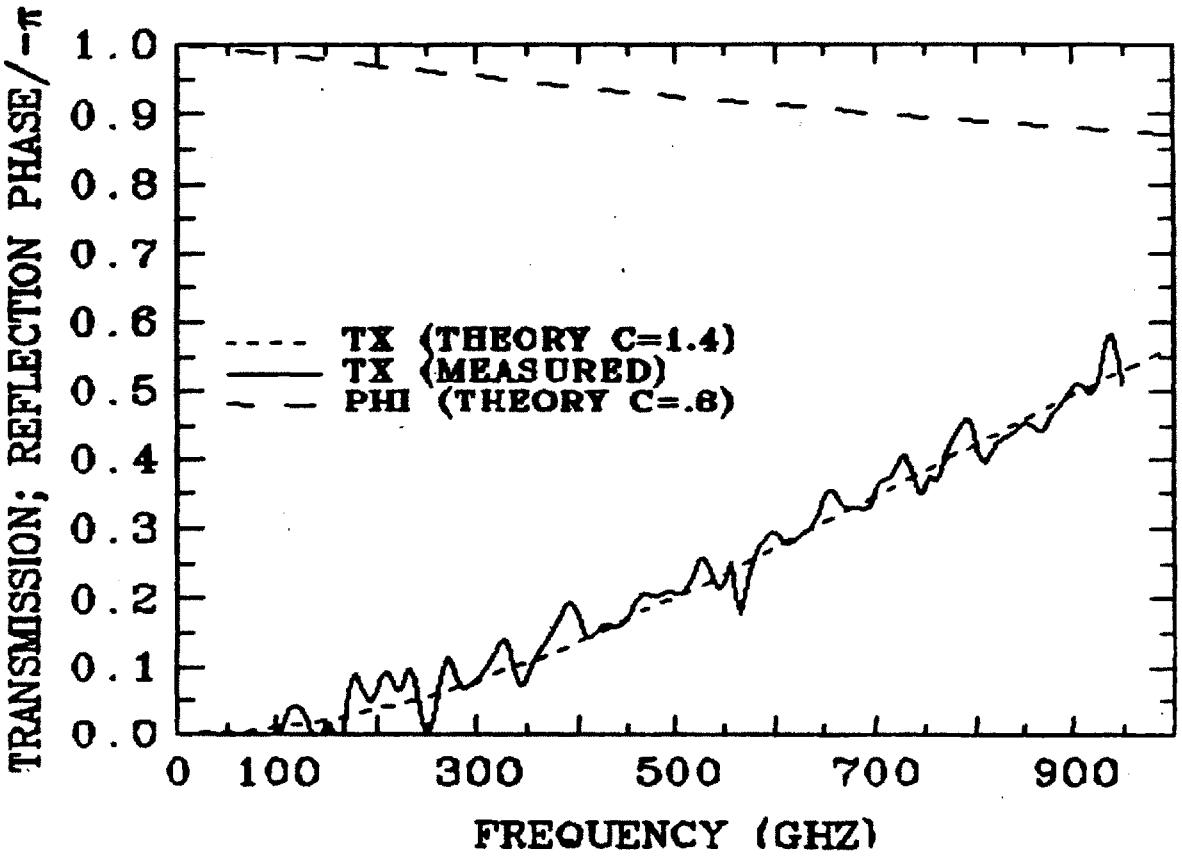

Figure 3.13 — 200 line per inch Metallic Mesh Transmission and Reflection Phase Shift Spectrum.

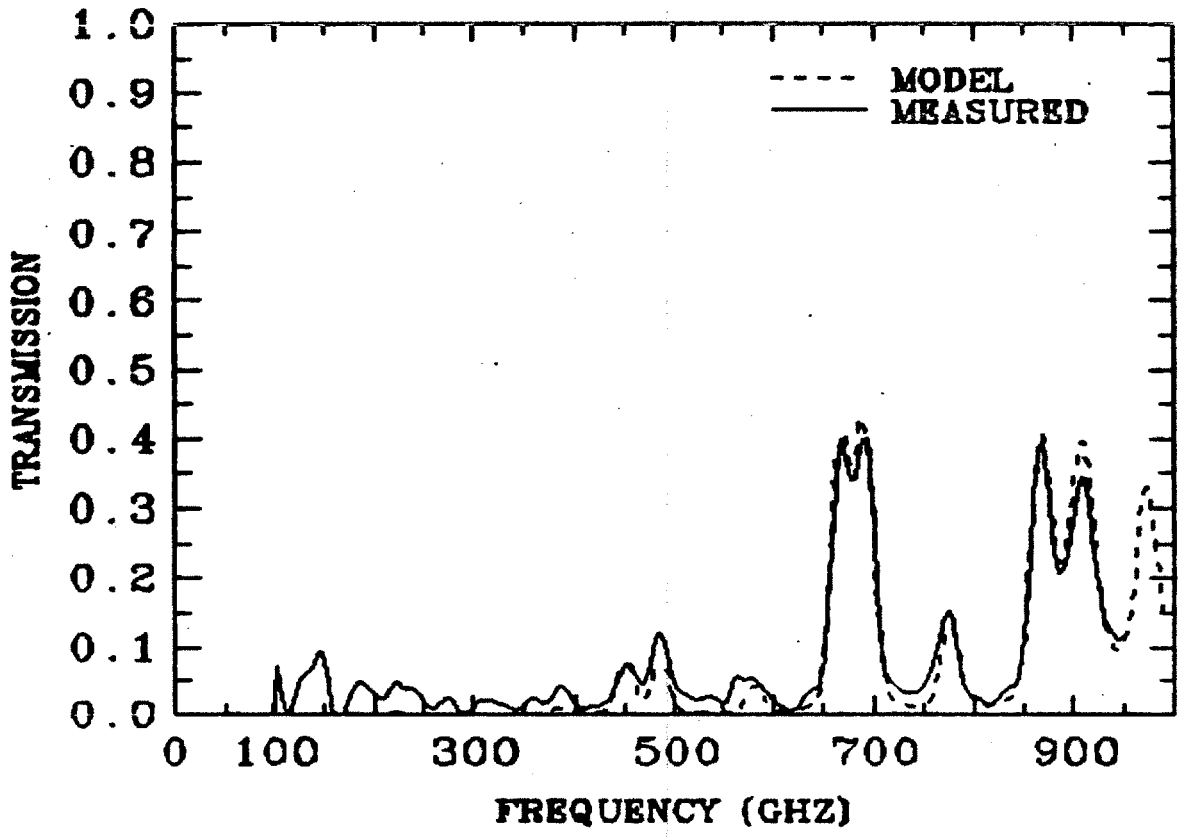

Figure 3.14 — Triple Mesh Fabry-Perot Filter Transmission Spectrum. $\lambda = 432.6\ \mu$m, 200 line per inch metallic mesh, Order 1 = 3, Order 2 = 7, Attenuation = .12, Resolution = 16 GHz.

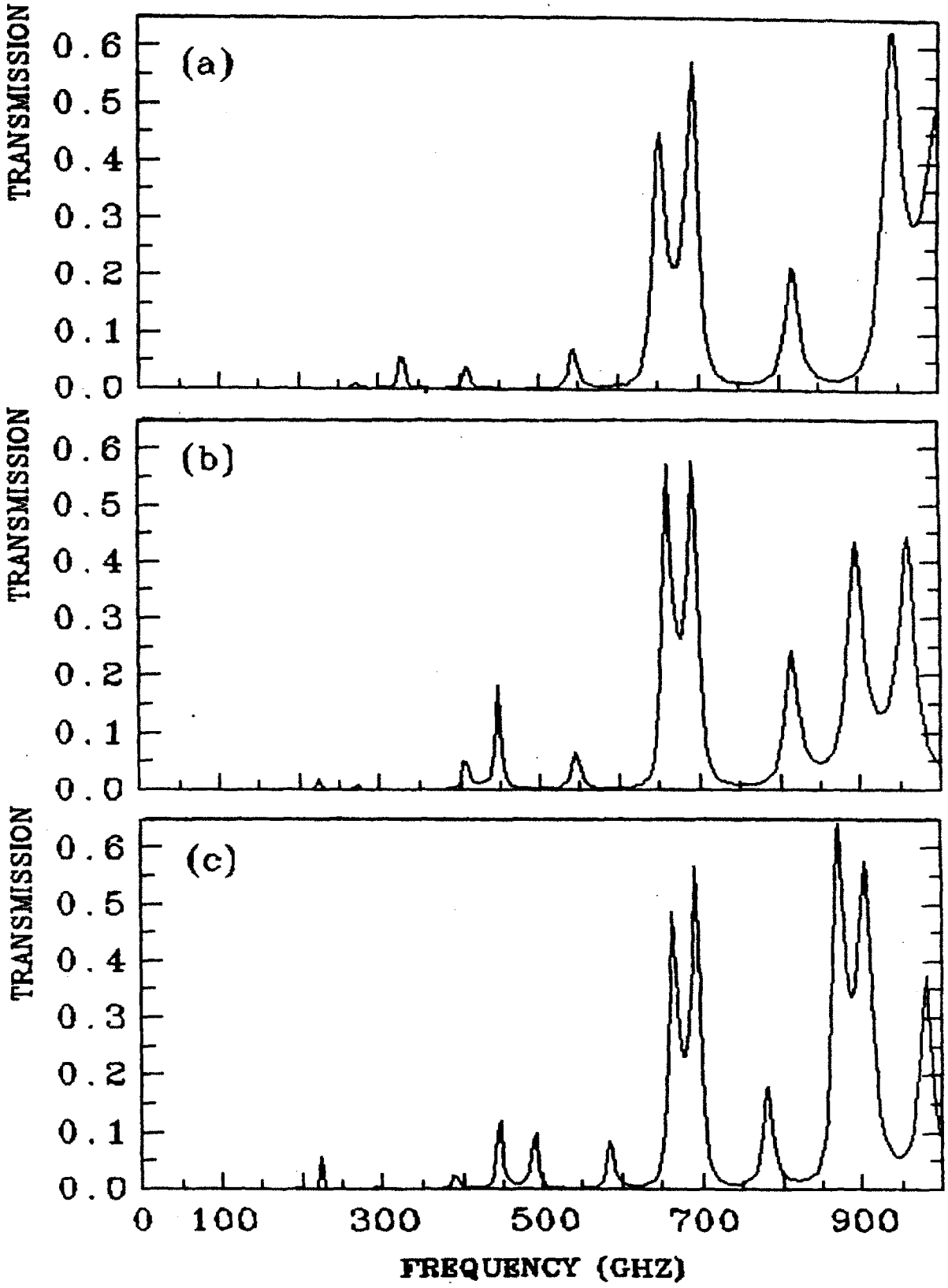

Figure 3.15 — Transmission Spectra of Triple Mesh Filter with Adjacent Mesh Pairs in Differing Orders. Resolution = 4 GHz, remaining data as in figure 3.14. (a) 1,5 (b) 3,5 (c) 3,7.

2 inch metal mesh covered aperture. The presence of this 200 LPI metal mesh served to provide an additional, non-interferometric, enhancement of $3\omega_c$ transmission relative to $2\omega_c$ in the Transmission channel. Helium vapors evolved by the dewar were vented directly out of the enclosure via a mesh capped metal tube. This was necessary in order to avoid rapid penetration of the dewar vacuum seals by He vapor concentrated in the enclosure, with a subsequent catastrophic loss of thermal isolation. The transmitted radiation was focused onto the detector element by a final 3/4 inch diameter Polyethylene lens.

The transmitted and reference signals were routed out of the experiment cell in Triax cable, up to the control room for entry into the data acquisition system. The signals were stored on a magnetic drum, and were available in the control room for inspection between shots. The signals were digitized at 5 kHz and archived by the VAX 11/780 for future recall and analysis, along with other data produced during the plasma shot.

3.4 Chapter Summary

The individual assemblies and components used in measuring the plasma transmission have been described. The optically pumped laser source has been detailed, including a novel counterbalance design for the FIR waveguide laser which proved to be very successful, and a description of the characteristics of the molecular laser lines used in this work. The optical train responsible for transporting the radiation has been described, and the unique properties of overmoded waveguide propagation have been examined in some detail. The high transmissions measured for the waveguide assemblies are attributed to properties of the characteristic modes of the overmoded circular metallic waveguide. The triple metal mesh Fabry-Perot filter has been studied theoretically and experimentally, and application of the device in filtering radiation collected in the experiment has been illustrated.

Chapter 4

DATA REDUCTION, ANALYSIS, AND INTERPRETATION

With use of the apparatus described in the preceding chapter, raw transmission data is produced in a format which requires reduction and analysis prior to interpretation. This chapter describes how raw data is reduced to obtain the absolute transmission, and how such information is unfolded to provide diagnostic information regarding the plasma electron temperature. Sources of experimental uncertainty and noise are identified and their effects are assessed. These are found to determine the range of applicability of the diagnostic technique.

4.1 Data Reduction and Analysis

Digitized ECA experiment data generated by the CAMAC hardware is archived by the VAX as a sequential access file with a dynamic range of ± 10 V and a maximum duration of 800 msec. A typical example of the Transmission and Reference 100 Hz modulated raw data channels is shown in figure 4.1, along with basic plasma data traces.

A digital Boxcar Analyzer routine, Program LOCKIN, was written to process and analyze the raw data. Transmission and Reference data are retrieved from magnetic tape or the system disk and conditioned for transient noise. A square wave phase function is then generated which divides the modulation cycle into quadrants, as shown in figure 4.2, and identifies the quadrant of each sample via the Real function:

$$\Phi(N) = \text{Modulo}\left[\frac{N-\phi_0}{T/4}\ ,\ 4.0\right]\ ,\ 0.0 \leq \Phi(N) \leq 4.0\ ,$$

where N is the CAMAC data sample number, ϕ_0 is the phase delay at the start of the shot, and T is the modulation period.

A discrete partial sum is calculated for each quadrant, and then weighted by the number of samples in the sum to produce a Real value. Each "off" quadrant sum is subtracted from the adjacent "on" sum to yield a value which represents the

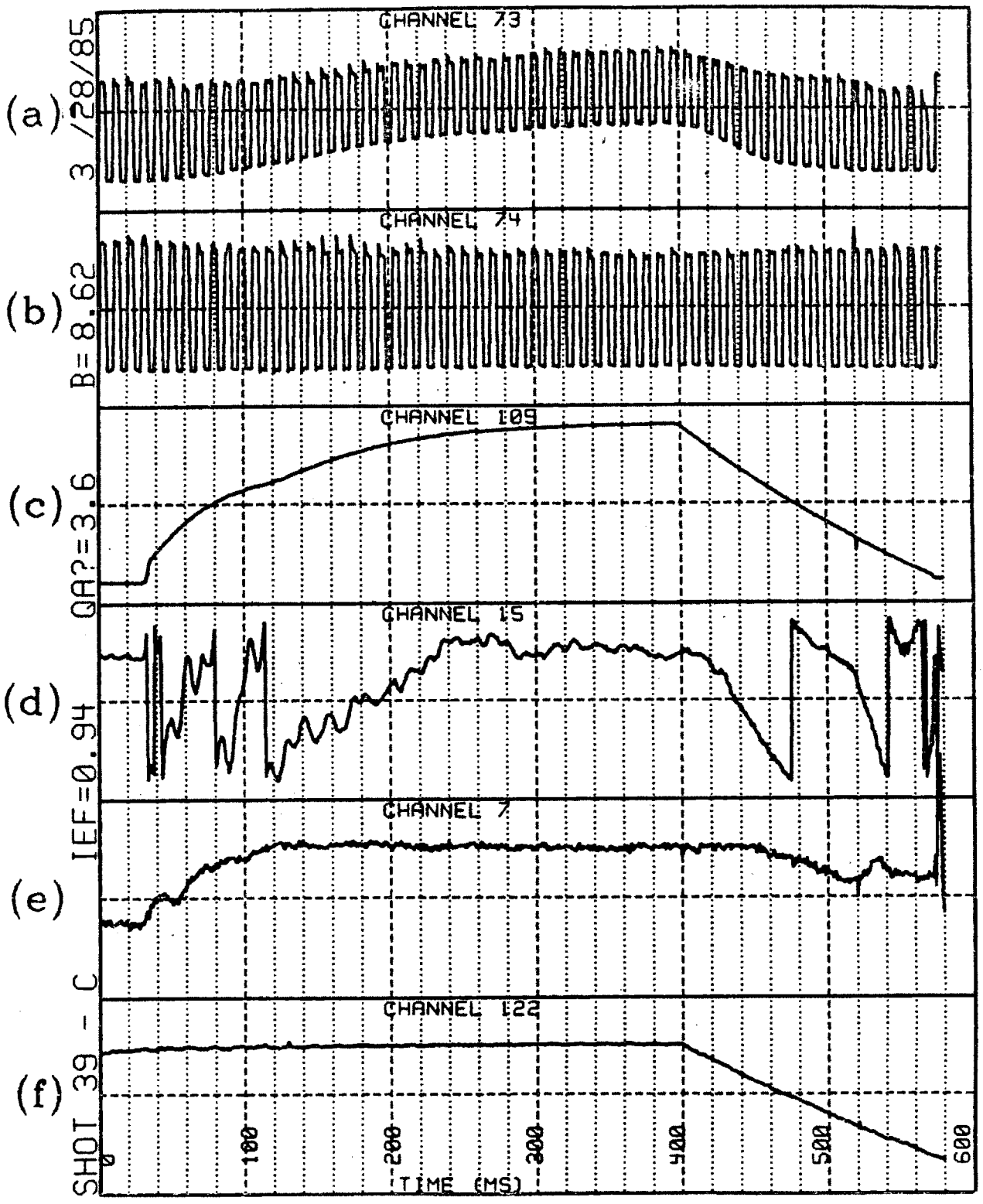

Figure 4.1 — Typical Plasma Shot Data, 3/28/85, Shot #39. Shown are (a) Raw transmitted signal (b) Raw reference signal (c) Plasma current, 2.5 V/div (d) Central chord averaged electron density (e) H_α emission (f) Toroidal Field.

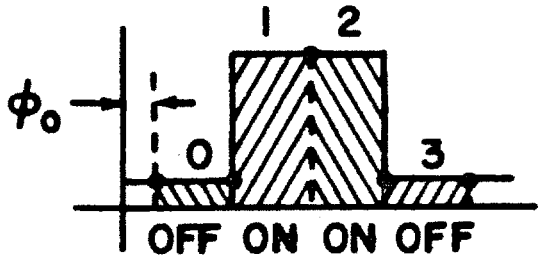

Figure 4.2 — Square Wave Phase Function. ϕ_0 is the phase delay from the data system time origin.

integrated laser power during the corresponding half cycle. The values are summed over the entire shot, and the resulting sum is maximized with respect to the phase delay and frequency of the phase function. Once an optimum fit to the transmission and reference data is obtained, each half cycle sum is normalized to an averaged pre-plasma value, and the normalized transmission and reference arrays are divided to yield a transmission which has been corrected for any change in the laser power:

$$\mathbf{T}_{\mathrm{corr}}(t) = \mathbf{T}_{\mathrm{raw}}(t)/\mathrm{Ref}(t)$$
$$= \frac{V_{\mathrm{T}}(t)}{V_{\mathrm{T0}}} \Big/ \frac{V_{\mathrm{Ref}}(t)}{V_{\mathrm{Ref0}}}$$

The reference, corrected transmission, and raw transmission traces are calculated and displayed versus time on a three section plot, shown in figure 4.3 . Also made available by LOCKIN is a run-time data log which documents the key parameters necessary to verify that the analysis proceeded without error. The traces may then be subjected to post-processing which provides for the interpolation of transients due to RF turn-on and turn-off, computation of values averaged over segments of time, smoothing the traces with a running average, and displaying the resulting traces for inspection and further processing.

The partial sums for the "off" quadrants of the transmission data represent the quadrant integrated plasma emission, and are retained in a separate array.

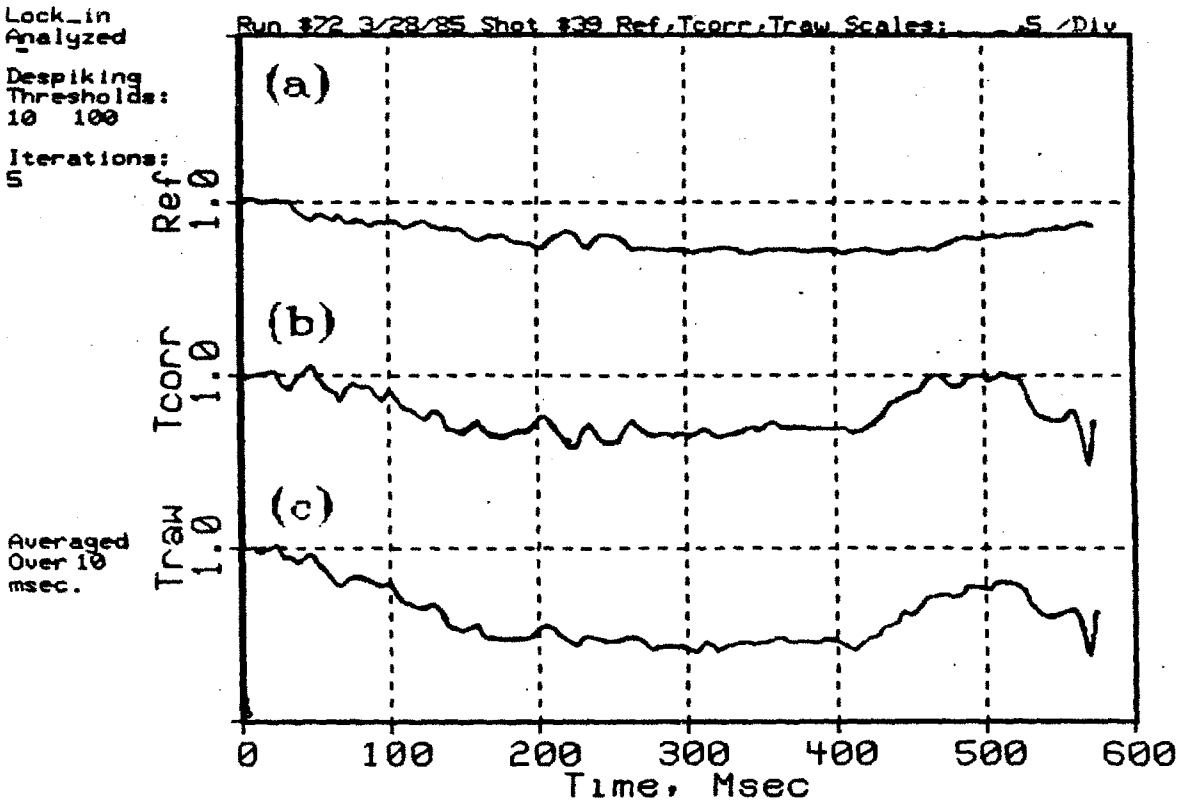

Figure 4.3 — Program LOCKIN Reduced Data Output. Shown are (a) Normalized laser power (b) Absolute transmission corrected for the change in laser power indicated in trace a (c) Raw (uncorrected) transmission.

emission and transmission data obtained concurrently in this manner, the source function can be calculated (to within a multiplicative constant) and displayed along with the absorption and emission, versus time, as shown in figure 4.4 . The source function and the procedure by which it is obtained will be discussed in section 5.3, along with various applications.

Program LOCKIN contains 1900 lines of code in 16 subroutines, and executes in a user friendly, menu-driven format. The code can be run in a diagnostic mode, in which simulated data can be constructed and used to study the effects of white or transient noise, disruptions, RF, or other plasma behavior on the code performance. Also in this mode, a detailed diagnostic run menu is available, with which output and diagnostic data may be accessed within the deepest levels of execution. These capabilities proved invaluable in the development, testing, optimization, and modification of the code. The analysis typically requires 30 to 60 CPU seconds per shot to run on the VAX 11/780, and the code may be run either interactively, or in batch mode, which outputs only the 3 graph transmission plot in a standard format, along with the precise frequency.

With use of the code diagnostic capabilities, the LOCKIN algorithm was found to be extremely reliable, typically returning a frequency which is within 0.3% of the shot averaged value. In addition, because of the parallel treatment of the Transmission and Reference channels and their subsequent division, small frequency drifts or errors have no effect on the corrected transmission trace. Large errors in frequency or phase manifest themselves quite evidently as artifacts in the resulting traces, or as incorrect values in the run-time data which is examined after every LOCKIN run. In general, the initial trial frequency must be within 5% of the actual frequency in order for the analysis to converge on the correct result. Outside of this range, the analysis tends to converge on subsidiary maxima, leading to obviously implausible results.

4.2 Electron Temperature Analysis

Once the absolute plasma transmission at a given laser frequency is known, along with the electron density and toroidal field, one can extract the electron

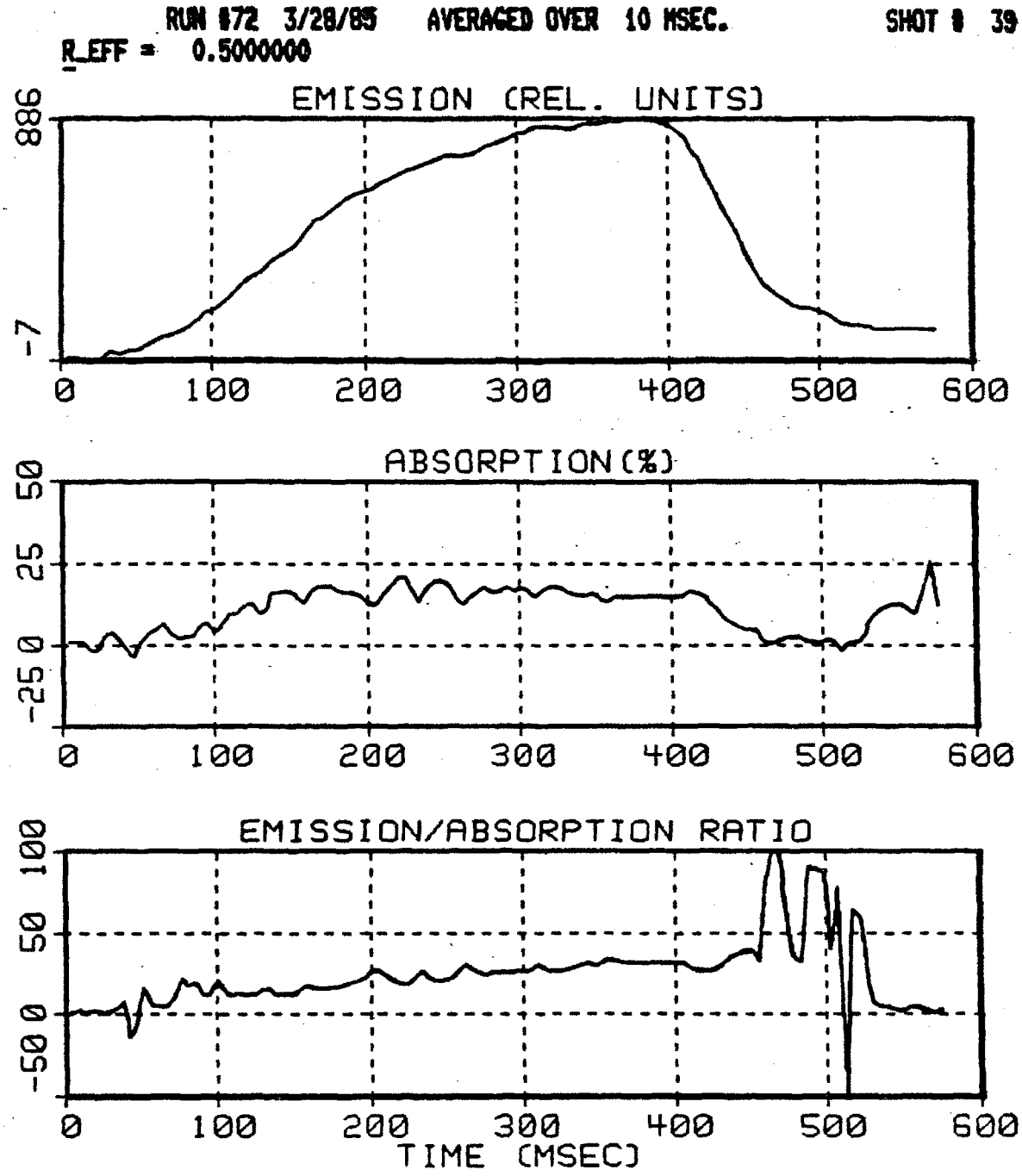

Figure 4.4 — Emission, Absorption, and Source Function Curves Derived from the LOCKIN Data Analysis.

temperature at the location of the nth resonance using the fundamental $n_e T_e^{n-1}/B_t'$ scaling of the optical depth introduced in Chapter 2.

Electron density data in ALCATOR C is provided by a submillimeter wave interferometer system, which measures the line averaged density along four chords, with a fifth chord blocked by the ECA collection waveguide. The equilibrium density profile is usually poloidally symmetric, and is described by

$$n_e(r) = n_{e0}\left[1 - \left(\frac{r}{A_n}\right)^2\right]^{\beta} ,$$

with $A_n \approx 17.5$ cm, $\beta \approx .5$, and n_{e0} the peak on-axis value. The fit is best in the interior regions of the discharge where the density variation is rather slow, with

$$n_e(r = 15 \text{ cm}) = .5\, n_{e0} .$$

Most plasmas studied in this work are well described with the above choice of parameters, with the notable exception of Pellet fueled discharges, which are not considered in this work, and very low density discharges. LHRF Current Drive typically requires operation at densities of $7 \times 10^{13}\text{cm}^{-3}$ and below, for which the value $\beta = 1$ is found to be more appropriate, and is used in the analysis.

The line averaged density is recorded in "fringes", as seen in figure 4.1, trace d, for the central chord, designated channel 15. Each fringe corresponds to a line averaged density of $.565 \times 10^{14}$ cm^{-3}, with the peak value a factor of either $4/\pi = 1.27$, or 1.5, times the line average, for $\beta = .5$ or 1.0, respectively. Another quantity in common use is n_e^{14}, which is the line averaged density along the central Tokamak chord expressed in units of 10^{14} cm^{-3}.

The toroidal field trace is shown in trace f, with the plateau value calculated from a TF coil diagnostic shunt. Using an FIR grating spectrometer to measure the absolute frequency at which the $2\omega_c$ X mode emission, and hence the temperature, is maximum, the shunt can be calibrated to give the toroidal field in the discharge center, which is Shafranov shifted outward from the toroidal axis by .5 to 1 cm. This calibration factor was found to be between .72 and .73 kG/kA, and is taken to be .725 in this work.

The electron temperature profile is also found to be poloidally symmetric, and is described by the Gaussian

$$T_e(r) = T_{e0} e^{-(r/A_t)^2}$$

where T_{e0} is the central value, and A_t is a temperature width which varies with the discharge conditions. For sawtoothing discharges, it has been determined experimentally that in the inner regions of the discharge[42]

$$A_t = \frac{18.03}{\sqrt{q_l}} ,$$

$$q_l = \frac{2\pi B_t r_l^2}{\mu_0 I_p R} ,$$

where q_l is the limiter safety factor, r_l is the limiter radius, and I_p is the plasma current. During the high power Ohmic conditions typical of ALCATOR C discharges, q_l is near 4, so that A_t is approximately 9 cm. For higher q_l discharges, sawtooth activity ceases, and A_t approaches a value of approximately 7 cm. For the low density, low current discharges of LHRF Current Drive a further decrease in A_t has been observed during the RF pulse, to a value near 6 cm.

With a knowledge of the laser frequency and the toroidal field, the resonant position is calculated, and the local density is obtained from the measured line averaged density and profile information. The local temperature is then deduced from the measured optical depth. This analysis is performed by Program HTAU, which takes the input data described above and calculates local contributions to the absorption by any resonances along the ray path, and the overall plasma transmission. For an off axis resonance, the peak temperature can be inferred from the local temperature by calculating or inputting a temperature profile width. For resonances within a few centimeters of the center, the small interpolation required to obtain the peak temperature introduces little additional error because the temperature variation is small near the center, and the sensitivity to the temperature width is weak. This is illustrated by data from a typical HTAU run, for which we examine the sensitivity of the local temperature and overall transmission to the width A_t:

Input Data	Output Data
$\lambda = 432.6\mu$m	$r_3 = -1.9$ cm
$B_{t0} = 8.0$T	$q_l = 3.403$
$I_p = 500$ kA	$A_t = 9.77$ cm
$T_{e0} = 2.0$ keV	$T_e(r_3) = 1.93$ keV
$n_e(0) = 2.16 \times 10^{14}$ cm^{-3}	$n_e(r_3) = 2.15 \times 10^{14}$ cm^{-3}
$R = 64$cm	T = .803
$a = 16.5$ cm	

Sensitivity to T_e Width A_t

$A_t = 8$ cm	$A_t = 10$ cm	$A_t = 11$ cm
$T_e(r_3) = 1.89$ keV	$T_e(r_3) = 1.93$ keV	$T_e(r_3) = 1.94$ keV
T= .809	T= .802	T= .800

This method has been used, when necessary, to obtain the central value of T_e. When the resonance is far from the center, the transmission is used to provide an accurate measurement of the local off-axis temperature.

4.3 Error and Sensitivity Analysis

4.3.1 Noise Characteristics

The viability of the electron temperature analysis is determined by the validity of the integral methods employed by Program LOCKIN in the transmission data reduction process. Plasma transmission and emission levels reported by LOCKIN represent an average value over the 5 msec modulation half-cycle. Although noise at frequencies much above the modulation frequency is averaged out in this integration process, the data often contains low frequency noise in the 35-100 Hz range as well. These are caused by mechanical oscillations and vibrations which are common in

the cell environment, driven by the eddy currents or structural transients which accompany the intense magnet pulses. Transmission data used in the temperature analysis is averaged over a period which is sufficient to remove these effects, typically 10 to 50 msec, and this period constitutes the final time resolution obtained. This period is shorter than the timescale of many plasma events, and it is these "steady state" events which are the focus of this work.

In addition, transients on the modulation timescale violate the basic premise of the LOCKIN analysis, and the half cycles during which they occur must be considered invalid. This situation is routinely encountered in the LHRF turn-on and turn-off transients, which disqualify one to two cycles (10 to 20 msec) each. A more severe case may be encountered during Current Drive in low density plasmas with large spontaneous impurity injections, when conditions of bursting or unsteady $3\omega_c$ emission may invalidate an entire shot. The unique challenges posed by the analysis of Current Drive discharges will be considered below in a discussion of the uncertainties of measurement.

4.3.2 Accuracy of the Temperature Determination

The uncertainty in each parameter which enters the temperature analysis diminishes the overall accuracy of the final result. The propagation of these uncertainties depends on the scaling and magnitudes appropriate to each type of result presented in this work.

Effects of a Transmission Uncertainty:

Although the LOCKIN routine can detect absorptions at the 1% level in test data, the presence of low frequency noise introduces an inherent uncertainty of 2 to 5 percent in the actual transmission determination. The 5 percent figure constitutes a somewhat conservative appraisal of the standard deviation found in time averaged data for repeated transmission measurements under routine circumstances, and is the basis of the discussions which follow.

For the $n = 3$ determination, the uncertainty in the temperature, $\Delta_3 T_e$, due to an uncertainty in the transmission, ΔT, scales as

$$\Delta_3 T_e \propto \frac{\Delta \mathbf{T}}{n_e T_e \mathbf{T_3}}$$

evaluated at the resonance location. This is illustrated in figure 4.5, in which the temperature uncertainty is plotted versus local temperature, for two line averaged densities. The asterisks represent experimental ALCATOR C operating points, and reflect the fact that for a given plasma current an increase in density is accompanied by a decrease in temperature, and visa versa. The uncertainty for Ohmic heated ALCATOR C plasmas is seen to lie between 10 and 15 percent, with the 8 percent point at a higher temperature corresponding to the SiC limiter Lower Hybrid RF Heating result.

For the second harmonic n=2, the temperature uncertainty scales as

$$\Delta_2 T_e \propto \frac{\Delta \mathbf{T}}{n_e \mathbf{T_2}}$$

evaluated at the resonance location. This is plotted in figure 4.6 for the n=2 resonance at $r = -12$ cm, in the appropriate temperature range, and two values of line averaged density. The density at $r = -12$ cm is .7 times the central value for $\beta = .5$. Also shown is a measured ALCATOR C operating point corresponding to this case. The uncertainty is seen to lie between 15 and 20 percent for a wide range of temperatures and densities.

Effects of a Density Uncertainty

Uncertainty in the density originates in two ways. First, there is a .1 fringe uncertainty in tallying the central channel fringe count due to the presence of the low frequency amplitude noise described in section 4.3.1 . Second, there is an error in interpolating the local density from the line averaged values and profile information, and due to local deviations from the best-fit profile. The first effect is generally small, amounting to a few percent for typical ALCATOR C densities. The profile effect is small in the interior region of the discharge, where the profile fit

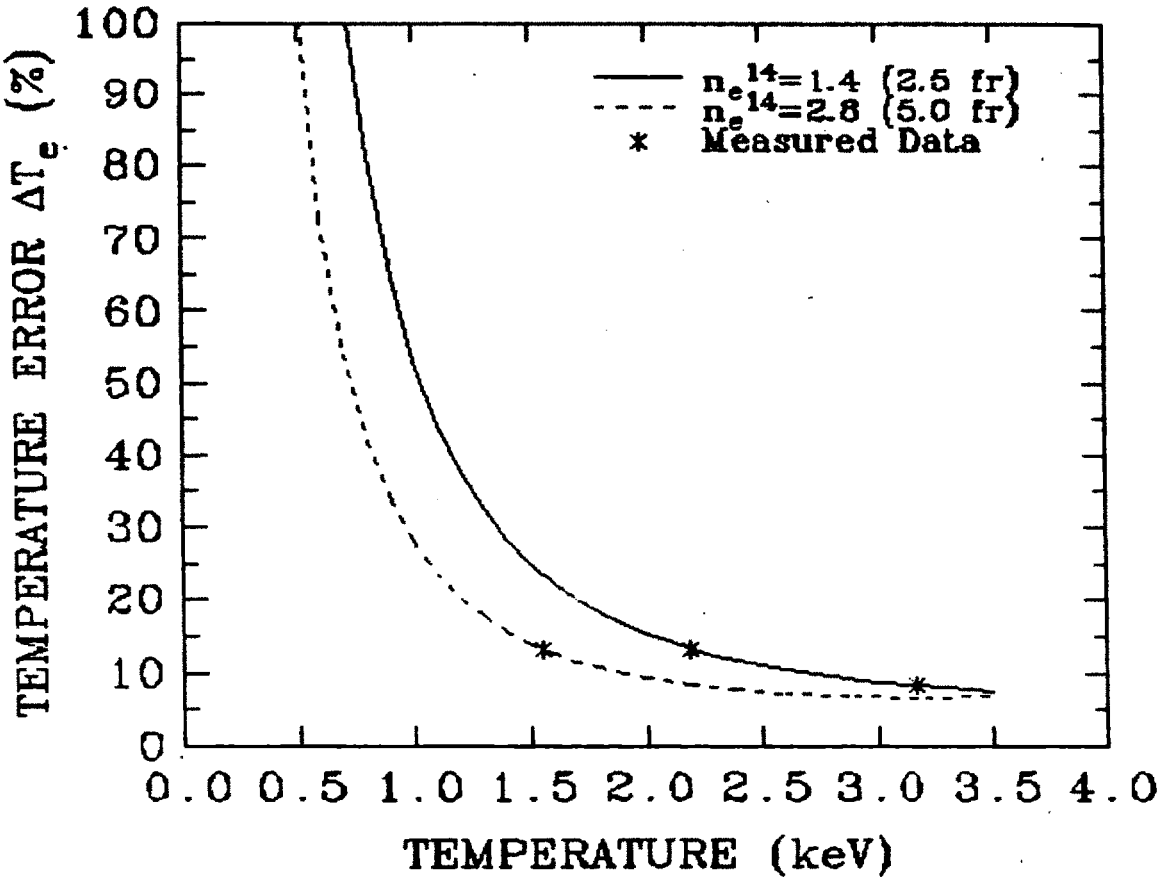

Figure 4.5 — Uncertainty in Temperature Due to a 5% Uncertainty in the Third Harmonic X Mode Transmission.

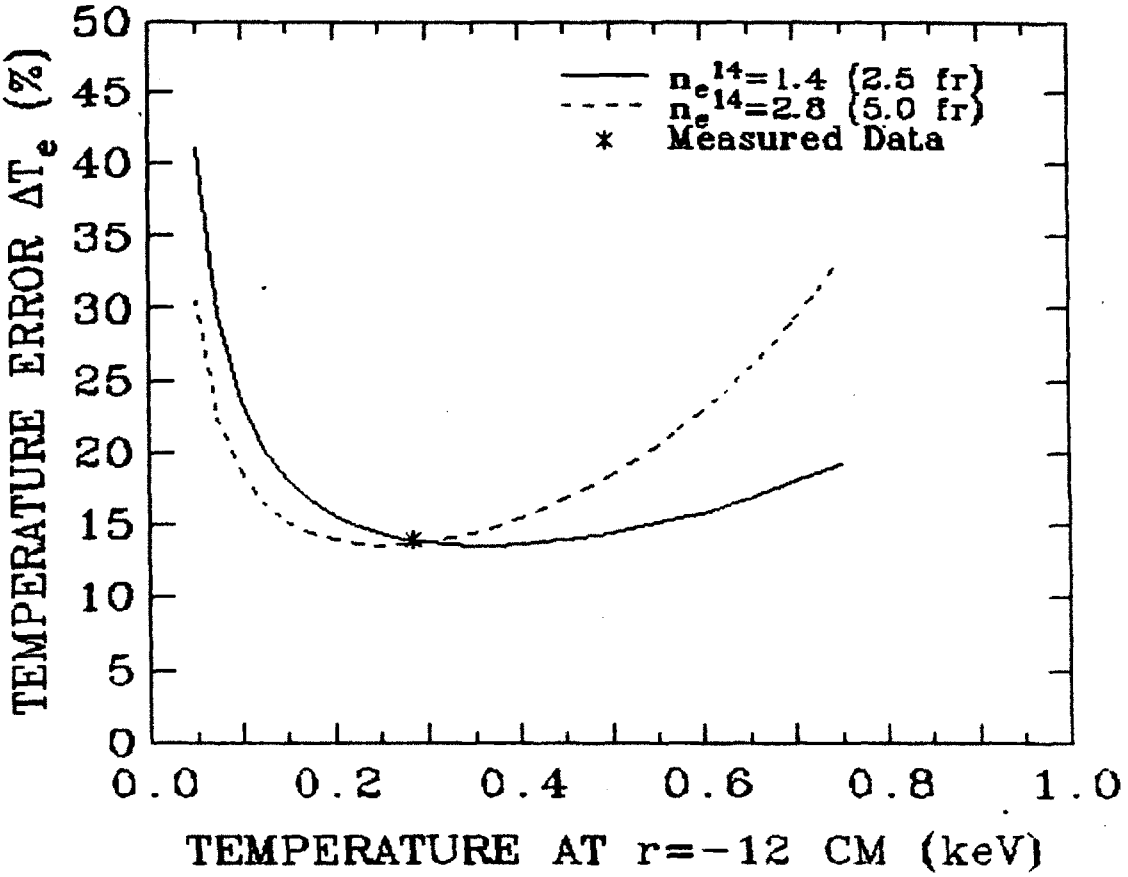

Figure 4.6 — Uncertainty in Temperature at $r = -12$ cm Due to a 5% Uncertainty in the Second Harmonic X Mode Transmission.

is best and the density varies rather slowly, but near the plasma edge, interpolated densities can be in error by 50 percent or more.

The density induced uncertainty in the temperature is found to be

$$\frac{\Delta_3 T_e}{T_e} = \frac{1}{2}\frac{\Delta n_e}{n_e}$$

$$\frac{\Delta_2 T_e}{T_e} = \frac{\Delta n_e}{n_e}$$

for the third and second harmonics, respectively. For a typical case near the plasma center, we may find

$$n_e = 2.5 \text{ fringes} \quad , \Delta n_e = .1 \text{ fringe} \, ,$$

$$\frac{\Delta n_e}{n_e} = .04 \quad , \frac{\Delta_3 T_e}{T_e} = .02 \, ,$$

whereas for $r > 14$ cm, we may find

$$\frac{\Delta n_e}{n_e} = .5 \quad , \frac{\Delta_2 T_e}{T_e} = .5 \, .$$

Thus, density induced uncertainties tend to be small for the $n = 3$ interior measurements, but for the $n = 2$ outer plasma measurements, they can contribute a large source of uncertainty.

Effects of a Toroidal Field Uncertainty

The uncertainty in the absolute calibration of the toroidal field shunt reading relative to the field at the discharge centroid manifests itself in two ways. To local temperature determinations, it introduces an uncertainty in the spatial location of the resonance. Alternatively, to interpolations of the peak temperature from near-axis data it brings an uncertainty in temperature.

The spatial uncertainty, δr, due to an uncertainty in the calibration factor, δC, is given by

$$\delta r = (R + r)\frac{\delta C}{C} \, .$$

Thus, the values $C = .725$, $\delta C = .01$ produce a spatial resolution of .7 to 1.0 cm for $-15 < r(\text{cm}) < +6$, the spatial range encountered in this work.

The uncertainty in the central temperature, ΔT_{e0}, interpolated from transmission data with a resonance at radius r, is given by

$$\frac{\Delta T_{e0}}{T_{e0}} \approx \frac{2r\ \delta r}{A_t^2}$$

where A_t is the Gaussian width of the temperature profile. For the representative case of $A_t = 9$ cm, $r = -2$ cm, $\delta r = .9$ cm, we find a 4.4 percent uncertainty in the peak temperature.

The above uncertainties are summarized below. For each of the types of analyses performed in this work, the range of total temperature uncertainty is given, in percent, with the contributing factors described above:

1) Local temperature derived from $3\omega_c$ data (10-17%)
   - calculated transmission effect
   - density noise effect
   - .7 to 1.0 cm spatial accuracy
2) Central temperature interpolated from near-axis $3\omega_c$ data $r \leq 2$ cm (14-21%)
   - calculated transmission effect
   - density noise effect
   - spatial interpolation effect
3) Local temperature from $2\omega_c$ data in the central region $r \leq 12$ cm (15-20%)
   - calculated transmission effect
   - density noise effect
   - .7 cm spatial accuracy
4) Local temperature from $2\omega_c$ data near the plasma edge $r \geq 14$ cm (65-100%)
   - calculated transmission effect
   - density profile effect
   - .7 cm spatial accuracy

The error bars seen in the presentation of diagnostic results correspond to the values calculated above .

4.3.3 Range of the Temperature Determination

We have seen in figure 4.5 that for a given density, the uncertainty in the $3\omega_c$ temperature determination rises rapidly at low temperatures. As the total attenuation approaches the 5% transmission uncertainty, the temperature uncertainty must become large. Thus, a practical limit exists on the applicability of the diagnostic technique, in that a minimum amount of absorption must be present for the analysis to provide temperatures with useful accuracy. This is illustrated in figure 4.7, where we have plotted the density required for 10% absorption, versus central temperature. This constant absorption curve corresponds to approximately 30% uncertainty in the final $3\omega_c$ central temperature result, and constitutes a reasonable, if somewhat arbitrary, boundary in parameter space below which the diagnostic performance is no longer comparable with other central temperature diagnostic methods under normal circumstances.

Another limit on the diagnostic performance appears at high densities. When the density rises above a critical value, n_m, a Marfe appears at the plasma edge.[43,44] This cold, high density plasma mantle scatters submillimeter radiation very strongly with local density gradients of the order of 10^{14} cm^{-3} /mm in the Marfe region. The Marfe is heralded by an abrupt increase in H_α emission or by a change in one or more submillimeter interferometer channels, and may cause an abrupt drop in the $3\omega_c$ transmission or other effect. As this behavior acts to obfuscate the central plasma cyclotron absorption measurement, Marfe conditions must clearly be avoided. The threshhold line averaged density is experimentally found to depend primarily on the plasma current, with the empirical scaling[43]

$$n_m(10^{14}\mathrm{cm}^{-3}) = .00635\ I_p(\mathrm{kA}) - .409\ ,\quad (I_p > 300\mathrm{kA}).$$

This limiting density is also indicated in figure 4.7, for several values of the plasma current. At lower currents, the Marfe threshold is found to be at least twice the value given by the above formula, and this limit is indicated for the 150 kA case. Thus, diagnostic performance is best in the region lying between the 10% absorption curve and the appropriate Marfe threshold curve. Since a Marfe may occur whenever

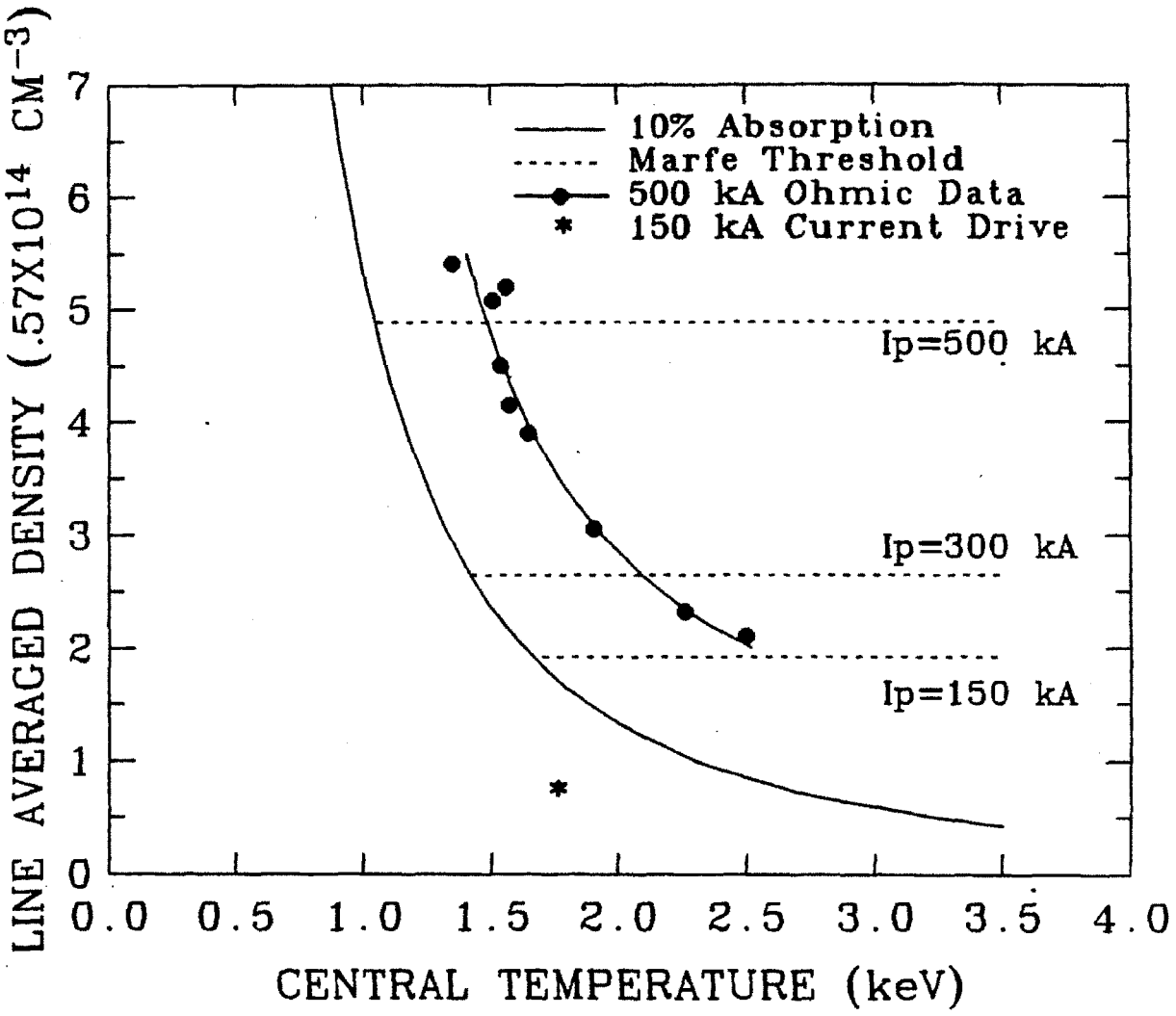

Figure 4.7 — Third Harmonic X Mode Transmission Temperature Diagnostic Parameter Space for a Toroidal Field of 8 Tesla.

the threshold density is exceeded for the current at that time, the current rise and post-inversion portions of the discharge are also susceptible to Marfe effects. Consequently, transmission data is usually taken during the flat portion of the discharge.

Also shown in figure 4.7, for comparison, is a fit to experimentally measured ALCATOR C temperature-density data. The 500 kA plasma current Ohmic operation curve reflects the aforementioned inverse relationship between density and temperature at a fixed plasma current. It is found that routine ALCATOR C Ohmic operating conditions lie well within the optimum performance region except at the highest densities, and thus support the type of diagnostic studies undertaken in this work quite well. These discharges are characterized by a 15 to 30% absorption level, and a 10 to 21% temperature uncertainty for n=3, as discussed above.

A contrasting situation is encountered for Lower Hybrid Current Drive discharges, which pose the severest test of the LOCKIN algorithm. These are characterized by low density and plasma current, and a $3\omega_c$ absorption of 5% or less. The 150 kA Current Drive operation point is seen to lie beyond the boundary of the the 10% absorption curve, a characteristic of the tenuous LHCD conditions. In addition, because the filtered $3\omega_c$ emission background can be 5 to 10 times larger than the laser signal for these tenuous discharges, the transmission data is particularly susceptible to the effects of noise, which consists of mechanical vibrations as well as possible fluctuations in the large emission baseline and bit noise in the subtraction process used to obtain the laser power. Consequently, no temperature determination is performed in this work for Current Drive discharges. However, the full integral/synchronous-averaging capabilities of the LOCKIN algorithm are utilized to extract useful transmission levels, which are averaged over identical shots and compared with expected transmissions based on other data, and with levels measured for Ohmic simulations.

4.3.4 Effects of a Non-Resonant Attenuation (NRA)

Transmission through the plasma may be accompanied by an attenuation which is independent of the occurrence of an $n\omega_c$ layer along the ray path. In ALCATOR C, two types of non-resonant attenuation have been observed. The first is associated with the appearance of a Marfe, as has been discussed in the previous section. The second type of non-resonant attenuation observed (and that referred to herein as "NRA"), is constant during most of the shot (NRA $\approx$ 5-30%), and is distinct from Marfe related effects. The NRA scales strongly with the peak electron density reached during the shot, although it exhibits little dependence on the instantaneous central density or temperature, toroidal field, or on RF injection conditions. Although the existence of a source of non-resonant attenuation poses an additional complication in the analysis of transmission data, the apparent weak dependence on the time evolution of central plasma parameters and other conditions allows the non-resonant correction to be obtained consistently for a given experiment environment, using a number of methods.

Examples of the peak density scaling of the NRA are shown in figures 5.5 and 5.14, for data obtained in 1983 and 1985, respectively. The considerable difference in the magnitude and character of the NRA seen in these two curves is attributed to differences in the Tokamak and/or experiment configurations at the two times. These and related issues will be examined more closely in chapter 6, when the origins and phenomenology of the NRA are considered.

In this work, the NRA is treated empirically as a correction factor which is applied when required. The presence of an NRA, as indicated by a consistent subunity transmission for non-resonant experiment conditions, requires that resonant $n\omega_c$ transmission data be divided by a factor taken from NRA data for similar conditions, prior to the HTAU temperature analysis. Since this correction factor is obtained experimentally, the uncertainty in the correction invariably propagates into the final result, effectively increasing the uncertainty in the transmission. The total uncertainty in the corrected transmission ΔT_c, is given by[45]

$$\frac{\Delta T_c}{T_c} = \left[\frac{1}{T^2_{meas}} + \frac{1}{T^2_{nra}}\right]^{\frac{1}{2}} \Delta T - (\text{Covariance term})$$

where $\mathbf{T_{meas}}$ is the uncorrected transmission, $\mathbf{T_{nra}}$ is the NRA correction, $\mathbf{T_c} \equiv \mathbf{T_{meas}}/\mathbf{T_{nra}}$ is the corrected transmission, and $\Delta\mathbf{T}$ is the uncertainty in the determination of $\mathbf{T_{meas}}$ or $\mathbf{T_{nra}}$. The covariance term is positive definite, and acts to reduce the final uncertainty, but we will assume that the fluctuations in $\mathbf{T_{meas}}$ and $\mathbf{T_{nra}}$ are statistically independent, in which case the value is zero. The additional uncertainty due to the NRA correction is found to lie in the range

$$1.37 < \frac{\Delta \mathbf{T_c}}{\Delta \mathbf{T}} < \sqrt{2}$$

for the parameters considered in this work, and the conservative upper limit is used throughout the data presentation.

Although the presence of the above experimental effect reduces the absolute certainty with which the temperature can be determined, there are, however, certain mitigating circumstances. Indeed, in the density range for which the NRA is less than the uncertainty of the data, no explicit correction is made, and the errors remain as described in the previous sections. Fortunately, this range is of great interest in routine Tokamak operation, and much data is available there. Also, due to the large resonant absorption of the second harmonic ($15\% < \mathbf{T_2} < 50\%$), the ultimate effect of the NRA on the local temperature is quite minimal for these points. The effect on $3\omega_c$ temperature data is found to be approximately linear, so that points which require an NRA correction have a transmission induced temperature uncertainty which is 40% greater than those that do not. The overall uncertainties given at the conclusion of section 4.3.2 for the $3\omega_c$ data are thus increased to 13-23% for local temperatures, and to 17-27% for interpolated central temperatures.

In the presentation of each result in Chapter 5, the non-resonant correction, the method by which it is obtained, and its application to the transmission data will be discussed, and representative errors will be calculated and displayed for each range or class of data points seperately. If no well matched NRA data is available from which to formulate a correction, possible effects which this may have on the results are examined.

4.4 Chapter Summary

In this chapter, the reduction of the raw data by Program LOCKIN and the temperature diagnostic analysis of the transmission by Program HTAU were described. The theoretical dependence of the cyclotron harmonic transmission on the electron density, temperature, and magnetic field is exploited to obtain the electron temperature or radiation temperature from the measured absolute transmission. Uncertainties in the constituent parameters determine the overall uncertainty in the final temperature, in a manner which depends specifically on the role each parameter plays in the absorption process. The range of applicability of the experimental technique is determined by a deteriorating accuracy at low density and temperature, and by interference from Marfes at high density. Routine ALCATOR C operation was seen to lie in an optimal region of temperature diagnostic parameter space for the applications considered in this work. Finally, the effect of a non-resonant attenuation was assessed, and a method of correction was described.

Chapter 5

PLASMA DIAGNOSTIC RESULTS

The principles, tools, and methods of the preceding chapters are now applied in a number of diagnostic applications. First, experimental data is shown which verifies the theoretical analyses of Chapter 2, and validates the temperature diagnostic operation of the experiment. Also, temperatures obtained from the cyclotron transmission are compared with those from standard temperature diagnostics, in an extended temperature range. Plasma observations are made for discharges with RF Heating and Current Drive, in a variety of important applications. Further observations are made regarding the behavior of the radiation temperture, and of MHD related phenomena.

5.1 Scaling of the Electron Temperature and $3\omega_c$ Transmission

According to the results presented in chapter 2, the third harmonic X mode optical depth,

$$\tau_3^X \equiv -\ln \mathbf{T_3} \ ,$$

should scale as $n_e T_e^2 / B_t'$. This expectation is born out experimentally in figure 5.1, where the measured $3\omega_c$ optical depth for the resonance at the plasma center is plotted versus $n_e T_e^2 / B_t'$. Data in the range $1.5 \leq T_e$ (keV)≤ 3.3, $.6 \leq n_e^{14} \leq 3.1$, and $B_t = 8$ or 9 T are included, with temperatures obtained from Thomson Scattering (TS) or second harmonic X mode Electron Cyclotron Emission (ECE). Each point characterizes a specific set of plasma conditions, with the total number of shots for a given date or type shown in parenthesis. Experiment conditions are generally of Ohmic heating in Hydrogen at 8 Tesla with Molybdenum limiters, with exceptions designated in the legend as Lower Hybrid RF heating (LHH) or Current Drive (LHCD), Deuterium fill gas (D_2), 9 Tesla (9T), or Silicon Carbide limiters (SiC). Points which have been corrected for a non-resonant attenuation are so indicated (NRC). The data represented in figure 5.1 and 5.2 are examined in detail throughout

this chapter, along with a discussion of the analysis methods, NRA corrections, error bars, and other pertinent features.

In figure 5.1, the range of Ohmic data is constrained from above by MHD stability and profile considerations which act to limit the on-axis current density and the available central Ohmic input power. In addition, the inverse relationship between density and temperature in ALCATOR acts to mitigate the effect which the five-fold density variation in the data ultimately has on the optical depth.

The SiC limiter RF heated points are seen to lie above the cluster of Ohmic heated points, a result of the large increase in heating power available during RF injection. The Current Drive data lies below the Ohmic points, reflecting the fact that the tenuous, low current conditions required for LHCD operation fall considerably short of the high density, high power ohmic conditions more typical of ALCATOR C operation. Discharges much below the Ohmic range shown have very small $3\omega_c$ absorption ($< 5\%$) and are not usually the object of a temperature analysis due the deteriorating accuracy discussed in Chapter 4.

The same data may be presented in a manner which allows an evaluation of the performance as a temperature diagnostic. In figure 5.2, the central temperature obtained from the LOCKIN analysis described in Chapter 4 is directly plotted versus the temperature reported by the Thomson scattering or ECE diagnostics on the same shots. Agreement is seen to be good over a wide range of temperatures, for the variety of conditions described above.

With the demonstrated consistency between the theoretical description and measurement technique, we may examine various characteristics of the electron temperature using measurements of the X mode transmission. As one raises the toroidal field, the resonant layer at which $\omega_{laser} = 3\omega_c$ for a given laser line moves from inside of the toroidal axis ($r < 0$) to the outside ($r > 0$). At still higher fields, the second harmonic layer enters the plasma from the inside and moves toward the center, with a third harmonic transmission of unity, as discussed in detail in Chapter 2. This translation of the resonance layer across the plasma profile is demonstrated in figure 5.3, for the toroidal field variation $7.5 < B_t$ (Tesla)< 10.5 . The points lying

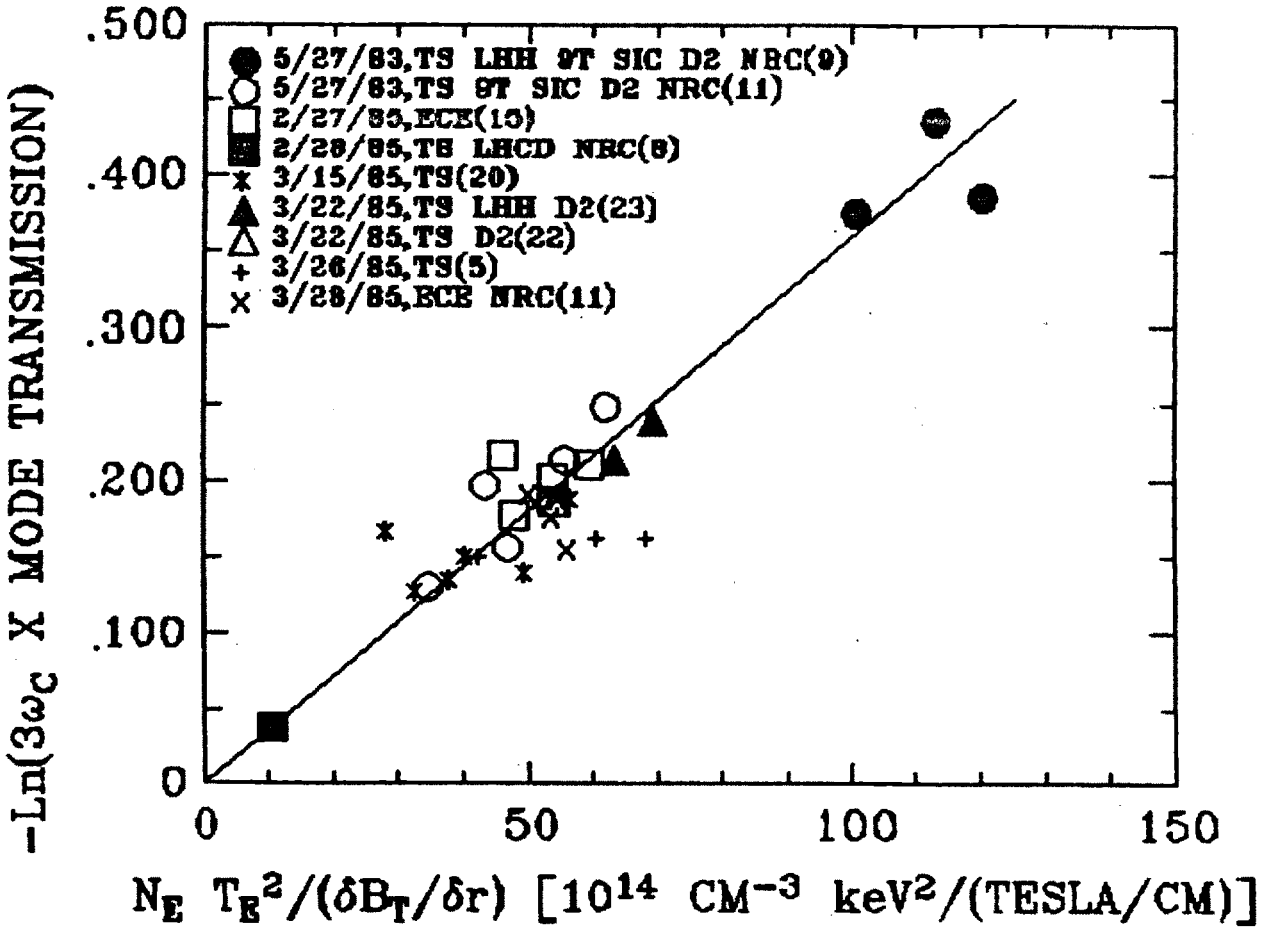

Figure 5.1 — Parameter Scaling of Third Harmonic X Mode Optical Depth $B_t = 8$ Tesla, H_2 fill, Mo Limiters, unless noted.

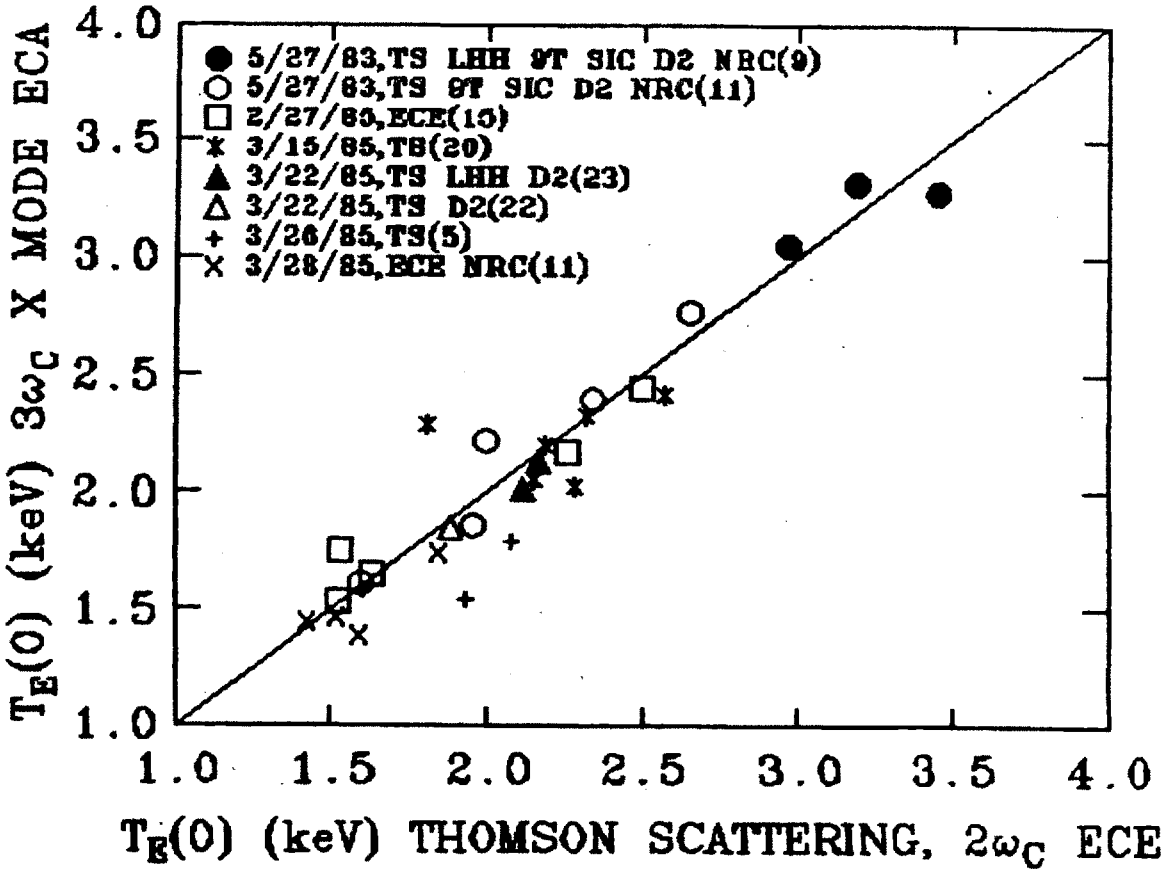

Figure 5.2 — Central Temperature Diagnostic Performance of Third Harmonic X Mode Transmission. $B_t = 8$ Tesla, H_2 fill, Mo Limiters, unless noted.

between -15 and -10 cm are obtained from second harmonic absorption, while the remainder are obtained using the third harmonic. The spatial range of these points is restricted by a diminishing third harmonic at locations far from the plasma center, and a blackening second harmonic as one approaches the plasma center, respectively. Although the plasma characteristics change significantly as the field varies, with q_l ranging from 3.4 to 4.7, the qualitative effect of traversing the plasma profile is quite evident. Also shown for comparison are Gaussian profiles fit to Thomson scattering data at the lowest and highest fields present in the data, for the intermediate density of 2.0×10^{14} cm^{-3}. The data is plotted versus density in figure 5.4, and has been grouped by proximity to the center. As in figure 5.3, points at or below the 10 cm line are obtained from second harmonic measurements, while those at or above 6 cm are from third harmonic. A consistent trend is again seen, with temperature decreasing away from the plasma center. The characteristic decrease in temperature with increasing density is also seen. Although the considerable variation in the plasma parameters precludes a more detailed consideration of this data, the trends with resonance position and density observed in the preceding graphs serve to clearly demonstrate the diagnostic value of cyclotron harmonic transmission measurements.

The ECA transmission temperature diagnostic method requires only that the density and field be known at the site of the resonance, and that the plasma be semi-transparent to the radiation. It is thus complementary to the $2\omega_c$ ECE method, which requires that the plasma emission be blackbody at the frequency under consideration. This quality validates the transmission method in precisely the region in which the emission method loses its applicability in most cases, near the plasma edge. Furthermore, the spatial resolution of $2\omega_c$ ECE measurements is determined by the finesse of the frequency resolving instrument, typically resulting in a 3 to 4 cm resolution for a scanning Fabry-Perot, and a 2 to 3 cm resolution for an FIR grating spectrometer.

The $n\omega_c$ transmission measurements, however, feature essentially local absorption, as we have seen in chapter 2. The resolution in this case is limited by the

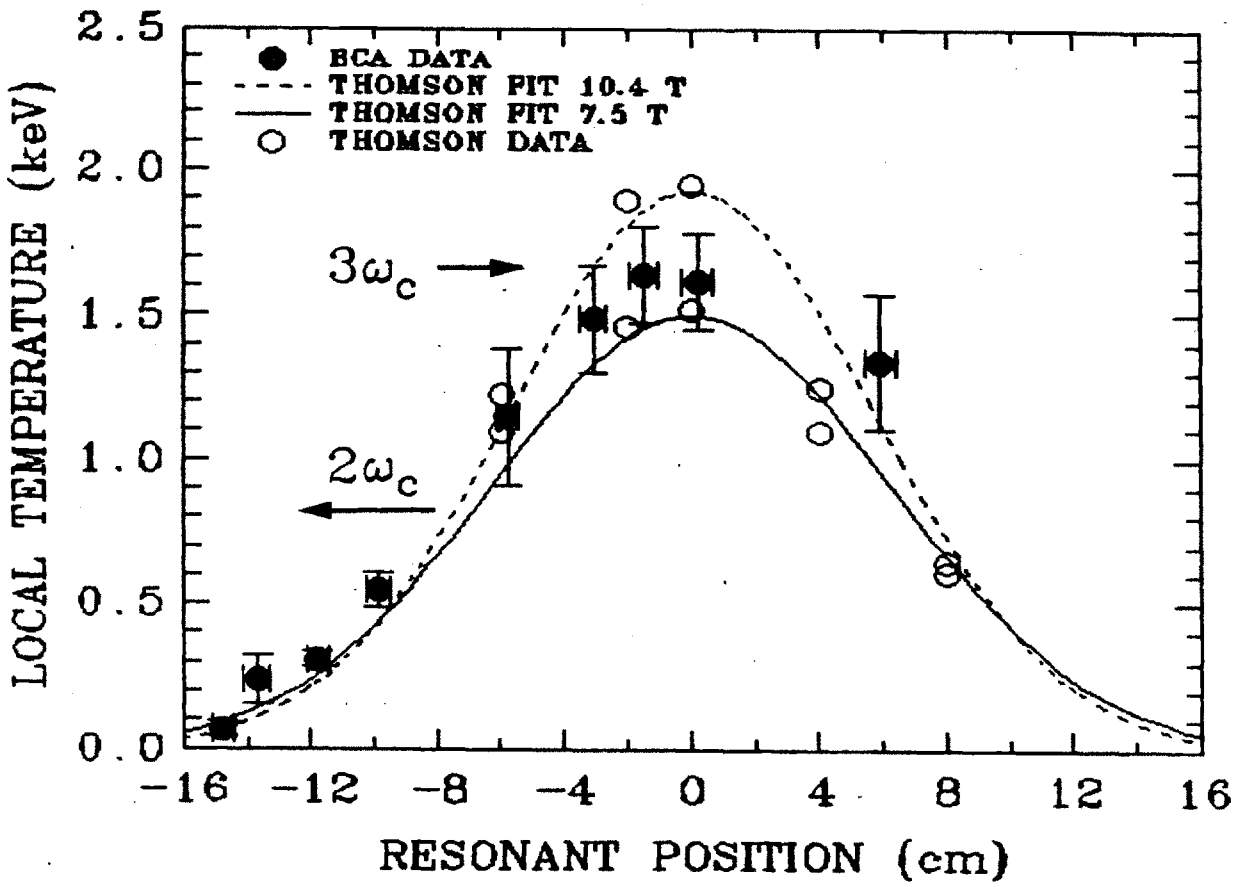

Figure 5.3 — Electron Temperature From Second and Third Harmonic X mode Transmission Vs. Position, 3/26/85, 3/28/85. $B_t = 7.5 - 10.4$ T, $n_e = 1.6 - 2.4 \times 10^{14}$ cm^{-3}, $I_p = 450$ kA, $q_l = 3.4 - 4.7$, $\lambda = 432.6$ μm (from 30 shots).

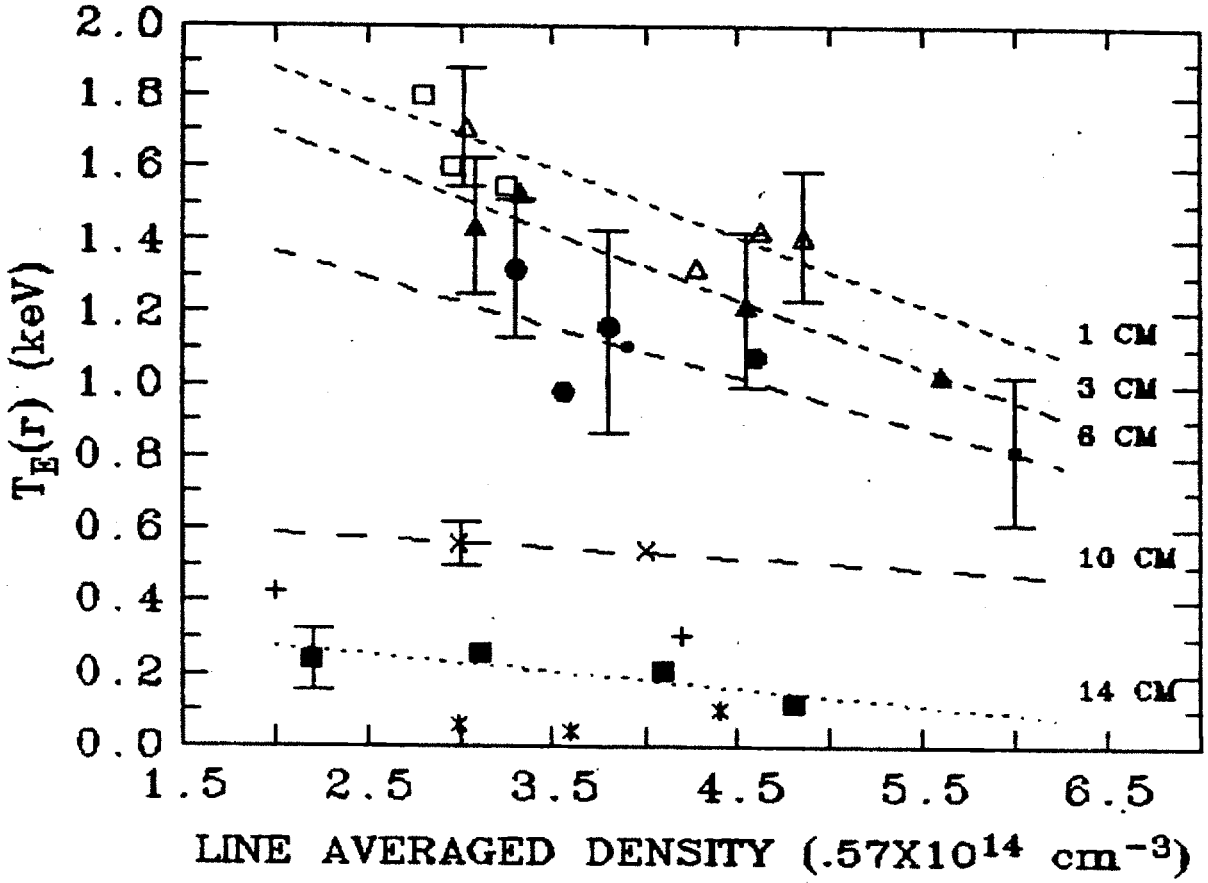

Figure 5.4 — Local Electron Temperature From Second and Third Harmonic X mode Transmission Vs. Density and Distance from Discharge Center, 3/26/85, 3/28/85. $B_t = 7.5 - 10.4$ T, $I_p = 400 - 500$ kA, $\lambda = 432.6$ μm (from 45 shots).

toroidal field induced spatial uncertainty, which is 1/2 to 1 cm (chapter 4). In addition, whereas suprathermal emission invalidates the ECE method during Lower Hybrid RF injection, the transmission method is ideal for RF heated plasmas, providing accurate bulk temperatures in the presence of high energy RF produced electron tails.

Alternatively, Thomson scattering methods are based on a spectrographic reconstruction of the scattered radiation spectrum, and thus require that a sufficient number of detectors be placed in the scattered frequency range, and that adequate dispersion is maintained throughout that range. This necessitates the construction of frequency specific multichord spectrometric and optical instrumentation, for which bandwidth comes at a costly premium. However, the entire 75 eV to 3.5 keV range of temperatures in figures 5.2, 5.3, and 5.4 was measured by second or third harmonic cyclotron transmission with the same experimental arrangement and measurement technique along a single horizontal chord, with considerable savings in cost and complexity compared to a Thomson scattering system of comparable performance. In addition, the pulsed Ruby lasers commonly used in Thomson scattering systems provide data at one instant during the shot, requiring a sequence of identical shots for a study of temporal behavior, whereas cyclotron transmission data is available continuously. Rapid pulse Nd-YAG Thomson scattering systems have only recently become available and still constitute a state of the art technology of considerable cost.

Although the utility and effectiveness of the ECA method are to a degree restricted by the existence of possible sources of non-resonant attenuation, in this work it is demonstrated that the NRA can be effectively calibrated out of the data with the various techniques discussed below. To the extent that this can be done, the unique physical attributes of the Cyclotron harmonic absorption technique should win it a place in the roster of all too scarce Tokamak electron temperature diagnostics.

Because of the decreasing opacity at $2\omega_c$ and the absence of Thomson scattering chords in the last few centimeters of the plasma in ALCATOR, direct electron

temperature measurements such as the second harmonic points in figure 5.3 are rare. A comparison of the measured $2\omega_c$ ECA temperature profile and the 10.4 Tesla Thomson scattering profile fit to the central plasma data suggests that the outer temperature profile may be somewhat broader than the Thomson fit would indicate, assuming the local density is as given by the extrapolated density profile. What this observation actually implies is that the local plasma pressure near the edge, $n_e T_e(r)$, of which the $2\omega_c$ transmission is a direct measure, may be somewhat higher than that obtained by multiplying the extrapolated values from the central n_e and T_e profiles. An alternative possibility is that the density in the region $-14 < r(\text{cm}) < -10$ may be higher than the extrapolated central value, although this conjecture is not supported by the line averaged density measurements. The effect, although small, is observed consistently in the $2\omega_c$ outer plasma transmission data, and will be encountered again in a discussion of the effects of RF Current Drive on the temperature profile.

The data shown in figures 5.3 and 5.4 have been corrected for the non-resonant attenuation shown in figure 5.5. This non-resonant data was obtained during the same run as the resonant data to which it is applied, by lowering the field to 6.8 T, at which the resonant transmission is expected to be .99 or greater. A correction is made for data above $n_e^{14} = 2.0$ (3.5 fringes) by taking linear interpolations between the quiescent H_α points shown. These are differentiated from Marfeing shots, shown as solid points, which are not considered in the correction. In the range $.75 < n_e^{14} < 2.0$ the effect is below the uncertainty of the measurements, and no explicit correction is made. In addition, the effect on the $2\omega_c$ points is 10 to 20 eV, and is not shown. Thus, only the $3\omega_c$ points in figure 5.3 at +6 and −6 cm, and in figure 5.4 along the 1,3, or 6 cm lines at densities of 3.5 fringes or above, required correction. If not accounted for, the effect of the NRA is to move the temperatures shown for these points upwards by 200 to 300 eV. Points in the NRA range are seen to have larger error bars, incurred in the additional analysis required.

The scaling of the central temperature with density is presented in figure 5.6, where temperatures reported by $3\omega_c$ cyclotron transmission, Thomson scattering,

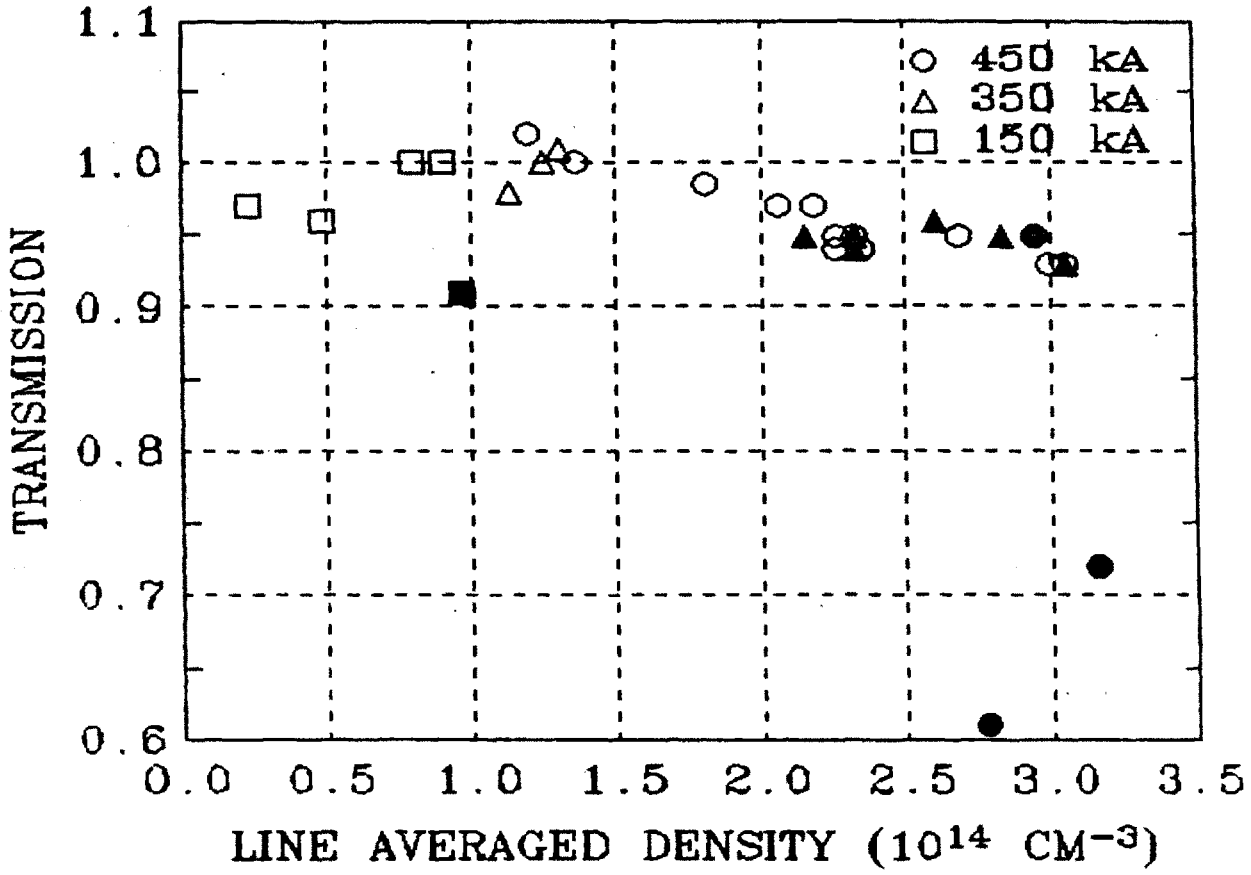

Figure 5.5 — X Mode Non-resonant Transmission Vs. Density and Current, 3/26/85, 3/28/85. Mo limiters, $B_t = 7$ T, H_2 fill, $\lambda = 432.6$ μm. Solid points correspond to H_α active shots, open points are quiescent shots.

and $2\omega_c$ cyclotron emission are all shown. Also plotted for comparison is a numerical fit to all the temperature data in the figure, for which T_e varies inversely with line averaged density,

$$T_e(\text{keV}) = .8 + 2.0/n_e^{14} .$$

Because the experimental data will not readily allow linear scaling to be distinguished from root or other powers, the numerical fit may not be extrapolated outside of the density range shown. However, figure 5.6 does serve to illustrate a point encountered repeatedly in this work pertaining to the deterministic relation between density and temperature in ALCATOR, and the small variation in density-temperature products brought by a large variation in density alone.

Due to the unavailability of non-resonant transmission data for this run, no NRA correction has been made. Although the data shown in figure 5.5 indicates an NRA in the high density range above 2.8×10^{14} cm^{-3}, agreement between the ECA and other diagnostics in figure 5.6 is seen to be within the overall scatter of the data. This discrepancy may result from differences in the plasma currents of figures 5.5 and 5.6. The NRA data of figure 5.5 was taken at 450 kA and below. In figure 5.6, data at or above 2.8×10^{14} cm^{-3} was obtained with plasma currents of 490 to 550 kA, while data at 2.5×10^{14} cm^{-3} and below was obtained with a plasma current of 450 kA. It is possible that the since the high density data in figure 5.6 is at a higher current that the corresponding data in figure 5.5, a current related threshold may exist between 450 and 550 kA beyond which the NRA diminishes. Data at lower currents such as that of figure 5.5 suggests that once the NRA is present, it does not appear to be affected by decreasing the current. However, data at higher currents is lacking, and questions relating to the behavior of the NRA at high plasma current remain open.

The dependence of the central temperature on plasma current is shown in figure 5.7, where little variation is seen over a 200 kA range. The presence of sawtooth activity for these discharges reflects the influence of the aforementioned MHD limit on the current density at the center, such that increasing the total current serves

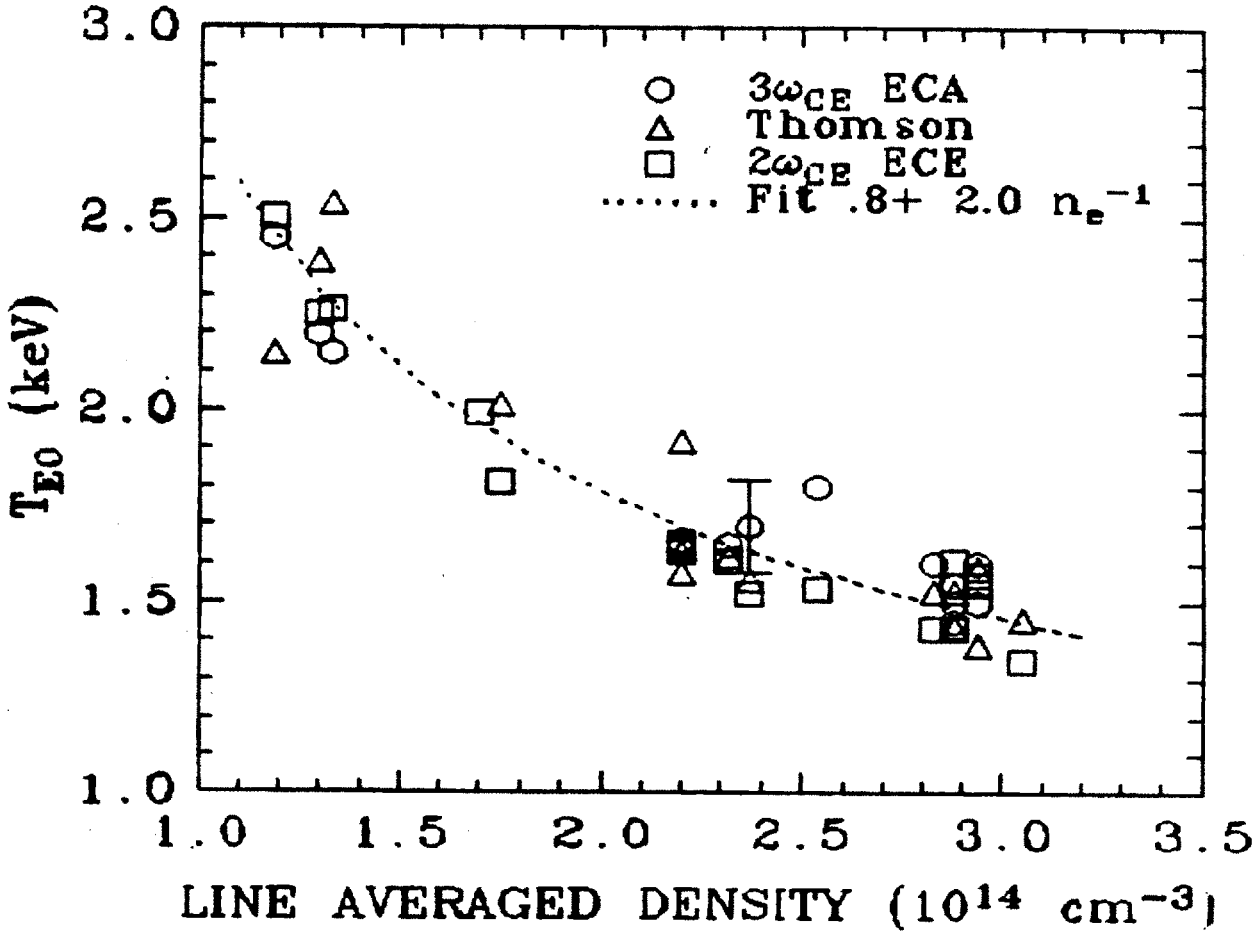

Figure 5.6 — Central Electron Temperature Vs. Density, 2/27/85. $B_t = 8$ T, $I_p = 450 - 550$ kA, $\lambda = 432.6$ μm.

only to broaden the current profile. An NRA is not observed to be present in this density range.

5.2 Lower Hybrid RF Injection

The injection of high power radiation near the Lower Hybrid frequency can have a dramatic effect on the plasma characteristics.[55] Radiation at 4.6 GHz is injected into ALCATOR C via two 4x4 tall waveguide arrays separated toroidally on the machine by 180°, each fed by four 250 kW Varian klystrons. The relative phase between adjacent columns in each grill determines the $k_{\|}$ spectrum of the launched waves, and this in turn determines the nature of the interaction between the Lower Hybrid waves and the plasma.

5.2.1 Plasma Heating

For a relative waveguide phasing of π, electrons are heated directly via collisionless Landau damping of the Lower Hybrid waves. The RF power $k_{\|}$ spectrum is symmetric for this phase, and no net momentum is imparted to the electron distribution.

The effects of RF heating are demonstrated in figures 5.8,5.9 and 5.10, for densities in the range $1.6 < n_e^{14} < 2.0$ and RF powers in the range $500 < P_{RF}(\mathrm{kW}) < 700$. Molybdenum limiters were used for this run, which dates from March, 1985.

Plasma diagnostic raw data traces are shown in figure 5.8. Upon plasma initiation, the density, current and temperature profiles develop and stabilize. During the RF pulse (trace f), the raw transmission signal shows a two-fold increase in the $3\omega_c$ emission baseline. This is due to the presence of high energy electrons which are accelerated in the RF field, and emit strong, broadband radiation up to very high harmonics. These highly energetic electrons do not absorb any of the $3\omega_c$ radiation, however, because of the low density of the energetic component and the strong relativistic downshift of the absorption line out of the plasma. The rising or falling baseline caused by the RF on-off transients distorts several modulation half cycles, which are removed from the transmission data. These points are indicated

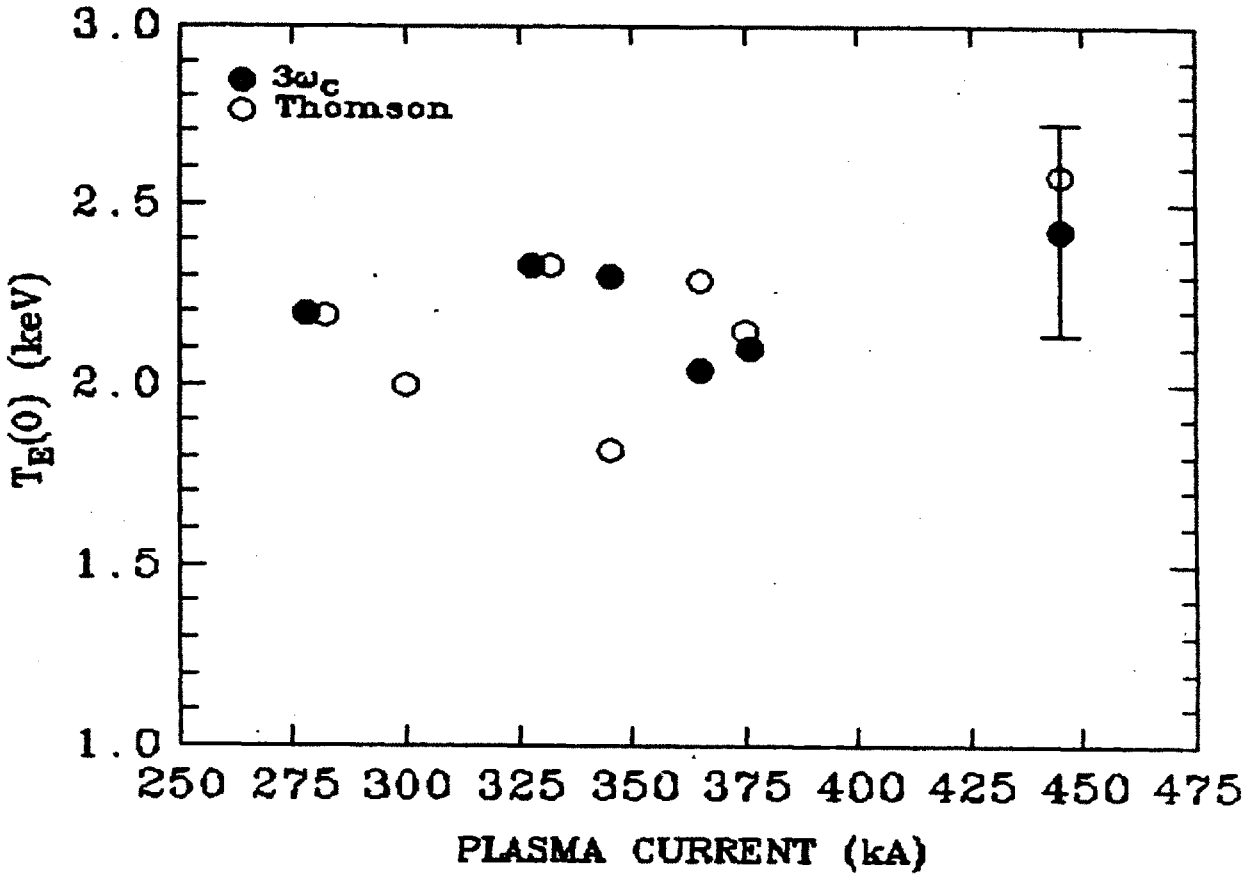

Figure 5.7 — Central Electron Temperature Vs. Plasma Current, 3/15/85. $B_t = 8$ T, $n_e = 1.0-1.2\times10^{14}$ cm^{-3}, $q_l = 3.0-4.9$, $\lambda = 432.6\ \mu$m (from 20 shots).

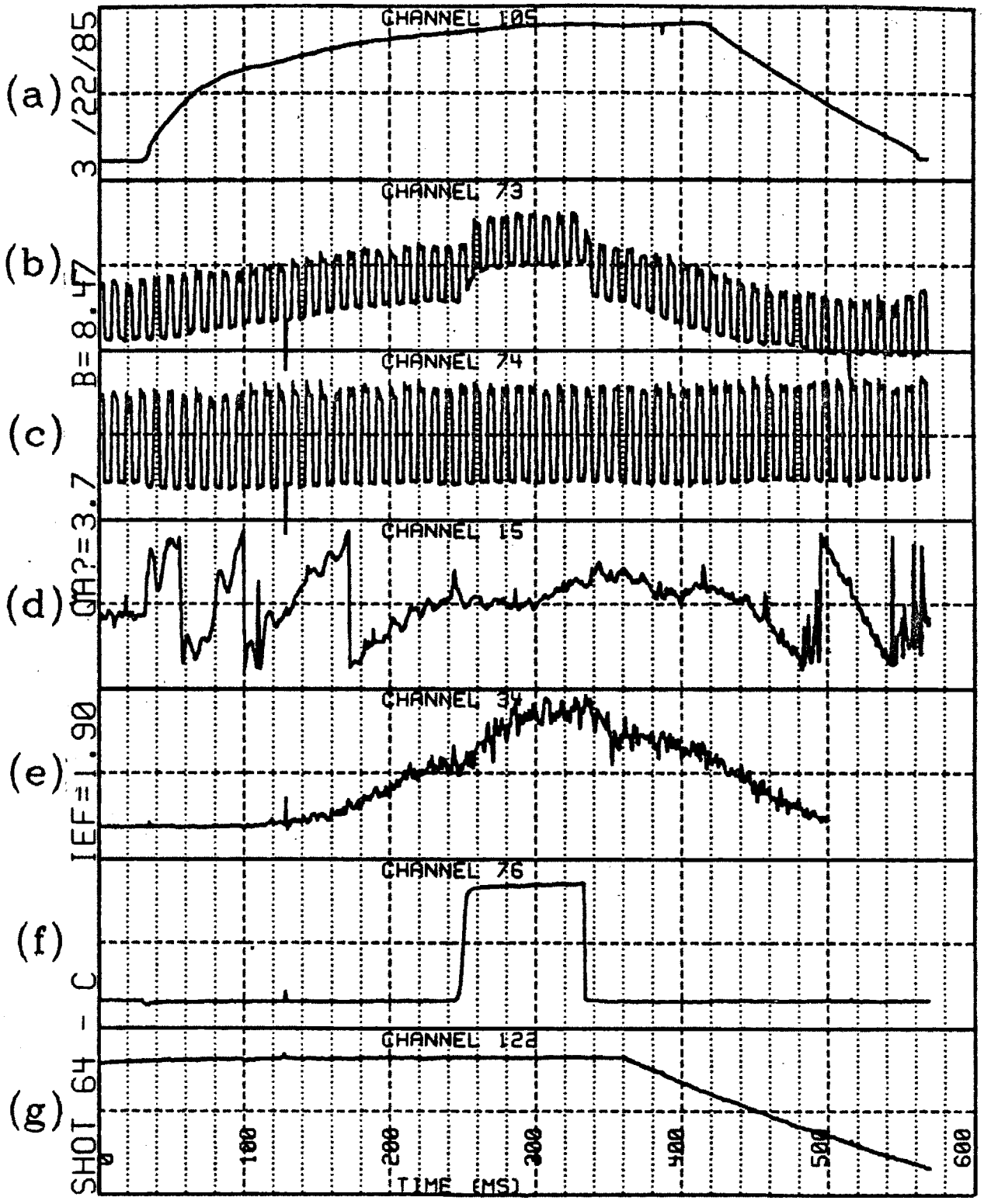

Figure 5.8 — Plasma Data During Lower Hybrid RF Heating with Molybdenum Limiters, 3/22/85, Shot #64. Traces shown are (a) Plasma Current, 2.4 V/div (b) Raw $3\omega_c$ Transmission (c) Laser Reference (d) Central Density (e) Broadband Hard X-Rays (f) MW1 RF Pulse (g) Toroidal Field.

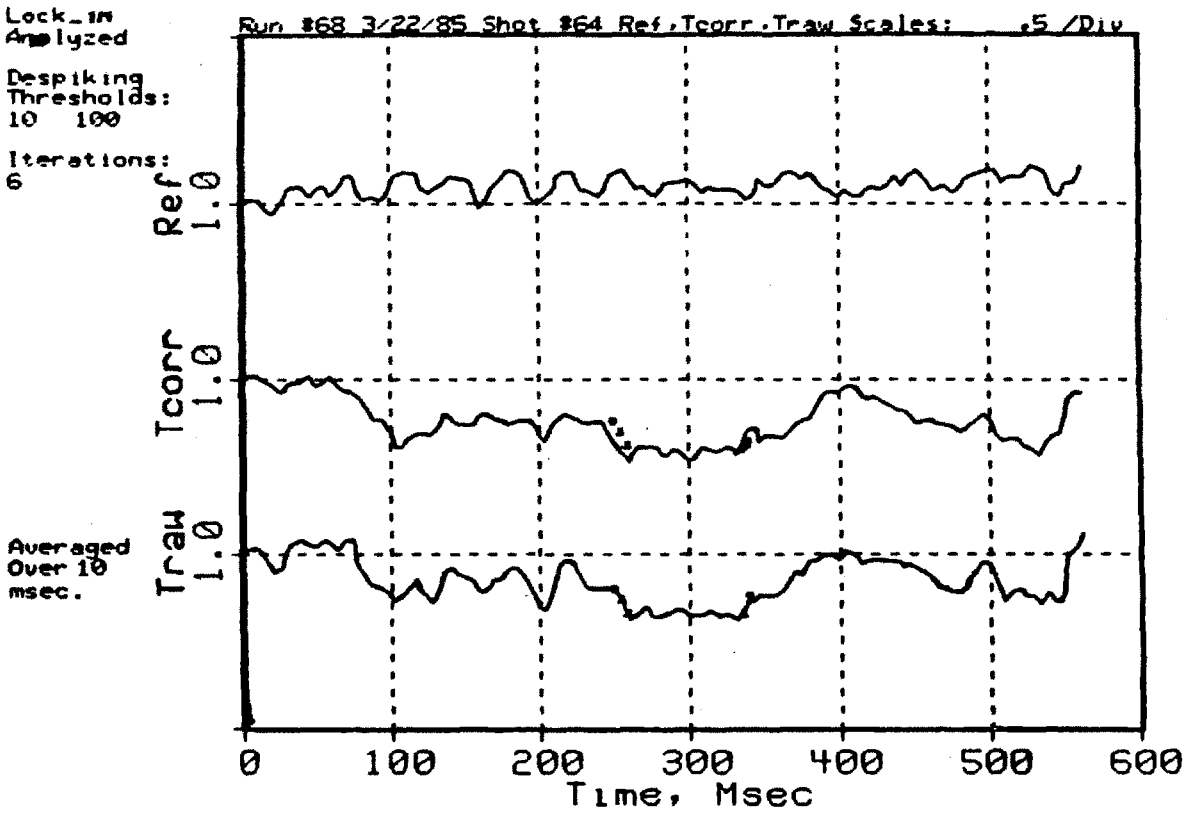

Figure 5.9 — Transmission During Lower Hybrid Heating, 3/22/85, Shot #64.

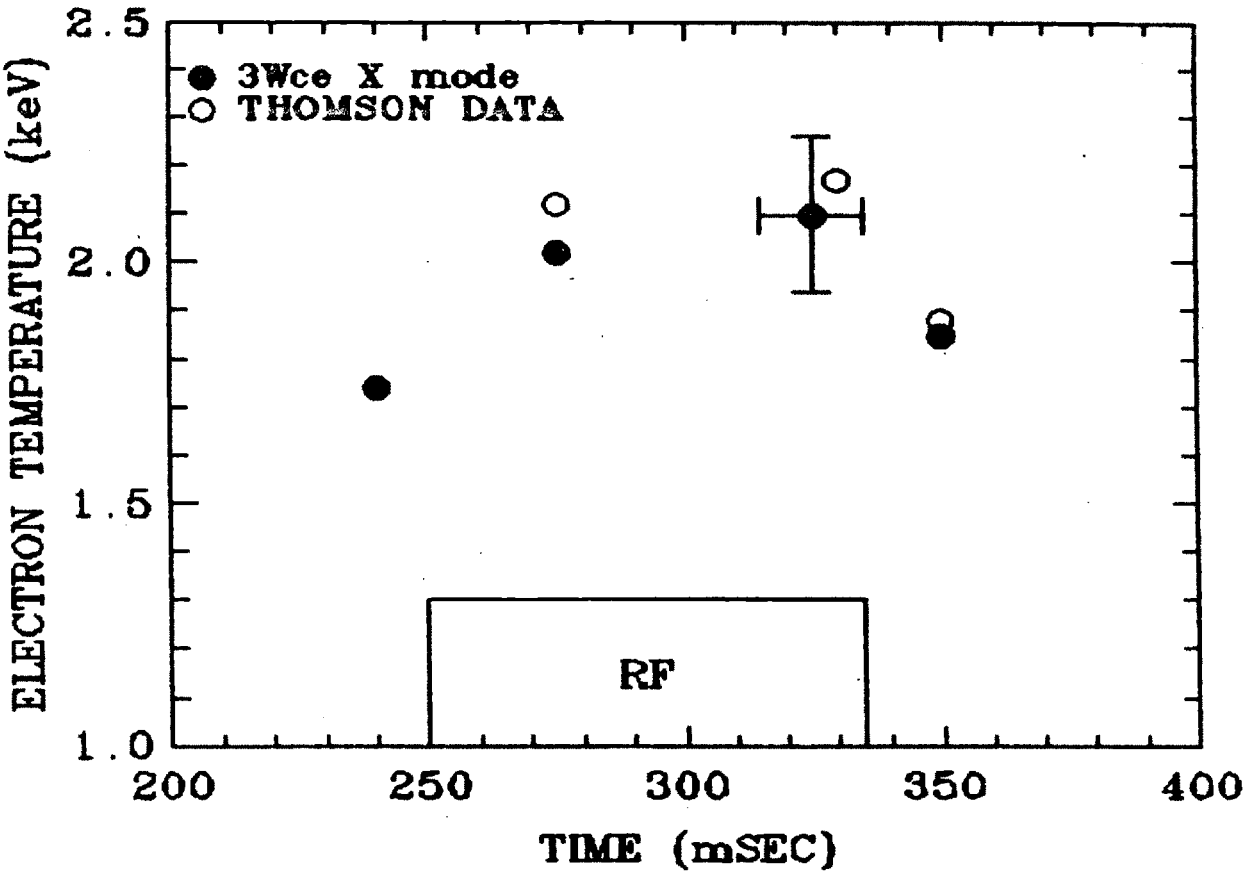

Figure 5.10 — Electron Temperature From Third Harmonic X mode Transmission During RF Heating with Mo Limiters Vs. Time, 3/22/85. D_2 fill, $B_t = 8$ T, $n_e = 1.6 - 2.0 \times 10^{14}$ cm^{-3}, $I_p = 400 - 500$ kA, $q_l = 3.4 - 4.7$, $\lambda = 432.6$ μm, $P_{RF} = 500 - 700$ kW (from 28 shots).

in figure 5.9 by asterisks, which represent a linear interpolation between quiescent data segments. Interpolated segments are not used in the data analysis.

In the quiescent period preceding the RF pulse, the transmission is indicative of conditions at the target Ohmic discharge center. After the RF initiation, conditions again stabilize, and a new equilibrium is reached. A decrease in the transmission is evident during the RF pulse, indicating that while the density shown in figure 5.8 (trace d) has remained approximately constant, the temperature has increased. Upon termination of the RF, a second transient is encountered, and conditions are maintained for 25 msec, at an increased transmission level. At 380 msec, the toroidal field commences its downward ramp, and the transmission rises as the resonance moves inward, away from the plasma center. Late (and early) in the shot, when the current is low, Marfe related phenomena may be active, so that temperature diagnostic information is in general only inferred during the flat portion of the discharge.

The temperatures obtained from the $3\omega_c$ transmission data are shown as a function of time in figure 5.10, along with Thomson scattering results. The latter were obtained from a sequence of shots during which the Thomson scattering ruby laser firing time was advanced, as is standard procedure with these systems. Both the Thomson and the ECA data have been grouped by time and averaged over similar shots. The data shows an average temperature increase of 360 eV over the pre-RF value, with little systematic variation with density evident in the RF or OH data for the 1.6 to 2.0 $\times 10^{14}$ cm^{-3} range present.

The effect of LHRF heating in plasmas of lower density ($1.2 < n_e^{14} < 1.5$), higher field (9 T), higher RF power (800 kW), and with Silicon Carbide limiters is seen in the results of May, 1983 shown in figure 5.11. Here, temperatures obtained from $3\omega_c$ transmission and Thomson scattering are shown plotted versus density, for plasmas with RF injection and without. Under these conditions, a maximum temperature rise of over 1 keV is observed, which diminishes as the density increases to 1.5×10^{14} cm^{-3}.

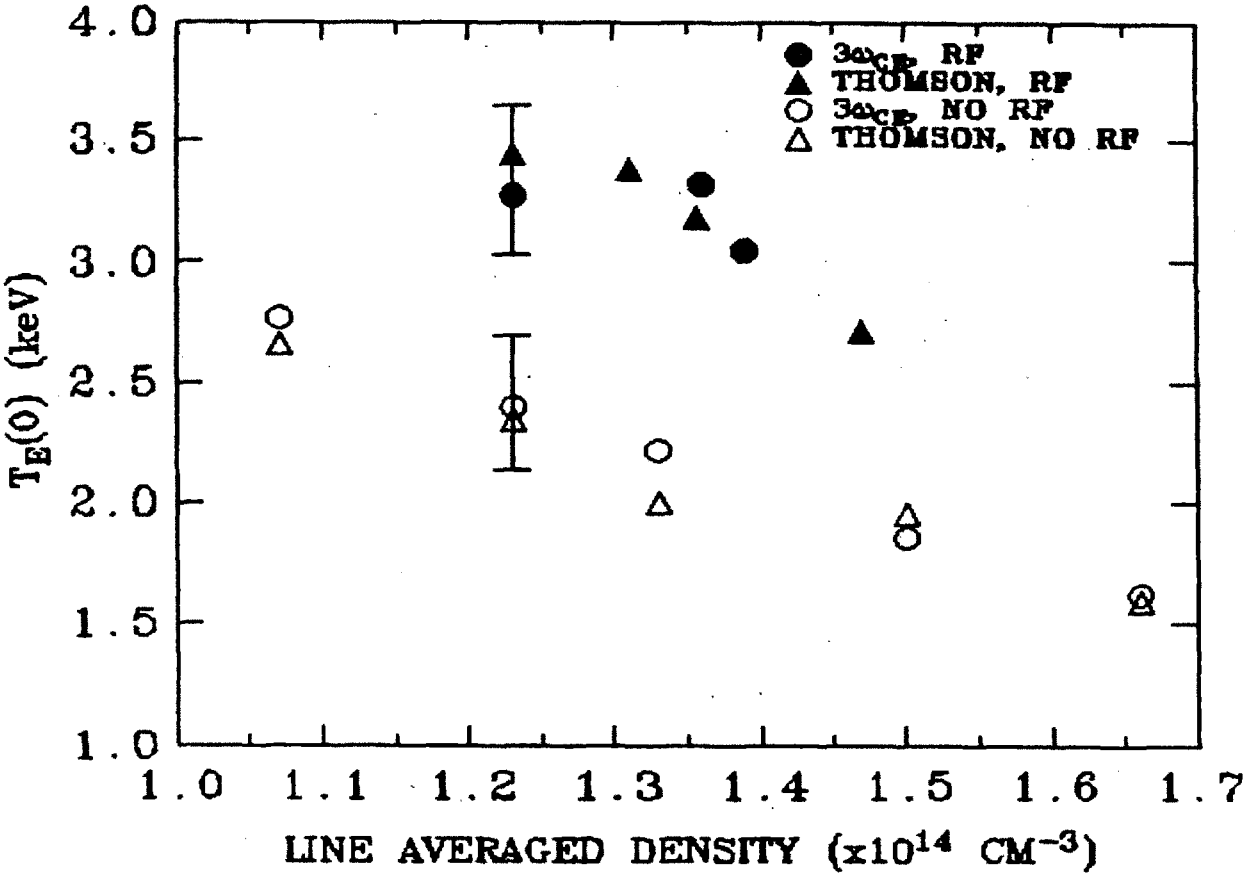

Figure 5.11 — Electron Temperature From Third Harmonic X mode Transmission During RF Heating with SiC Limiters Vs. Density, 5/27/83. D_2 fill, B_t = 9 T, I_p = 410 kA, λ = 432.6 μm, P_{RF} = 800 kW (from 20 shots).

The observed difference in performance between the data in figures 5.10 and 5.11 can be reconciled in terms of the differing conditions which characterized the two experiments. LHRF heating efficiency, like the the Tokamak temperature itself, is a sensitive function of many parameters, including the toroidal field, electron density, plasma impurity levels, and limiter material. These factors, and others, are thought to affect the RF heating efficiency by the influence which they have on wave-plasma coupling and accessibility, or on radiative power balance. The use of a Molybdenum limiter in the data of figure 5.10 places a source of high Z impurities in intimate contact with the plasma. The RF pulse generates fast electrons which may impact the limiter and drive injections of high Z material (Mo) into the plasma. Such injections cool the plasma rapidly via line radiation losses, and depending on their severity, may disrupt the plasma entirely. For a Carbon limiter, Z_{eff} values as high as 5 are easily tolerated during the RF pulse. Thus, Mo limiter operation is necessarily constrained to higher densities, where the effects of fast electron generation and spontaneous impurity injection are diminished. This, however, tends to reduce the heating efficiency, which is a decreasing function of density. A decreasing trend is observed in figure 5.11 for the SiC case, which is relatively benign with respect to the impurity problem. This does not insure that if the impurity injection problem could be eliminated, and lower density operation were thus allowed, the heating performance with Mo limiters would approach that shown in figure 5.11 for SiC. The effects of limiter material on Tokamak operation and RF performance are subtle, and are at present neither fully diagnosed nor understood.

For the density range of figure 5.10, the 1985 non-resonant data of figure 5.5 indicates that the NRA should be 3% or below. Since a small fraction of the data is at the higher densities, the NRA effect is actually minimal. No explicit correction is made, and agreement with Thomson scattering results is evident. In addition, the transmission attained during the toroidal field rampdown has been found to constitute an upper limit on the NRA present during a shot. This level is expected to approach unity in the absence of any other attenuation, prior to the onset of

Marfe activity. The level which is reached at 400 msec during the toroidal field rampdown in figure 5.9 indicates an effect at 1.9×10^{14} cm^{-3} which is consistent with the above considerations, to within the experimental accuracy.

For the 1983 experiment shown in figure 5.11, the above NRA criteria of toroidal field rampdown level, comparison with Thomson scattering results, and examination of measured non-resonant transmission data, all indicate quite a different conclusion. For this data, a significant NRA is found for all densities examined. The non-resonant correction used to obtain figure 5.11 is shown in figure 5.12. The "Thomson Calibration" points are obtained by dividing the experimentally measured transmission before the RF by the value expected from the interferometer and Thomson scattering data at that time. The resulting quotient represents the non-resonant contribution. The "Post TF Ramp" points in figure 5.12 are measured at a time when the transmission is expected to be unity, as explained above. The effect of the NRA is shown in figure 5.13, where we compare the measured optical depths to those calculated from the interferometer and Thomson scattering data, before and after the measured points have been corrected for the NRA. The discrepancy between the measured and calculated results is seen to be large, before correction. The temperatures shown in figure 5.11 have been grouped by density and averaged, a procedure which is applied in the same manner to the Thomson scattering and ECA data. The ECA temperatures may be calculated using various approaches to the NRA correction and analysis procedure, and the same results obtain, regardless of the approach used, to within the accuracy of the measurements.

A fuller view of the NRA scaling for 1983 data is offered in figure 5.14, which shows the measured non-resonant transmission at 8T. A strong peak density dependence is again evident, along with an apparent threshold type behavior setting in at a density of 2.5×10^{14} cm^{-3}. It is also important to note that high power, low power, and no RF shots have similar NRA behavior, indicating that the RF has no effect on the NRA magnitude or dynamics. Agreement between all three methods of obtaining the NRA is well within the accuracy of the measurements.

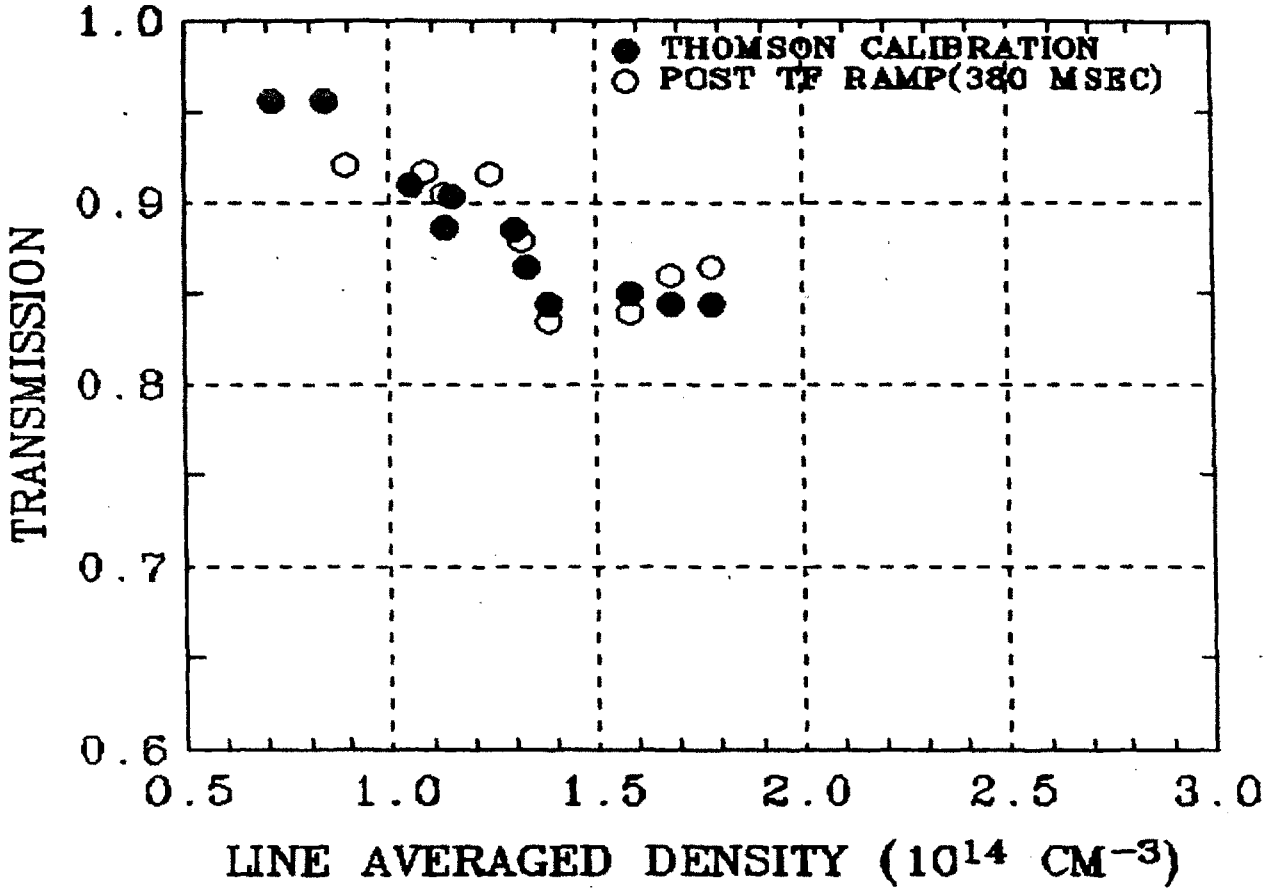

Figure 5.12 — X Mode Non-resonant Transmission with SiC Limiters Vs. Density, 5/27/83. D_2 fill, $B_t = 9$ T, $I_p = 410$ kA, $\lambda = 393.6$ μm (from toroidal field rampdown transmission level and Thomson scattering data.)

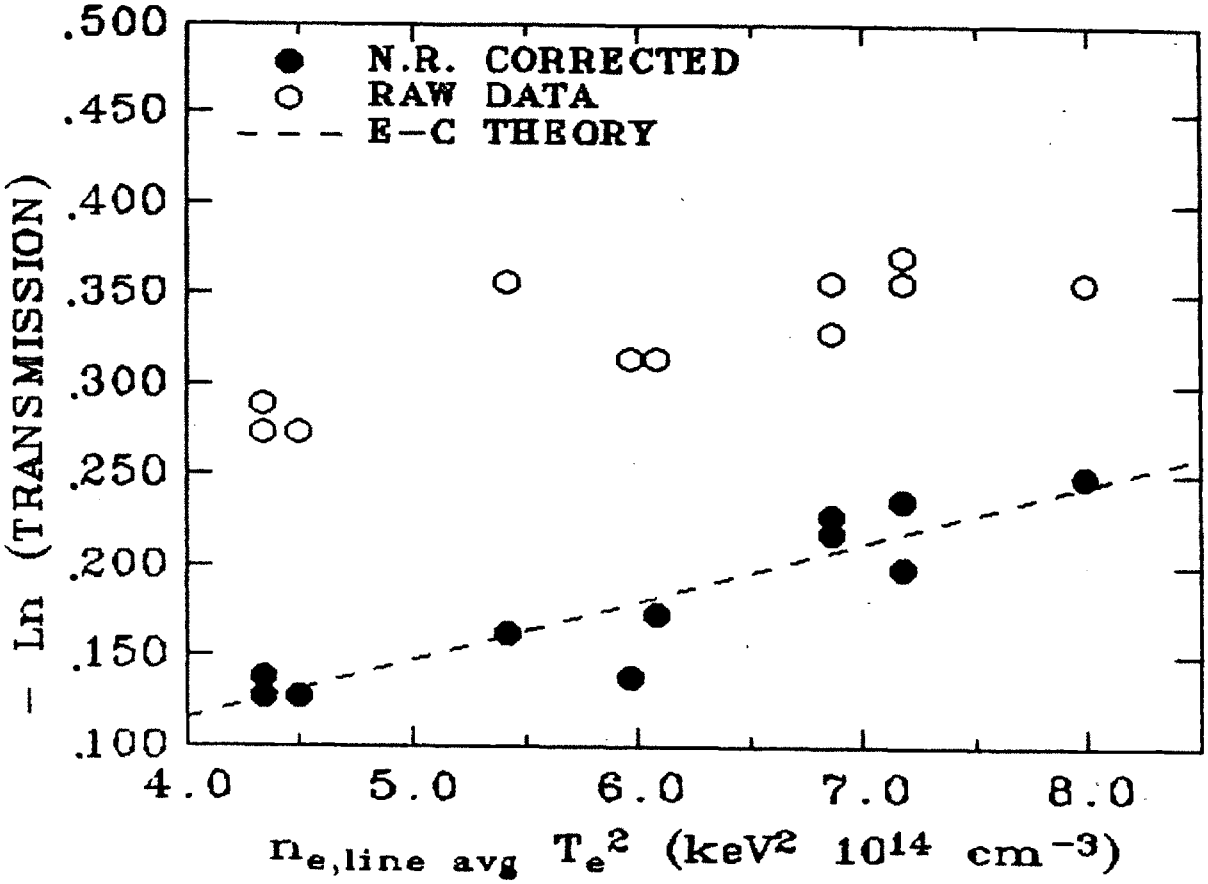

Figure 5.13 — Effect of a Non-resonant Attenuation on the $3\omega_c$ X Mode Optical Depth, 5/27/83. D_2 fill, $B_t = 9$ T, $n_e = 1.2 - 1.8 \times 10^{14}$ cm $^{-3}$, $I_p = 400$ kA, $\lambda = 393.6$ μm.

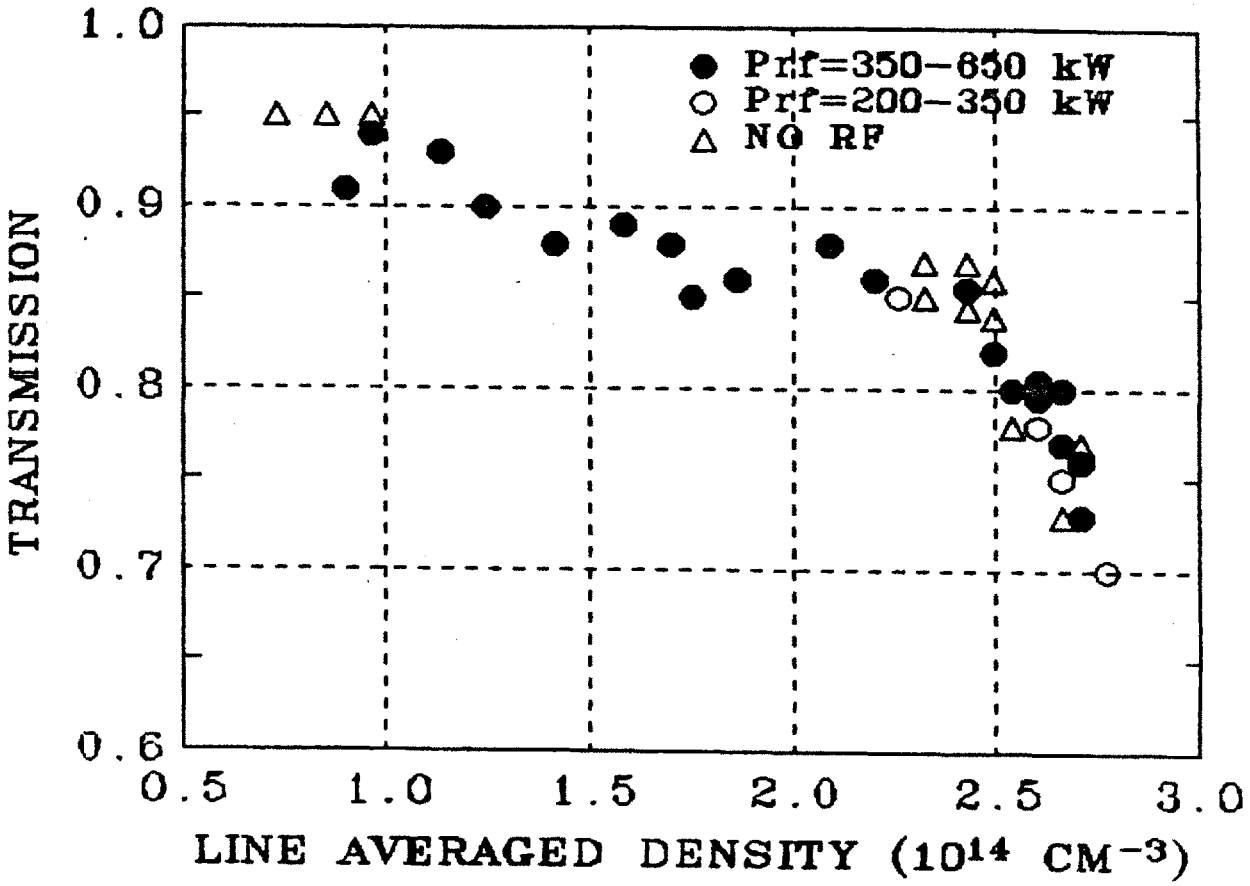

Figure 5.14 — X Mode Non-resonant Transmission with SiC-Mo Hybrid Limiters Vs. Density, 7/21/83. D_2 fill, $B_t = 8$ T, $I_p = 350 - 400$ kA, $\lambda = 381.0$ μm.

5.2.2 Current Drive

If the RF power spectrum is not symmetric in $k_{\|}$, net momentum is coupled to the electron distribution, and a steady current can be driven solely by the action of the Lower Hybrid waves.[61] For a relative waveguide phasing of $\pi/2$, 70% of the RF power resides in low $k_{\|}$ values, and drives current in the electron drift direction, while the remainder resides in high negative $k_{\|}$ values, and is absorbed in the thermal bulk distribution.

A typical $\pi/2$ Current Drive shot is shown in figure 5.15, for a density of 4×10^{13} cm^{-3}, a plasma current of 140 kA, and an RF power of 480 kW. The plasma current (trace c) is seen to peak at 80 msec, at which time the OH circuit is opened and the current begins its inductive decay. Upon initiation of the RF pulse, the current recovers and is maintained solely by the RF, with a loop voltage of zero (trace g). As with RF heating, the raw transmission signal shows an increase in the emission baseline during the RF, consisting of emission by the current carrying suprathermal electrons. It is found experimentally that these relativistic electrons do not enhance the absorption of $n\omega_c$ radiation, a consequence of their high energies and low number densities.

The $3\omega_c$ transmission for this shot is shown in figure 5.16. Because of the difficulties brought by very low absorption and a sensitivity to low frequency noise, the transmission is obtained by averaging over the steady portion of the RF pulse, and over nominally identical shots. The results of such measurements are shown in figure 5.17, where we have plotted the experimentally measured transmission divided by the value calculated for a thermal plasma of the temperature and density reported by the Thomson scattering and interferometer on the same shots. Results are shown for Current Drive flattop shots with $\pi/2$ phasing, as well as for Ohmic Simulation shots, in which the Ohmic current and density are programmed to duplicate Current Drive conditions, in the absence of RF. Such shots provide a direct comparison of discharge characteristics with and without the RF waves. It is observed that the measured transmissions are within $\pm 3\%$ of the expected (theoretical) values. There is no marked systematic difference between the Lower Hybrid injected shots and the

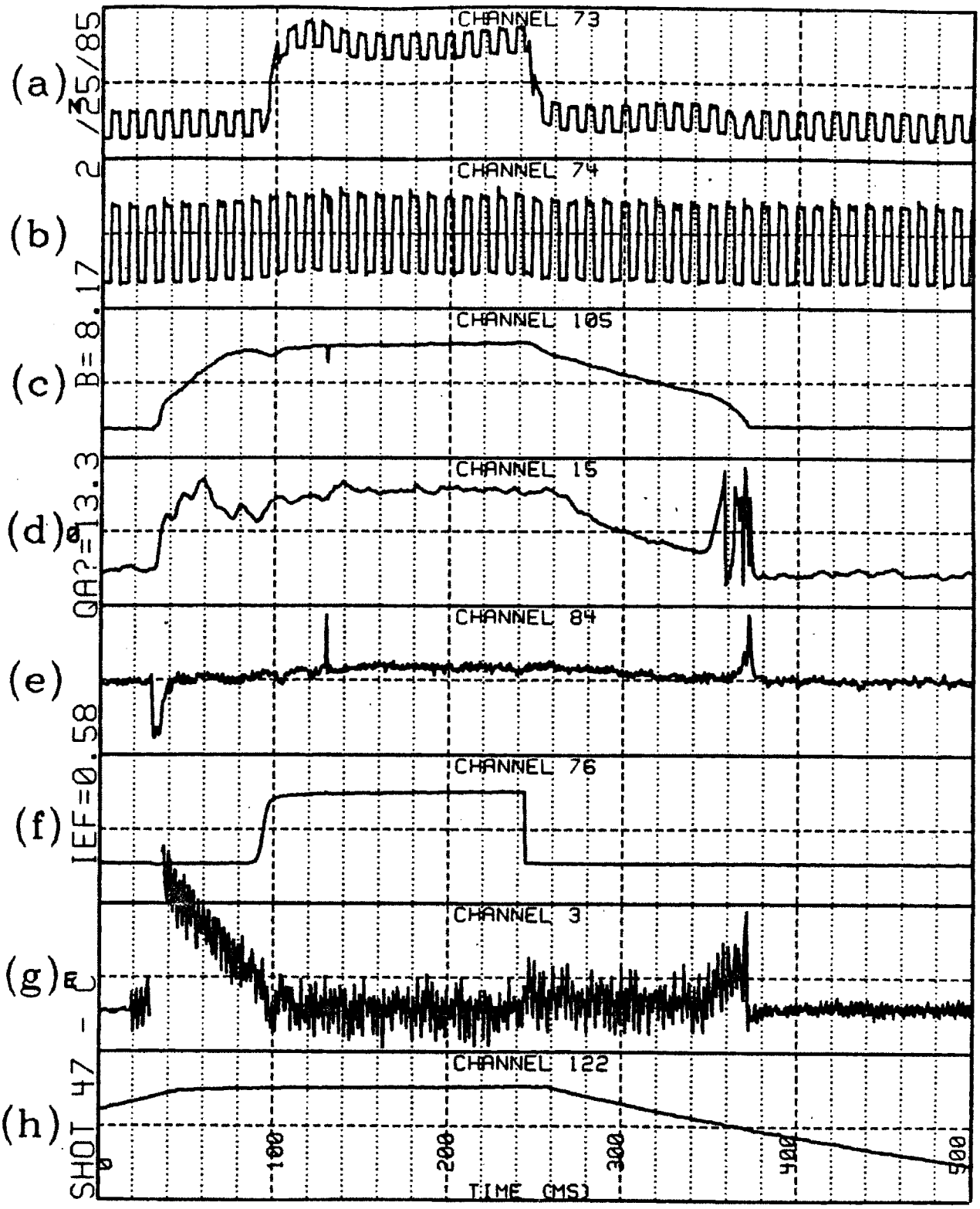

Figure 5.15 — Plasma Data for Lower Hybrid RF $\pi/2$ Current Drive with Molybdenum Limiters, 2/25/85, Shot #47. Traces shown are (a) Raw $3\omega_c$ Transmission (b) Laser Reference (c) Plasma Current, 1 V/div (d) Central Density (e) H_α (f) MW1 RF Pulse (g) Loop Voltage, .5 V/div (h) Toroidal Field.

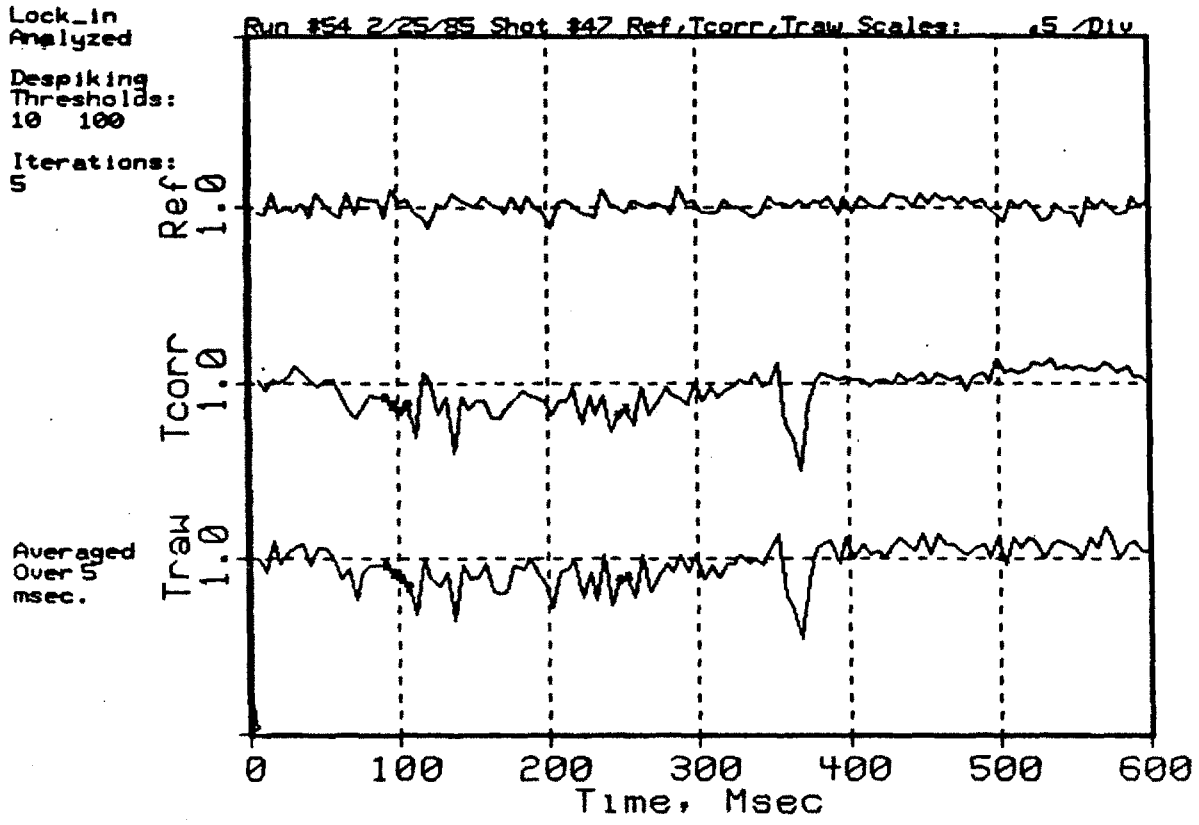

Figure 5.16 — Transmission During Lower Hybrid $\pi/2$ Current Drive Vs. Time, 2/25/85, Shot #47.

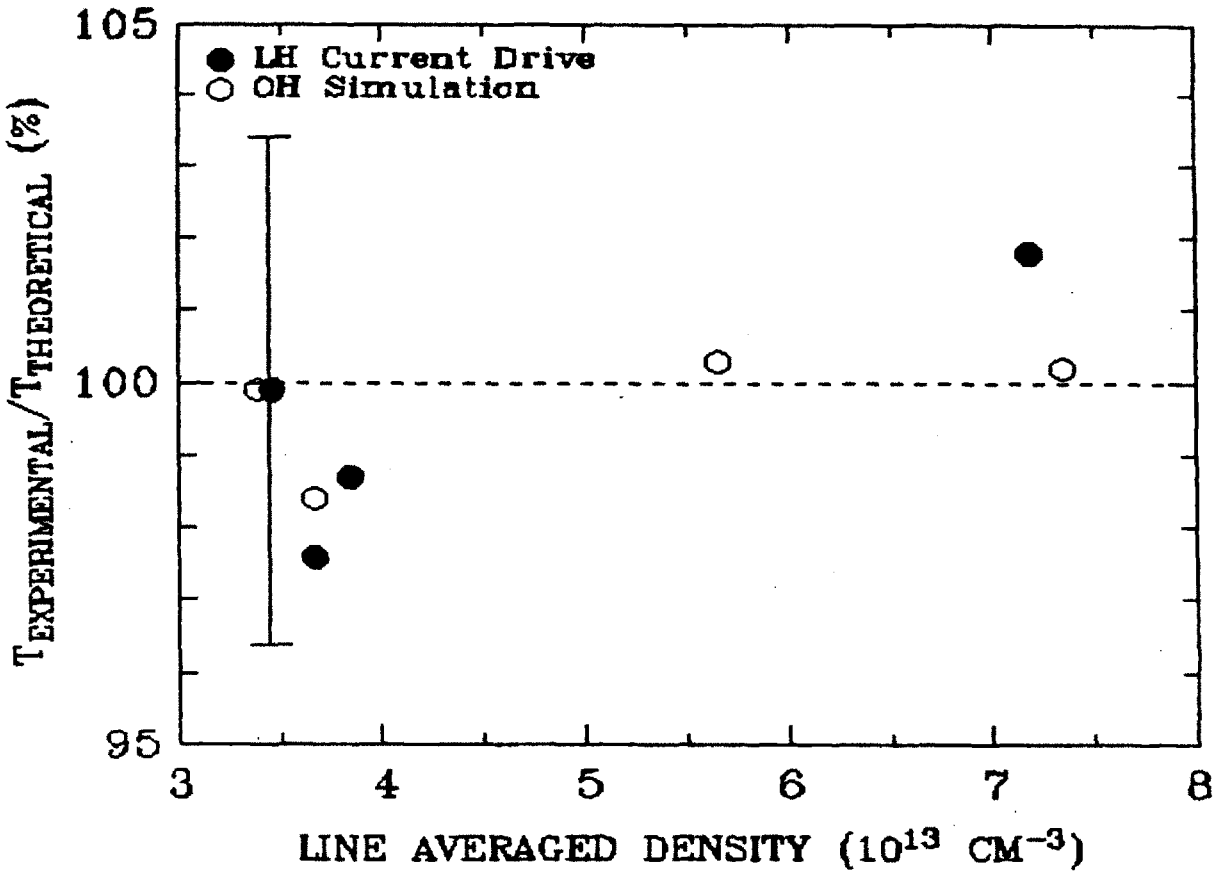

Figure 5.17 — $3\omega_c$ Transmission During Lower Hybrid Current Drive and Ohmic Simulations Vs. Density, 2/14/85–3/21/85. $B_t = 8$ T, $I_p = 125 - 145$ kA, $\lambda = 432.6$ μm (from 17 LHCD flattop and 19 OHS shots).

Ohmic Simulations, indicating that the absorption of the suprathermal component must be less than the 3.5% accuracy of the determination, if present at all. This is in agreement with theoretical computations, which predict absorptions of less than 1% for a wide variety of Maxwellian class distribution functions with a tenuous, energetic electron population, as discussed in detail in chapter 2.

In the Current Drive parameter range of figure 5.17, non-resonant transmission measurements indicated that a small NRA was present. The NRA data used to correct the experimental transmissions of figure 5.17 is shown in figure 5.18, taken at three different fields. The 8T data was obtained using the 393.6μm line, for which a near unity resonant transmission is expected. Taken during $\pi/2$ Current Drive, transmissions of these 8T shots constitute a direct measurement of the non-resonant attenuation during LHCD. The 7 and 9 T points were measured in Ohmic discharges with the 432.6μm line, at fields which place the $3\omega_c$ resonance inside or outside of the center, respectively. Marfeing shots in figure 5.18 are again differentiated from quiescent ones, and appear as solid points of reduced transmission. An illustration of Marfe dynamics at low density is seen in figure 5.16, where an abrupt decrease in the transmission is observed at 360 msec, when figure 5.15 indicates a density of 1×10^{13} cm^{-3} and a current of 60 kA. The density trace is seen to go through a "fast fringe" as the Marfe abruptly turns on, followed by a breakup of the interferometer signal, in a manner characteristic of Marfe activity. Current Drive type discharges are susceptible to Marfe effects due to their low currents, and care must be taken even though the density may be quite low.

The effect which Current Drive has on the temperature profile is studied in figure 5.19, where the Gaussian half width of the temperature profile is shown for Ohmic Simulation (OHS) and LHCD discharges. The Thomson scattering data (triangles) is obtained by fitting a symmetric Gaussian profile to 5 points in the central plasma region between -6 and $+8$ cm. ECA data (circles) is shown only at 10.5T, when the $2\omega_c$ resonance is located at -10.2 cm, and is obtained by fitting a Gaussian to the peak Thomson scattering value at the center and the local temperature at -10.2 cm measured by the ECA. Thus, for a given Thomson scattering peak

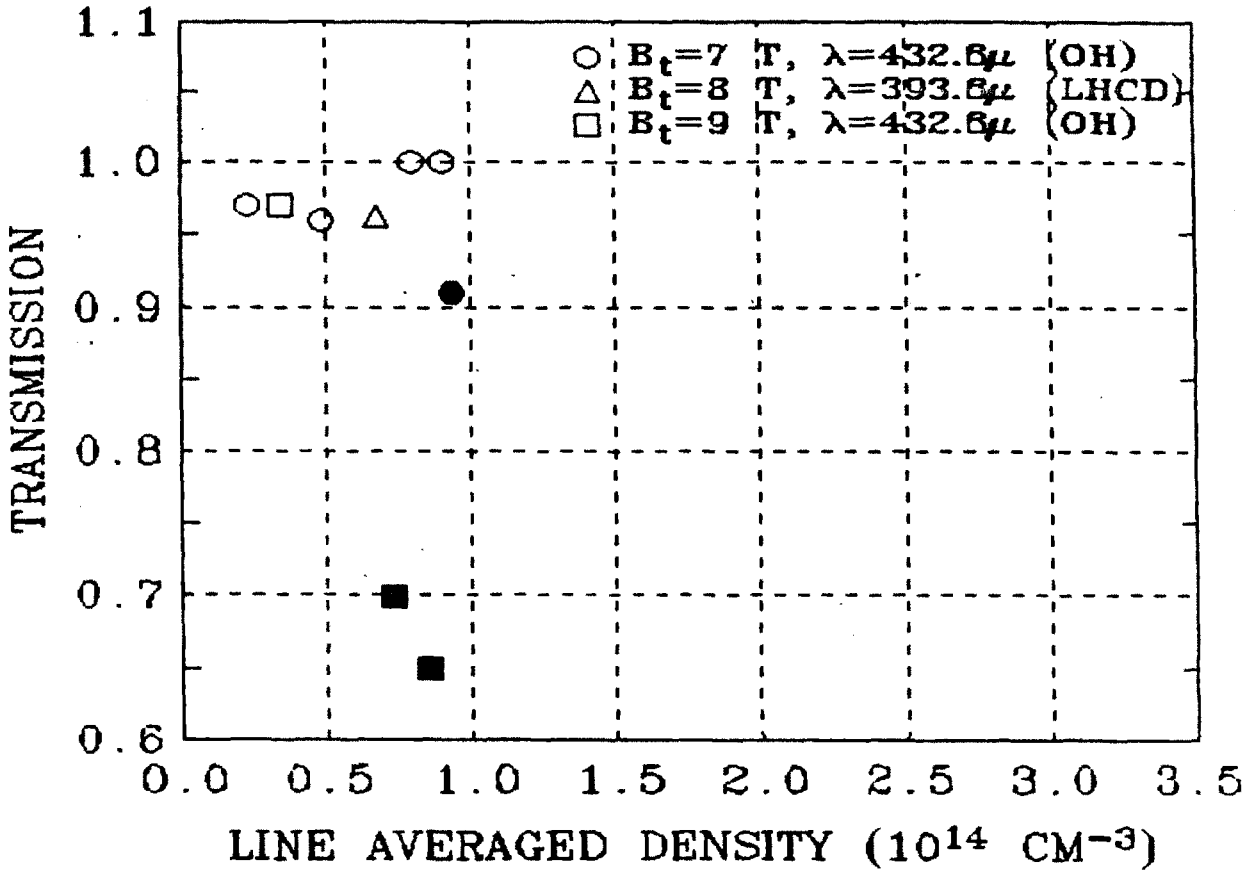

Figure 5.18 — X Mode Non-resonant Transmission Vs. Density and Field, 2/28/85, 3/28/85. Mo limiters, H_2 fill, $I_p = 150$ kA, $\lambda = 432.6$ μm. Solid points correspond to H_α active shots, open points are quiescent shots.

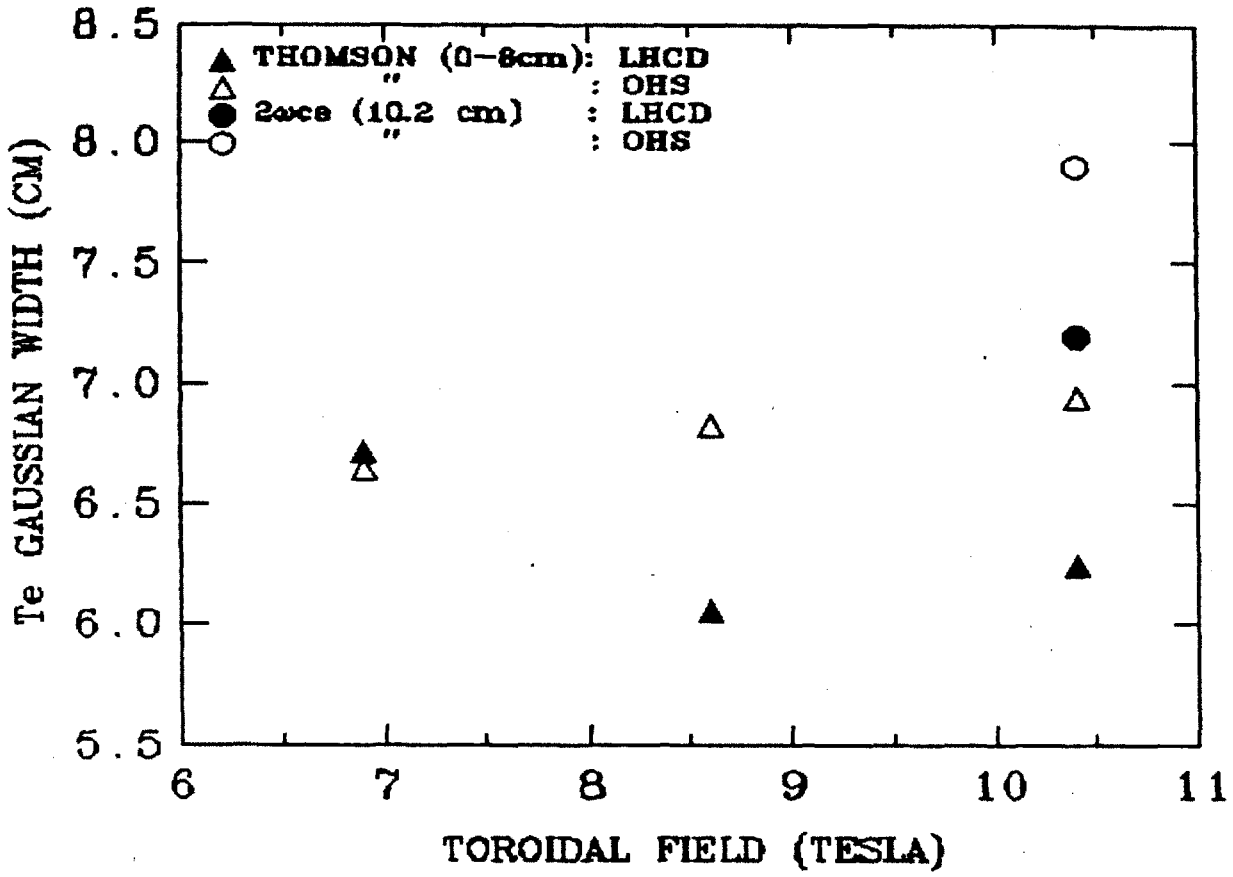

Figure 5.19 — Temperature Profile Widths During Lower Hybrid Current Drive and Ohmic Simulations, 3/5/85. $n_e = .5 \times 10^{14}$ cm^{-3}, $I_p = 150$ kA, $\lambda = 432.6$ μm. (From Gaussian fits to the Thomson scattering central data and second harmonic outer resonance X mode transmission data.)

temperature, the Thomson data fit is weighted with the central plasma data, while the $2\omega_c$ ECA data fit is characteristic only of the outer plasma profile. Both Thomson and ECA meaasurements show a narrowing of the LHCD temperature profile as compared to the corresponding Ohmic value. However, as observed earlier, the outer (ECA data) profile fit is seen to be broader than the central (Thomson data) profile fit, in both the RF and Ohmic cases. The implications of this observation are as discussed previously in section 5.1 .

5.3 Other Plasma Observations

5.3.1 Radiation Temperature

The Equation of Transfer, equation 2.1 of section 2.2.3, is a simple prescription which describes the intensity of radiation emerging from a plasma medium at a specific frequency. Thus far, we have utilized only the first term of this equation describing the transfer of laser power through the plasma, and have used the modulation of the laser to distinguish it from the plasma emission. In order to characterize the emission, we must modify equation 1.2 to include the effects of wall reflections and finite viewing geometry.

The presence of a corrugated stainless steel vacuum wall of reflectivity R_{eff} around the plasma torus acts to intensify the radiation received at a harmonic with transmission $\mathbf{T_n}$, reflecting an additional factor of $1/(1 - R_{\text{eff}}\mathbf{T_n})$ of radiation into the collection system over that arriving by direct emission.[15] In addition, only a fraction C_e of the emitted irradiance transits the collection system for detection, due to redistribution in the optical train and propagation losses.

Within the framework of the LOCKIN analysis described in Chapter 3, the Equation of Transfer describing the semi-opaque third harmonic signals $V_3(t)$ during the on-off probe beam modulation cycle leads to the equations

$$V_3^{\text{on}}(t) = V_{\text{laser}}(t)\mathbf{T_3}(t) + V_3^{\text{off}}(t)$$

$$V_3^{\text{off}}(t) = C_e S_3(t)\left[\frac{1 - \mathbf{T_3}(t)}{1 - R_{\text{eff}}\mathbf{T_3}(t)}\right]$$

$$V_{\text{laser}}(t) = V_3^{\text{on}}(t=0)\left[\frac{V_{\text{ref}}(t)}{V_{\text{ref}}(t=0)}\right] ,$$

where

$$\mathbf{T}_3(t) = e^{-\tau_3\left[T_e(t)\right]} \ , \ S_3(t) = \frac{\left(3\omega_c(r_3)\right)^2}{8\pi^3 c^2 T_{\text{rad}}(t)} . \qquad [5.1] .$$

The above equations relate the thermal and radiation temperatures, T_e and T_{rad}, to the experimentally measured signals V_3^{on}, V_3^{off}, and V_{laser}, via $\mathbf{T}_3$ and S_3, in terms of the calibration factor C_e and the effective reflectivity R_{eff}.

The parameter R_{eff} is a composite factor which takes into account the specular reflection properties of the metal at the working frequency and the effects of wall corrugation and internal structure. From polarization studies of externally viewed second and third harmonic emission,[46,42] R_{eff} was found to be between .6 and .9 . In the present configuration, the collection etendue subtends the diagnostic slot and quartz window, and is restricted by the forward peaked transmission characteristic of the waveguide assembly, [32,33] so that the appropriate R_{eff} is likely to be lower. However, in the above equations, the dependence on the exact value of R_{eff} alone is weak. For the purposes of this study, R_{eff} is somewhat arbitrarily taken to be .5, and all subsequent fitting is accomplished via C_e. The factor C_e must be obtained by calibration with absolute temperature data under thermal conditions, when the radiation temperature and thermal temperatures are equal. Once obtained, C_e remains constant as long as the optical train is left undisturbed, which is limited to one experimental run or less.

Solving for $\mathbf{T}_3$ and S_3, we obtain

$$\mathbf{T}_3(t) = \frac{V_3^{\text{on}}(t) - V_3^{\text{off}}(t)}{V_{\text{laser}}(t)}$$

$$S_3(t) = \frac{V_3^{\text{off}}(t)}{C_e}\frac{1 - R_{\text{eff}}\mathbf{T}_3(t)}{1 - \mathbf{T}_3(t)} \ .$$

A concurrent determination of the emission and transmission thus allows us to directly examine the scaling of the radiation temperature. This principle is demonstrated for two cases considered previously in figures 5.6 and 5.10.

In figure 5.20 the scaling of the radiation temperature is compared to the thermal temperature derived from concurrent $3\omega_c$ ECA and $2\omega_c$ ECE measurements,

which were used for calibration. The points in figure 5.6 which indicated an unexpectedly high T_e due to possible non-resonant effects naturally indicate a low T_{rad} value, since T_e and T_{rad} share an inverse relationship in equation [5.1]. Also, the apparently elevated T_{rad} at the lowest densities may indicate an enhancement of suprathermal electron production in the low density regime.

A marked difference between T_{rad} and T_e is observed during RF heating, shown in figure 5.21. In this case, T_{rad} was calibrated at 240 msec with T_e derived from the $3\omega_c$ transmission, before the RF pulse. During the RF, a large increase of radiation temperature is observed relative to the thermal temperature, caused by enhanced emission by suprathermal electrons produced by the RF waves. After the RF pulse terminates, the plasma quickly re-thermalizes, and T_{rad} once again equals T_e.

5.3.2 MHD Effects

Under a wide variety of operating conditions, discharges in ALCATOR support several types of MHD activity, during which the temperature and density profiles are disturbed from their equilibrium configurations. Since the $3\omega_c$ absorption is characteristic of plasma conditions at the resonance location, the $n_e T_e^2$ dependence of the $3\omega_c$ transmission may render these spatial perturbations plainly visible. This has been observed experimentally in a number of situations. Although the fine structure comprising these effects lies somewhat beyond the spirit of the experiment, their observation in the ECA signals provides an important confirmation of some of the basic assumptions underlying the measurement.

Sawteeth

This MHD instability is observed in clean ($Z_{eff} \approx 1$) discharges for which the safety factor on axis, q_0, falls below unity.[47] It is characterized by a rapid flattening of the density and temperature profiles within a region $\sqrt{2}$ times the $q = 1$ radius, and a subsequent, slower, linear recovery, oscillating with a frequency near 500 Hz. At the bottom of the sawtooth the temperature and density profiles assume their values at the $q = 1$ surface, resulting in typical modulations at the center of 10% of the temperature and 5% of the density during the sawtooth cycle. This modulation

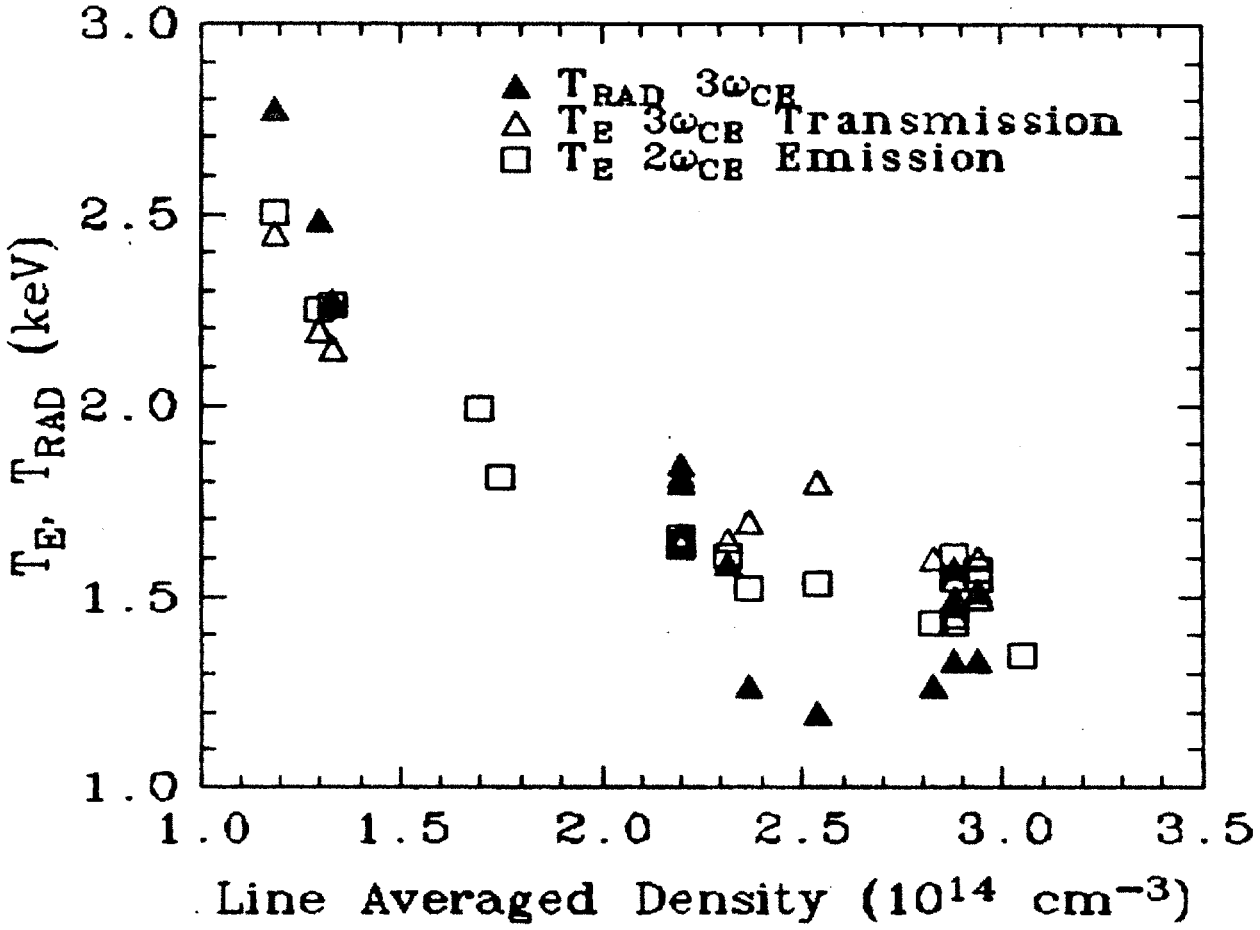

Figure 5.20 — $3\omega_c$ Relative Radiation Temperature Vs. Density, 2/27/85. $B_t = 8$ T, $I_p = 450 - 550$ kA, $\lambda = 432.6$ μm. (Third harmonic T_{rad} has been calibrated using the second harmonic emission data.)

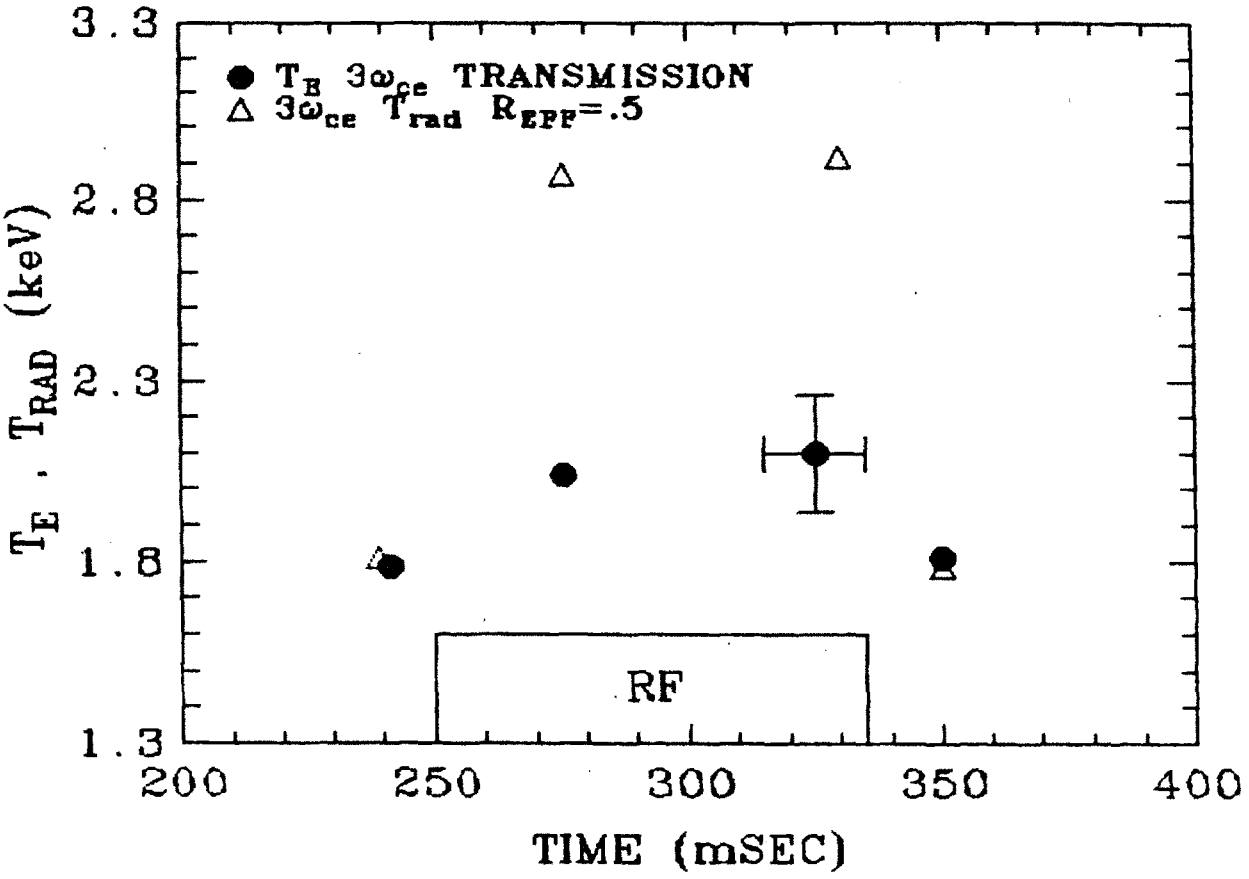

Figure 5.21 — $3\omega_c$ Relative Radiation Temperature During Lower Hybrid RF Heating Vs. Time, 3/22/85. Mo limiters, D_2 fill, B_t = 8 T, $n_e = 1.8 \times 10^{14}$ cm^{-3}, I_p = 440 kA, λ = 432.6 μm, P_{RF} = 610 kW. (From 7 shots)

produces the characteristic signature on the $2\omega_c$ ECE and soft X-ray diagnostics after which the effect is named. A typical sawtoothing shot is shown in figure 5.22, in which sawtooth activity is seen on the ECE and other data after 120 msec.

The interpretation of sawteeth on the raw ECA transmission is complicated by the fact that the transmitted laser signal appears on top of the plasma emission. Since the emission increases with increasing density and temperature, while the transmitted laser signal decreases with increasing density and temperature, the sawteeth on the emission and transmission proceed in opposite directions, and when added together, tend to cancel. Thus, sawteeth on the emission alone, when the laser is off, are larger than those appearing when the laser is on. The size of the observed emission sawteeth is determined by the resolution of the frequency resolving apparatus. Since at the sawtooth crash the profiles are flattened at their $q = 1$ surface values, emission at frequencies emanating from outside the $q = 1$ surface display sawteeth which are inverted relative to those emanating at frequencies inside $r(q = 1)$. Thus, distinct positive going sawteeth only appear in a narrow frequency band around the center frequency. As the bandwidth about the center is increased from zero, the sawteeth decrease in amplitude, and vanish as the inverted emission from beyond $r(q = 1)$ was included in the sawtoothing signal.

The 50 GHz resolution in $3\omega_c$ emission corresponds to the region ± 2.5 cm, which is approximately half of the $q = 1$ radius. Thus, in figures 5.22 and 5.23 the emission sawteeth on the raw $3\omega_c$ signal, seen when the laser is off, are distinct and positive going, as expected. Sawteeth are visible when the laser is on, but they are indeed observed to be smaller, and to have additional noise present which originates in the lasers or injection optics and does not affect the emission. A comparison of the sawteeth at different times is shown in figure 5.24, where an emission only sawtooth and an emission plus laser signal sawtooth are taken from nominally identical adjacent sawteeth cycles at 471 msec, and aligned at the time of their crashes. The dashed line represents the effect of a linear ramp-up of 10% of the temperature and 5% of the density over the sawtooth cycle. The relative amplitudes

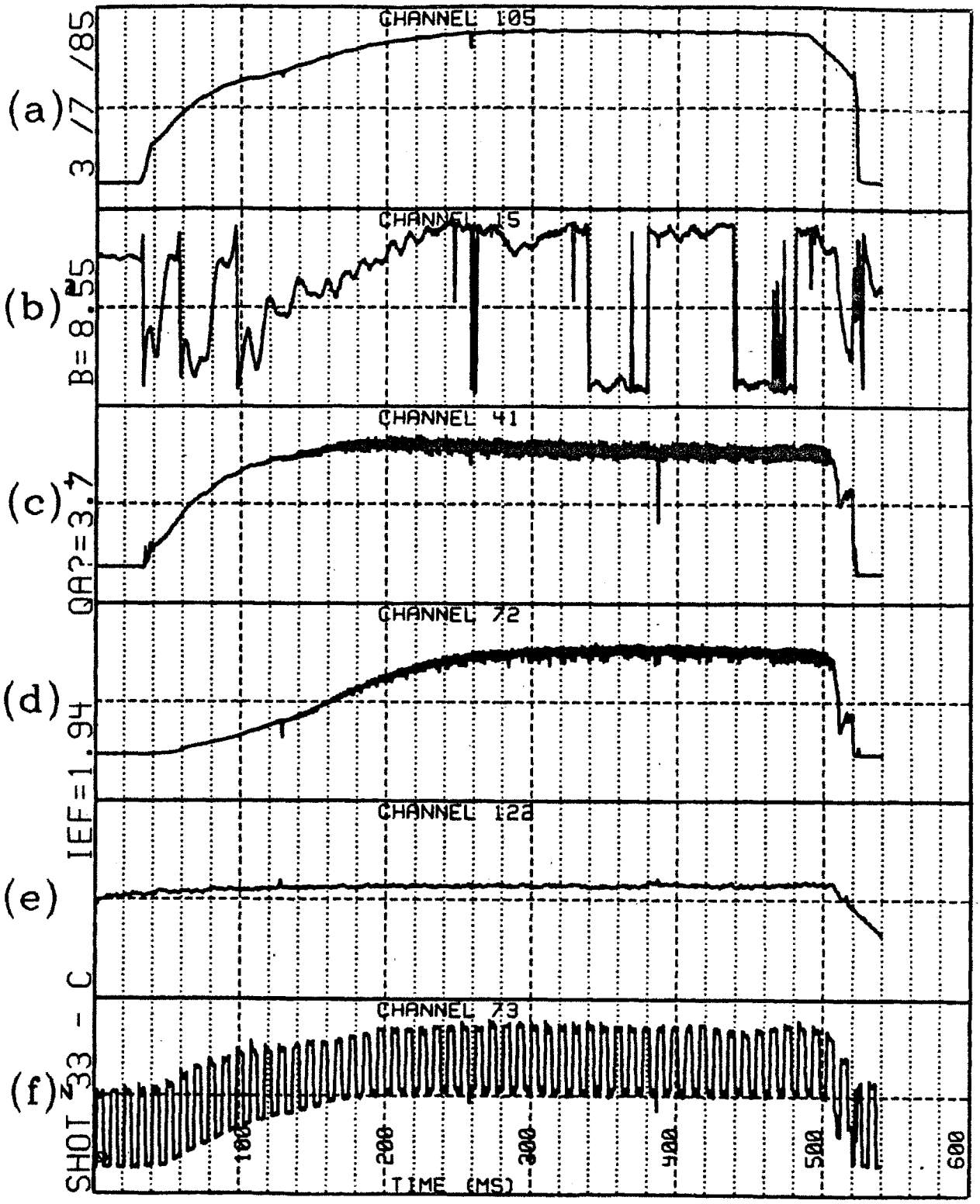

Figure 5.22 — Plasma Data for Sawtoothing Discharge, 3/7/85, Shot #33. Traces shown are (a) Plasma Current, 2.5 V/div (b) Central Density (c) $2\omega_c$ Cyclotron Emission (d) Central Soft X-Rays (e) Toroidal Field (f) Raw $3\omega_c$ Transmission.

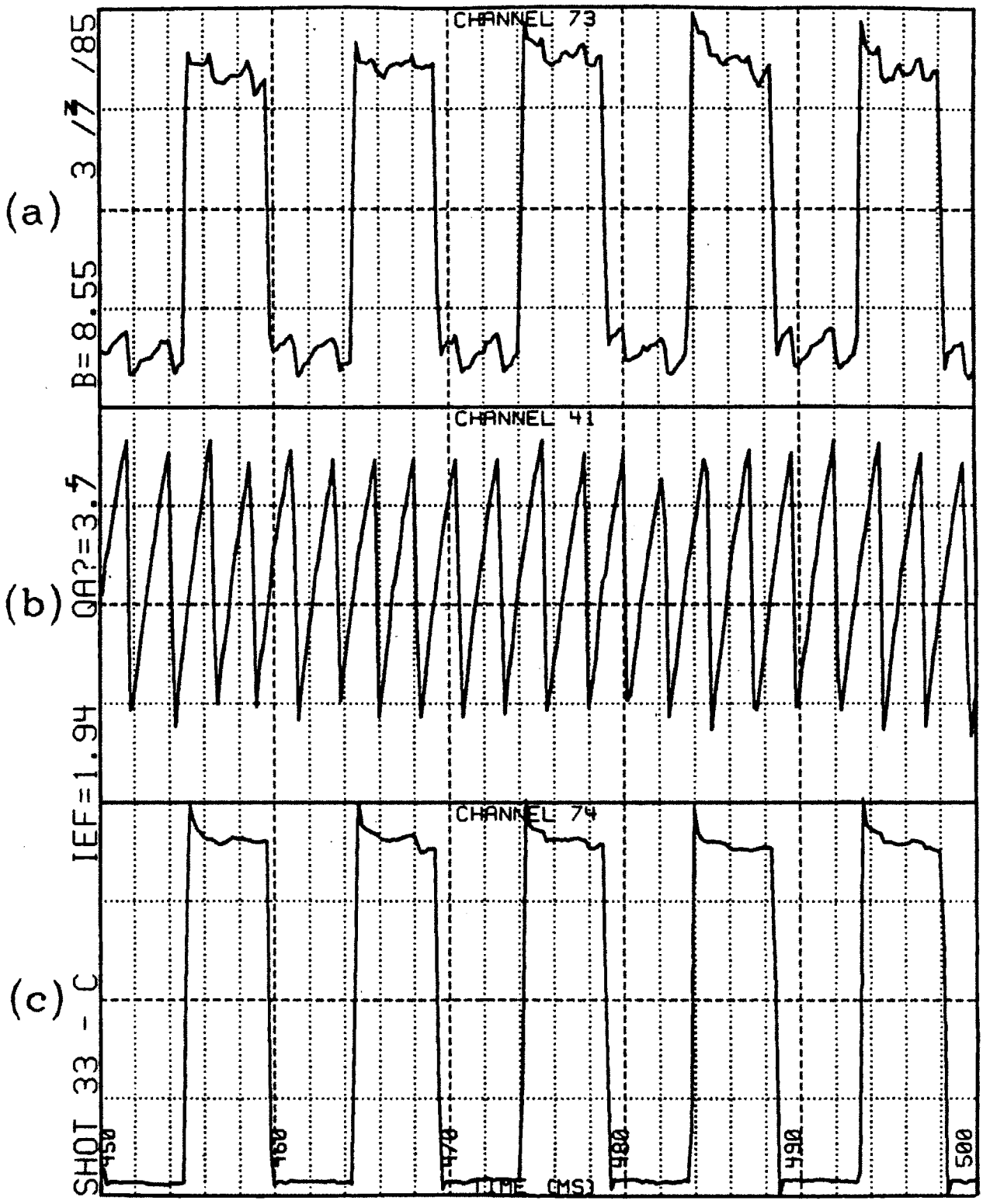

Figure 5.23 — Expanded View of Sawteeth at 450 msec, 3/7/85, Shot #33. Traces shown are (a) Raw $3\omega_c$ Transmission (b) $2\omega_c$ Cyclotron Emission (c) Laser Reference.

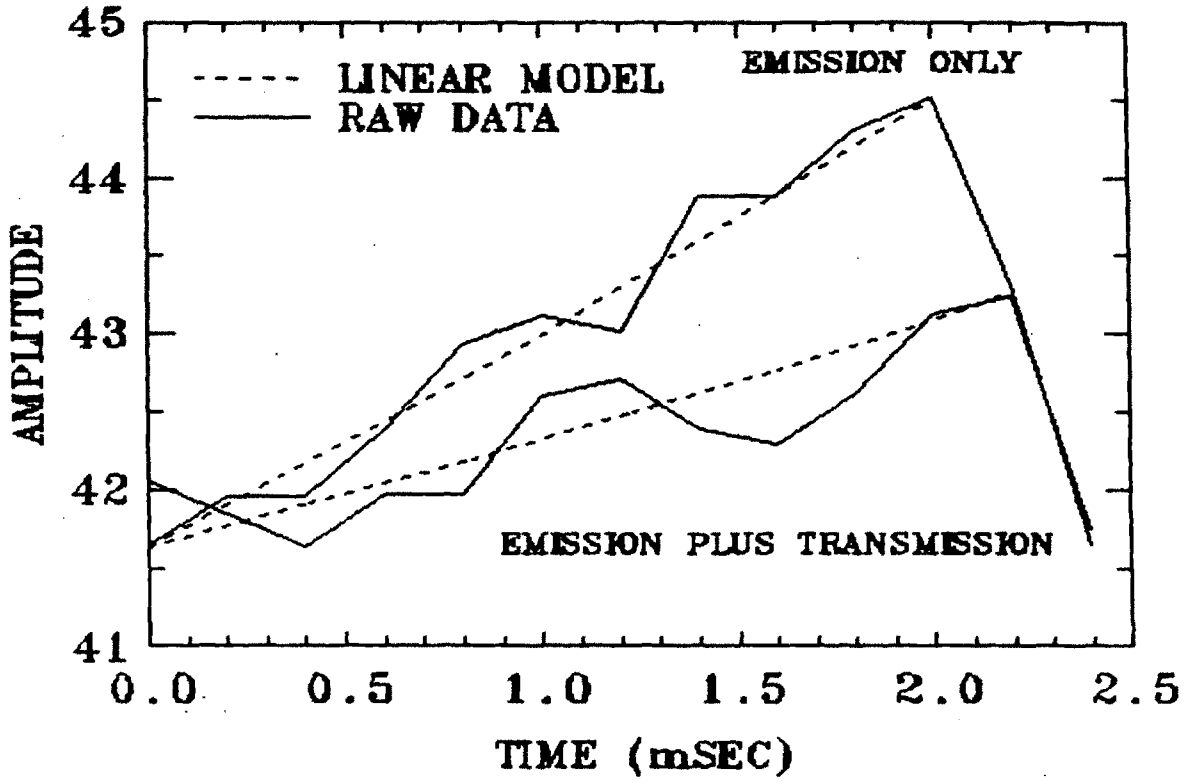

Figure 5.24 — Comparison of Adjacent "Emission Only" and "Emission Plus Transmission" Sawteeth at 471 msec, 3/7/85, Shot #33. He fill, $B_t = 8$ T, $I_p = 500$ kA, $n_e = 1.8 \times 10^{14}$ cm^{-3}, $T_e = 2.0$ keV, $r(3\omega_c) = -2$ cm. $\lambda = 432.6$ μm.

are consistent with the model, although the sawtooth crashes are unresolved at the 5 kHz digitization rate used.

By effectively clamping the central current density, the sawtoothing instability observed above is a mechanism which limits the Ohmic power available for heating the discharge center, and thus the range of Ohmic central temperatures accessible at a given density. This action was seen to be of some importance in understanding the data in figures 5.1 and 5.7.

m=1 Activity

Following Pellet injection, in which a solid pellet of frozen fuel gas is fired at high speed into the plasma, large amplitude sustained m=1 oscillations may occur.[47] These are characterized by a periodic displacement of the plasma centroid from the toroidal axis and a poloidally asymmetric compression of the flux surfaces within the $q = 1$ surface. The resulting oscillations in density and temperature vary in amplitude across the plasma, with a minimum near the toroidal axis and maxima several centimeters off axis. An example of m=1 activity is seen in figure 5.25, in which a pellet is injected at 215 msec. The m=1 activity is seen to erupt on the -2 cm soft X-ray trace at 315 msec, following plasma current inversion.

An expanded view of the m=1 episode is shown in figure 5.26. The m=1 modulation is clearly visible on the $3\omega_c$ laser signal, and is observed to be larger after the toroidal field rampdown has begun (353 msec) than before (323 msec). Prior to the TF ramp, the laser is resonant at the plasma center, and reflects the amplitude at that position. After the TF ramp has commenced, the resonance moves inward, away from the center. The migration of the resonance layer inward is coincidentally timed to pick up the late m=1 burst when it is near the off-axis ($r < 0$) modulation maximum. Hence, the amplitude shown on the laser is greater, even though the oscillation itself is smaller at the later time. The noise on the transmission signal after 360 msec is due to incipient Marfe activity associated with the falling plasma current.

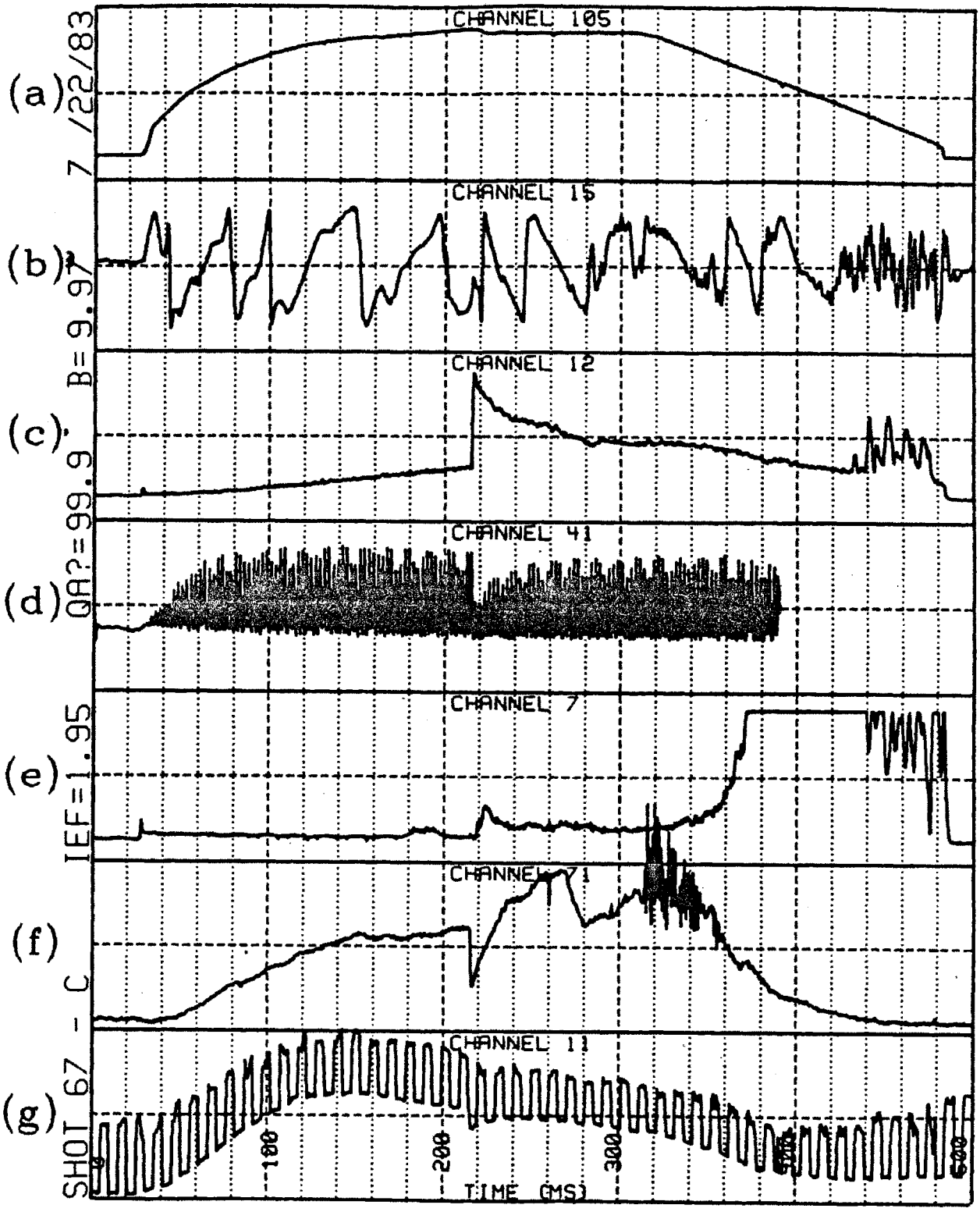

Figure 5.25 — Plasma Data for Discharge Exhibiting M= 1 Activity, 7/22/83, Shot #67. Traces shown are (a) Plasma Current (b) Central Density (c) Raw Z_{eff} (d) $2\omega_c$ Cyclotron Emission (e) H_α (f) Soft X-Rays at $r = -2$ cm (g) Raw $3\omega_c$ Transmission.

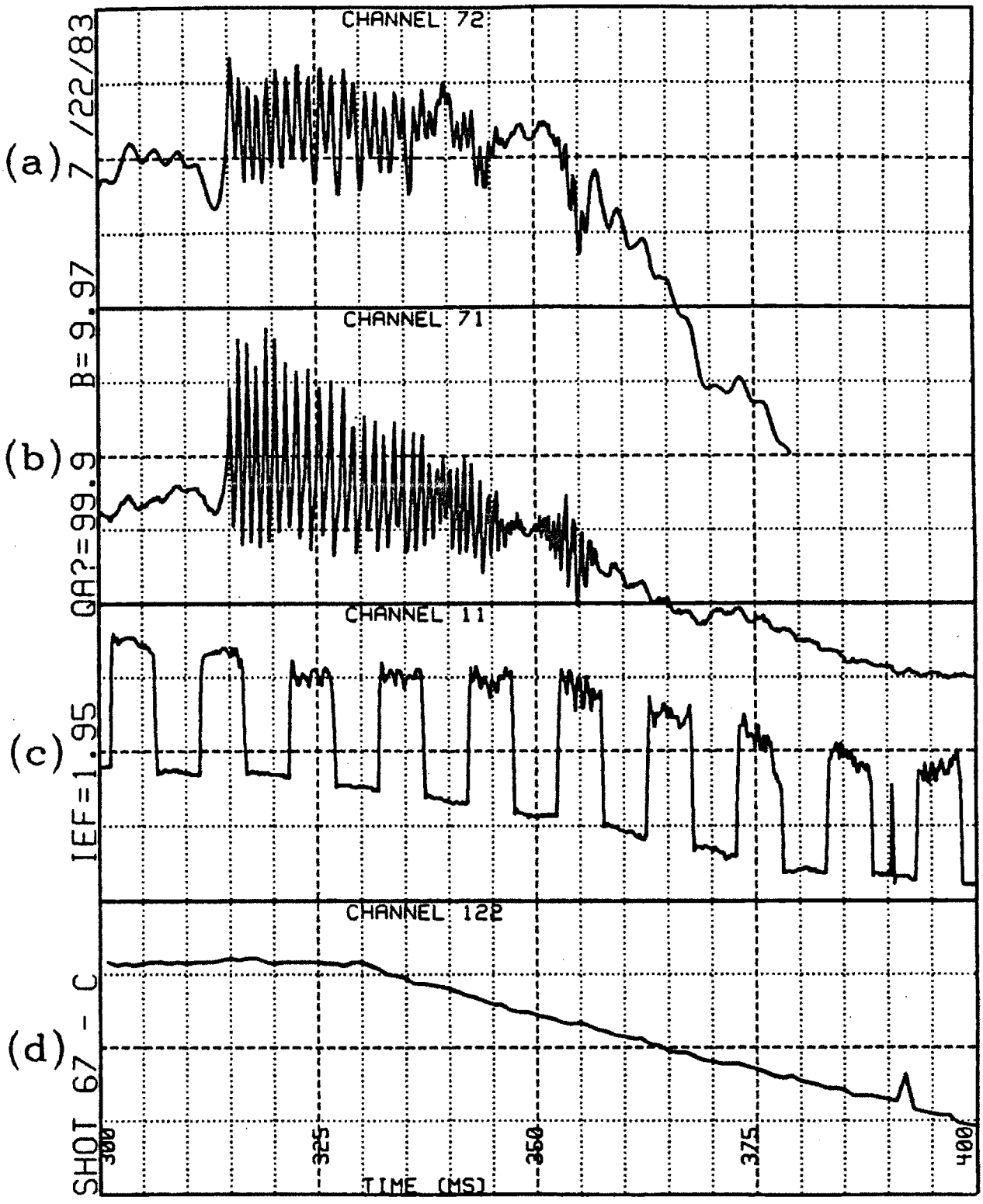

Figure 5.26 — Expanded View of M= 1 Episode, 3/7/85, Shot #33. Traces shown are (a) Soft X-Rays at $r = 0$ cm (b) Soft X-Rays at $r = -2$ cm emission (c) Raw $3\omega_c$ Transmission (d) Toroidal Field.

The relation between pellet injection, which occurs outside the $q = 1$ surface,[48] and occurence of the sustained $m = 1$ activity described above, which occurs inside the $q = 1$ surface, is still the subject of investigation.[47]

5.4 Chapter Summary

The diagnostic capabilities of X mode cyclotron harmonic transmission measurements have been demonstrated in a variety of applications. The magnitude of the transmission has been found to agree with theoretical results of lowest significant order in finite density and FLR effects, and temperatures reported using the transmission technique were in agreement with standard Tokamak temperature diagnostics over a wide range of temperatures and conditions. The ECA measurement technique was shown to be complementary to other temperature diagnostic methods, and to be competitive in matters of performance, accuracy, and cost. Bulk plasma electron temperatures have been measured during Lower Hybrid Heating, and these are in agreement with temperatures obtained from Thomson scattering. No additional absorption was found during Lower Hybrid Current Drive, in agreement with theoretical predictions. The radiation temperature, however, did show a large increase during RF injection. Sawteeth and m= 1 activity were observed on the raw third harmonic transmission signal. These behaved in the expected manner, and were well correlated with other diagnostics of MHD activity. In this chapter, the non-resonant attenuation was successfully accounted for in the data analysis in any of several ways as a phenomenological correction.

Chapter 6

Interpreting the Non-Resonant Attenuation

In this chapter we consider the nature and possible origins of the non-resonant attenuation. The effects of plasma refraction and turbulence generated edge structure are assessed, and the role of differences in the experiment configuration are discussed. Additional, qualitative, observations are presented which may have some bearing on the identity of the non-resonant attenuation.

6.1 Plasma Refraction Effects

The existence of a steady non-resonant attenuation has been reported in several transmission experiments in the electron cyclotron range of frequencies. Examples of this include observations at $2\omega_c$ in the Model C Stellarator[9] where $T_{nra} \approx 30\%$, and at ω_c in the PLT Tokamak [10]where $T_{nra} \approx 50\%$. In these cases the effect is attributed to refraction of the incident radiation by an electron density gradient which intersects the ray path.

In chapter 2 it was shown that as a consequence of the restricted access in Alcator C, the injected radiation is constrained to nearly perpendicular propagation. Similar structural constraints dictate that, if the injection and collection of the probing radiation occurs as designed, the beam trajectory must intersect the toroidal axis in a perpendicular plane, entirely along the density gradient. In this configuration the effects of refraction are expected to be minimal, and cannot be responsible for the NRA found in ALCATOR.

In order to investigate the effect of plasma refraction on the beam transmission we must examine the degrees of freedom which constitute a source of possible beam displacement under normal circumstances, calculate the maximum effect which such displacements may be expected to have on the vacuum and plasma transmission, and obtain experimental evidence which indicates that our analytical assessment is supported by fact.

Although under ideal conditions refraction might well be negligible, practical deviations from the ideal are readily identifiable. Since the beam has a finite extent, some degree of refraction must occur for the off axis rays. Also, the entire plasma may be displaced vertically by ± 1 cm from the toroidal axis in the course of routine tokamak operation. Finally, since optimum optical alignment is not always maintainable, a small offset may be present which may not affect the vacuum transmission in an obvious manner. A vertical displacement of the beam trajectory relative to the plasma centroid as a result of any of the above considerations could give rise to a further refraction of beam away from the centroid. This would in turn divert the beam vertically from the waveguide aperture during the discharge, producing an apparent attenuation.

In order to estimate the magnitude of possible optical misalignments, we must consider the details of the diffraction limited injection geometry shown in figure 6.1. Because of the large vertical extent of the horizontal keyslot, a vertical clearance constraint is posed only by the circular vacuum window which the beam must transit successfully in order to enter the Tokamak with minimal diffraction. For a Gaussian beam of field half width ω_0 transiting an aperture of radius ρ, diffraction effects begin to become noticable when $\rho < \sqrt{2}\omega_0$, at which point the Gaussian profile and propagation begin to become affected. For a clear aperture of 9.8 cm and a beam field diameter of 5.6 cm at the window, this criterion indicates nearly undiffracted transmission for displacements of 1.0 cm or less, and errors of this size could in principle go undetected.

Conversely, if the centered beam successfully transits the port internal structure and keyslot as a Gaussian, then a marked decrease in the transmission should be observed if diffraction at the window begins to occur. This effect is shown in figure 6.2, in which the beam was translated across the window, starting from the center. The maximum transmission obtained has been normalized to the value with the beam centered on the window, and is plotted versus the location of the beam axis from the center. A transition is observed to occur between 1.1 and 1.5 cm, as diffraction begins to affect the transmitted beam, consistent with the expected

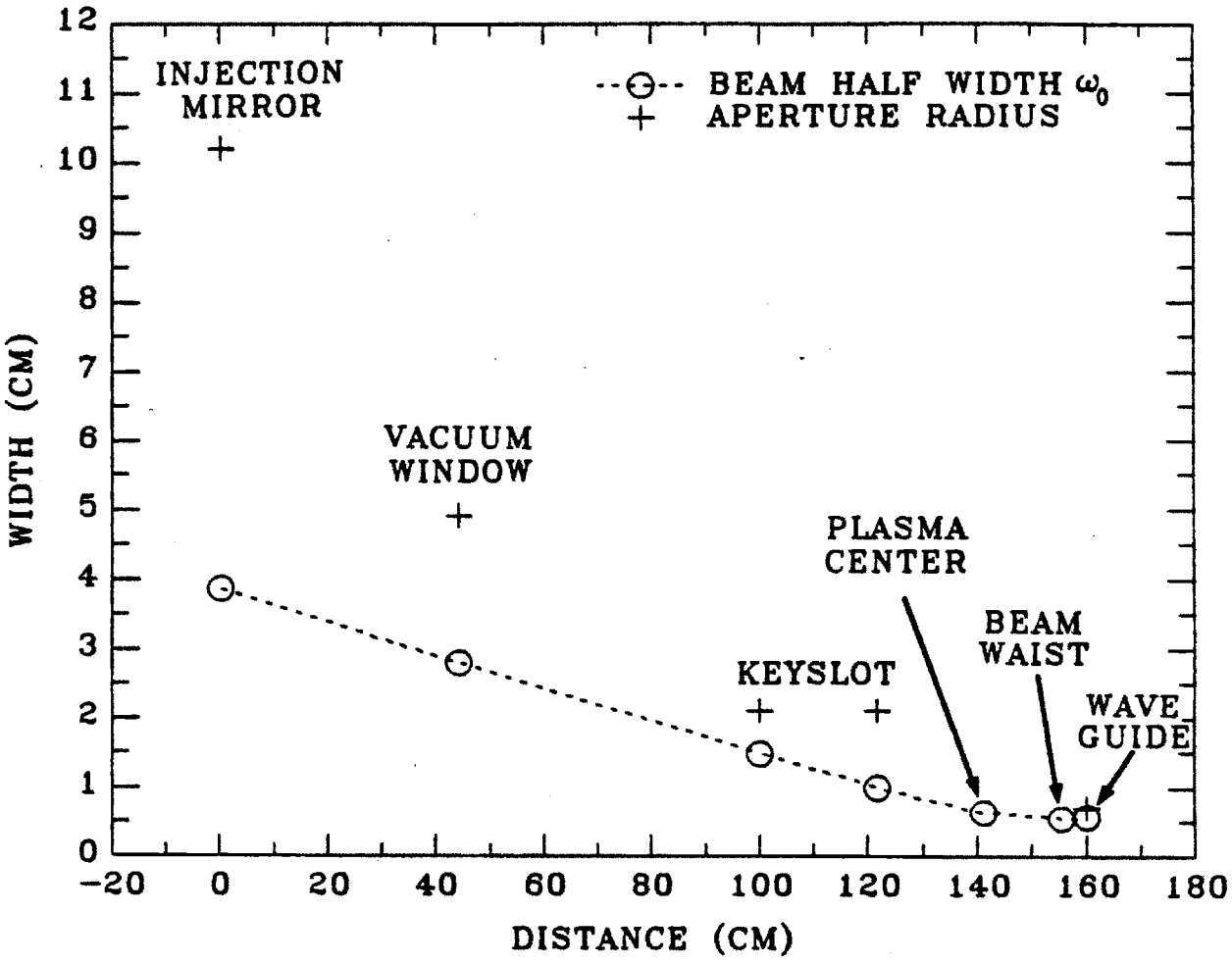

Figure 6.1 — Probe Beam Tokamak Injection Geometry. Shown are the Gaussian field half width and clearance at various locations in the optical path, from the final f=1.02 M injection mirror to the waveguide aperture. The plasma center is located at 141 cm, and extends ±16.5 cm about that point.

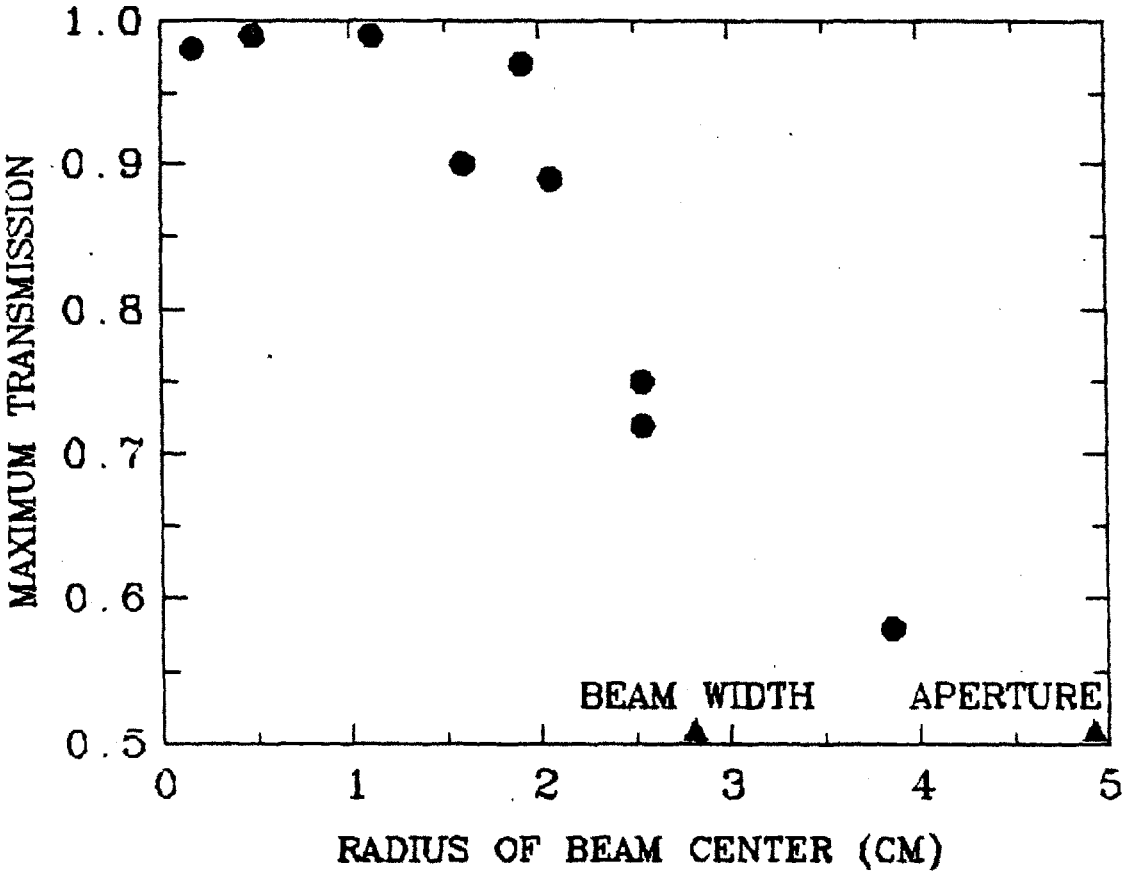

Figure 6.2 — Effect of Beam Alignment on Entrance Flange Transmission. The Gaussian field half width and aperture at the window are as indicated.

value of 1 cm. However, a 1.5 cm misalignment at the window produces an offset of only .24 cm at the plasma center. Thus, displacements of the beam in the vertical as well as horizontal dimensions are well constrained by structural considerations, in addition to being aided by collinear HeNe laser alignment capabilities, and any sizable offset would have been noticable in the course of daily optical adjustments.

Even though gross misalignments may be absent, we must still establish the magnitude of the refraction effect for on axis and near axis propagation. A beam of finite extent will diverge in the dimension perpendicular to the toroidal axis due to the density gradient. This causes an elliptical distortion of the beam arriving at the waveguide, and a reduced transmission. To estimate this effect, we calculate the broadening of a beam of initial field half width ω_0 in its traversal of the plasma. It arrives at the waveguide with a broadened width ω_x in the x direction perpendicular to the toroidal axis, and an unperturbed width ω_0 in the y direction along the toroidal axis, as shown in figure 6.3a. We then calculate the transmission of the elliptical Gaussian for a waveguide of radius ρ. We assume that in the absence of refraction the beam has a constant width equal to its value at the waveguide, and that the interaction is adequately described using the deflection of the beam width. These assumptions are justified near the beam waist, and as long as the beam remains nearly Gaussian.

The deflection of an off axis ray by a plasma of radius a and a dielectric function which depends only on radius has been calculated by Shmoys,[49] who has formulated the deflection angle $\theta(b)$ as a function of the impact parameter b relative to the plasma center. For the case of a parabolic plasma density variation, explicit formulae are given for $\theta(b)$, the maximum deflection $\theta_{\max}$, and the value $b_{\max}$ at which this occurs. For the present case, $b_{\max}$ is approximately $a/\sqrt{2}$, or 12 cm in ALCATOR C. The observation is also made that variations in the deflection characteristics of plasma density profiles which vary quadratically near the center are small as long as b is less than or equal to the impact parameter of maximum deflection $b_{\max}$. For $\omega_{\text{laser}} = n\omega_c(r=0)$, and $n_e = n_0(1-r^2/a^2)$, the result is

$$\theta(b) = \sin^{-1}\left[V_0 \sqrt{\frac{\left[(b/a)^2 - (b/a)^4\right]}{\left[V_0(b/a)^2 + \left[\frac{1}{2}(1-V_0)\right]^2\right]}} \right]$$

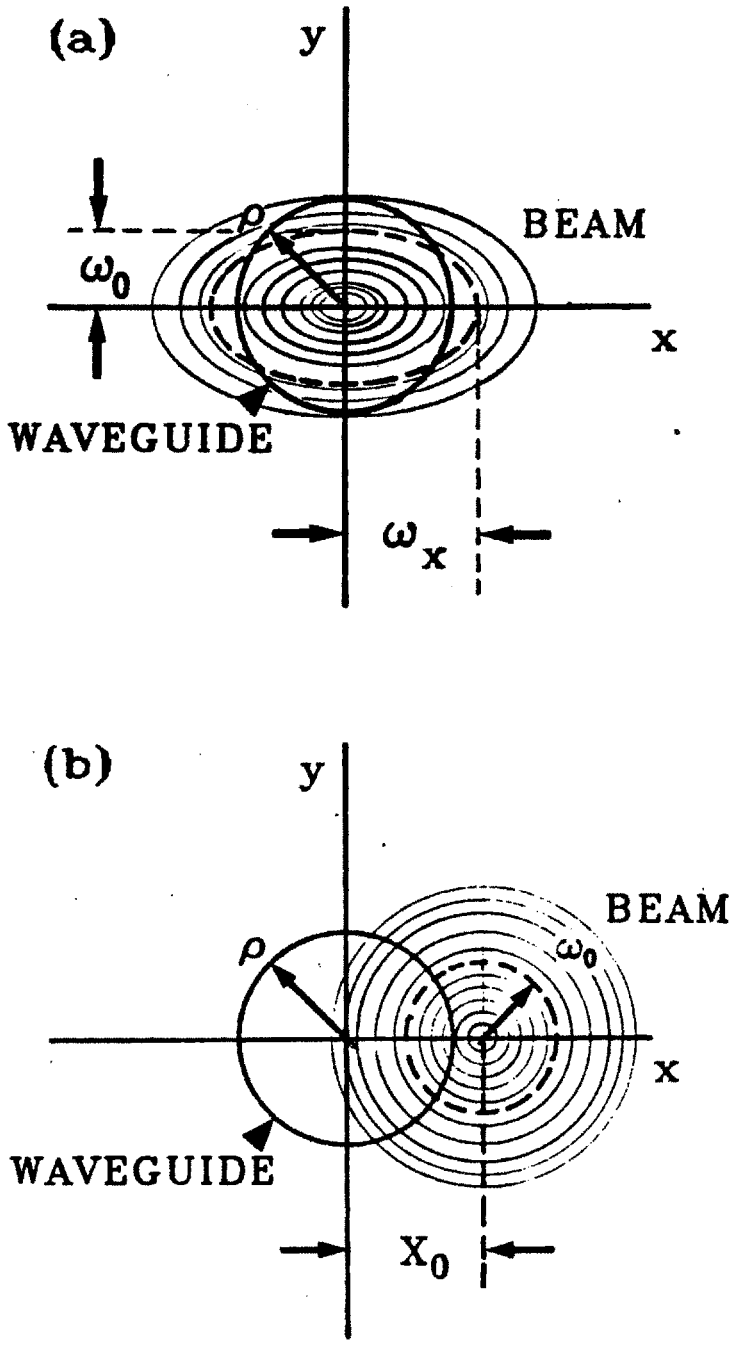

Figure 6.3 — Plasma Refraction Effects. Shown are the waveguide aperture and Gaussian beam. (a) Elliptical beam at waveguide aperture. (b) Offset Beam Geometry.

$$V_0 \equiv \frac{\omega_p^2}{\omega_{laser}^2 - \chi\omega_c^2} = \frac{1}{n^2 - \chi} \quad \frac{\omega_p^2(0)}{\omega_c^2(0)}$$

where $\chi = 1$ for the X mode and $\chi = 0$ for the O mode. Knowing the exit angle of a ray with $b = \omega_0$, and the distance from the plasma center to the waveguide r_{wg}, the final broadened width can be written as $\omega_x \approx \omega_0 + \theta(\omega_0) r_{wg}$.

The portion of the broadened beam which enters the waveguide is readily calculated. The elliptical Gaussian intensity profile is

$$I(x,y) = I_0 e^{-\left(\frac{2x^2}{\omega_x^2}\right)} e^{-\left(\frac{2y^2}{\omega_0^2}\right)} ,$$

and the energy entering the waveguide is

$$E(\omega_0, \omega_x) = 4 \int_{x=0}^{\rho} \int_{y=0}^{\sqrt{\rho^2 - x^2}} I(x,y)\, dy dx .$$

From this we derive an explicit expression for the fraction of the energy entering the waveguide,

$$\frac{E}{E_0} = \frac{2}{\sqrt{\pi}} \int_0^k e^{-t^2} \operatorname{erf}\left[\frac{\omega_0}{\omega_x}\sqrt{k^2 - t^2}\right] dt ,$$

where $E_0 = \frac{\pi}{2}\omega_x\omega_0 I_0$ is the total beam energy, $\omega_0 = \sqrt{2}\omega_{I0} = .585$ cm is the unperturbed field half width, $\rho = .714$ cm is the waveguide aperture radius, and $k \equiv \sqrt{2}\rho/\omega_0 = 1.727$.

The above expressions for the broadened beam width and the transmission are implemented by Program SPREAD, which calculates $\omega_x(\omega_0)$ and $\mathbf{T}(\omega_x)$ for a given line averaged density, initial beam half width, toroidal field, and laser frequency. The error function and integral are evaluated numerically using the IMSL[50] routines MERF=ERF and DCADRE.

For a case with $B_t = 8$T, $\lambda = 381\mu$m, and a line averaged density $n_e = 3 \times 10^{14}$ cm^{-3}, the field half width at the waveguide is $\omega_x(.585\text{ cm}) = .652$ cm, an increase of 11%, and a transmission of .93 is obtained. Normalizing by the .95 transmission of the unbroadened beam, we find that the divergence produces a 2% effect on the external transmission, even at the highest density encountered in this work.

Next we estimate the effect of a small offset of the beam relative to the plasma centroid, as shown in figure 6.3b. To accomplish this, we calculate the beam offset X_0, produced at the waveguide by plasma refraction for a Gaussian beam with impact parameter b relative to the plasma centroid, and then calculate the transmission T for a waveguide of radius ρ as a function of the beam offset.

We make the assumption that any radiation which enters the waveguide is transmitted with an efficiency which is independent of alignment. This assumption is justified for small X_0/ρ, but may not be justified when $X_0/\rho \leq 1$, and the beam energy is primarily coupled into high order modes which have large concentrations of field energy near the metallic waveguide wall, and thus have higher damping. We also assume that the elliptization of the beam by the plasma is small, and that the beam remains nearly Gaussian circular. This assumption is justified in light of the previous calculation.

The deflection of the beam center by the plasma is again calculated using the formalism of Shmoys, and the amount of radiation which enters the waveguide is calculated as above. The Gaussian intensity profile for the shifted beam is now

$$I(x,y) = I_0 e^{-\left[\frac{2(x-X_0)^2}{\omega_0^2}\right]} e^{-\left[\frac{2y^2}{\omega_0^2}\right]},$$

and the energy entering the waveguide is

$$E(X_0) = 2 \int_{x=-\rho}^{\rho} \int_{y=0}^{\sqrt{\rho^2-x^2}} I(x,y)\, dy dx\ .$$

From this we obtain an explicit expression for the fraction of the shifted beam energy entering the waveguide,

$$\frac{E(X_0)}{E_0} = \frac{1}{\sqrt{\pi}} \int_{-k}^{k} e^{-2\left(\frac{t-X_0}{\omega_0}\right)^2} \operatorname{erf}\left[\sqrt{k^2-t^2}\right] dt$$

where $E_0 = \frac{\pi}{2}\omega_0^2\ I_0$ is the total beam energy, $\omega_0 = .585$ cm is the beam field half width, $\rho = .714$ cm is the waveguide aperture radius, and $k \equiv \sqrt{2}\rho/\omega_0 = 1.727$.

The above expressions for the beam deflection and the offset transmission are applied to the geometry of figure 6.3b in Program REFRACT, which performs the integrals numerically in a manner similar to Program SPREAD, using the MERF=ERF and DCADRE routines. Given values for the beam impact parameter to the plasma center, toroidal field, and laser frequency, REFRACT calculates the beam deflection at the waveguide and the external transmission as a function of the line averaged density. For the case $B_t = 8\text{T}$, $\lambda = 381\mu\text{m}$, a line averaged density $n_e = 3 \times 10^{14}$ cm^{-3}, and a beam impact parameter of 1 cm, an offset $X_0 = .123$ cm is obtained, and a transmission of .94. Normalizing by the transmission of the unbroadened beam .95, we find that the beam shift produces a 1% effect, which is even smaller than the spread effect calculated previously. In order to obtain a transmission which is comparable to the NRA effect of figure 5.14, an impact parameter of 7 cm is required, which is much greater than that allowed by physical and geometrical constraints in ALCATOR. Consistent with our initial assumptions, more plausible values of b do not appear to take us into the regime where a deteriorating mode structure may be expected to degrade the transmission, or where the details of the density profile may become significant.

Thus, beam spreading and shifting effects due to plasma refraction are too small to account for the non-resonant attenuation, even if the effects are synergistic to some degree. To account for the 5 to 30% attenuation level displayed in figures 5.12 and 5.14, a different explanation of the non-resonant attenuation must be proffered.

Although for a properly aligned beam of the designed specifications refraction effects are small, we must still ascertain that the beam transits the slot undiffracted and focuses down as intended. While no direct evidence of this is obtainable, the body of circumstantial evidence does suggest that this is the case. In order to transit the Tokamak structure with minimal losses, it is imperative that collimation be maintained and that diffraction be avoided. Were this not true, the radiation would necessarily diffract from the 4.2 cm keyslot and illuminate the 1.6 cm^2 waveguide aperture 40 cm away as a diffuse spot. However, the overall transmission of the assembly was measured to be within 5% of the transmission projected from the

measurements of the individual components given in chapter 3. This could only be realized if significant diffraction did not occur and the beam spot effectively focused down to 1.2 cm design value at the waveguide.

Additional circumstantial evidence that the beam transited the Tokamak structure undiffracted and focused down to the desired spot size at the waveguide are offered by practical experience. For a waveguide aperture $2\rho = 1.43$ cm and a beam field diameter $2\omega_0 = 1.316$ cm, the fraction of the beam energy radiation entering the waveguide is

$$\frac{E}{E_0} = 1 - e^{-2\left(\frac{\rho}{\omega_0}\right)^2} = .95 .$$

The remaining 5% of the radiation is reflected about the Tokamak interior. This small amount of radiation was detected by the ECE diagnostic located on the same horizontal port directly above the laser injection window. When the optical adjustment was deliberately misaligned, the ECE signal was observed to increase by a factor of 20 to 30. To the extent that the background ECE signal is a measure of the diffuse scattered beam energy, this observation supports the view that most of the radiation normally enters the waveguide when the beam is aligned. In addition, the sensitivity of the final vertical adjustment was observed to be consistent with that expected for the designed Gaussian mode size.

6.2 Edge Turbulence Effects

It has been widely observed that large amplitude fluctuations exist in the Tokamak plasma edge region $r/a \geq .8$, and these have generally been attributed to the existence of broadband, incoherent microturbulence.[51] Although the origins and details of this phenomenon are still under investigation, there does exist a large body of consistent experimental observations which document the macroscopic effects of often large fluctuations in density, potential, and fields occuring near the plasma edge.

One such observation has been the discovery of toroidal filamentary structures within the apparent turbulence.[52] These have a relatively long coherence length

along the magnetic field, and are clearly evident as striations in visible light emission from the edge.[53] Each filament is associated with a density peak,[52] and a total density fluctuation of as much as 100% of the ambient density. It is of interest to determine whether these turbulent structures can diffuse the Gaussian, and to assess the effect which this may have on the overall transmission of $3\omega_c$ radiation.

The filamentary scattering may be modeled heuristically for a spherical Gaussian beam of field half width ω_0 incident on a plasma which contains poloidal edge layer of thickness L in which turbulent filamentation is present. We assume that small angle forward scattering in the layer causes the beam to diverge, but that the beam remains nearly Gaussian. Although the beam must transit the layer upon entering and leaving the plasma, the exit layer is located 1.6 cm from the waveguide, while the entrance layer is 35 cm away. We therefore consider scattering in the first layer, which is expected to be the dominant effect, in the manner depicted in figure 6.4a.

The filaments are assumed to be cylindrical, so that broadening occurs only in the y direction due to the action of the filaments, and the beam emerges from the layer as an elliptic Gaussian. We also assume that the divergence of the beam is solely due to the interaction with the filaments, and the beam half width ω_0 along the filaments remains unchanged throughout the propagation. This would be approximately true near the beam waist, as in the present case. The elliptical beam arrives at the waveguide with a a broadened field half width $\omega_y(Z)$ in the y direction.

The filaments are assumed to be stacked in a square lattice with an areal density $N_f = 1/4r_f^2$, where r_f is the radius of a filament. r_f is taken to be half the experimentally measured correlation length $l_{\rm corr}$. The filaments are assumed to have a density profile of the form

$$n_f(r) = n_{f0}(1 - r^2/r_f^2) + n_b \ ,$$

where the first term represents a parabolic component of peak value n_{f0}, and the second a non-fluctuating background component n_b, as shown in figure 6.4b. n_{f0}

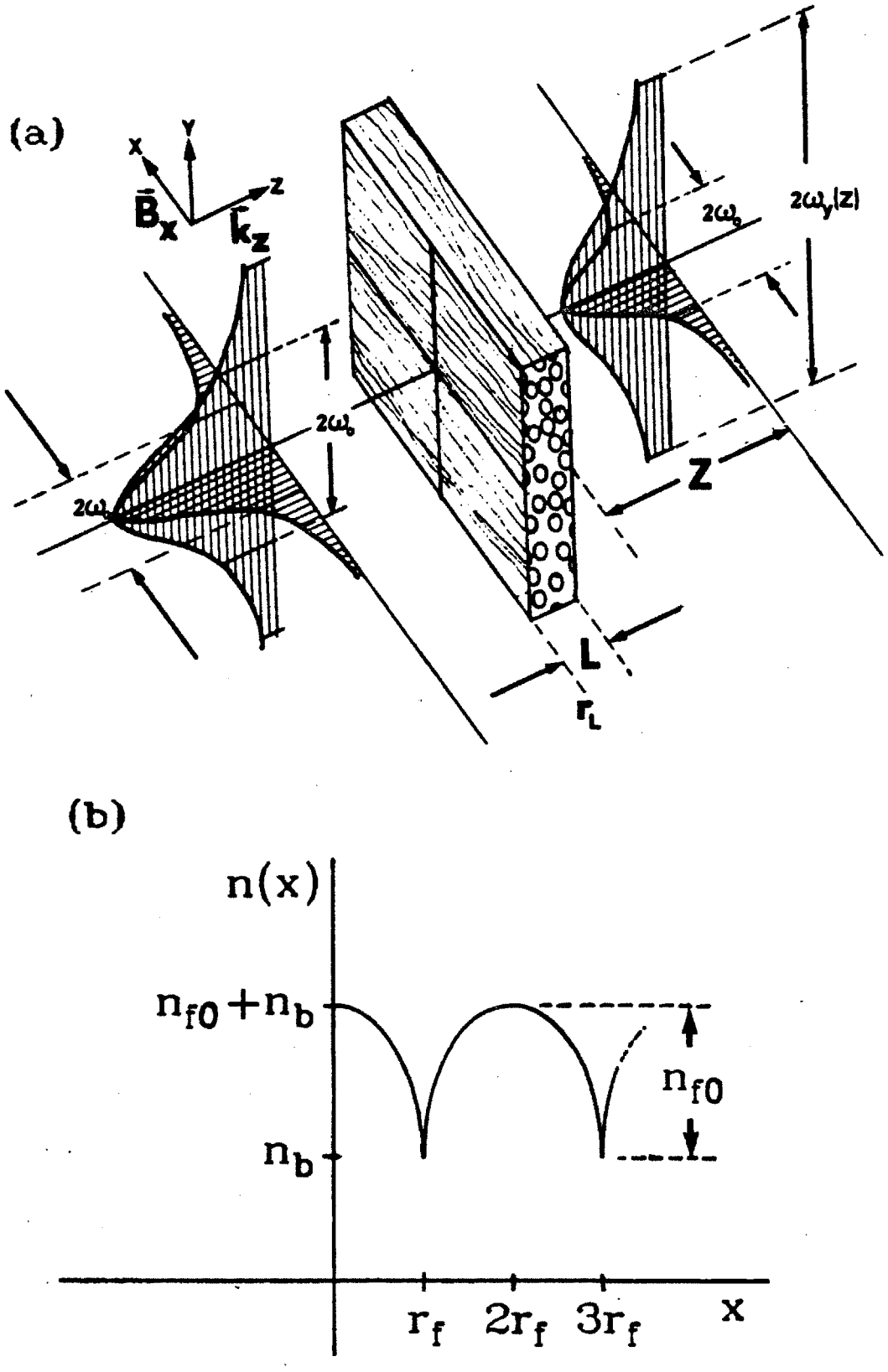

Figure 6.4 — Filamentary Refraction Model. (a) Scattering Geometry. The laser mode is incident on the layer from the left, and the waveguide is located a distance Z from the layer. (b) Parabolic Filament Model.

is taken to be $2(\tilde{n}/n)\bar{n}$, where $\bar{n}$ is the RMS density in the layer and $(\tilde{n}/n)$ is the experimentally measured fluctuation half amplitude. By requiring that density be conserved throughout the fluctuation, we may obtain n_b, but this quantity is not required in the scattering calculation.

The refraction by a single filament is again described using the formalism of Shmoys detailed in section 6.1. We average $\theta(b)$ over impact parameter b to obtain the root mean square average forward scattering angle for a single parabolic density filament, $\theta_{\rm rms} \equiv \sqrt{\bar{\theta}^2}$. The result for a parabolic density profile is $\theta_{\rm rms} = .73\ V_0$, where V_0 depends only on the peak density of the filament in the layer but not its size.

For the present case, a complication arises in the fact that the parabolic density component of peak density n_{f0} is immersed in a uniform background plasma of density n_b. On an intuitive basis one would expect that a uniform surrounding medium would have little effect on the refraction. By considering the transformation properties of the refractive index in the scalar wave equation one may show when this is indeed the case.[54] The scalar wave equation considered by Shmoys is of the form[49]

$$\left[\nabla^2 + \frac{\omega^2}{c^2} N^2(x)\right]\psi = 0.$$

We consider the O mode, for simplicity, but the principles which follow apply to X mode dispersion as well, which differs only slightly from the O mode in the present case. We express the refractive index squared as a sum of constant and spatially varying parts,

$$N^2(x) \equiv \left(1 - \frac{\omega_p^2[n_b]}{\omega^2}\right) + \left(-\frac{\omega_p^2[n_f(x)]}{\omega^2}\right) \equiv N_b^2 + \Delta(x)\ .$$

We transform the spatial coordinate with $x' = N_b x$, and write

$$\left[\nabla'^2 + \frac{\omega^2}{c^2}\left(1 + \frac{\Delta(x')}{N_b^2}\right)\right]\psi = 0.$$

Upon examination of the equations with and without a uniform background one finds the transformation of the refractive index

$$N^2 \Leftrightarrow \left(1 + \frac{\Delta(x')}{N_b^2}\right)$$

from which

$$\omega_p^2[n_f(x)] \Leftrightarrow \frac{1}{N_b^2}\omega_p^2[n_f(N_b x)] \ .$$

Since the average scattering angle is independent of the spatial scale, we may write, for the RMS scattering angle,

$$\theta_{\rm rms} \Rightarrow .73\frac{V_0(n_{f0})}{N_b^2} \ .$$

Thus, the presence of a constant background introduces a factor of

$$\left(1 - \frac{\omega_p^2[n_b]}{\omega^2}\right)^{-1}$$

as compared to the zero background result, a correction of 1% or less in the present case.

The refractive properties of a single filament are illustrated in figure 6.5, where the scattering angle is plotted versus normalized impact parameter b/r_f for a peak density of $n_{f0} = .8 \times 10^{14}$ cm^{-3}. For this case we find that $\theta_{\rm rms} = 8.1$ mrad.

We model the transport of the beam as a random walk through the filamentary layer. The toroidal filaments scatter the rays randomly in one dimension with a Gaussian distribution of angular standard deviation σ and $1/e$ angular width $\sqrt{2}\sigma$. The angle σ is given by the square root of the number of encounters in the layer, $\sqrt{L/2r_f}$, times the root mean square scattering angle for a filament, $\theta_{\rm rms}$. The final profile width at the waveguide is given by a convolution of the original Gaussian field distribution, and the scattered field distribution of spatial width $[(\sqrt{2}\sigma)Z]$. The final transverse beam field width is thus[45]

$$\omega_y(Z) = \sqrt{\omega_0^2 + (\sqrt{2}\sigma Z)^2} = \sqrt{\omega_0^2 + \left(\frac{L}{r_f}\,\theta_{\rm rms}^2\, Z^2\right)}$$

We obtain the transmission of the broadened beam by integrating the elliptical Gaussian

$$I(x,y) = I_0 e^{-2\left(\frac{x}{\omega_0}\right)^2} e^{-2\left(\frac{y}{\omega_y(Z)}\right)^2}$$

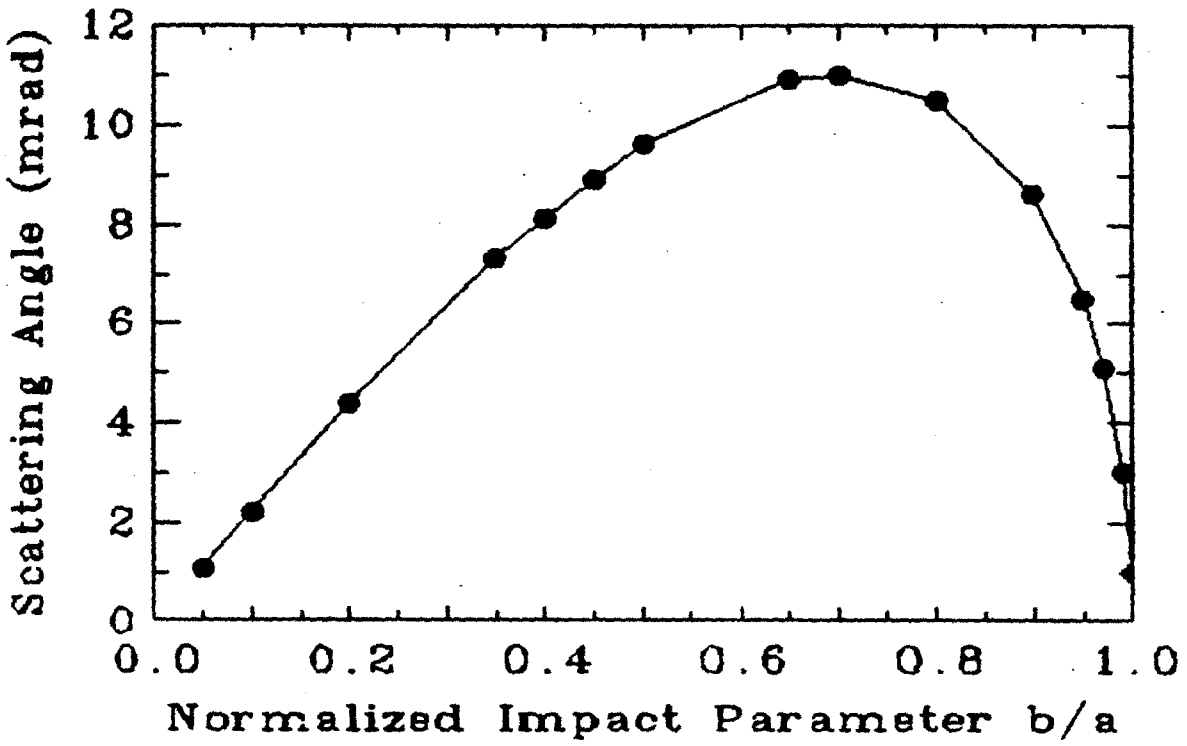

Figure 6.5 — X Mode Refraction Due to a Filament with a Parabolic Density Profile. $B_t = 6.4$ T, $n_{f0} = .8 \times 10^{14}$ cm^{-3}, $\lambda = 381\mu$m.

over the waveguide aperture of radius ρ. The resulting equations are as presented in the plasma refraction beam spreading calculation of section 6.1.

The above calculation is performed by Program TURBREF, which computes the final beam width and external transmission as a function of local edge density $\bar{n}$. The code requires input values of the central magnetic field, wavelength λ, fluctuation level $\tilde{n}/n$, correlation length l_{corr}, thickness of the filamentary region L, and distance from the filament layer edge to the waveguide Z.

The result of a TURBREF run is shown in figure 6.6, for $L = 1$ and 2 cm, $\tilde{n}/n = .25$ and .5, $B_t = 8$ T, and $\lambda = 381\mu$m. The electron density varies sharply in the edge region, ranging from approximately .5 to 5 $\times 10^{13}$ cm^{-3} at $r = 16.8$ cm to 10^{14} cm^{-3} or greater 1 to 2 cm inside the discharge, depending on the central density. The above calculation assumes a uniform density throughout the layer, and this is plotted in the figure. The value $l_{corr} = .13$ cm used in the calculation is a typical value for ALCATOR C,[55] estimated from the width of the k spectrum of edge fluctuations measured experimentally by CO_2 scattering.[56,57] The values of $\tilde{n}/n$ used are plausible for the large fluctuations which occur near the edge.[55] $L = 1$ to 2 cm is a thickness of the turbulent region which is consistent with CO_2 scattering data.[56,57] With the above choice of parameters, it is seen that attenuations of 15 percent can easily result from the filamentary refraction, for a variety of conditions.

The above computations comprise a geometrical ray optics description of the scattering interaction. This approach is most appropriate when the size of the scatterers is much larger than the wavelength of the incident radiation. Since for the present case of $\lambda \approx .04$ cm, and $l_{corr} = .13$ cm, one might be concerned about the effect that diffraction might have on the ray optics result. In the regime believed to be the domain of the current problem, $r_f/\lambda \geq 1$, the scattering is strongly forward peaked, and diffraction effects tend to increase the scattering somewhat over the geometrical optics result.[58] In experiments involving the scattering of Lower Hybrid waves by plasma edge density fluctuations, the predictions of ray optics and random walk calculations were evaluated and found to be within a factor of two of the experimental data[56] and detailed numerical studies,[59] for the case $\lambda_{perp}^{LH} \approx$

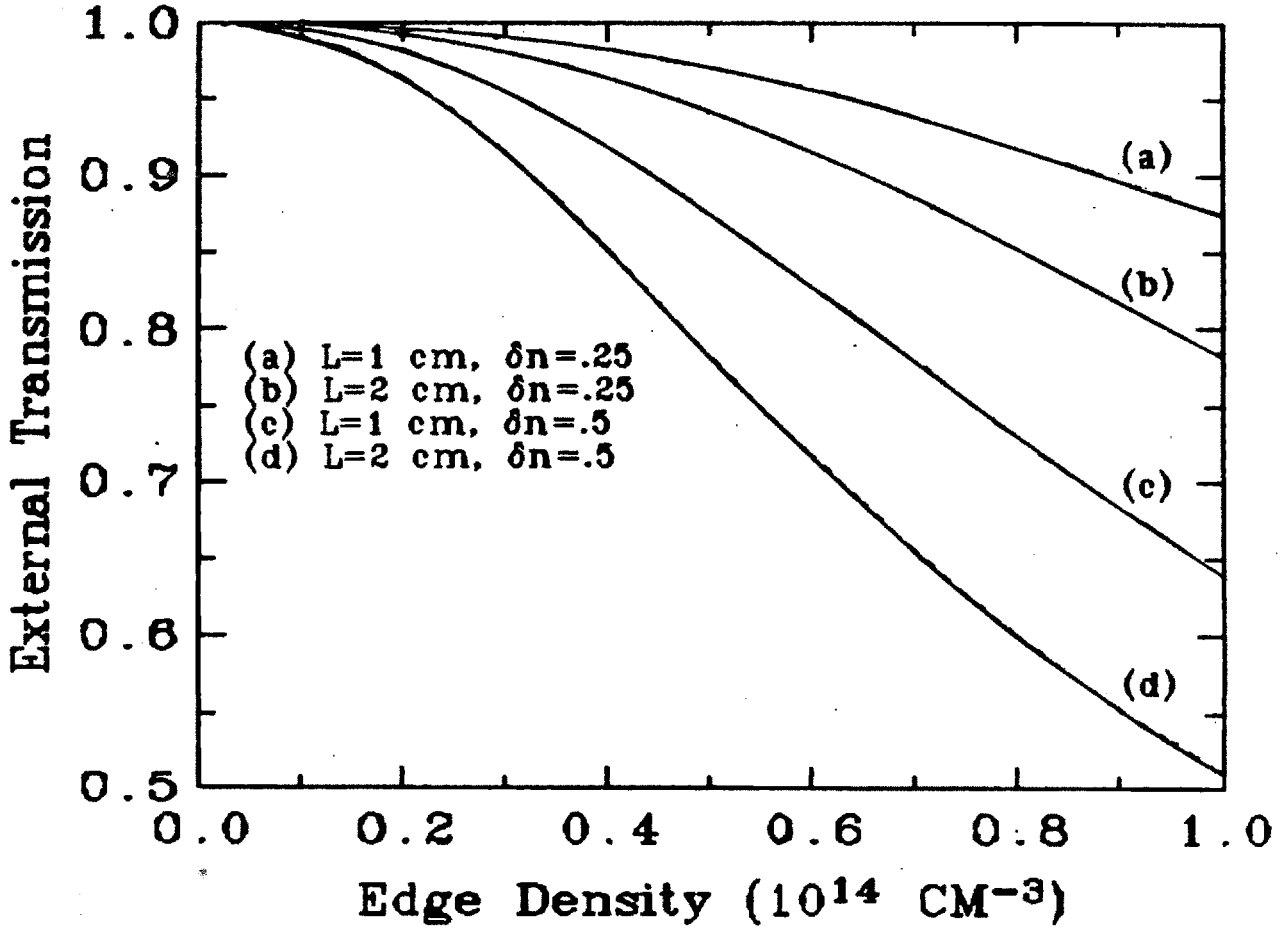

Figure 6.6 — External X Mode Transmission Through the Filamentary Layer Vs. Edge Density. $L = 1$ and 2 cm, $\delta n \equiv \tilde{n}/n = .25$ and .5, $B_t = 8$ T, $\lambda = 381\mu$m.

.07 cm, and l_{corr} = .2 cm. Similar numerical studies of wave scattering at the cyclotron frequency by large amplitude density fluctuations at the edge indicate that significant scattering may in fact occur.[60] The above simple exercise motivates on a macroscopic level the hypothesis that edge filamentation alone can give rise to a significant attenuation at the electron cyclotron harmonics, regardless of its origins.

However, we must still account for the density dynamics evident in the measured NRA data, or for the marked difference between the 1983 and 1985 data in figures 5.14 and 5.5. While the 1983 NRA data of figure 5.14 shows a 5 to 30% effect with strong central density dynamics, the 1985 NRA data of figure 5.5 shows a 0 to 10% effect which is largest at high densities, but reappears slightly at low densities. Although the dynamical structure of the effect remains to be explained, one cannot, a priori, rule out the possibility that edge fluctuations and the complex turbulent structures which they produce play some role in generating the NRA.

6.3 Comparison of the 1983 and 1985 Experiments

The two series of experiments which produced figures 5.5 and 5.14 contained numerous differences in both the experiment arrangement and in the Tokamak configuration. The observed difference in these figures is presumably attributable to some aspect of these physical differences, so that changes in both the experiment and the Tokamak must be considered.

The experience gained in the 1983 experiments suggested many improvements in the apparatus, and these were implemented in the 1985 experiments. In order to reduce the effects associated with mechanical vibrations and stray magnetic field pickup, the detector assembly was moved off of the Tokamak top. This necessitated that the length of external Copper waveguide running from the Tokamak vacuum window to the detector be increased from 6 to 16 ft, and that 3 miter joints be used instead of 2. The simple Fabry-Perot filter was replaced by a triple mesh filter which allowed a narrower bandwidth in emission, and a capacitive low pass filter was added. In the Reference channel, the pyroelectric detector used in the initial

experiments was replaced by an InSb detector similar to that used in the Transmission channel. It was also necessary to enclose the detectors and electronics in sealed metal cabinets to avoid a large RF pickup signal, a situation not encountered in the 1983 experiments. This is presumed to be in part due to the use of different electronics, replacement of the Reference pyroelectric detector, and relocation of the transmission detector to the top of the RF Klystron platform. The internal collection assembly, injection optics, and laser assembly remained exactly as in 1983.

The most obvious change in the Tokamak consisted of the use of uncoated and SiC coated Graphite limiters in 1983 and Molybdenum limiters in 1985. The use of Graphite in 1983 deposited a heavy coating of Carbon on the internal machine surfaces which recycled into the plasma discharges long after the Graphite limiters were removed. Thus, Tokamak operation appeared to remain characteristic of Carbon limiter operation throughout 1983. For the 1985 experiments, following 7 months of Tokamak operation with a Mo limiter and a period of continuous glow discharge cleaning, the salient aspects of Mo limiter operation were regained, although levels of Carbon line radiation from the plasma interior remained high. Although the complex interplay between limiter history and extant limiter configuration remains rather unclear, numerous differences have been documented for the Mo and C cases, individually. These differences are of greatest consequence in the context of Lower Hybrid RF injection, and are recounted briefly below.

RF Current Drive and Heating performance has shown a marked dependence on limiter material and limiter history. For Current Drive, the LHCD efficiency obtained is a sensitive indication of almost every aspect of Tokamak conditions. Lower LHCD efficiencies were obtained with Carbon limiters than with Molybdenum.[61] This observation is consistent with the possibility that the edge density and Z_{eff} may be higher with C limiters than with Mo, due to the large desorption of fuel gas and low Z materials observed to occur with C limiters. This enhanced recycling was manifest as an increased difficulty in stabilizing the Tokamak density with C limiters. A higher edge density would increase collisional damping of the Lower Hybrid

waves at the edge, while a higher Z_{eff} would dissipate the Current Drive tail energy more effectively. Either of these circumstances would act to reduce the overall Current Drive efficiency. Also, the absolute density fluctuation near the plasma edge may be linked to the local density, which determines the local gradients available to drive the turbulence. Fluctuations have been observed to peak nearer to the limiter with rising density, [55,57] and these fluctuations were found to adversely affect the coupling of the Lower Hybrid waves[56] at densities above 2×10^{14} cm^{-3}. Additional changes in the fluctuation spectrum were observed by Watterson in ALCATOR C for different limiter materials.[55]

Conversely, although a higher steady state Z_{eff} is typical for Carbon limiter discharges, spontaneous impurity injections during the RF pulse are necessarily of lower Z than for Molybdenum. This reduces the radiational cooling of the plasma interior during RF Heating, so that higher temperatures and heating efficiencies are obtained with Carbon than with Molybdenum limiters.[62] These considerations have been encountered previously in the interpretation of the RF Heating results presented in Chapter 5.

The above observations demonstrate that subtle but pervasive differences in the edge and outer plasma environment can be associated with a change in the limiter material. However, it remains to ascertain what combination of attributes characterize the operation of a Tokamak with a mixed history of limiter materials, as was the case during the 1985 experiments. Although it is unclear exactly what key parameters were affected between the 1983 and 1985 experiments, there are indications that something was in fact different. This is seen in the effect of a Marfe on the ECA signal in discharges from the two periods. The ability of a Marfe to scatter submillimeter radiation is one of the primary effects which characterize the phenomenon, as is the dependence of Marfe activity on density.[43,44]Figure 6.7 shows a 5.1 fringe shot from July, 1983, taken with SiC-Mo hybrid limiters, and figure 6.8 shows a 6 fringe shot from March, 1985, taken with Mo limiters. In figure 6.7, a vertical inside H_α view (trace b) shows the abrupt onset of a large Marfe at 175 msec, at which time a sharp decrease is evident on the raw $3\omega_c$ signal (trace a).

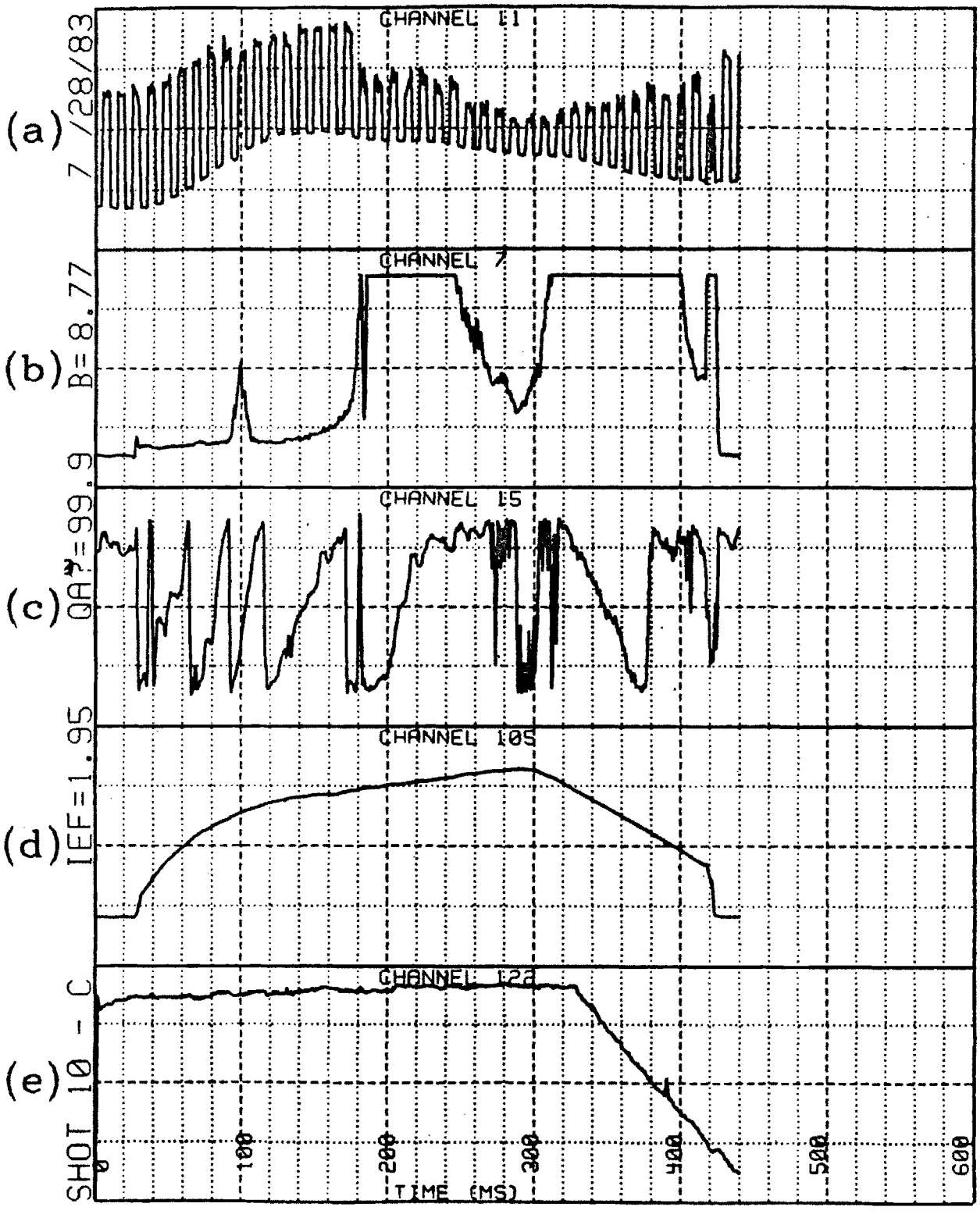

Figure 6.7 — Plasma Data From 1983 With SiC-Mo Hybrid Limiters. 7/28/83, Shot #10. Traces shown are (a) Raw $3\omega_c$ Transmission (b) H_α on F Port, Vertical Inside View (c) Central Density (d) Plasma Current, 1.5 V/div (e) Toroidal Field.

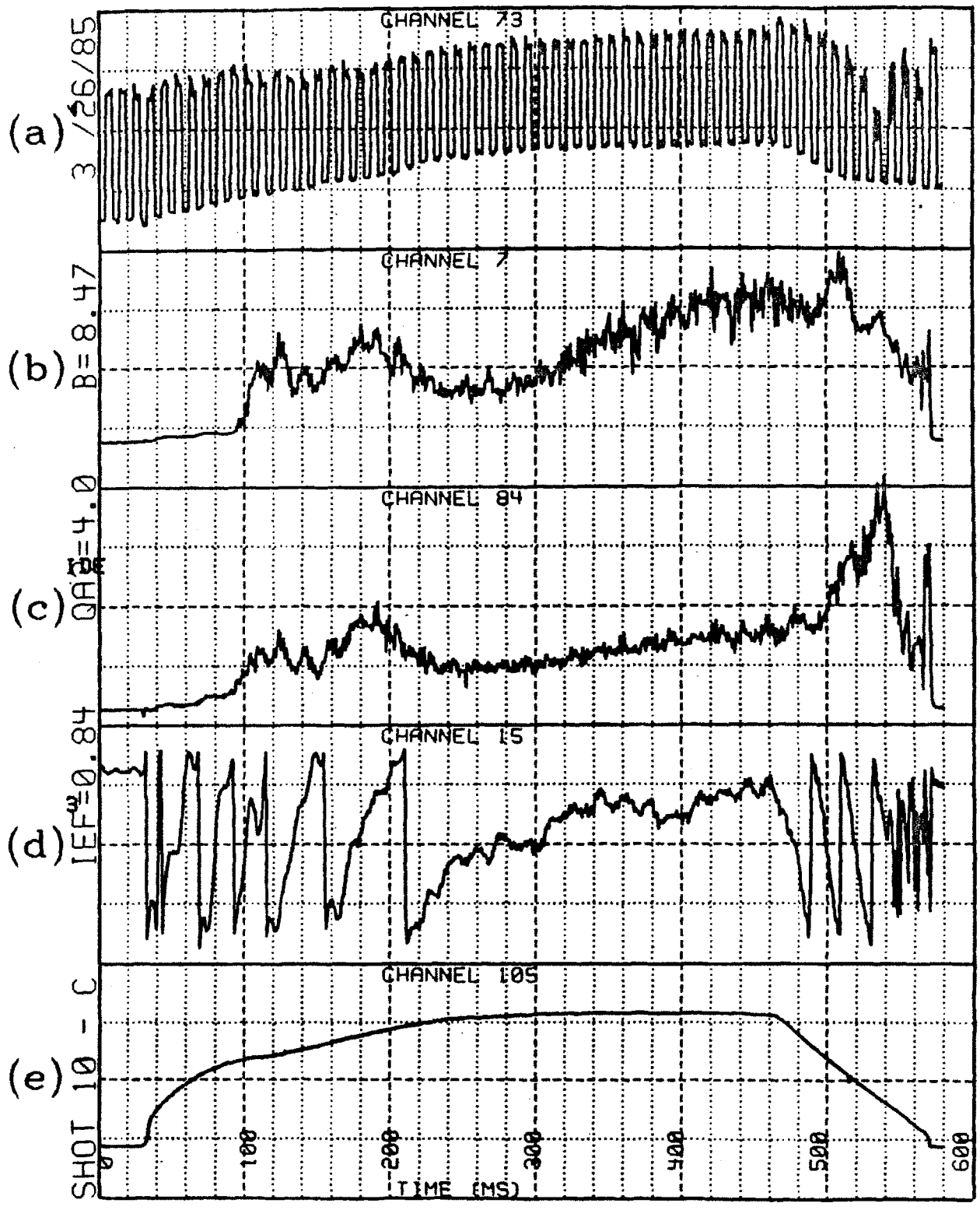

Figure 6.8 — Plasma Data From 1985 With Mo Limiters. 3/26/85, Shot #10. Traces shown are (a) Raw $3\omega_c$ Transmission (b) H_α on B Port, Vertical Inside View (c) H_α on B Port, Horizontal Midplane View (d) Central Density (e) Plasma Current, 1.5 V/div.

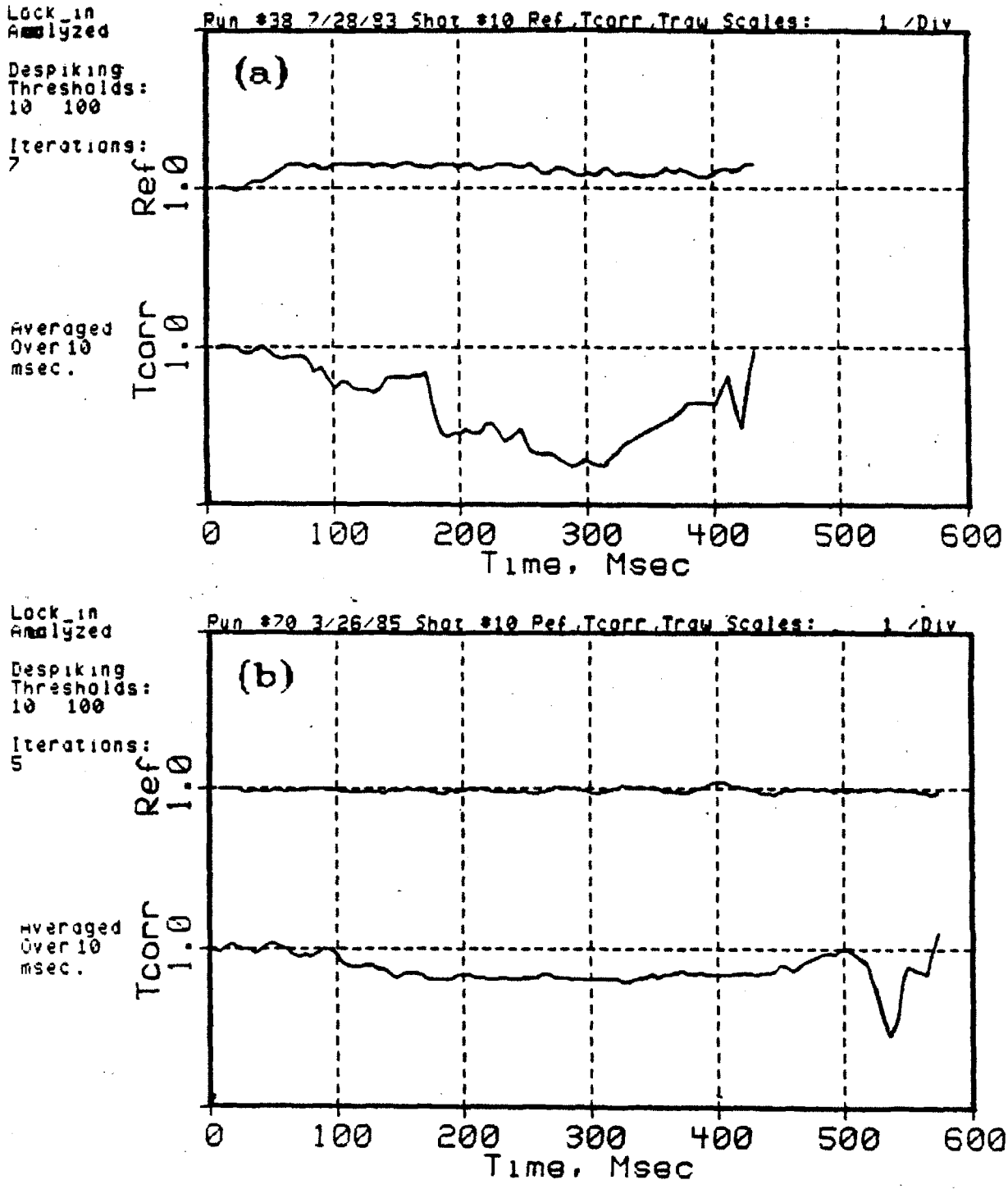

Figure 6.9 — $3\omega_c$ X Mode Transmission During a Marfe at High Density Vs. Time. 1.0/div, (a) 7/28/83, Shot #10 (b) 3/26/85, Shot #10.

In figure 6.8, vertical inside and horizontal midplane views of the H_α signal (traces b and c) show heavy Marfeing throughout the shot, but a minimal effect is seen on the $3\omega_c$ trace. The transmission during these shots is shown in figure 6.9. The 1983 trace shows a minimum transmission of 25% during the Marfe, while the 1985 trace shows a transmission which is unaffected by the Marfe, even at the higher density.

The obvious effect on the ECA signal in figures 6.7 and 6.9 was typical of Marfe behavior in 1983, whereas in 1985, the effect of the Marfe appeared to be related to other plasma parameters. This is demonstrated in figure 5.18, where similar Marfeing discharges have a quite different ECA effect at 7 and 9 Tesla at low densities, and in figure 5.5, where Marfeing is seen to have a variable effect on the transmission at high densities. These differences may be due to variations in the structure, size, or position of the Marfe, or all three factors.

The observed experimental differences between Carbon and Molybdenum limiter operation and in the Marfe effect between 1983 and 1985 suggest the hypothesis that the non-resonant attenuation of figures 5.14 and 5.5 is a manifestation of some fundamental plasma process which changed with Tokamak conditions over the period of time separating the two series of experiments. Unfortunately, due to the large spatial asymmetries which are known to exist in the edge plasma outside the limiter radius,[44] direct comparisons from experiment to experiment or from year to year are quite difficult to make. In addition, precious little data is available to document the active plasma region just inside the limiter, and to validate or subvert the above hypothesis. In this region, large radial density gradients exist and no parallel connection to the limiter is made by the field lines, and it is here that the turbulent dynamics, filamentation, and Marfes originate and have their strongest effect.

A related observation deserves mention due to its possible significance. In spatially resolved FIR scattering experiments on the TEXT tokamak, Brower, et al[63] have reported strong spatial asymmetries in the distribution of density fluctuations in the plasma interior. The broadband microturbulence was found to be four to ten times larger near the Tokamak top than anywhere else, concentrated in a region

at or inside the limiter radius and near the plasma $r = 0$ centerline. The sense of this vertical asymmetry was found to reverse with the direction of the plasma current. In addition, a horizontal scan revealed a concentration of strong narrowband fluctuations located near the plasma inside edge lying on the toroidal midplane for $r/a < -.6$. This observation was attributed to the presence of a locally quasi-coherent mode in the plasma interior.[64] The experimentally measured dispersion of the density fluctuations associated with this mode agrees well with linear drift wave theory, yielding a phase velocity approximately equal to the electron diamagnetic drift velocity. On ALCATOR C, CO_2 laser crossed beam correlation measurements detected a similar vertical asymmetry in the broadband fluctuations only during or prior to the onset of Marfe activity, when a strong peak is measured at the machine top.[55] The DENSEPACK experiments found no such poloidal variation of the fluctuations in the limiter shadow, for radii $r > 16.8$ cm, an indication that if present, the effect is confined to the plasma interior.

These observations have strong implications regarding the question of scattering of cyclotron harmonic radiation. If large asymmetries are possible in the fluctuation levels inside the limiter radius, and if these fluctuations can be partially coherent due to the presence of a specific mode, then small variations in the position, structure, or strength of the active region could have a disproportionately large influence on the locally observed scattering. The location of quasi-coherent region found in TEXT would lie directly in front of the ECA waveguide aperture, and a mode of this type could scatter submillimeter radiation many times more efficiently than a purely turbulent spectrum.

The possibility remains that the complicated transmission characteristics of the overmoded waveguide collection system is somehow involved in the observation of the NRA and its apparent change over time. The marked and reproducible density dependence shown in figure 5.14 immediately rules out the possibility that the NRA is an artifact of entirely instrumental origin. Also, the resemblance between the 3 regime density behavior of figures 5.14 and 5.5 and the effect of density fluctuations on Lower Hybrid waves reported by Surko and Slusher in Alcator A[56] suggest that

a serious consideration of the effect on physical terms may be warranted. It is, however, conceivable that the NRA as observed arises from an instrumental sensitivity to a genuine physical effect. If this sensitivity were to change due to an alteration of the radiation transport, filtering, or detection apparatus, then the observed response to the physical effect may be expected to change as well. This conjecture is somewhat difficult to substantiate, in light of the apparent constancy and reproducibility of the NRA effect independent of instrumental factors such as alignment, optical filtering, or noise, or of the inevitable variation in the machine operating characteristics over the days, weeks and months of the two series of experiments. Nevertheless, the complex instrumental attributes of the experiment should be cited as a factor of possible significance.

The observation of a strong non-resonant attenuation at frequencies as high as $3\omega_c$ and its scaling with line averaged density may be of considerable import in the design and upscaling of key auxiliary Heating, Current Drive, or diagnostic systems to high density regimes. The existence of an NRA could renders such projections non-trivial, and may demand that the performance of key systems be verified experimentally as progressively higher parameter ranges become accessible in contemporary and next generation devices.

In any event, the seemingly boundless detail and the scarcity of unambiguous data bearing on the problem conspire to dictate that a definitive explanation of the non-resonant attenuation await future investigations.

6.4 Chapter Summary

In this chapter it was shown that structural constraints arising from the experiment geometry preclude the possibility of a significant attenuation arising from plasma refraction alone.

Regarding the possible effect of turbulent edge filamentation on the cyclotron harmonic transmission, a heuristic random walk ray optics model attempted to treat the phenomenon on a purely macroscopic basis. Using this model, attenuations of up to 50% were obtained for various values of the edge density, fluctuation level,

and turbulent layer thickness. These observations suggests the possibility that the NRA may occur at the edge, and thus may be of general relevance to Tokamak operation in the high density regime. Changes in the experiment instrumentation over the period of the experiments were largely superficial, and cannot be related to observed changes in the NRA in an obvious manner. The evolution of the Tokamak conditions, however, were complex, due to changes in the limiter material, and not entirely known. These factors were shown to have a profound effect on the Tokamak operation. Several additional possibilities were identified which may have some bearing on the origins of the non-resonant attenuation, but these require independent investigation. Although no definitive identification of the NRA can be made based on the data which is currently available, the observations made in this work provide valuable empirical information about the effect, of possible relevance to the design of future experiments and devices.

Chapter 7

SUMMARY AND CONCLUSIONS

This chapter recapitulates the thesis' highlights and salient results. The final section contains numerous conclusions which may be drawn from these results, along with recommendations which may be of relevance to future undertakings in this area.

7.1 Thesis Summary

7.1.1 Introduction

In this work, the unique plasma diagnostic capabilities offered by cyclotron harmonic absorption in a hot, dense Tokamak plasma were suggested, developed, and demonstrated. An experimental study of Extraordinary mode transmission at the second and third electron cyclotron harmonic frequencies was performed, in which a narrow beam of laser radiation was used to illuminate the plasma and provide a continuous measurement of the transmission. Tasks which were set forth and accomplished in the course of this work are:

- The experimental investigation of ECR harmonic absorption under conditions of high density, temperature, and magnetic field;
- An evaluation of theoretical descriptions of cyclotron absorption in an extended parameter range;
- The experimental investigation of ECR harmonic absorption during Lower Hybrid RF Heating and Current Drive, in the presence of suprathermal electron components;
- Proof-of-principle applications of ECR harmonic absorption measurements as a bulk plasma electron temperature diagnostic which remains valid during RF injection;
- Investigation of other effects which are relevant to the propagation of high frequency radiation in a high density, high temperature Tokamak plasma.

The current work represents a simultaneous advance in the magnetic field, density, and temperature regimes studied, and for the first time, the absorption at $3\omega_c$ was measured. The ranges of density, temperature, and frequency investigated approach those expected for future high field ignition devices, under a variety of reactor relevant conditions, such as during RF Heating and Current Drive.

7.1.2 Theoretical Aspects of the Experiment

The cold plasma formulation provides a description of the fundamental modes which propagate perpendicular to the external magnetic field. These are the Extraordinary mode, with $\mathbf{E} \perp \mathbf{B}$, and the Ordinary mode, with $\mathbf{E} \parallel \mathbf{B}$. For the range of central plasma parameters studied in this work, the cold plasma cutoff and resonance frequencies lie below 1.6 ω_c, and are not encountered in the harmonic transmission measurements. Furthermore, no absorption appears at the cyclotron harmonics in the cold plasma limit.

Although the general problem of ECR absorption and emission is quite complex, division of the problem along physical lines allows a particular solution to be sought for the specific case of interest. The frequency, propagation angle, and polarization of the radiation play a fundamental role in this respect. In addition, finite temperature, finite density, and relativistic effects can determine the character of the absorption, and these must be retained to an order appropriate for each case considered.

When spatial variations are slow and the absorption is weak, the Equation of Transfer provides a compact description of the radiation transport in terms of the optical depth $\tau \equiv -\int \alpha_\omega(\mathbf{s})ds$. This quantity relates the theoretical absorption coefficient, $\alpha_\omega(\mathbf{s})$, and the transmission, $\mathbf{T} \equiv e^{-\tau}$, which is the principle experimentally measured quantity of this work.

In the weakly relativistic regime of the present work, a series representation of the dielectric function leads to an explicit expression for the optical depth, in terms of measurable quantities. For the low temperature, quasi-tenuous, and quasi-perpendicular conditions of this work, lowest WKB and FLR order results were

found to be sufficient to describe absorption by a Maxwellian plasma for semi-opaque second and third harmonics. The X mode optical depth for a semi-opaque harmonic $n \geq 2$ was found to be directly related to the electron density, electron temperature, and magnetic field at the resonance location, via the factor $n_e T_e^{n-1}/B_t'$. This proportionality forms the basis for diagnosing the local plasma temperature by measuring the plasma transmission, given data on the density and magnetic field which are in general readily obtainable.

The physical principles governing the absorption were also found to determine performance characteristics of a plasma diagnostic scheme. Under the conditions of the present experiment, an unambiguous position-frequency correspondence exists, with a spatial resolution for absorption of 1 cm or less.

Due to the low densities of suprathermal components likely to develop in ALCATOR, and the strong relativistic downshift of the central harmonic resonance to frequencies which lie outside of the plasma, the transmission was theoretically found to be largely unaffected by these components. This circumstance would allow the transmission to be used as a bulk plasma temperature diagnostic during RF injection.

7.1.3 Experiment Configuration and Components

The transmission experiment required a direct, continuous observation of the plasma transmission. Because of the high frequencies involved, it was necessary to construct an optically pumped far-infrared waveguide laser system to produce radiation in the 700 GHz range. Molecular laser lines in Formic acid, HCOOH, and its deuterated analog DCOOD were used which produced powers at the 10 mW level at the laser. A novel FIR laser design involved the use of a suspended weight to counterbalance the atmospheric force acting on the output coupler, which also served as the vacuum window.

The probe radiation was transported from the laser to the Tokamak in free space as a Gaussian beam, and was focused to a 1.2 cm diameter spot at the far side of the plasma. The transmitted beam was collected by a 1.4 cm diameter steel

waveguide assembly, which conducted the radiation out of the Tokamak. From the device, the radiation was led in circular Copper waveguide to the InSb photoconductive detector. The collected radiation, which included the plasma emission, was filtered by a triple metal mesh Fabry-Perot filter and a commercial low pass filter prior to detection. The filters passed a band of approximately 50 GHz about the laser frequency, which allowed third harmonic emission to be received from the central 5 cm region of the plasma. Data produced by the experiment was digitized at 5 kHz, and archived by the VAX 11/780 computer.

The high working frequency and restricted diagnostic access conditions of the experiment represent a novel application of overmoded waveguide propagation. The high transmissions measured for the various waveguide assemblies result from the relatively low losses for the characteristic modes of the overmoded circular metallic waveguide.

7.1.4 Data Reduction, Analysis, and Interpretation

The FIR probe beam was chopped at 100 Hz to differentiate it from the more slowly varying plasma emission background present in the transmission signal. A portion of the beam was diverted at the laser to a power monitor, which provided a power reference signal. With this data, changes in the laser power were divided out of the raw transmission, and absolute plasma transmissions were obtained. The reduction of raw data was performed by Program LOCKIN, a digital boxcar analyzer routine, which processed the data and generated plots of absolute transmission versus time.

Diagnostic analysis of the reduced transmission data was performed by Program HTAU. Exploiting the $n_e T_e^{n-1}/B_t'$ dependence of the cyclotron harmonic absorption, the measured absolute transmission data was unfolded to provide diagnostic information regarding the plasma electron temperature. Furthermore, with harmonic emission data which was simultaneously collected in the experiment, information about the radiation temperature was deduced.

Each of the three experimentally measured parameters n_e, B_t, and T which enter the electron temperature analysis introduces an uncertainty in the temperature which results. The propagation of these uncertainties depends specifically on the role each parameter plays in the absorption process. The overall temperature uncertainties in the regime of this work are in the 10% to 21% range for measurements in the interior plasma region $r < 12$ cm, and in the 50% to 100% range for the edge temperature measurements.

The above considerations also determine the range of applicability of the experimental technique, which is limited by a deteriorating accuracy at low density and temperature, and by interference from Marfes at high density. Routine ALCATOR C discharges lie in an optimal region of temperature diagnostic parameter space for the applications considered in this work.

A non-resonant attenuation was observed in the course of this work which, when present, must be divided out of the transmission prior to temperature analysis. For third harmonic measurements, this additional analysis can in some cases increase the above temperature uncertainties by 40%.

7.1.5 Plasma Diagnostic Results

The diagnostic value of X mode cyclotron harmonic transmission measurements has been demonstrated in a variety of applications. Experimental transmission data for the third harmonic at the plasma center agrees with lowest significant finite density and FLR order theoretical results, and follows the $n_e T_e^2/B_t'$ scaling from 1 to 12×10^{15} [cm^{-3} keV^2/(Tesla/cm)]. Data in the range $.6 \leq n_e(10^{14}\mathrm{cm}^{-3}) \leq 3.1$ and $1.5 \leq T_e(\mathrm{keV}) \leq 3.3$ have been included, under Ohmic or Lower Hybrid RF Heating and Current Drive operation. No additional absorption was found during Lower Hybrid Current Drive, in agreement with theoretical predictions. The radiation temperature, however, did show a large increase during RF injection. Electron temperatures obtained with the ECA transmission technique were in agreement with those reported by Ruby laser Thomson scattering and second harmonic ECE

temperature diagnostics in the aformentioned parameter range. In addition, a temperature of 75 eV has been directly measured at $r = -15$ cm using the ECA technique. The above performance confirms the validity and versatility of the ECA transmission temperature diagnostic technique for high temperature and high density Tokamak plasmas.

Observations have also been made of MHD related phenomena. Sawteeth and m= 1 activity were observed on the raw third harmonic transmission signal. These behaved in the expected manner, and were well correlated with other diagnostics of MHD activity.

A correction for the non-resonant attenuation was successfully applied in the analysis of temperature data. The non-resonant attenuation was found to depend on the maximum density reached during a shot, but to be relatively insensitive to the temporal evolution of central plasma parameters. Methods of obtaining an NRA correction factor include monitoring the transmission of a non-resonant laser line, lowering the magnetic field by 10% to move the resonance to a plasma region where near unity transmission is expected, and comparisons with other temperature diagnostic data. The NRA did change considerably between the 1983 and 1985 experiments, and account was taken of this fact in the analysis of data from the two periods.

7.1.6 Interpreting the Non-Resonant Attenuation

Due to physical constraints which arise from the restricted diagnostic access of ALCATOR and the experiment geometry, the ECA probe beam was constrained to lie within 1 cm of the plasma center. In this configuration refraction effects due to beam spreading and shifting are estimated to be a few percent at the highest density studied in this work, and to diminish rapidly at lower densities. This circumstance precludes the possibility of a significant non-resonant attenuation arising due to plasma refraction alone.

To estimate the effect of turbulent edge filamentation on the cyclotron harmonic transmission, a heuristic random walk ray optics model attempted to treat the effect

on a purely macroscopic basis. Using this model, attenuations of up to 50% were obtained for various values of the edge density, fluctuation level, and turbulent layer thickness. These observations suggests the possibility that the NRA may occur at the edge, and thus may be of general relevance to Tokamak operation in the high density regime.

The data on which this work is based was obtained in two series of experiments performed in May through August, 1983, and February through March, 1985. Changes in the experiment instrumentation between the two periods primarily consisted of the relocation of the transmission detector away from the Tokamak, and improved frequency filtering of the collected radiation. The instrumental changes were largely superficial, and cannot be related to observed changes in the NRA in an obvious manner. The evolution of the Tokamak conditions between the two periods was complicated by the use of Carbon limiters in 1983, and Molybdenum limiters in 1985, and the effects of this are not entirely known. The limiter material was found to have a profound influence on Tokamak operation and on the performance of RF Heating and Current Drive. A dramatic change was also noted in the effect of large Marfes on the ECA signal for the two series of experiments. These observations suggest that a change in the Tokamak edge environment occurred which may also be responsible for the observed change in the magnitude and character of the NRA.

Several additional possibilities were identified which may have some bearing on the non-resonant attenuation. These include the observation of asymmetries in the fluctuation levels of the outer plasma and limiter shadow regions on ALCATOR, and the observation of a region of quasi-coherent fluctuations on TEXT. The existence of regions of enhanced turbulence or partially coherent fluctuations could greatly affect the submillimeter wave transmission.

Because of the complexity of the problem and the lack of unambiguous data with which to formulate a clear interpretation, no definitive identification of the NRA can be made at this time. Rather, the observations made in this work are of qualitative, empirical value, and bear further investigation.

The observation of a strong non-resonant attenuation at frequencies as high as $3\omega_c$, and its scaling with electron density may be of considerable import in the design and upscaling of auxiliary plasma operation systems or diagnostic schemes to high density regimes. The existence of an NRA could renders such projections non-trivial, and may demand that the performance of key systems be verified experimentally as progressively higher parameter ranges become accessible in contemporary and next generation devices.

7.2 Conclusions

7.2.1 Electron Cyclotron Absorption (ECA) as a Plasma Diagnostic

Extraordinary mode transmission measurements at the semi-opaque second and third cyclotron harmonic frequencies are of unique diagnostic value for high temperature, high density Tokamak plasma research. With standard electron density and magnetic field data which is generally available in Tokamaks, the electron temperature can be obtained with an accuracy, spatial resolution and range which equals or surpasses the performance of existing temperature diagnostic techniques. Furthermore, with emission data which is concurrently available in the ECA measurements, the radiation temperature can be directly obtained.

The basic parameter scaling set forth in the extensive theoretical literature which describes X mode absorption at the cyclotron harmonics in the weakly relativistic quasi-perpendicular regime appears to be both qualitatively and quantitatively correct for the specific conditions of this experiment, to which lowest significant order WKB, FLR, and finite density descriptions apply. The fundamental physical principles governing the cyclotron absorption process endow the ECA diagnostic scheme with numerous unique attributes which make it complementary or superior to other temperature diagnostic methods. These include diagnostic capabilities which remain unaffected by a wide variety of generic Maxwellian class superthermal electron distributions, and performance which improves with increasing temperature. These characteristics make the ECA technique ideal for diagnosing

RF heated plasmas, and also qualify the ECA technique for use as a primary temperature diagnostic in future devices. Application of the technique at the third cyclotron harmonic using the Extraordinary mode minimizes the effects of plasma refraction which can become appreciable for lower harmonics at high plasma densities.

The ECA technique can also be applied to measure the local electron density, if temperature data is available, or local density-temperature products if neither density nor temperature are available. Where the second harmonic is semi-opaque, direct measurements of local plasma pressure may thus be obtained. This technique is particularly useful in measuring the local pressure near the plasma edge, where neither accurate density nor accurate temperature data is available. In addition, temperature or density related fine structure, such as sawtooth activity, can be monitored using the raw data.

7.2.2 Limitations of the ECA Technique

A number of limitations on the use of the ECA technique stem from the same physical and practical considerations which give the technique its usefulness. Implementation of the ECA temperature measurement technique is dependent on the existence and accuracy of electron density and magnetic field data. The accuracy of the temperature determination degrades rapidly for conditions of low density or temperature, due to the low absorption. Plasma variations on the modulation timescale or faster are averaged out in the analysis. The analysis routine itself is sensitive to transient noise such as bursting cyclotron harmonic emission produced by fast velocity space instabilities. These features make the temperature diagnostic technique difficult to apply to very tenuous or noisy plasmas, or to RF Current Driven plasmas, which are are generally both noisy and tenuous.

Furthermore, the appearance of Marfes at high densities provides an additional complication, and may preclude the use of the technique during solid pellet fueling, which frequently precipitates Marfe activity. Marfe conditions, however, are spatially localized and readily identified using standard Tokamak diagnostics, and are thus in principle readily avoided.

A remaining drawback lies in the possible existence of a non-resonant attenuation. Although it has been shown that the effect, when present, can be measured in a number of ways, and can be applied to the temperature analysis in a straightforward manner, its existence does complicate the implementation of the ECA diagnostic technique considerably. A significant non-resonant attenuation in the high density Tokamak regime is likely to complicate the application of other plasma diagnostic and control schemes as well, such as RF Heating, Current Drive, or plasma scattering, in the Electron Cyclotron or Lower Hybrid frequency bands. This factor may be of some concern to those planning or designing future experiments and devices.

7.2.3 Recommendations for Future Work

The above considerations suggest the importance of conducting experiments to investigate the scattering of submillimeter radiation by density fluctuations in the active plasma edge region $.8 \leq r/a \leq 1.0$, specifically for the high density regime of this work. While FIR scattering experiments have been done in the past, these have been at lower density, where a significant non-resonant attenuation was not observed. In addition, submillimeter transmission provides a particularly sensitive, spatially resolved diagnostic for the study of Marfe and NRA effects.

In future temperature diagnostic applications, it is recommended that non-resonant attenuation characteristics be investigated in the regime, device, and geometry of interest, in order to determine the degree to which the effect will influence the diagnostic scheme. In cases where a significant NRA effect is found, capabilities should be developed early on to provide adequate correction data, using either the methods developed in this work, or simultaneous multiple frequency transmission, as suggested below. It is also of paramount importance to have adequate Marfe and edge plasma diagnostics located at the site of the optical path to clearly monitor these effects.

The development of Free Electron Laser and Gyrotron technologies hold the promise of revolutionizing submillimeter wave plasma applications. For use as a routine temperature diagnostic at a fixed frequency, these devices offer unsurpassed

power and reliability. For circumstances in which a non-resonant correction is required, multiple harmonic generation in a Free Electron Laser[65] or Gyrotron[8] could provide for the simultaneous production of resonant and non-resonant radiation with a single source. The harmonics would be separated following transmission, and simultaneous collinear resonant transmission and non-resonant correction data could thereby be obtained. Typical powers available from these devices are orders of magnitude larger than that required to accomplish the transmission measurements, so that the above scheme should be realizable with little difficulty, even if output power were to diminish considerably with increasing harmonic.

For more developmental studies or applications requiring operation with a wide range of frequencies, the optically pumped waveguide laser still provides unequaled versatility in wavelength selection and quality of the output probe beam. Complete optically pumped laser systems are at present commercially available, or a system may be custom designed for a specific application using commercial optical systems and components. If the custom design option is chosen, the counterweight scheme developed in this work is recommended for the FIR cavity. Care should be taken to insure CO_2 mode stability via laser system thermal stability and environmental isolation. For the large FIR laser cavities necessary to obtain high power operation, bakeable high vacuum construction would be a great asset to maintaining vacuum integrity and laser gas purity, and would facilitate gas switching or operation with costly laser gases. Swage or O ring type construction should be avoided wherever possible. For the study of plasmas with suprathermal components or nonthermal distributions, high powers would be useful in maintaining a high signal to noise ratio in noisy discharges which have a large cyclotron harmonic emission background.

For the larger confinement devices currently in operation or under design, diagnostic access is generally not a serious problem, and one or two pass Gaussian free space propagation should be used whenever possible. However, for circumstances which offer limited line of sight access, overmoded circular waveguide may be used to transport radiation in the submillimeter band for applications which do not require that polarization be preserved during the propagation. Under conditions of restricted access, waveguide propagation is quite versatile, and offers relatively high transmission even with numerous curves, angles, and bends.

REFERENCES

1. Trubnikov, B. A., *"Magnetic Emission of High Temperature Plasma"*, Thesis, Institute of Atomic Energy, Moscow, 1958; (English translation in USAEC Technical Information Service, Report AEC-tr-4073, June, 1960).

2. Drummond, W. E., Rosenbluth, M. N., *Phys. Fluids* **3**, (1960) 45 and 491.

3. Wharton, C. B., in *"Proc. 2nd Int. Conf. on Peaceful Uses of Atomic Energy"* **32**, (1958) 393, U.N., Geneva.

4. Engelmann, F., Curatolo, M., *Nuc. Fus.* **13**, (1973) 497.

5. Costley, A. E., Hastie, R. J., Paul, J. W. M., Chamberlain, J., *Phys. Rev. Lett.* **33** (1974) 758.

6. Alikaev, V. V., Bobrovskij, G. A., Poznyak, V. I., Razumova, K. A., Sannikov, V. V., Sokolov, Yu. A., Shmarin, A. A., *Sov. J. Plasma Phys.* **2** (1976) 212.

7. Colson, W. B., Sessler, A. M., *"Free Electron Lasers"* Larwrence Berkeley Laboratory Report number LBL-18905, University of California, Berkeley, California, January, 1985.

8. Byerly, J. L., Danly, B. G., Kreischer, K. E., Temkin, R. J., Mulligan, W. J., Woskoboinikow, P., *Int. J. Electronics* **57**,6 (1984) 1033. Also,
Danly, B. G., Mulligan, W. J., Temkin, R. J., Sollner, T. C. L. G., *Appl. Phys. Lett.* **46**,8 (1985) 728.

9. Arunasalam, V., Meservey, E. B., Gurnee, M. N., Davidson, R. C., *Phys. Fluids* **11**,5 (1968) 1076.

10. Efthimion, P. C., Arunasalam, V., Hosea, J. C., Princeton Plasma Physics Laboratory Report PPPL-1607 November, 1979, Princeton, New Jersey.

11. McDermott, F. S., *"Experimental Studies of Thermal and Non-thermal Electron Cyclotron Phenomena in Tokamaks"*, Thesis, Department of Physics, Massachusetts Institute of Technology, Cambridge, Massachusetts, December, 1984.

12. Mazzucato, E., Efthimion, P., Fidone, I., *Nuc. Fus.* **25**,11 (1985) 1681.

13. Pachtman, A., Gandy, R., Wolfe, S. M., *Bull. Am. Phys. Soc.* **28**,8 (1983) 1249; Pachtman, A., Wolfe, S. M., *Bull. Am. Phys. Soc.* **29**,8 (1984) 1223; Pachtman, A., Wolfe, S. M., *Bull. Am. Phys. Soc.* **30**,9 (1985) 1496.

14. Weggel, C., Hamburger, W., Montgomery, B., Pierce, N. *Engineering Problems of Fusion Research* **1**, October, 1977.

15. Bekefi, G., *"Radiation Processes in Plasmas"* John Wiley and Sons, 1966.

16. Bornatici, M., Cano, R., De Barbieri, O., Engelmann, F., *Nuc. Fus.* **23**,9 (1983) 1153, and references therein (this is a monumental review paper on Electron Cyclotron emission and absorption, with an extensive bibliography).

17. Trubnikov, B. A., *"Plasma Physics and the Problem of Thermonuclear Reactions"* **3**, (1959) 122, Leontovich, M. A., Editor, Pergamon Press, London.

18. Shkarovsky, I. P., *Phys. Fluids* **9**, (1966) 561 and 570.

19. Abramowitz, M., Stegun, I. A., *"Handbook of Mathematical Functions"*, page 258. U.S. Department of Commerce, National Bureau of Standards, June, 1964.

20. Hutchinson, I. H., *Plas. Phys.* **21**, (1979) 1043.

21. Propietary versions of the OPAKE2 and ECSORB codes were kindly made available by their author, Dr. Stephen Tamor, for use in the present work.

22. Tamor, S., *Nucl. Fus.* **18** (1978) 229.

23. Tamor, S., *Nucl. Fus.* **19**,4 (1979) 455.

24. Tamor, S., Science Applications, Inc. report SAI-023-82-230LJ La Jolla, California, August, 1982.

25. Mansfield, D. K., Semet, A., Johnson, L. C., *Appl. Phys. Lett.* **37**,8 (1980) 688.

26. Hodges, D. T., Foote, F. B., Reel, R. D., *Appl. Phys. Lett.* **29** (1976) 662.

27. Wagner, R. J., Zelano, A. J., Ngai, L. H., *Opt. Commun.* **8**,1 (1973) 46.

28. Deldalle, A., Dangoisse, D., Splingard, J. P., Bellet, J., *Opt. Commun.* **22**,3 (1977) 333.

29. Foote, F. B., Hodges, D. T., Dyson, H. B., *Int. J. Infrared mm Waves* **2**,4 (1981) 773.

30. Fecteau, M. L., *SPIE* Vol. 259 *Millimeter Optics* (1980) 31.

31. Abrams, R. L., *IEEE J. Q. E.* Vol. **QE-8**,11 (1972) 838.

32. Crenn, J. P., Association Euratom-CEA Sur La Fusion, Report EUR-CEA-FC-924, Fontenay-Aux-Roses, France, 1978.

33. Loewenstein, E. V., Newell, D. C., *J. Opt. Soc. Am.* **59**,4 (1969) 407.

34. Lee, C. S., Lee, S. W., Chuang, S. L., *IEEE Trans. Micro. Th. Techn.* Vol. **MTT-34**,3 (1985) 271.

35. Wood, R. A., Brignall, N., Pidgeon, C. R., Al-Berkdar, F., *Infrared Phys.* **16** (1976) 201.

36. Birch, J. R., Dromey, J. D., Lesurf, J., *Infrared Phys.* **21** (1981) 225.

37. Smith, D. R., Loewenstein, E. V., *Appl. Opt.* **14**,10 (1975) 2473.

38. Russel, E. E., Bell, E. E., *J. Opt. Soc. Am.* **57** (1967) 341.

39. Baker, E. A. M., Walker, B., *J. Phys. E: Sci. Instrum.* **15** (1982) 25.

40. Scanning Michelson spectra were kindly provided by Mr. Kosuke Kato. The instrument is described in: Hutchinson, I. H., Kissel, S. E., *"Proc. Fourth Int. Conf. on Infrared and mm Waves and their Applications"*, Miami Beach, Florida (1979) 76.

41. Hammer, J. M., *IEEE J. Q. E.* Vol. **QE-20**,11 (1984) 1252. A typographical error occurs on page 1254: the last two equations in (14) should have plus signs instead of minus.

42. Kissel, S. E., *"Thermal and Non-thermal Submillimeter Emission From ALCATOR Tokamak"* Thesis, Department of Physics, Massachusetts Institute of Technology, Cambridge, Massachusetts, June, 1982.

43. Lipshultz, B., LaBombard, B., Marmar, E. S., Pickrell, M. M., Terry, J. L., Watterson, R., Wolfe, S. M., *Nuc. Fus.* **24** (1984) 977.

44. LaBombard, B., *"Poloidal Asymmetries in the Limiter Shadow Plasma of the ALCATOR C Tokamak"* Thesis, Department of Nuclear Engineering, Massachusetts Institute of Technology, Cambridge, Massachusetts, April, 1986.

45. Bevington, P. R., *"Data Reduction and Error Analysis for the Physical Sciences"* McGraw-Hill, Inc., 1969.

46. Hutchinson, I. H., Komm, D. S., *Nuc. Fus.* **17**,5 (1977) 1077.

47. Granetz, R. S., Camacho, J. F., *Nuc. Fus.* **25**,6 (1985) 727.

48. Parker, J. K., *"Density Fluctuations Following Fuel Pellet Injection on the ALCATOR C Tokamak"*, Thesis, Department of Physics, Massachusetts Institute of Technology, Cambridge, Massachusetts, May, 1985.

49. Shmoys, J., *J. of Appl. Phys.* **32**,4 (1961) 689.

50. International Mathematical and Statistical Libraries, Inc., *"The IMSL Libraries"*, Vol. 3, Edition 9.2, Houston, Texas, November, 1984.

51. Liewer, P. C., *Nuc. Fus.* **25**,5 (1985) 543 and references therein. This is a thorough review of Tokamak turbulence theory and experiments.

52. Zweben, S. J., McChesney, J., Gould, R. W., *Nuc. Fus.* **23**,6 (1983) 825.

53. Goodall, D. H. J., *J. Nucl. Mater.* **111** (1982) 11.

54. Hutchinson, I. H., private communication, Massachusetts Institute of Technology, Plasma Fusion Center, August 1, 1986.

55. Watterson, R. L., Slusher, R. E., Surko, C. M., *"Low Frequency Density Fluctuations in the ALCATOR C Tokamak"*, MIT Plasma Fusion Center Report PFC/JA-85-7, Cambridge, Massachusetts, February, 1985.

56. Slusher, R. E., Surko, C. M., Schuss, J. J., Parker, R. R., Hutchinson, I. H., Overskei, D., Scaturro, L. S., *Phys. Fluids* **25**,3 (1982) 457.

57. Slusher, R. E., Surko, C. M., *Phys. Rev. Lett.* **40**,6 (1978) 400.

58. Born, M., Wolf, E., *"Principles of Optics"*, Pergamon Press, Oxford, 1970, page 662.

59. Bonoli, P. T., Ott, E., *Phys. Fluids* **25** (1982) 359.

60. Hui, B., Ott, E., Bonoli, P. T., Guzdar, P. N., *Nuc. Fus.* **21**,3 (1981) 339.

61. Porkolab, M., Schuss, J. J., Lloyd, B., Takase, Y., Texter, S., Bonoli, P. T., Fiore, C., Gandy, R., Gwinn, D., Lipschultz, B., Marmar, E., Pappas, D., Parker, R., Pribyl, P. *Phys. Rev. Lett.* **53**,5 (1984) 450.

62. Porkolab, M., Lloyd, B., Takase, Y., Bonoli, P. T., Fiore, C., Gandy, R., Granetz, R., Griffin, D., Gwinn, D., Lipschultz, B., Marmar, E., McCool, S., Pachtman, A., Pappas, D., Parker, R., Pribyl, P., Rice, J., Terry, J., Texter, S., Watterson, R., Wolfe, S., *Phys. Rev. Lett.* **53**,13 (1984) 1229.

63. Brower, D. L., Peebles, W. A., Luhmann, Jr., N. C., Savage, Jr., R. L., *Phys. Rev. Lett.* **54**,7 (1985) 689.

64. Brower, D. L., Peebles, W. A., Luhmann, Jr., N. C., *Bull. Am. Phys. Soc.* **29**,8 (1984) 1394.

65. Davidson, R. C., *Phys. Fluids* **29**,1 (1986) 267.